POLITECNICO DI MILANO

Scuola di Ingegneria Industriale e dell'Informazione

Dipartimento di Energia

Dipartimento di Chimica, Materiali e Ingegneria Chimica "Giulio Natta"

FIRST PRINCIPLES ASSESSMENT OF SEMI-EMPIRICAL RATE CONSTANTS FOR STRUCTURE-DEPENDENT MICROKINETIC MODELING

Relatore: Prof. Matteo MAESTRI

Tesi di Laurea Magistrale in Ingegneria Chimica di:

Filippo MOTTA

Matricola 817188

A.A. 2014-2015

ABSTRACT

A first principles assessment of semi-empirical relations to predict chemical reactivity at different surfaces has been performed by means of periodic planewave Density Functional Theory (DFT) calculations. In particular Unity Bond Index-Quadratic Exponential Potential (UBI-QEP) and Brønsted-Evans-Polanyi (BEP)-type relations to predict structure sensitivity in heterogeneous catalytic reactions has been assessed by the analysis of three dissociation reactions of CO, CH and CH_2 on three low index surfaces (100), (110) and (111). The analysis has been performed according to a theory-to-theory comparison. In particular, at the first principles level, Climbing-Image-Nudged-Elastic-Band (CI-NEB) method using periodic DFT with PBE exchange and correlation functionals is employed for the calculation of activation energies of different dissociation reactions which have been analyzed in terms of BEP and UBI-QEP methods.

The results of this work reveal that BEP relation, which is a two parameter model, is able to relate activation energies on different surfaces by means of thermochemical parameters and information on transition state of the investigated class of reaction. Instead, UBI-QEP method shows a applicability range more limited than BEP and this can be related to the quadratic potential used in the method.

All in all, these relations can be used for a first estimation of the activation energy of a reaction at different surfaces only by means of the calculation of the thermochemical properties of reactants and products at a constrained uncertainty with respect to explicit first-principles calculations. This will be of direct use for the application of the hierarchical multiscale methodology to the development of structure dependent microkinetic models in heterogeneous catalysis.

SOMMARIO

Una valutazione “first-principles” di relazioni semiempiriche per predire la reattività chimica su diverse superfici è stata condotta all’interno di questo lavoro di tesi con l’utilizzo di calcoli periodici a onde piane di Density Functional Theory (DFT). In particolare sono state sviluppate relazioni del tipo “Unity Bond Index-Quadratic Exponential Potential” (UBI-QEP) e Brønsted-Evans-Polanyi (BEP) per prevedere la sensitività strutturale di reazioni di catalisi eterogenea. La valutazione dei due modelli semiempirici si è concentrata su tre reazioni di dissociazione di CO, CH e CH_2 sui tre piani prevalenti (100), (110) e (111). In particolare, a livello di principi primi, sono impiegati metodi CI-NEB che sfruttano la DFT con funzionali di correlazione e scambio PBE per il calcolo di energie di attivazione di differenti reazioni di dissociazione le quali sono state interpretate secondo i metodi BEP e UBI-QEP.

I risultati di questo lavoro rivelano che la relazione BEP, che è un modello a due parametri, è in grado di prevedere l’energia di attivazione su diverse superfici attraverso parametri termochimici e il carattere dello stato di transizione della classe di reazione analizzata. Invece, il metodo UBI-QEP è meno predittivo rispetto a BEP, dovuto al fatto che la presenze di un potenziale quadratico è intrinseco al metodo. Il suo campo di applicabilità è risultato essere più piccolo rispetto alla BEP, ristretto a stesse strutture di stessi metalli.

Nel complesso, queste relazioni possono essere utilizzate per una prima stima dell’energia di attivazione di una reazione su diverse superfici unicamente attraverso il calcolo di proprietà termochimiche di reagenti e prodotti con un incertezza limitata rispetto ai calcolo “first-principles”. Questo sarà di impiego diretto nell’applicazione della metodologia gerarchica multiscala per lo sviluppo di modelli microcinetici dipendenti dalla struttura in catalisi eterogenea.

CHAPTER 1. Introduction.

GENERAL OVERVIEW AND STATE OF THE ART

Catalysis plays a fundamental role in modern process history and in particular in Chemical Engineering field. Application of catalytic processes range from energy supply to the enhancing of existing chemical productions, particularly from the economical and environmental point of view. Heterogeneous catalysis alone is responsible for more than 20% of the industrial production in the world [1] and this trend is intended to grow for the years to come.

Several industrial realities need the utilization of catalytic supported particle, such as oil and pharmaceutical companies and those aimed at protecting the environment. For example, in oil and gas industry, the use of catalysts is needed in order to achieve high added value products from crude oil. In pharmaceutical industry, catalysis is needed to obtain complex organic molecules from elementary building blocks. Other catalytic process aim at remove waste pollutants or hazardous substances from industrial outflows.

The development of chemical engineering and catalysis has stimulated the scientific community to gain a deep understanding of the reaction mechanisms. In particular the works of G. Somorjai and G.Ertl [2-3] has clarified a clear interaction between surface structure and reactivity of the catalysts, whose understanding is key for the development of new and improved processes.

The detailed understanding of metal catalysts by theoretical methods is widely acknowledged as an important goal for the scientific community [4-10].

Several works are present in the literature, for instance Silvestrelli, Hütter et al.[11]. In 1997 they studied the dissociation of CO_2 into CO and O on a Pt (111) surface. This work led to the identification of a Langmuir Hinshelwood mechanism through the resolution of a pseudopotential code with LDA and GGA correction.

In 2000 Michealides and Hu [10] performed a DFT analysis for nine catalytic reactions taking place on a Pt (111) surface, determining specifically microscopic reaction pathways for hydrogenation of C to CH and of CH to CH_2. Exchange and correlation effects are approximated using a GGA of Perdew and Wang. The platinum slab was a 3x2 periodic cell.

In 2002 Andreas Eichler [12] published a density functional theory calculation applied to the CO oxidation reactions over Pt, Pd, Rh (111) and (100) surfaces, using VASP code and RPBE GGA ultrasoft pseudopotential. Transition states and reaction pathways were determined using the Nudged Elastic Band (NEB) method and vibrational frequencies were used to determine the prefactor of the rate constant.

In 2002 Nørskov et al. [13] showed that for a class of catalytic reactions there is a universal and reactant independent relation between the reaction activation energy and reactants adsorption energies. Using DFT calculation with a RPBE approximation they investigated the existing relationship existing for CH and CO dissociation onto different (110) and (111) metal surfaces. This investigation was explained by the aim of rationalizing through this universal principle the catalytic design in order to improve it.

Mavrikakis et al. [14] used extensive DFT calculations on Rh (111) and the stepped Rh (211) surface to investigate CO dissociation and the influence of catalyst structure on its ability of breaking C-O bond. They found out that CO dissociation belongs to the class of reactions that are extremely structure sensitive.

In 2004 Morikawa and Nakamura et al. [15] esamined the adsorption behavior and the thermal activation of CO_2 on Cu (100), (110), (111) surfaces , with the package “STATE” used for the resolution of the DFT adsorption problem.

In the same year Gajdoš, Eichler and Hafner [16] studied the trends in CO adsorption on transition and noble metals using VASP code with GGA gradient correction of various flavours (PW91 and RBPE). Metal is modeled by four layers of metals separated by a vacuum layer of approximately double the thickness. The aim of their work was to reproduce lattice constant experimental data and to evaluate the strongest adsorption site for CO.

Assessment and analysis of the effect of the structure are scarce in the literature, in particular, state-of-the-art microkinetic models in heterogeneous catalysis do not account explicitly for the nature of the active site which is responsible for the chemical transformation [17]. Consequently, these models are structureless and they cannot be used for the analysis of fundamental issues of chemical catalysis, such as the structure sensitivity. In fact, all the details regarding each active site (e.g., the prevalent crystallographic planes, edges, corners, defects, electron vacancies, kinks and their relative distribution) are lumped together in the general and abstract concept of “free site”, available at the catalyst surface.

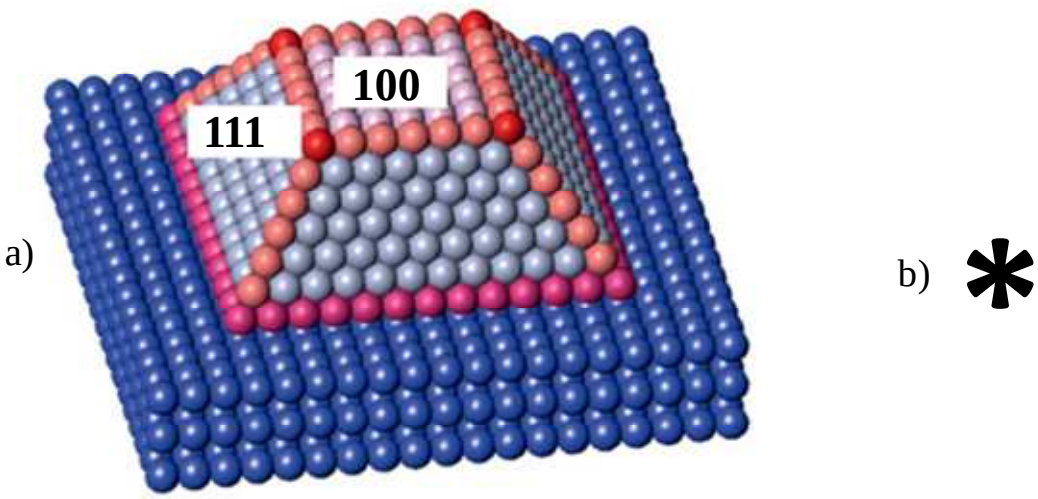

Figure 1:a) Detailed description of a supported nanoparticle metal catalyst versus b) abstract concept of active site typically used in microkinetic modeling.

Attempts for the assessment of semiempirical methods have been performed in literature, such as the BEP relationship and the UBI method.

Michaelides et al. [9] performed DFT calculations to determine transition and final state geometries and energies for a large set of reactions, those are key types of elementary reactions in heterogeneous catalysis. They investigated the linear relationship existing between activation energy and heats of adsorption for dissociative reactions which is BEP relationship. The investigation encompassed more than 50 elementary steps on Pt (111).

The BEP relationship was also studied by Bligaard et al. [18] in 2004, when they investigated the dissociative chemisorptions of N_2, CO, NO, O_2 both on flat and stepped surfaces. The unexpected result they found was that not only do many surface reactions follow the BEP relationship, but there are also classes of similar reactions which follow the same "universal" relationship. They concluded stating that the dissociative chemisorptions energy is a good descriptor of the catalytic activity for series of simple catalytic reactions, and that BEP relations can be considered a universal criterion for the optimal catalyst for all the reactions belonging to the same class.

In 2011 Wang et al. [19] investigated the transition state energies of a large number of essential bond breaking and forming reactions, including among others C-O and C-C bond breaking. All their calculations were performed using the DACAPO plane wave pseudopotential DFT code, describing cores with a ultrasoft pseudopotential; The validation of the relation has been performed on a variety of transition metal surfaces.

In 2011 Maestri and Reuter [20] modified the traditional parameterization procedure of the UBI-QEP method achieving a significant improvement of the accuracy of the UBI against the DFT reference for dissociation reactions.

This poses important challenges for the derivation of fundamental models in applied catalysis [21]. In fact, given the presence of only one general active site, such models cannot be integrated with first-principles calculations, because it is not trivial, even for the case of structure insensitive reactions, which crystallographic plane should be used as model for the first-principles analysis. As typically found in literature, (111) planes are used for this modeling. As result, these models can be applicable only to single (111) ideal crystal catalysts, by assuming negligible the presence of point defects, which is already an harsh approximation [22].

All in all, although the structure of a catalyst has been an important factor in heterogeneous catalysis since the discovery of structure sensitive reactions in single crystal studies [23] its effect on reactivity is neglected in the state-of-the-art microkinetic modeling. Actually, the catalyst particle is dynamic since it changes its structure, shape and size at different conditions in the reactor environment. The inclusion of these effects within the framework of the microkinetic modeling, albeit extremely complex, is of enormous importance in the quest of engineering the chemical transformation at molecular level [24].

MOTIVATION AND SURVEY OF THE MAIN RESULTS

The main goal of this work is the description in an engineering way of relations that can account for the effect of the structure of the catalyst on its intrinsic reactivity. Papers present in literature have investigated the behavior of industrial catalysts progressing from single crystal work in ultra-high vacuum (UHV) conditions to model nanoparticle system [25-27] but a general investigation of structure sensitive relations is lacking.

The use of semi-empirical relations, such as BEP (Brønsted-Evans-Polanyi), UBI, herein validated, and the comprehension of the applicability field of these formulas can rationalize the reactivity of supported nanoparticles, allowing a faster screening and design of catalytic materials.

This work answers the quest of the validation of BEP and UBI relations in the field of heterogeneous catalysis, since this simple relations have extensively been validated outside the field of interest. This simplification allows for the saving of extensive and computational

expensive DFT calculation, and connects the reactivity of a catalytic surface to one or few descriptors, thus very useful for the rapid discovery of promising candidates for a certain type of reaction.

The validation of scaling relations has been performed through the use of DFT; the use of this approach is commonly referred as “first principle” since it is based on the explicit calculation of the electronic structure of the atoms involved in the transformation.

In this work three reactions have been studied for the validation of the scaling relations: these are CO, CH and CH_2 dissociation, whose properties have been analyzed on four different metals as Rhodium, Platinum, Copper and Silver and on three different low Miller index surfaces, namely (100), (110),(111). In particular CO dissociation has also been analyzed at different oxygen coverage.

This work is divided into 5 chapters:

Chapter 2

This second chapter is a brief introduction to quantum-mechanics, that is a theory developed to allow the characterization of matter at atomic scale by the numerical resolution of the Schödinger equation. The main problem linked to the resolution of this equation is the fact that it is function of the position of all the atoms and electrons of the system in exam, thus an enormous computational effort is involved in its resolution. This is the main reason why its resolution requires the use of massive parallel supercomputers. Another problem linked to the resolution of the Schödinger equation is the lack of an exact formulation of its expression. In particular, the electron-electron interaction is necessarily approximated. The resolution is computationally feasible when DFT is implemented, since it guarantees the reduction of the dimensionality of the problem and the Hohenberg and Kohn theorems assure that no approximation is introduced. Some approximation are unavoidable because the problem still remains extremely complex. In the second part of Chapter 2 a brief theoretical introduction to all the semi-empirical models is presented, in particular referring to the BEP relations and the UBI method.

Chapter 3

This third chapter lists the calculated data from the simulations performed. This chapter is divided into three main parts corresponding to the three reactions taken into account which are CO CH and CH_2 dissociation. Each section will make a comparison among the four

different metals and the three surfaces. Carbon monoxide dissociation will also take into account different oxygen coverage effects, so to have another cross-link comparison among metals and surfaces. It is presented that molecules and atoms bind differently onto various adsorption sites of the catalyst, giving rise to different affinity between the metal and the adsorbate.

Binding energies of the various chemical compounds and activation energies of the dissociation reactions have been computed with quantum-ESPRESSO, an integrated suite of Open-Source computer codes for electronic-structure calculations and materials modeling at the nanoscale. It is based on the DFT, plane waves and pseudopotentials (as illustrated in Chapter 2).

Simulations are held on a 2x2 supercell with 3 layers of fixed atoms, obtained by manual parameterization of the atoms of the surface and later verified by the Atomic Simulation Environment (ASE), that is a set of tools and Python modules for setting up, manipulationg, running, visualizing and analyzing atomistic simulations. This code is freely available under the GNU LGPL license.

Chapter 4

The fourth section of this work consists of the systematic analysis of data presented in Chapter 3 with BEP and UBI-QEP relations. The deep survey on the nature of Transition States is herein investigated, and properties of each reaction are rationalized. The Chapter is divided into two different parts, the first one regarding the assessment of BEP relationships and the second one regarding the UBI-QEP. Each of these two sections will provide an assessment of the semiempirical models starting from the most general dissociation reaction class and then focusing on smaller reaction classes: biatomic, triatomic, CH, CO dissociation. In each reaction class the effect of the change of surface within the same metal catalyst and the effect of change of metal within the same catalytic surface have been analyzed.

CHAPTER 2. Methods.

This chapter deals with a brief introduction about the basic concepts underlying the Density Functional Theory (DFT) and the calculation of Minimum Energy Path. The second part of the chapter reports the theoretical basis of the two semiempirical methods BEP and UBI-QEP whose assessment is the aim of this work.

2.1 DFT: A THEORETICAL INTRODUCTION

For an isolated system of given set of interacting electrons moving in an external potential field generated by a set of fixed nuclei (or ions, assumed as a punctual charge) it is fundamental to find the state of electrons with the lowest energy configuration, which we refer to as "ground state energy". The energy is computed by solving the Schrödinger equation which, in the time independent, non relativistic, Born-Oppenheimer approximation is:

$$H\Psi(r_1, r_2, \dots, r_N) = E\Psi(r_1, r_2, \dots, r_N) \tag{2.1}$$

The Hamiltonian operator H is the sum of three terms; the kinetic energy, the interaction with the external potential (V_{ext}) and the electron-electron interaction (V_{ee}). That is:

$$H = -\frac{1}{2}\sum_{i}^{N} {\nabla_i}^2 + V_{ext} + \sum_{i<j}^{N} \frac{1}{|r_i - r_j|} \tag{2.2}$$

In materials simulation the external potential of interest is simply the interaction of the electrons with the atomic nuclei;

$$V_{ext} = -\sum_{\alpha}^{N_{at}} \frac{Z_\alpha}{|r_i - R_\alpha|} \tag{2.3}$$

Here, r_i is the coordinate of the electron *i* and the charge of the nucleus at R_α is Z_α. In order to simplify the notation the spin coordinate is omitted here and throughout this treatise. Eq. (2.1) is solved for a set of Ψ subject to the constraint that the Ψ are anti-symmetric, meaning that they change sign if the coordinates of any two electrons are interchanged. The lowest energy eigenvalue, E_0, is the ground state energy and the probability density of finding an electron with any particular set of coordinates $\{r_i\}$ is $|\Psi_0|^2$.The average total energy for a state specified by a particular Ψ which is not necessarily one of the eigenfunctions of Eq. (2.1), is the expectation value of H:

$$E[\Psi] = \int \Psi^* H \Psi dr \equiv \langle \Psi | H | \Psi \rangle \tag{2.4}$$

The notation emphasizes the fact that the ground energy is a functional of the wavefunction. The energy is higher than that of the ground state unless Ψ corresponds to Ψ_0 - which is known as the variational theorem;

$$E[\Psi] \geq \mathrm{E}_0 \tag{2.5}$$

The ground state wavefunction and energy may be found by searching all the possible wavefunctions for the one that minimizes the total energy.

Hartree-Fock theory consists of an ansatz for the structure of Ψ which is assumed to be an antisymmetric product of functions (ϕ_i), each of which depends in the coordinates of a single electron, that is:

$$\Psi_{HF} = \frac{1}{\sqrt{N!}} \det[\phi_1 \phi_2 \phi_3 \dots \phi_N] \tag{2.6}$$

Where det indicates the matrix determinant. Substitution of this ansatz for Ψ into the Schrödinger equation results in an expression for the Hartree Fock energy:

$$\begin{aligned} E_{HF} = \int \phi_i{}^* (r) \left(-\frac{1}{2} \sum_i^N \nabla_i{}^2 + V_{ext} \right) \phi_i(r) dr \\ + \frac{1}{2} \sum_{i,j}^N \frac{\phi_i{}^*(r_1) \phi_i(r_1) \phi_j{}^*(r_2) \phi_j(r_2)}{|r_i - r_j|} dr_1 dr_2 \\ - \frac{1}{2} \sum_{i,j}^N \frac{\phi_i{}^*(r_1) \phi_j(r_1) \phi_j{}^*(r_2) \phi_i(r_2)}{|r_i - r_j|} dr_1 dr_2 \end{aligned} \tag{2.7}$$

The second term is simply the classical Coulomb energy written in terms of the orbitals and the third term is the exchange energy. The ground state orbitals are determined by applying the variation theorem to this energy expression under the constraint that the orbitals are orthonormal. This leads to the Hartree-Fock (or SCF) equations;

$$\left[-\frac{1}{2} \nabla^2 + V_{ext}(r) + \int \frac{\rho(r')}{|r - r'|} dr' \right] \phi_i(r) + \int v_x(r, r') \phi_i(r') dr' = \varepsilon_i \phi_i(r) \tag{2.8}$$

Where the non-local exchange potential, v_x, is such that :

$$\int v_x(r, r') \phi_i(r') dr' = -\sum_j^N \int \frac{\phi_j{}^*(r) \phi_j(r')}{|r - r'|} \phi_i(r') dr' \tag{2.9}$$

The Hartree-Fock equations describe non-interacting electrons under the influence of a mean field potential consisting of classical Coulomb potential and a non-local exchange potential.

From this starting point better approximation (correlation methods) for Ψ and E_0 are readily obtained but the computational cost of such improvements is very high and scales prohibitively quickly when the number of electrons increase. In addition, accurate solutions require a very flexible description of the wavefunction's spatial variation.

The above discussion establishes that the direct solution of the Schrödinger equation is not currently feasible for systems of interest in condensed matter science, that is the main motivation for the development and use of density functional theory. The main question that arises is: is it necessary to solve the Schrödinger equation and determine the 3N dimensional wavefunction in order to compute the ground state energy?

The Hamiltonian operator (Eq.(2.2)) consists of single electron and bi-electronic interactions, meaning that operators involve coordinates of one or two electrons only. In order to compute the total energy we do not need to know the 3N dimensional wavefunction. Knowledge of the two particle probability density, namely the probability of finding an electron at r_1 and an electron at r_2, is sufficient.

A quantity of great use in analyzing the energy expression is the second order density matrix, which is defined as:

$$P(r_1', r_2', r_1, r_2) = \frac{N(N-1)}{2} \int \Psi^*(r_1', r_2', \dots, r_N') \Psi(r_1, r_2, \dots, r_N) dr_3 dr_4 \dots dr_N \tag{2.10}$$

The diagonal elements of P_2, often referred to as the two-particle density matrix or pair density, are:

$$P_2(r_1, r_2) = P_2(r_1, r_2; r_1, r_2) \tag{2.11}$$

This is the required two electrons probability function and completely determines all two particle operators. The first order density matrix is defined in a similar manner and may be written in terms of P_2 as:

$$P_1(r_1', r_1) = \frac{2}{N-1} \int P_2(r_1', r_2; r_1, r_2)\, dr_2 \tag{2.12}$$

Given P_1 and P_2 the total energy is determined exactly;

$$E = tr\,(H\,P) \tag{2.13}$$
$$= \int \left[\left(-\frac{1}{2}{\nabla_1}^2 - \sum_{\alpha}^{N_{at}} \frac{Z_\alpha}{|r_1 - R_\alpha|} \right) P_1(r_1', r_1) \right]_{r_1 = r'_1} dr_1$$
$$+ \int \frac{1}{|r_1 - r_2|} P_2(r_1, r_2) dr_1 dr_2$$

We conclude that the diagonal elements of the first and the second order density matrices completely determine the total energy. This appears to vastly simplify the task in hand. The solution of the full Schrödinger equation for Ψ is not required, because it is sufficient to determine P_1 and P_2 and the problem in a space of 3N coordinates has been reduced to a problem in a 6 dimensional space.

Approaches based on the direct minimization of $E(P_1,P_2)$ suffer from the specific problem of ensuring that the density matrices are legal that is, they must be constructible from an antisymmetric Ψ. Imposing this constraint is non trivial and is currently unsolved problem. In view of this we conclude that Eq. (2.12) does not lead immediately to a reliable method for computing the total energy without calculating the many body wavefunction.

The observation which underpins density functional theory is that we do not even require P_2 to find E- the ground state energy is completely determined by the diagonal elements of the first order density matrix- the charge density.

2.2 The Hohenberg-Kohn Theorems

In 1964 Hohenberg and Kohn proved the two theorems [28]. The first theorem may be stated as follows:

The electron density determines the external potential (to within an additive constant)

If this statement is true then it immediately follows that the electron density uniquely determines the Hamiltonian operator (Eq.(2.2)). This follows because the Hamiltonian is specified by the external potential and the total number of electrons, N, which can be computed from the density simply by the integration over all space. Thus, in principle, given the charge density, the Hamiltonian operator could be uniquely determined and wave functions Ψ(of all states) and all material properties computed.

Hohenberg and Kohn gave a straightforward proof of this theorem, basing the demonstration on a reduction ad absurdum.

Even if the theorem confirms the existence of a tight/narrow correlation between ground state electron density and ground state wavefunction Hohenberg and Kohn theorem does not explain what kind of shape should have the functional that can solve the Schrödinger equation.

The second theorem establishes a variational principle:

The energy of the overall functional is minimized only by the true electron density which matches the full solution of the Schrödinger equation

The theorem asserts that only the true ground state electron density can be used to return the correct ground state energy. The proof of this theorem is straightforward from the first theorem. This theorem restricts density functional theory studies of the ground state. A slight extension allows variation to excited states that can be guaranteed orthogonal to the ground state but in order to achieve the knowledge of the exact ground state wavefunction is required.

The two theorems lead to the fundamental statement of density functional theory:

$$\delta\left[E[\rho]-\mu\left(\int \rho(r)dr-N\right)\right]=0 \tag{2.14}$$

The ground state energy and the density correspond to the minimum of some functional $E[\rho]$ subject to the constraint that the density contains the correct number of electrons. The Lagrange multiplier of this constraint is the electronic chemical potential μ .

The above discussion establishes the remarkable fact that there is a universal functional $E[\rho]$ which, if we knew its form, could be inserted into the above equation and minimized to obtain the exact ground state density and energy.

2.3 The energy functional

From the form of the Schrödinger equation (Eq.(2.1)) we can see that the energy functional contains three terms: the kinetic energy, the interaction with the external potential and the electron-electron interaction and so we can rewrite the functional as:

$$E[\rho]=T[\rho]+V_{ext}[\rho]+V_{ee}[\rho] \tag{2.15}$$

The interaction with the external potential is trivial;

$$V_{ext}[\rho] = \int \widehat{V_{ext}}\,\rho(r)dr \tag{2.16}$$

The kinetic and electron-electron functional are unknown. If good approximations to these functionals could be found direct minimization of the energy would be possible, and this possibility is nowadays subject of matter of research.

Kohn and Sham proposed the following approach to approximating the kinetic and electron-electron functionals [29]. They introduced a fictitious system of N non-interacting electrons to be described by a single determinant wavefunction in N "orbitals" ϕ_i. In this system the kinetic energy and the electron density are known exactly from the orbitals;

$$T_s[\rho] = -\frac{1}{2}\sum_{i}^{N}\langle\phi_i|\nabla^2|\phi_i\rangle \tag{2.17}$$

Here the suffix emphasizes that this is not the true kinetic energy but is that of a system of non-interacting electrons, which reproduce the true ground state density;

$$\rho(r) = \sum_{i}^{N}|\phi_i|^2 \tag{2.18}$$

The construction of the density explicitly from a set of orbitals ensures that it is legal, i.e. that it can be constructed from an asymettric wavefunction.

If we also note that a significant component of the electron-electron interaction will be the classical Coulomb interaction of Hartree energy (this is simply the second term of Eq. (2.7) written in terms of density);

$$V_H[\rho] = \frac{1}{2}\int\frac{\rho(r_1)\rho(r_2)}{|r_1 - r_2|}dr_1 dr_2 \tag{2.19}$$

The energy functional can be rearranged as:

$$E[\rho] = T_s[\rho] + V_{ext}[\rho] + V_H[\rho] + E_{xc}[\rho] \tag{2.20}$$

Where we have introduced the exchange-correlation functional. E_{xc} is simply the sum of the error made in using a non-interacting kinetic energy and the error made in treating the electron-electron interaction classically. Writing the functional (Eq. (2.15)) explicitly in terms of densitiy built from non interacting orbitals (Eq. (2.14)) and applying the variational theorem (Eq. (2.13)) we find the orbitals, which minimize the energy andsatisfy the following set of equations;

$$\left[-\frac{1}{2}\nabla^2 + V_{ext}[r] + \int \frac{\rho(r')}{|r-r'|}dr' + v_{xc}(r)\right]\phi_i(r) = \varepsilon_i\phi_i(r) \tag{2.21}$$

In which we have introduced a local multiplicative potential which is the functional derivative of the exchange correlation energy with respect to the density,

$$v_{xc}(r) = \frac{\delta E_{xc}[\rho]}{\delta\rho} \tag{2.22}$$

This set of non-linear equations (the Kohn-Sham equations) describes the behaviour of non interacting "electrons" in an effective local potential.

These Kohn-Sham equations have the same structure of the Hartree-Fock equations (Eq.(2.8)) with the non-local exchange potential replaced by the local exchange-correlation potential v_{xc}. We note at this point that the nomenclature in general use and reproduced here is very misleading. As stated above E_{xc} contains an element of the kinetic energy and is not the sum of the exchange and correlation energies as they are understood in the Hartree-Fock and correlated wavefunction theories.

The correspondence of the charge density and energy of the many-body and the non-interacting system is only exact if the exact functional is known. In this sense Kohn-Sham density functional theory is an empirical methodology because the exact functional is not known and neither a way of systematically approaching it. However, the functional is universal because it does not depend on the materials being studied. For any given system we could, in principle, solve the Schrödinger equation exactly and determine the energy functional and its associated potential. This, of course, involves a greater effort than a direct solution for the energy. Nevertheless the ability to determine exact properties of the universal functional in a number of systems allows excellent approximations to the functional to be developed and used in a unbiased and thus predictive studies of a wide rang of materials. For this reason the approximations to density functional theory discussed below are often referred to as ab initio or first principles methods.

The computational cost of solving the Kohn-Sham equations (Eq. (2.16)) scales formally as N^3 (due to the need to maintain the orthogonality of N orbitals) but in current practice is dropping towards N^1 through the exploitation of the locality of the orbitals.

For the calculations in which the energy surface is the quantity of primary interest DFT offers a pratical and potential highly accurate alternative to the wavefunction methods discusssed above. In practice, the utility of the theory rests on the approximation used for $E_{xc}[\rho]$.

2.4 Exchange correlation functionals

The concrete aim is to represent the real nature of the exact functional, and to implement it in an efficient algorithm. Several functional are now developed, but it is crucial to understand the similarities and the differences among them.

A useful classification, referred to a biblical verse from Genesis, is provided by John Perdew:

"*had a dream.. a ladder was set on the earth with its top stretching to heaven… and the angels of God were ascending and descending on it*" [Gen. 28]

Jacob's ladder establishes a list of functionals of increasing accuracy climbing the ladder itself, due to the greater amount of physical information (Figure 2

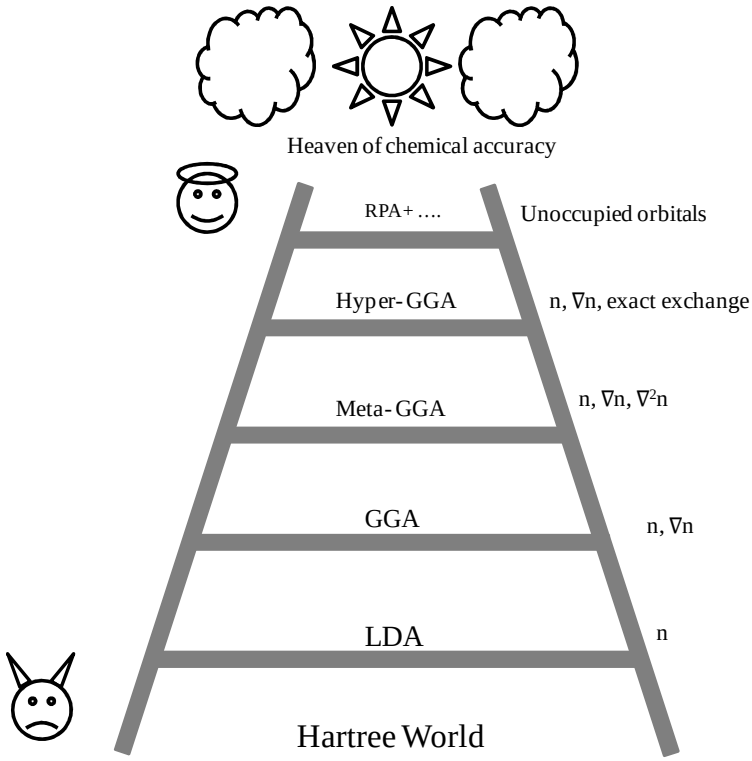

Figure 2: Jacob's ladder

For each of the rungs generally exists:

- Non empirical functionals
- Semi empirical functionals
- Empirical functionals

The simplest and widespread functionals are LDA and GGA, they are often used because of their ability to reproduce experimental data with good agreement by requiring a restricted number of information to characterize the functional expression. Although these functionals

may be mistaken and lose their capability to properly provide a good description of the electronic structure and to generate a reliable potential that affects inter-atomic interactions and thus all chemical and physical properties of matter.

The LDA is employed as assumption to build the corresponding pseudopotential. In the LDA approximation the exchange correlation potential selected is the one of spatially uniform electron gas, whose density is the local electron density.

In this reference system electrons move on a positive background charge, so that the total charge is zero. Electron density represents a constant value everywhere, and this gives a good physical description of a perfect metallic crystal, where the positive charge is produced by ions (nuclei and core electrons), unfortunately atoms and molecules often possess variable density.

$$E_{xc}^{LDA}[n(r)] = \int n(r)\varepsilon_{xc}[n(r)]dr \tag{2.23}$$

Where ε_{xc} is the exchange correlation energy per particle, it is weighted with the probability $n(r)$ to find an electron in r , and is composed by:

$$\varepsilon_{xc}[n(r)] = \varepsilon_x[n(r)] + \varepsilon_c[n(r)] \tag{2.24}$$

Where ε_x is the exchange energy, usually named Slater exchange:

$$\varepsilon_x[n(r)] = -\frac{3}{4}\sqrt[3]{\frac{3n(r)}{\pi}} \tag{2.25}$$

And ε_c instead is not explicit but accurately estimated by Monte Carlo simulations of the homogeneous electron gas; however various authors have proposed analytical expression based on interpolation's procedures.

LDA often fails in accurately describing atoms and molecules whose electron density varies rapidly, so most of the applications in chemistry require a greater accuracy than that one that LDA can assure, as consequence an extension of LDA has been developed, it is Generalized Gradient Approximation, and it is widely employed in solid state physics problems.

GGA considers much information than LDA, it computes not only $n(r)$ at a particular position r, but also takes account of information about gradient of $\nabla n(r)$:

$$E_{xc}^{GGA}[n(r)] = \int n(r)\varepsilon_{xc}[n_\alpha(r), n_\beta(r)]dr + \sum_{\sigma,\sigma'}\int C_{xc}^{\sigma,\sigma'}[n_\alpha(r), n_\beta(r)]\frac{\nabla n_\sigma(r)}{n_\sigma(r)^{2/3}}\frac{\nabla n_{\sigma'}(r)}{n_{\sigma'}(r)^{2/3}}dr \quad (2.26)$$

With σ, σ' referred to either α or β spin.

GGA functional is commonly a local operator in a mathematical sense because its value at r only depends on $n(r)$ and $\nabla n(r)$.

The desired improvement of accuracy is unfortunately not reached because of the loss of many physical properties of LDA, thus new constraints have to be added, in fact, if some parts of GGA violate the negative property of the exchange holes that former are set to zero.

As LDA also GGA is made up of two contributions:

$$E_{xc}^{GGA} = E_x^{GGA} + E_c^{GGA} \quad (2.27)$$

It is possible to build the exchange energy starting from the exchange part of the LDA:

$$E_x^{GGA} = E_x^{LDA} - \sum_\sigma \int F[S_\sigma(r)]\, n_\sigma(r)^{4/3}dr \quad (2.28)$$

S_σ is a dimensionless function, intended as a local inhomogeneity parameter, and is set to zero for the homogeneous electron gas.

This statement allows non-empirical GGA functionals to satisfy the uniform density limit, and several exact properties of the exchange –correlation hole. Even if GGA functionals are able to provide a correct description of several properties of the matter they are also extremely ineffective if particular aspects of certain materials want to be investigated, in fact van der Waals interactions are not properly described by GGA, which uses to underestimate binding energies if the intermolecular attraction is not accounted for. Furthermore, GGA approximately characterizes transition metals and in particular it miserably fails if a transition metal oxide wants to be studied in terms of electrical conductibility, in fact an oxide, with a band gap, is described by both LDA and GGA like a metal that has no gap. Thus more refined functionals have to be built in order to provide a better description of a large amount of physical aspects and to be able to well define disparate systems.

To provide a sensible qualification of the most complex atomic systems upper rungs are needed. Meta GGA functionals are positioned at the third rung of the Jacob's ladder and

include the second order derivative of the charge density, instead the fourth rung is occupied by Hyper GGA functionals that evaluate the exact exchange energy but also possess a critical part that is non local and requires to know the electron density to be properly calculated. Hyper GGA are by far much computationally demanding, they are built as a mixture of the exact exchange and a GGA exchange functional.

In this work PBE ultra-soft Vanderbilt pseudopotentials are employed, because it is widespread in heterogeneous catalysis for the description of reactions on metal surfaces.

2.4 IDENTIFICATION OF THE TRANSITION STATE

The shape of the "Potential Energy Surface" is actually unknown, but sometimes it is possible to guess an initial physical path according to symmetry considerations. With a large number of moving atoms this initial guess cannot be so easy to be defined, thus numerical method to find the correct Transition State have been implemented to carry on a blind search of the TS. This research can be numerically heavy, since a saddle point has to be found, and the Hessian Matrix made up of second derivatives needs to be evaluated. Although DFT already provides first order derivative, that are the forces acting on atoms ($F = -\nabla E$) but not second derivative, as consequence methods that follow low curvature directions from energy minima cannot be simply implemented.

Various minimization methods have been proposed although a continuous function cannot be properly represented with a calculator that has a finite amount of available memory. For this reason the MEP can be thought as a movie made up of a discrete number of snapshots or images which is linked to the next one and belongs to the MEP. Obviously, the more the images, the higher the resolution of the movie thus the better description of the MEP, but also the more computationally intense resources consumption. In fact the intermediate images are actually unknown and they have to be brought on the MEP.

The simplest method is called the "Drag" method, also known with other names since various editions of the same method have been proposed. One of the total N degrees of freedom of the system, the drag coordinate is held fixed while the energy of the system is minimized with respect to the others N-1. Step by step the drag coordinate is increased in order to bring the system from the initial state to the final configuration. The highest computed energy is representative for the Transition State and a good initial guess for the drag coordinate has to be done. Since it is usually unknown, a linear interpolation of the atomic positions between the initial and final state is performed. This initial linear interpolation can lead to a bad initial

path, reminding that the reaction coordinate should be the one that provides an imaginary normal mode at the Transition State. Otherwise the system will not pass through the TS, in fact if the reaction coordinate differs from the exact drag coordinate the drag method fails producing a discontinuous path.

The “Chain-of-State” method instead can work with more than two images connecting the initial and final state. If intermediate images are properly relaxed the method provides an approximation of the whole path and the location of the TS, but intermediate images guide the search in a particular way. The energy of each image, placed with a regular spacing along suitable reaction coordinate is computed; the highest energy image is relaxed along a particular direction defined by the gradient component orthogonal to the line connecting two neighboring images. When the orthogonal component of the gradient becomes close to zero within a certain threshold, no forces act on images to make them slide away from the current path, that is the MEP. When all images are all on the MEP the highest one is no longer relaxed but moved uphill the path towards the saddle point.

The “Elastic Band” method builds the initial path between the two minima by evenly spacing atoms along the path with variable spring constants and by linking the initial and final states with elastic bands. This method was developed by Hannes Jónsson and co-workers as a refinement of the earlier “chain-of-states” method. For a better explanation of this method, it is useful to report a diagram of a two-dimensional energy surface.

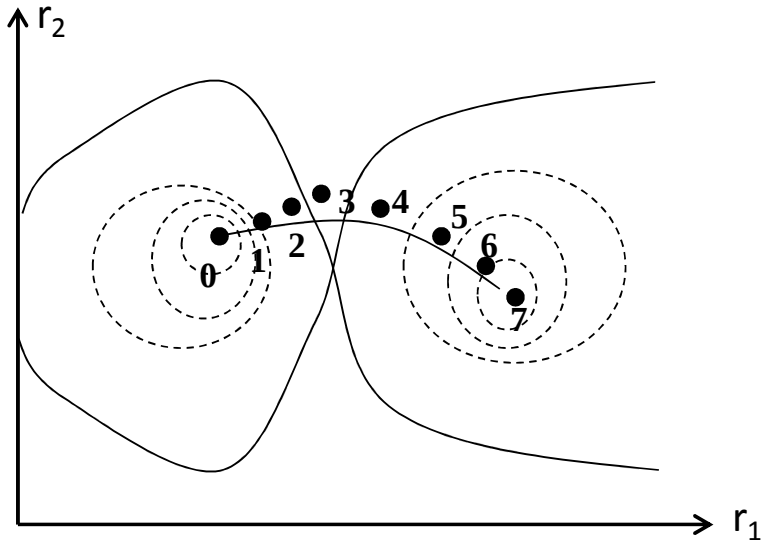

Figure 3: Minimum Energy Path (MEP) representation

In the figure, the MEP is represented by the smooth line connecting the reactant and the product minima passing through a maximum of energy which is the Transition State. Each image on the MEP is indicated with a number from 0 to 7. The calculation of the energy at each image would require eight independent DFT calculations. It is useful to remember that the forces on the atoms are defined by $F = -\nabla E$. Since image 0 and 7 are already located at an energy minimum, they have null forces acting on the atom sets. For all other images, the forces on the atoms are non zero. A MEP is by definition the path where any image along it has a total force oriented directly along the path.

The method is based on the concept that images along the MEP use the lowest energy to define the path between two minima and that images should be evenly spaced along the path.

Mathematically, this corresponds to the objective function:

$$M(r_1, r_2, \dots, r_P) = \sum_{i=1}^{P-1} E(r_i) + \sum_{i=1}^{P} \frac{K}{2}(r_i - r_{i-1})^2 \tag{2.29}$$

Where $E(r_i)$ is the total energy on the i-th image, and K is a constant that defines the stiffness of the harmonic springs (the "elastic bands") connecting adjacent images on the path. This objective function does not include image 0 and P since they are held fixed at the energy minima found with a relax calculation.

Two different problems have been found with this method: the "sliding down" and the "corner cutting" problem. The sliding down problem is linked to the fact that the slope of the MEP changes from image to image, thus moving a particular image along the path may lead to hard or soft spring stretching if a unique stiffness K is used. The corner cutting problem is instead linked to the fact that the set of images that minimizes the objective function does not pass through the Transition State. The difficulty lies in the fact that the true MEP follows a longer path located by the elastic band method.

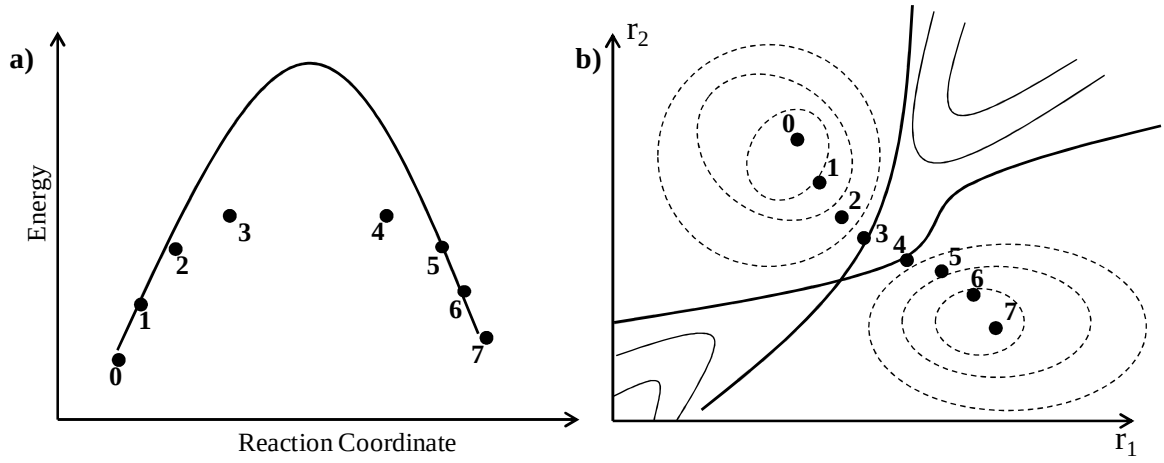

Figure 4: a) Sliding down problem and b)corner cutting

The Nudged Elastic Band method allows the solution to the sliding problem.

If the i-th image is considered, the path direction can be defined by the unit vector τ_i:

$$\tau_i = \frac{r_{i+1} - r_{i-1}}{|r_{i+1} - r_{i-1}|} \tag{2.30}$$

The i-th image will exactly belong to the MEP only if no force perpendicular to the path acts upon the image itself.

$$F_i = F_i^{\perp} + F_i^{\parallel} = F_i^{\perp} + (F_i \cdot \tau_i)\tau_i = (F_i \cdot \tau_i)\tau_i \tag{2.31}$$

In additional the downhill motion of the images is adjusted by considering the spring forces that keep image spread out along the path:

$$F_i^{\perp S} = F_i^{\perp} + F_i^{spring} = F_i^{\perp} + (K_{i+1}|r_{i+1} - r_i| - K_i|r_i - r_{i-1}|) \tag{2.32}$$

The relevant component of the real forces is the one perpendicular to the MEP, instead the interesting component of the spring forces is the one that points along the direction of the MEP. As a consequence only the projection of the spring forces is accounted for:

$$F_i^{Nudged} = F_i^{\perp} + \left(F_i^{spring} \cdot \tau_i\right)\tau_i \tag{2.33}$$

In this way the true force does not affect the distribution of the images along the path, but if this method is not used the spring forces can prevent the band from following the MEP, thus causing the corner cutting phenomenon. Even if the perpendicular force to the path acting on each image is less than the selected threshold there is no warranty that any of the images calculated with the NEB method lies on the Transition State, with the possibility of underestimating the real activation energy of the process.

Henkelman et al [30] introduced a slight modification of the NEB method in order to overcome this possible *impasse*. The development of the "Climbing Image Nudged Elastic Band" method allowed the image with the highest energy to move uphill in energy along the elastic band until the TS is reached. The CI-NEB method allows to have an idea of the whole MEP, which is essential for the understanding of the whole mechanism.

This method has been developed together with electronic structure calculations, in particular plane wave based DFT calculations. The typical scheme which is underlying a calculation of activation energy is to make a few iteration with NEB, in order to identify the image with the highest energy and then the force acting on this image is given by the following expression:

$$F_{i,MAX} = -\nabla E\left(R_{i,MAX}\right) + 2\nabla E\left(R_{i,MAX}\right) \cdot \tau_{i,MAX} \cdot \tau_{i,MAX} \tag{2.34}$$

$$F_{i,MAX} = F_{i,MAX}^{\parallel} + F_{i,MAX}^{\perp} - 2 \cdot F_{i,MAX}^{\parallel} = F_{i,MAX}^{\perp} - F_{i,MAX}^{\parallel} \tag{2.35}$$

The spring forces do not affect the maximum energy image and the spacing between images will be different, as on one side of the saddle point images are compressed and on the other they are stretched out. Variable spring constants can be used to settle interimage spacing, in particular more resolution close to the saddle point is necessary to have a more accurate estimate of the tangent to the MEP and thus stronger springs are used near the saddle point.

A very common practice is to choose the spring constant inside a selected range, varying it proportionally to the energy of the selected image.

$$K_i = \begin{cases} K_{MAX} - \Delta K\left(\dfrac{E_{MAX} - E_i}{E_{MAX} - E_{ref}}\right) & if E_i > E_{ref} \\ K_{MAX} - \Delta K & if E_i > E_{ref} \end{cases} \tag{2.36}$$

Where, given K_{MAX} and K_{MIN} as the maximum/minimum value of the spring constant, $\Delta K = K_{MAX} - K_{MIN}$, E_{MAX} is the maximum value of E_i, E_{ref} is the energy of the higher energy endpoint of the MEP.

All in all, CI-NEB method turns out to be the most efficient and the commonly used one.

Convergence is reached when the forces acting on each image, perpendicular to the MEP, are below the selected threshold, which is 0.15 eV/ Å.

2.5 NEB show case

An example of the CI-NEB is presented in this section of the chapter, for a the CH dissociation on (100) metal surface.

$$CH \rightarrow C + H$$

Since the NEB method requires the atomic coordinates of the initial and final state of the elementary step to be known; several relaxations are performed to bring reactants and products at local minima, choosing the lowest in energy as the best electronic structure because it is representative for the strongest adsorption site.

The electronic structure calculations are performed using the quantum-ESPRESSO code which is based on the DFT method in a plane wave pseudopotential implementation. PBE ultra-soft Vanderbilt pseudopotentials are employed; the plane wave cutoff used is 25 Ry (340 eV) for the wave function and 250 Ry (3400 eV) for the electron density. An 6x6x1 Monkhorst-Pack grid is chosen to map the Brillouin zone, with Marzari-Vanderbilt cold smearing of 0.001 Ry.

Once the initial and final states are completely defined, the NEB calculations can be initialized, in fact the NEB code requires to know the start and the end of the Minimum Energy Path. 12 images are used to describe the MEP. The intermediate images (10) are initially built with a linear interpolation of the atomic positions between the initial and final state, then the shape of the 10 intermediate images is adjusted in order to bring them on the MEP.

NEB calculations are very tricky to converge, the first 25 iterations are performed with low spring constants (k_{min} = 0.2 ; k_{max} = 0.7) in order to allow the intermediate images to easily move on the PES, a wide “ds” (ds=1) that is the “optimization step length” is used. Then, when a suitable shape of the MEP is obtained (forces are below 1 eV/Å) and the image with the highest energy can be univocally determined, the Climbing Image method can be turned on, in order to allow the selected image to climb up, by following the MEP and to exactly reach the Transition State. Spring constants are increased to k_{min} = 0.7; k_{max} = 2.5, in order bring the images surrounding the Transition State closer to it and to provide a better esteem of the tangent to the MEP, instead the optimization step length is shrunk to ds = 0.5 to allow forces to satisfy the convergence criterion.

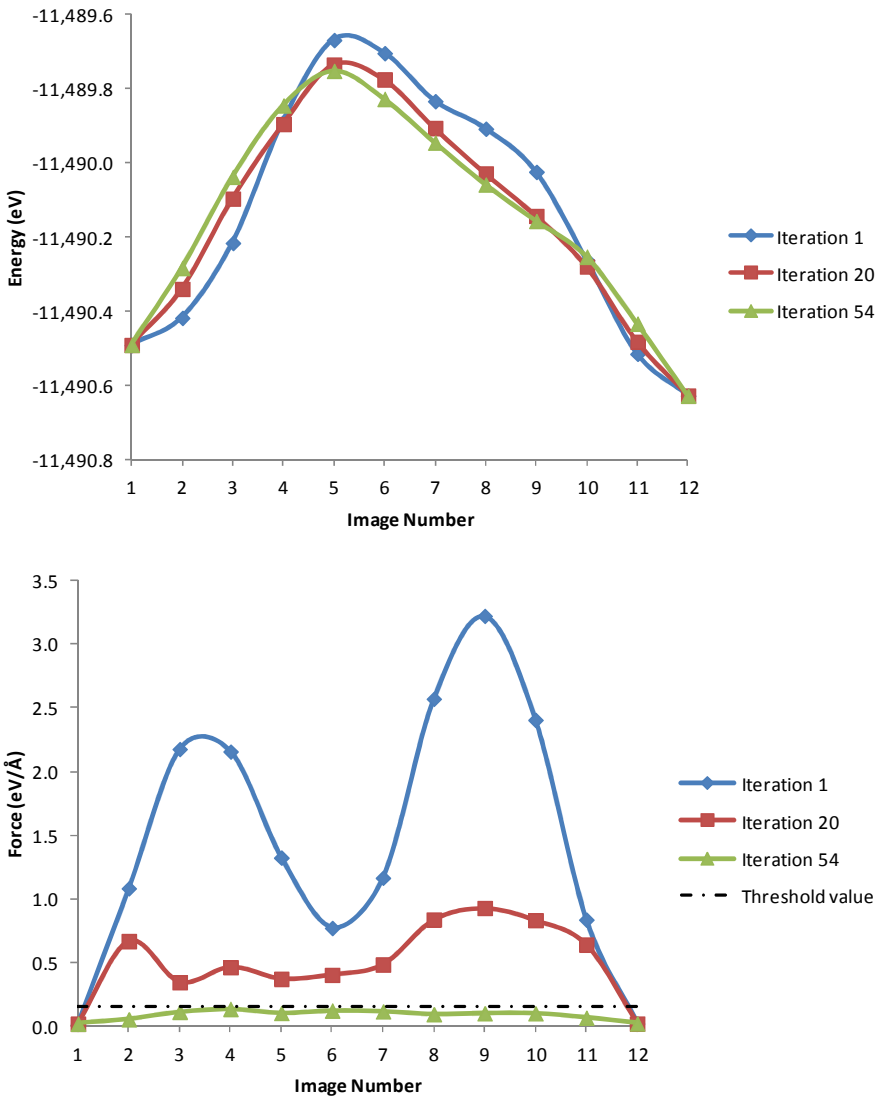

Figure 5: Levels of energy (upper panel) and of forces (lower panel) of each image used to map the MEP after 1, 20 and 54 iterations

The total energy and the force is displayed for all the 12 images (Figure 5), after 20 iterations images appear to belong to the MEP (upper panel) but each force is larger than the selected threshold, instead after 54 iterations the CI-NEB method satisfies the convergence criterion, and all the forces acting on each image are below 0.15 eV/Å.

The activation energy of the process is the interesting output of the various levels of energy calculated, thus an esteem of the barrier the reactant has to overcome is provided as the difference between the initial image and the highest on the MEP.

2.7 MODELS FOR ACTIVATION BARRIERS FOR ELEMENTARY REACTIONS

Over years many models were proposed to understand why elementary chemical reactions are activated. There are many different reasons why activation barrier arise during elementary chemical reactions, that are:

- Bond stretching and distortion during reaction cost energy. This is one of the major causes of barriers to reaction
- In order to get molecules close enough to react, the molecules need to overcome Pauli repulsion and other steric effects
- In certain special reactions there are quantum effects that prevent bonds in the reactants from converting smoothly from the reactants to the products.
- There are also few special cases where reactants need to be promoted into an excited state before a reaction can occur.

It needless to say but it is worth to remember that, while there are many theories about why barriers arise in chemical reactions, the models have not yet been completely quantified except in special cases we will look at. Consequently, while we do have many models, one still does not always know which model applies in each situation. The validation of semiempirical models and the clear identification of their range of applicability is the task this work is interested in.

2.7.1 BRØNSTED-EVANS-POLANYI (BEP) RELATIONSHIP

The Bronsted-Evans-Polanyi (BEP) relationship was first derived by Polanyi and Evans in 1935 and correlates activation energy with the heat of reaction. This is the BEP correlation [31]

$$E_a = E_a^0 + \gamma_P \Delta H_r \tag{2.37}$$

To develop the Polanyi equation we consider the elementary exchange reaction

$$A + BC \rightarrow AB + C \tag{2.38}$$

We consider the superposition of two attraction/repulsion potentials V_{BC}, V_{AB} similar to the Lennard-Jones 6-12 potential. For the molecules BC, the Lennard-Jones potential is:

$$V_{BC} = 4\varepsilon_{LJ}\left[\left(\frac{r_0}{r_{BC}}\right)^{12} - \left(\frac{r_0}{r_{BC}}\right)^{6}\right] \tag{2.39}$$

With r_{BC} distance between molecules (atoms) B and C.

In addition to the Lennard-Jones 6-12 model, another model often used is the Morse potential which has a similar shape

$$V_{BC} = D\left[e^{-2\beta(r_{BC}-r_0)} - 2e^{-\beta(r_{BC}-r_0)}\right] \tag{2.40}$$

When the molecules are far apart the potential V is zero. As they move closer together they become attracted to one another and the potential energy reaches a minimum. As they are brought closer together the BC molecules begin to repel each other and the potential increases. Recall that the attractive force between B and C molecules is

$$F_{BC} = -\frac{dV_{BC}}{dx} \tag{2.41}$$

A potential similar to atoms B and C can be drawn for the atoms A and B. the F shown on the figures below represents the attractive force between the molecules as they move in the direction shown by the arrows. That is the attractive force increase as we move towards the well r_0 from both directions, $r_{AB} > r_0$ and $r_{AB} < r_0$.

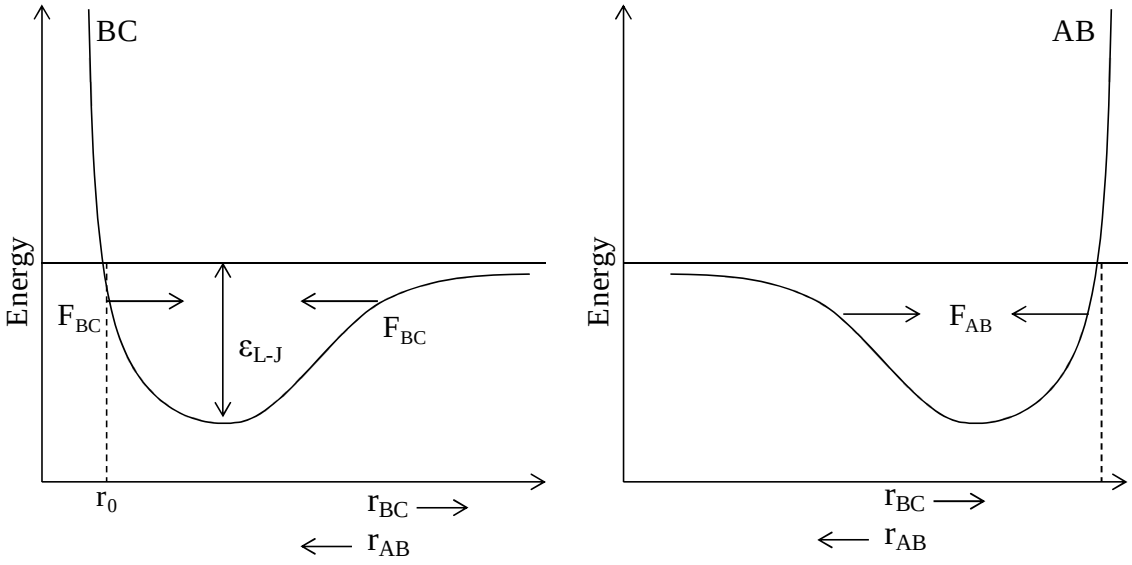

Figure 6:BC, AB potentials (Morse or Lennard Jones)

One can also view the reaction coordinate as a variation of the BC distance for a fixed AC distance,

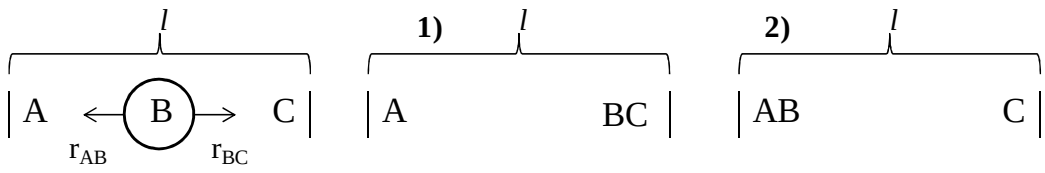

Figure 7: r_{AB} and r_{BC} illustration

For a fixed AC distance as B moves away from C the distance of separation of B from C r_{BC}, increases as B moves closer to A. As r_{BC} increases r_{AB} decreases and the AB energy first decreases then increases as the AB molecule become close. Likewise as B moves away from A and towards C similar energy relationship are found. This situation can be easily represented on a diagram energy vs. reaction coordinate: as B moves towards C from A, the energy first decreases due to the attraction then increases due to the repulsion of the AB molecules as they come close together at point (2) in the above figure. Superimposing the two potentials for AB and BC we can form the following figure:

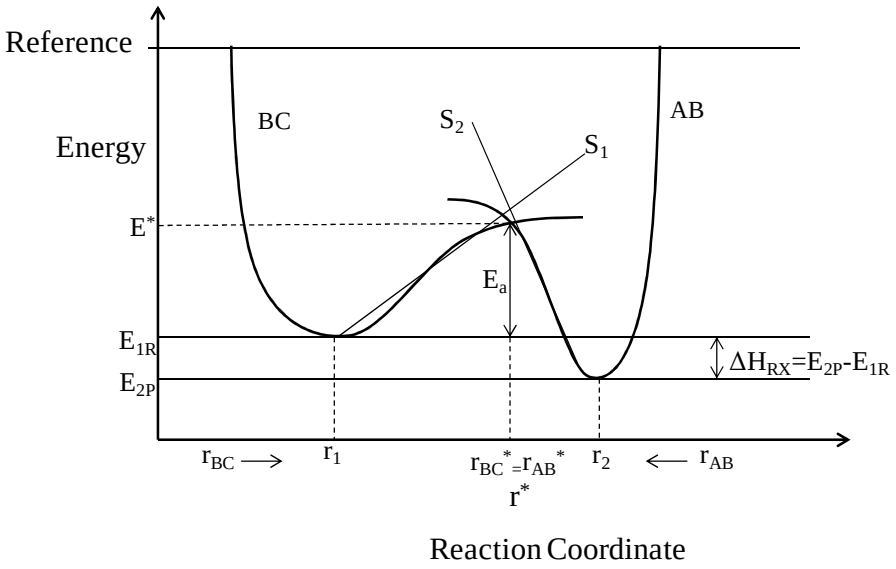

Figure 8: Overlap of potentials (Morse or Lennard-Jones)

Let S_1 be the slope of the BC trajectory between r_1 and $r_{BC}=r_{AB}=r^*$. starting at E_{1R} and r_1, the energy of BC, E_1, at a separation distance of r_{BC} can be calculated from the product pf the slope S_1 and the distance from r_1 at E_{1R} .

$$E_1 = E_{1R} + S_1(r_{BC} - r_1) \tag{2.42}$$

Let S_2 be the slope of the AB trajectory between r_2 and $r_{BC}=r_{AB}=r^*$. similarly for AB, starting on the product side at E_{2P}, as the distance r_{AB} increases the distance r_{BC} decreases and the energy E_2 at the distance r_{BC} is:

$$E_2 = E_{2P} + S_2(r_{BC} - r_2) \tag{2.43}$$

At the height of the barrier, B is equal distant from A and C,

$$r_{BC}^{*} = r_{AB}^{*} = r^{*} \qquad then \qquad E_1^{*} = E_2^{*} = E^{*} \tag{2.44}$$

Substituting E_1^{*} and E_2^{*}

$$E_{1R} + S_1(r^{*} - r_1) = E_{2P} + S_2(r^{*} - r_2) \tag{2.45}$$

And rearranging

$$S_1(r^{*} - r_1) = \Delta H_{RX} + S_2(r^{*} - r_2) \tag{2.46}$$

Solving for r^{*} and substituting back into the equation

$$E_a = E_1^{*} - E_{1R} = S_1(r^{*} - r_1) \tag{2.47}$$

Yields

$$E_a = E_a^0 + \gamma_P \Delta H_r \tag{2.48}$$

Which is the BEP correlation relating the activation energy and heat of reaction.

Where

$$E_a^0 = \left(\frac{S_1 S_2}{S_1 + S_2}\right)(r_2 - r_1) \tag{2.49}$$

$$\gamma_P = \frac{S_1}{S_1 + S_2} \tag{2.50}$$

The implication of this equation is that if one had some way to change either the enthalpy or the free energy of a reaction, the activation energy for the reaction would also change; the activation energy would also change if S_1 or S_2 were to change or if $(r_2 - r_1)$ changed.

A key application of the BEP relationship is that in general stronger bonds will be harder to break than the weaker bonds. To compare this it is useful to compare the potential plot for breaking of stronger bonds and weaker ones. Increasing the strength of the bond, one is increasing the slope S_1, and according to Eq. (2.59)

$$E_a = E_1^{*} - E_{1R} = S_1(r^{*} - r_1) \tag{2.51}$$

If everything else is equal, that should increase the barrier to reaction. The condition we have imposed to $(r_2 - r_1)$, S_1, S_2 to be constant is the reason why BEP relationship can fall when assessed over some particular classes of reaction.

Another important effect is that, if everything else is equal, as you increase $(r_2 - r_1)$ the barrier to reaction increase. One calls reactions with small values of $(r_2 - r_1)$ reactions with tight transition states; if the $(r_2 - r_1)$ distance is small, one does not have to stretch the bond very much for the reaction to happen. Consequently the reaction barrier will be small.

One instead calls reactions with large value of $(r_2 - r_1)$ reactions with loose transition states, with opposite features respect to tight transition states.

In actual practice, everything is rarely equal. Weaker bonds are not necessarily easier to break than harder ones. Reactions with loose transition state do not necessarily have larger barriers to reactions.

This brings up an important point, that is that activation barriers are subtle. If everything else is equal, making the reaction less exothermic will increase the barrier to reaction. If everything else is equal, increasing the amount of bond distortion in the transition state will increase the barrier to reaction. If everything else is equal, pulling electrons out of the transition state, which lowers Pauli repulsion, will lower the barrier reaction. But a substituent may increase the bond strength and decrease the amount of bond distortion. It is very difficult to know how the activation barrier will change in such situation.

Another difficulty is that BEP relationship does not work well all of the time. The linearity works over a limited range of ΔH_r. Moreover BEP relationship can give unphysical results for very exothermic reactions, namely when the product $\gamma_P \Delta H_r$ has an absolute value larger than E_a^0. Generally we can say that the BEP relationship is a useful approximation for reactions that are neither too exothermic nor too endothermic.

All in all, the BEP relationship derives from a linear interpolation of the potential energy diagram. The relationships that follows linearly connects the enthalpy and the activation energy of a reaction. The two fitting parameters E_a^0 and γ_P have a physical meaning: E_a^0 represents the order of magnitude of the activation energy of the reaction; γ_P is representative for the point where the two linear interpolation intersect. γ_P numerical value can range from 0 to 1 by definition; its numerical value is linked to the nature of the Transition State (TS) of the reaction. A value close to 0 means a TS structure that resembles the starting products. Such a transition state is called early TS, which is closer to the starting products on the left of the reaction coordinate than to the products on the right. Instead a value close to 1 is representative for a structure of the TS that resembles the products. Such a TS is called late TS, which is closer to the products on the right of the reaction coordinate than to the starting products on the left.

THE UBI-QEP METHOD

The unity bond index – quadratic exponential potential (UBI-QEP) technique has proved to be a useful approach applicable to small molecules among all semi-empirical methods.

In this method, the two-body interactions (Quadratic Exponential Potential-QEP) is:

$$E\big(x(r)\big) = a\big(x^2(r) - 2x(r)\big) \tag{2.52}$$

The total energy is constructed from additive two-body contributions:

$$E(X) = \sum_i a_i(x_i^2 - 2x_i) \tag{2.53}$$

Under the heuristic condition that the total bond index X of all interacting two-centre bonds is conserved at unity (UBI):

$$X = \sum_i x_i = 1 \tag{2.54}$$

This technique allows for the estimation of molecular binding energies from atomic binding energies and gas-phase bond dissociation energies. Activation barriers are estimated by minimizing the two-body adsorbate configuration modeled through the quadratic exponential potential. This double mapping from atomic binding energies to molecular binding energies and from molecular binding energies to activation energies allows the estimation of a whole microkinetic model just from atomic binding energies, a technique which has proven to be extremely powerful.

In the UBI-QEP approach the intrinsic reaction barrier associated with a surface dissociation reaction is developed from a variational procedure and an interpolation. The variational procedure gives the UBI-QEP mathematical expression for the energy maximum which is an overestimation. The following interpolations a correction for this overestimation.

To facilitate the discussion of reaction energetic, we present in Figure 9 a one-dimensional, potential diagram representing the chemisorptions and dissociation of a diatomic AB, composed of two energy curves: (1) the interaction energy between adsorbate AB as a function of distance from the surface and (2) the sum of the interaction energies of atom A and atom B as a function of the distance from the surface.

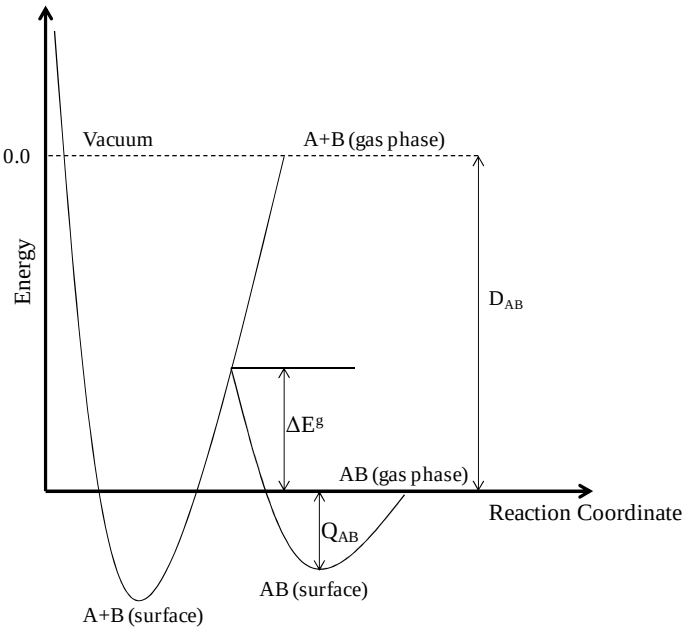

Figure 9: Potential diagram energy against reaction coordinate, meant to be as the AB distance

The first assumption of the UBI-QEP method is that in a many-body system the two body interaction are described by a quadratic potential of an exponential function of the distance called the bond index x. The total energy of the system is assumed to be additive of two-body contributions under the heuristic assumption that the total bond index of the system is conserved at unity.

The UBI-QEP energy expression for interaction energy between AB and the metal surface is:

$$E_{AB} = Q_A(x_A^2 - x_A) + Q_B(x_B^2 - x_B) + D_{AB}(x_{AB}^2 - x_{AB}) \tag{2.55}$$

Which is subject to the UBI constraint

$$x_A + x_B + x_{AB} = 1 \tag{2.56}$$

Where Q_A and Q_B are the binding energies of the atomic species A and B at the surface and D_{AB} the dissociation energy of AB in gas phase.

Since we wish to plot the minimum energy path for the adsorption of AB in the diagram, we optimize the energy with respect to x_A and x_B. The resultant expression is a one-dimensional energy equation that describes the minimum-energy path in terms of x_{AB} .

$$E_{AB} = \left[\frac{Q_A Q_B}{Q_A + Q_B} + D_{AB}\right] x_{AB}^2 + \left[2\frac{Q_A Q_B}{Q_A + Q_B} - 2D_{AB}\right] x_{AB} + \frac{Q_A Q_B}{Q_A + Q_B} - Q_A - Q_B \quad (2.57)$$

It is clear that AB bond index correlates E_{AB} with some measure of the distance of the AB molecule to the surface along the minimum energy path, such as the distance of the midpoint of AB bond.

The other energy curve comprising the potential is the sum of single A and B energy, non interacting ($x_{AB} = 0$).

$$E_{A+B} = E_A + E_B = Q_A(x_A^2 - x_A) + Q_B(x_B^2 - x_B) \quad (2.58)$$

No bond index conservation is imposed since the adatoms are independent of each other.

The maximum is the point at which the dissociation energy profile intersects the A+B chemisorption energy profile, and because everywhere along the E_{A+B} curve $x_{AB} = 0$, the transition state AB bond index, $x_{AB,LJ}$ is zero. Thus we can easily evaluate the energy of the maximum as:

$$E_{AB} = \frac{Q_A Q_B}{Q_A + Q_B} - Q_A - Q_B \quad (2.59)$$

If we convert this expression into a quantity for the reaction barrier , realizing that any point along the reaction energy profile can be expressed in terms of the chemisorptions energy minimum, E_{min} and an increment above the minimum

$$E_{AB} = E_{min} + \Delta E_{AB} = -D_{AB} - Q_{AB} + \Delta E_{AB} \quad (2.60)$$

Putting Eq. (2.62) and (2.63) equal to each other gives:

$$\Delta E_{AB} = \Delta E_{AB}^* = D_{AB} + Q_{AB} + \frac{Q_A Q_B}{Q_A + Q_B} - Q_A - Q_B \quad (2.61)$$

In which ΔE_{AB}^* is the activation barrier relative to the adsorbed AB. From the thermodynamic cycle composed of AB desorption, AB gas-phase dissociation and A and B chemisorptions, one obtains for the enthalpy of the surface reaction:

$$\Delta H = Q_{AB} + D_{AB} - Q_A - Q_B \quad (2.62)$$

So that the reaction barrier relative to the surface adsorbed reactants is:

$$\Delta E_{AB}^{*} = \Delta H + \frac{Q_A Q_B}{Q_A + Q_B} \tag{2.63}$$

This barrier is an overestimation. Since the AB dissociation energy profile is described by a quadratic expression, there can be only one extremum, which corresponds to the AB chemisorptions minimum.

If we could determine the value of the AB bond index at the transition state, we could get the transition state energy simply substituting the bond index into Eq. (2.58). Then the energy difference between the transition state and the chemisorbed state of AB would give the barrier height. The framework of the UBI-QEP method does not provide means to determine this transition state bond index. In lieu of this lack, we can go for the simplest interpolation, namely, taking the midpoint of the energy interval as point of dissociation. This gives for the activation barrier for the AB dissociation:

$$\Delta E_{AB}^{*} = \frac{1}{2}\left[\Delta H + \frac{Q_A Q_B}{Q_A + Q_B}\right] \tag{2.64}$$

This interpolation is tantamount to choosing a value for the AB bond index in the transition state that is dependent on the thermodynamic parameters of the system of interest.

In the common hybrid approach to UBI-QEP all the thermodynamic parameters such as binding energies would be determined by DFT, which is still computationally much less expensive than the explicit calculation of the activation energy.

M. Maestri and K.Reuter [20] in 2011 slightly modified the traditional UBI-QEP approach in order to overcome possible discrepancies between the model and the DFT calculation. Their assessment of the UBI-QEP method has been performed respect to (111) metal surfaces, proposing a modification to the original model that the next paragraph explains

First of all they find out that the choice of the empirical value 0.5 for the interpolation of the TS bond index does not grasp the true nature of the TS itself. If a TS has a geometry which can be interpreted as late, the value of ϕ should be larger than 0.5.

As second point, they find out a discrepancy between the calculated binding energy of AB molecule with the UBI-QEP method and the corresponding DFT value, which may not, in principle, coincide. This discrepancy appears highlighted by a closer inspection in Figure 10

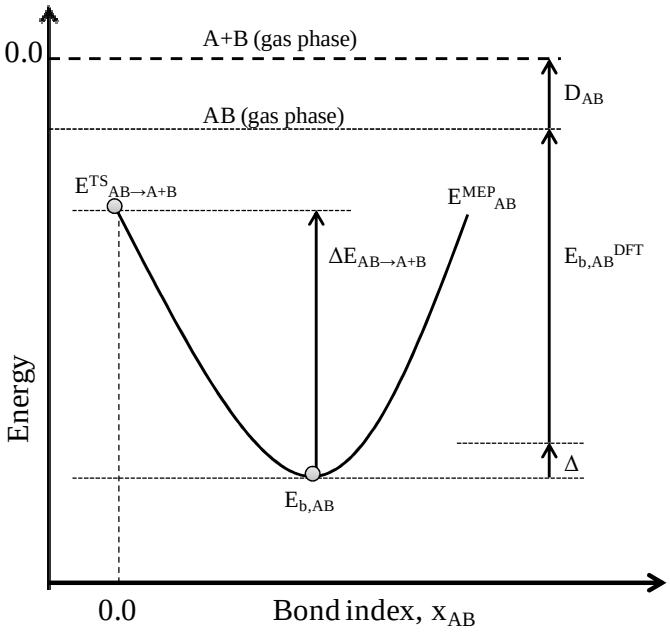

Figure 10: Illustration of the UBI-QEP minimum energy path for a diatomic molecule AB interacting with a solid surface.

As we can notice, the direct use of the Q_{AB} binding energy calculated by means of DFT in the evaluation of ΔH introduces a spurious contribution $\Delta = E_{b,AB}^{DFT} - E_{b,AB}^{UBI-QEP}$.

The deep root of the problem was found to be the inconsistency between the energy of the TS from the UBI-QEP potential and the binding energy of the diatomic molecule from DFT. A simple remedy for this is the shift of the MEP by Δ so that its minimum coincides with the proper DFT binding energy. All in all, instead of calculating the energy of the chemisorbed AB molecule through the equation for E_{min}, it is possible to analytical minimize the equation of the MEP, obtaining:

$$E_{act}^{UBI-QEP} = \phi \left[\frac{\left(\frac{Q_A Q_B}{Q_A + Q_B} - D_{AB} \right)^2}{\left(\frac{Q_A Q_B}{Q_A + Q_B} + D_{AB} \right)} \right] \tag{2.65}$$

This expression now only depends on DFT parameters avoiding the introduction of spurious contribution from the underlying UBI-QEP relations. A significant improvement in the accuracy of the UBI-QEP against DFT reference has been found.

CHAPTER 3. DFT based analysis of dissociation reaction on low index surfaces.

In this chapter DFT calculations for dissociation reaction on different metals and different low index surfaces are reported. These results will be exploited in chapter 4 for the assessment of BEP relationship and UBI-QEP method.

3. DFT analysis of dissociation

Chapter 3 deals with the analysis of dissociation of CO, CH, and CH_2 molecule. Each reaction has been analyzed on four metals, Rh, Pt, Cu, Ag and on three different low index surfaces (100), (110) and (111). CO dissociation has been also analyzed in terms of different oxygen coverage, namely 0 ML, 0.25 ML and 0.50 ML.

A systematic analysis procedure has been employed for the search and the selection of the configuration of reactants and products, which the NEB method requires as input data. Several relax calculations have to be performed in order to find the local minima, and only the lowest in energy is selected as the best electronic configuration for both reactants and products.

Methodology

All electronic structure configuration have been calculated using the quantum-ESPRESSO code, which is based on DFT method with plane wave and pseudopotentials. All unit cells employed to build the (100) (110) and (111) slabs are a 2x2 supercell with 3 fixed layers, a fourth layer allowed to relax in the direction perpendicular to the slab plane and 12 Å of vacuum left between slabs. Only the adsorbates are allowed to move in every directions, thus reducing the computational effort to the minimum for each relax calculation. The use of PBE Ultra-soft Vanderbilt pseudo potential for the representation of the core electrons is determined by the fact that they are widely used and validated for reactions at metal surfaces. In particular Vanderbilt pseudopotentials are able to reduce the cutoff energy if the majority of the weight of the wave function is not kept in the core, after relaxing the norm conservative rule.

The lattice constant of the used for the four metals Rh, Pt, Cu, Ag, later used in the calculation is linked to the Vanderbilt pseudopotential used. The following table shows the good

agreement between calculated and experimental lattice constant of the metals used in the following calculations.

Metal	Lattice Calculated (Å)	Lattice Experimental (Å)	Pseudopotential
Rh	3.85	3.80	Rh.pbe-nd-rrkjus.UPF
Pt	4.00	3.92	Pt.pbe-nd-rrkjus.UPF
Cu	3.65	3.61	Cu.pbe-dn-rrkjus_psl.0.2.UPF
Ag	4.15	4.09	Ag.pbe-dn-rrkjus_psl.0.1.UPF

Table 1: List of the lattice constants used in the calculations and comparison with experimental values. Experimental data taken from http://www.webelements.com/

Plane wave cutoff used during electronic structure's relaxation is 25 Ry (340 eV) for wave functions and 250 Ry (3400 eV) for the electronic density [14]. A 6x6x1 Monkhorst-Pack grid is chosen to map the Brillouin zone, with a Marzari- Vanderbilt smearing of 0.001 Ry. The convergence force threshold chosen is 10^{-3} Rydberg. The convergence criterion is satisfied when all components of all forces are smaller than the threshold.

Binding energies of the system are calculated starting from the total energy of the slab itself, the total energy of the reactant in gas phase, and the energy of the adsorbate bound to the surface.

$$B.E. = E_{slab} + E_{adsorbate,gas\ phase} - E_{slab+adsorbate}$$

This Binding Energy (B.E.) is the quantity of energy which is required to pull an adsorbate off the metal surface back to the gas phase. This value is representative of the strength of the chemical bond. The higher the B.E., the higher the energy to cleave the adsorbate-surface bond.

The electronic structures and the activation energy calculations are also performed using DFT with CI-NEB method implementing quantum-ESPRESSO code. The plane wave cutoff in the calculation used is 25 Ry (340eV) for the wave function and 250Ry (3400eV) for the electron density. A 6x6x1 Monkhorst-Pack grid is used for the k-point sampling of the Brillouin zone, with a Marzari-Vanderbilt smearing of 0.001 Ry.

The Nudged Elastic Band method is used to find the transition states and to map the MEP using 12 images (including the initial and final states). The initial guess of the MEP is a simple linear interpolation, and after a couple interactions, when the general shape of the MEP is obtained and the highest energy image is clearly identified, the CI method is applied.

Convergence is achieved when the projection along the perpendicular direction to the MEP of the force acting on each image is lower than a appropriately chosen threshold value, which is 0.15eV/Angstrom. The threshold value has been chosen as reference for all calculation as a compromise between a fair computational effort and a good accuracy of the calculations. Several convergence analysis have been performed on the limit value of forces of the CI-NEB calculations. The following plot shows that the difference in collected data is minimum, thus not requiring a strict limit on the forces.

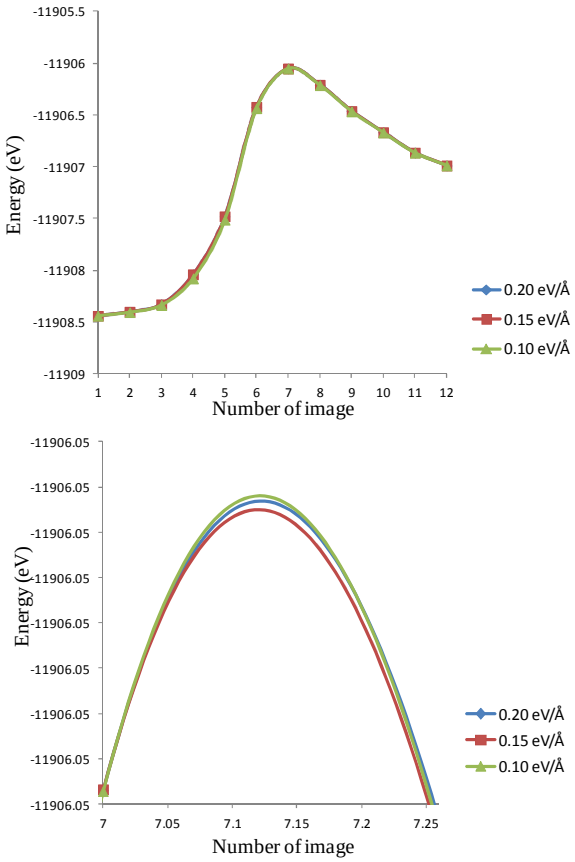

Force Threshold (eV/Å)	Activation Energy (eV)
0.20	2.3874025
0.15	2.3874176
0.10	2.387378

Figure 11: Convergence of activation energy at different forces threeshold

The use of 12 images is a perfect trade-off between the needing of a good accuracy in the calculation and a reasonable computational time. In fact each interaction requires the calculation of 12 electronic structures, and a greater number of images also brings a better mapping of the MEP but also more time consumed in each iteration.

Adsorption Sites on (100), (110), (111) low index surfaces.

Various adsorption sites are present and available on each low index metal surface. They are dependent on the geometry and the atom disposition within the same metal surface. Each

adsorption site is characterized by a different strength in the B.E. of the adsorbate, dependent on the adsorbate-site intrinsic interaction.

(100) Surface

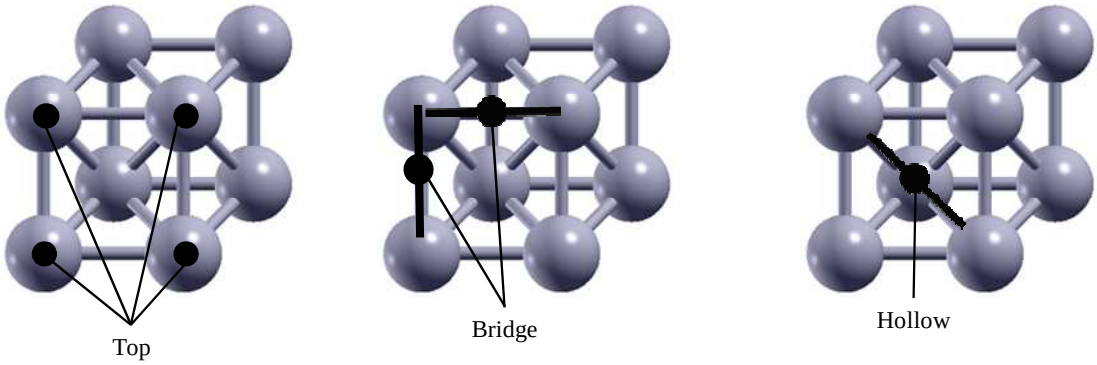

Figure 12: Available adsorption sites on a (100) metal surface

Three adsorption sites are present on a (100) surface, which are namely: the top adsorption site, positioned on the perpendicular direction respect to the metal surface, only respect to the highest layer metal atoms; the bridge adsorption site, which is the intermediate position between two top sites; the hollow adsorption site, which is the position in between four top position. This is the reason why the position is also known as fourfold adsorption site.

(110) Surface

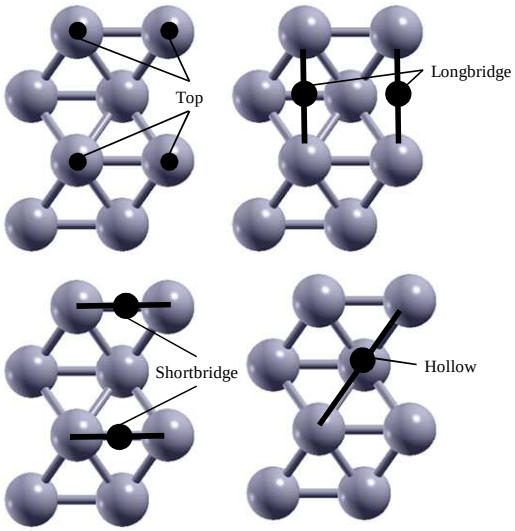

Figure 13: Available adsorption sites on a (110) metal surface

Four possible adsorption sites have been identified on the (110) metal slab. These are: the top adsorption site, which is perfectly perpendicular respect to the plane identified by the metal surface, on top of the metal atoms on the last metal layer. The bridge position of the (100)

metal slab has now two different lengths, due to the fact that if the (100) metal slab could be seen as quadratic one, this (110) slab is rectangular, thus having two different length for the bridge adsorption position: longbridge and shortbridge. The hollow adsorption position is the adsorption position in between four top adsorption sites, at the top position of a metal atom of the second to highest metal layer

(111) Surface

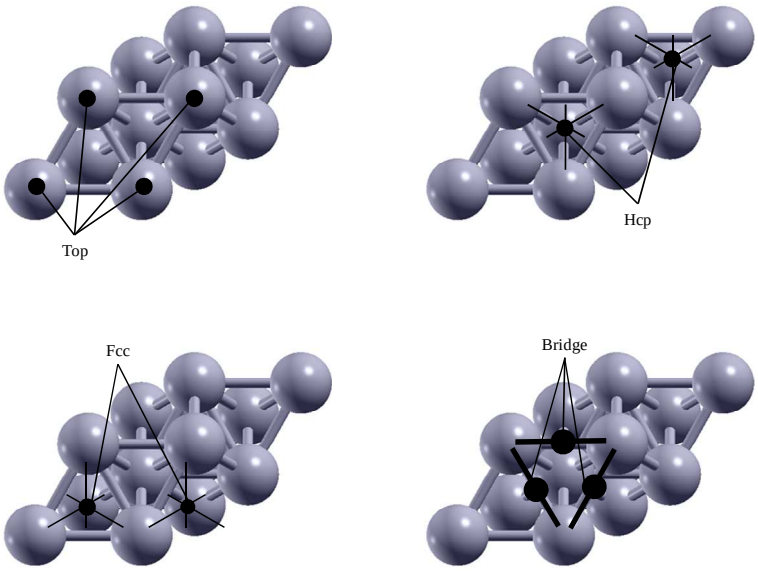

Figure 14: Available adsorption sites on a (111) metal surface

The (111) metal surface has 4 different possible adsorption sites. The first one is the top, which is the position above the metal atoms belonging to the highest metal layer. The hollow site of the (100) surface has now two different features, due to the mode the surface is built. There are two different hollow sites. The fcc one, where there is no other metal atoms directly underneath the adsorption site; in the hcp position, the metal atom belonging to the lower slab is directly underneath the adsorption position. The bridge position is the position in the middle between two top adsorption sites.

Binding Energies analysis of adsorbates

An energetic analysis of the strength of chemical bonds established between adsorbates involved in the reaction pathways is herein realized. These plots will be necessary for the interpretation on the base of chemical strength and the relative unbalancing along metals and surfaces of BEP and UBI trends. The reported binding energy is always referred to the most stable adsorption site among all of the surface, which is also the initial and final position of the NEB calculations later reported in this Chapter.

Analysis of binding energy strength of CH molecule

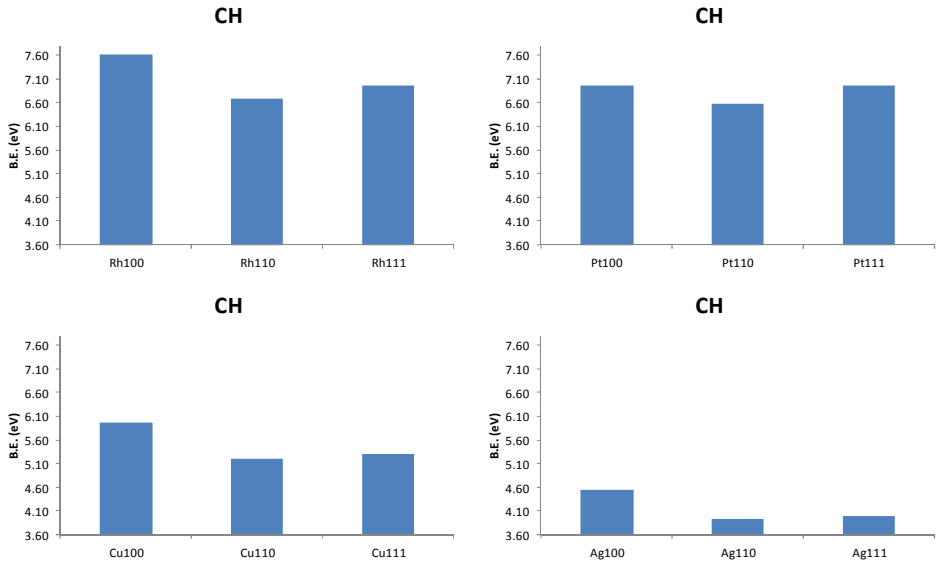

Figure 15: Trends of B.E. of CH molecule adsorbed onto Rh, Pt, Cu, Ag metal surfaces on the most stable adsorption sites

CH molecule shows a stronger binding energy on rhodium surfaces, with the (110) surface which is the weakest among all others in terms of adsorption stability among others. The level of stability among metals for CH adsorbate stability, starting from the highest and ending with the weakest, is Rh>Pt>Cu>Ag; the level of stability among surfaces, respected on every metal surface for CH molecule, is (100)>(111)>(110).

Analysis of binding energy strength of CH_2 molecule

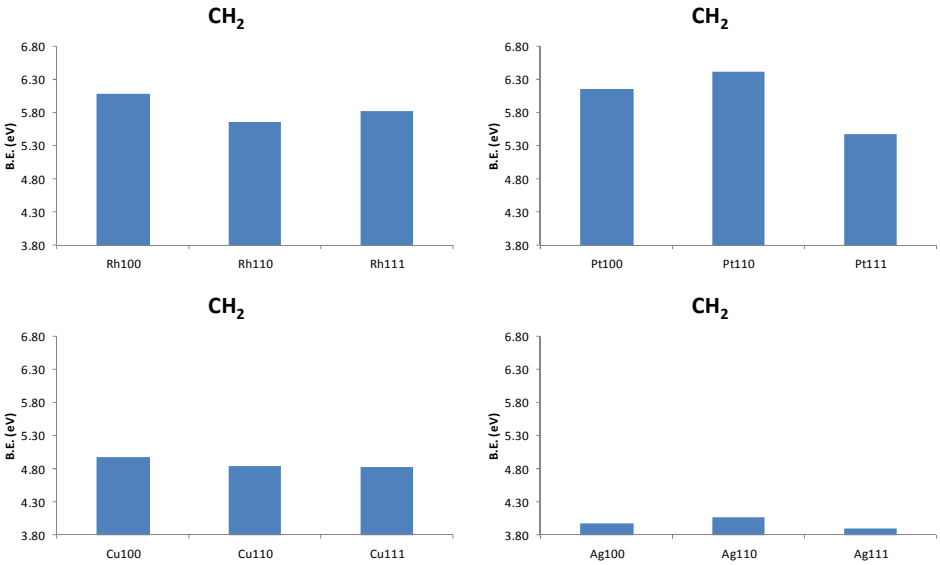

Figure 16: Trends of B.E. of CH_2 molecule adsorbed onto Rh, Pt, Cu, Ag metal surfaces on the most stable adsorption sites

CH molecule shows a stronger binding energy on platinum surfaces, followed by rhodium, copper and silver. The chemical adsorption strength among metals can be schematized as follows: Pt>Rh>Cu>Ag. No unique fashion can be detected on the same metal for different structures. Rh shows higher chemical strength for (100), followed by (111) and (110). Platinum surfaces show different trend. The most stable surface for CH_2 is (110) followed by the (100) and (111). CH_2 adsorption stability on copper follows the increasing index of the surfaces (100), then (110) and (111). Silver shows the same trend as for Platinum. Ag(110) has a better stability for CH_2 adsorption, followed by Ag(100) and Ag(111).

Analysis of binding energy strength of CO molecule

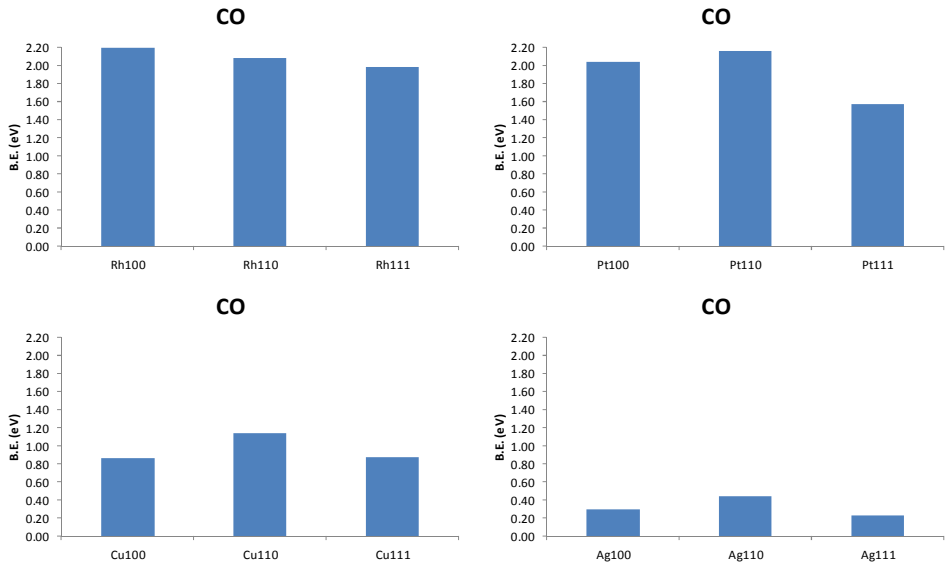

Figure 17: Trends of B.E. of CO molecule adsorbed onto Rh, Pt, Cu, Ag metal surfaces on the most stable adsorption sites

CO molecule has its strongest adsorption site on Pt (110) and Rh (100), which has a B.E. of 2.18 eV. Most stable metals for CO adsorption are Rh and Pt, while Cu and Ag show lower stability. CO adsorption trend among the same metal follows a common trend of platinum, silver and copper, which is (110)>(100)>(111). Rhodium has a particular behavior following a different fashion within the change of surface index which is (100) more stable than (110) followed by (111).

Analysis of binding energy strength of C atom

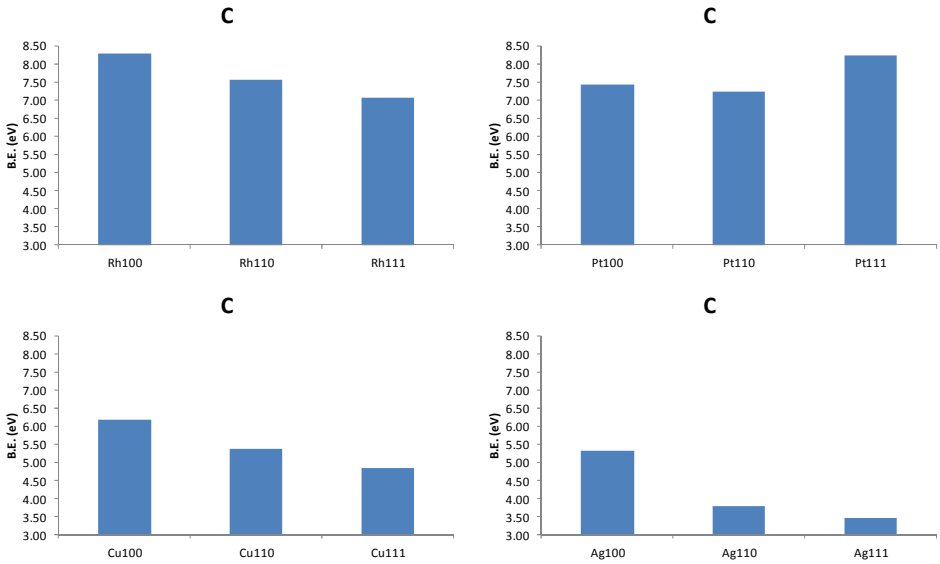

Figure 18: Trends of B.E. of C molecule adsorbed onto Rh, Pt, Cu, Ag metal surfaces on the most stable adsorption sites

C atom shows its most stable adsorption site on Rh(100). The trend for rhodium metal, among surfaces adsorption stability is (100)>(110)>(111). The platinum surface shows the same strength for binding energies, with a different trend of surfaces respect to rhodium: (111)>(100)>(110). Copper and silver metal surfaces show lower adsorption strength respect to rhodium and platinum surfaces, following the same trend of surfaces of rhodium: (100)>(110)>(111).

Analysis of binding energy strength of H atom

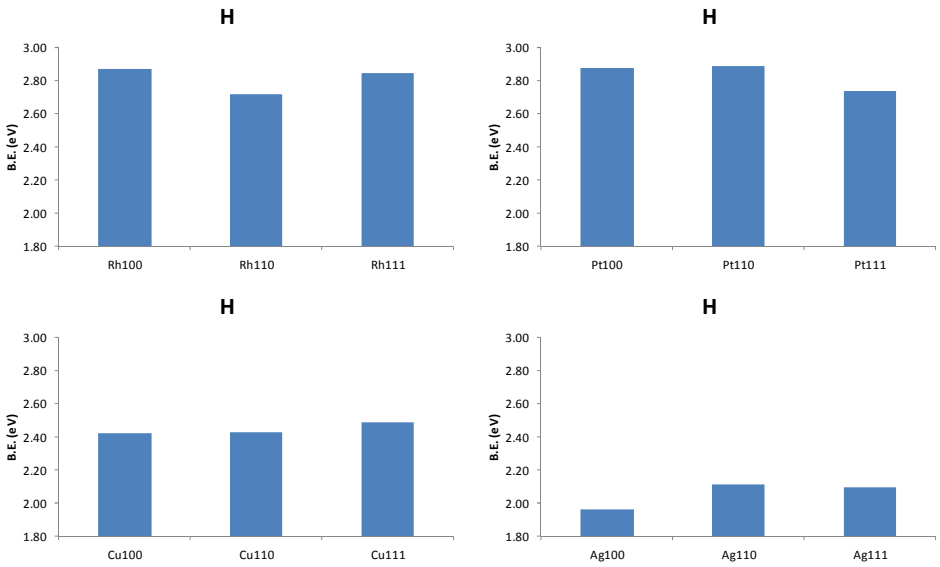

Figure 19: Trends of B.E. of H molecule adsorbed onto Rh, Pt, Cu, Ag metal surfaces on the most stable adsorption sites

H atom shows the highest stability on rhodium and platinum surfaces. Copper and silver have a lower ability to stabilize the adsorbed H atoms. The order of stability for the adsorbed molecule on rhodium surface is (100)>(111)>(110);for platinum surface is (110)>(100)>(111); for copper is (111)>(110)>(100); for silver (110)>(111)>(100). It is worth to notice that B.E. values are different among surfaces of the same metal of decimals of B.E., so that the difference is negligible.

Analysis of binding energy strength of O atom

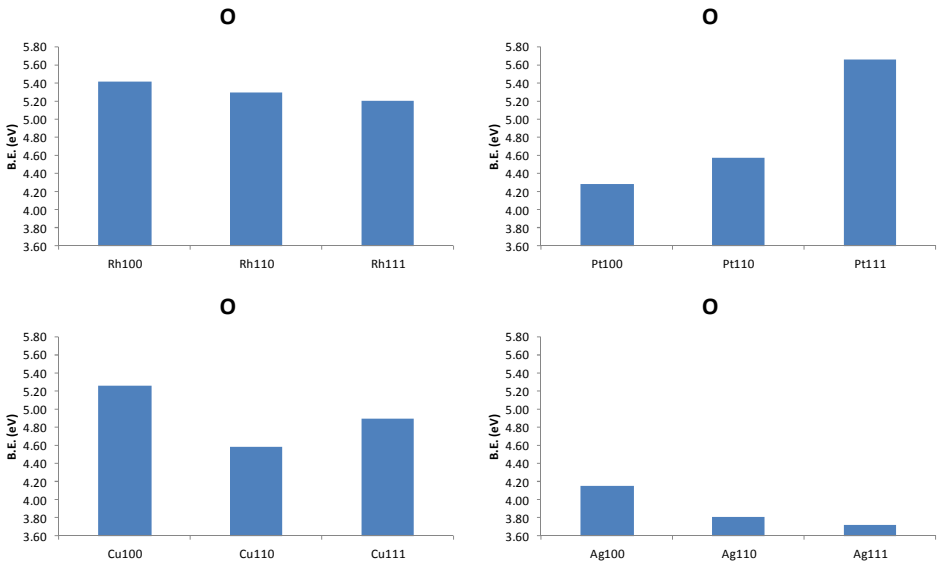

Figure 20: Trends of B.E. of O molecule adsorbed onto Rh, Pt, Cu, Ag metal surfaces on the most stable adsorption sites

O atom ha a decreasing adsorption stability on rhodium surfaces as the index of the surface increases: Rh(100)>Rh(110)>Rh(111). Platinum surfaces follow the opposite trend: the order of oxygen adsorption stability is Pt(111)>Pt(110)>Pt(100). For copper surfaces the order is the following: Cu(100)>Cu(111)>Cu(110). Silver, which shows the lowest adsorption stability, follows the same scheme of rhodium: Ag(100)>Ag(110)>Ag(111).

Elementary Step: CO → C+O

Chemical dissociation of CO molecule has been extensively investigated onto the four selected metals (rhodium, platinum, copper, silver) onto the three different surfaces ((100),(110),(111)) and three different coverage situation (0ML,0.25ML,0.50ML). A description of each metal structure, at different oxygen coverage is reported together with a description of the reaction MEP in terms of geometry of the initial, final and Transition State and activation energy.

Reaction pathways of CO dissociation on Rh (100) at different oxygen coverage

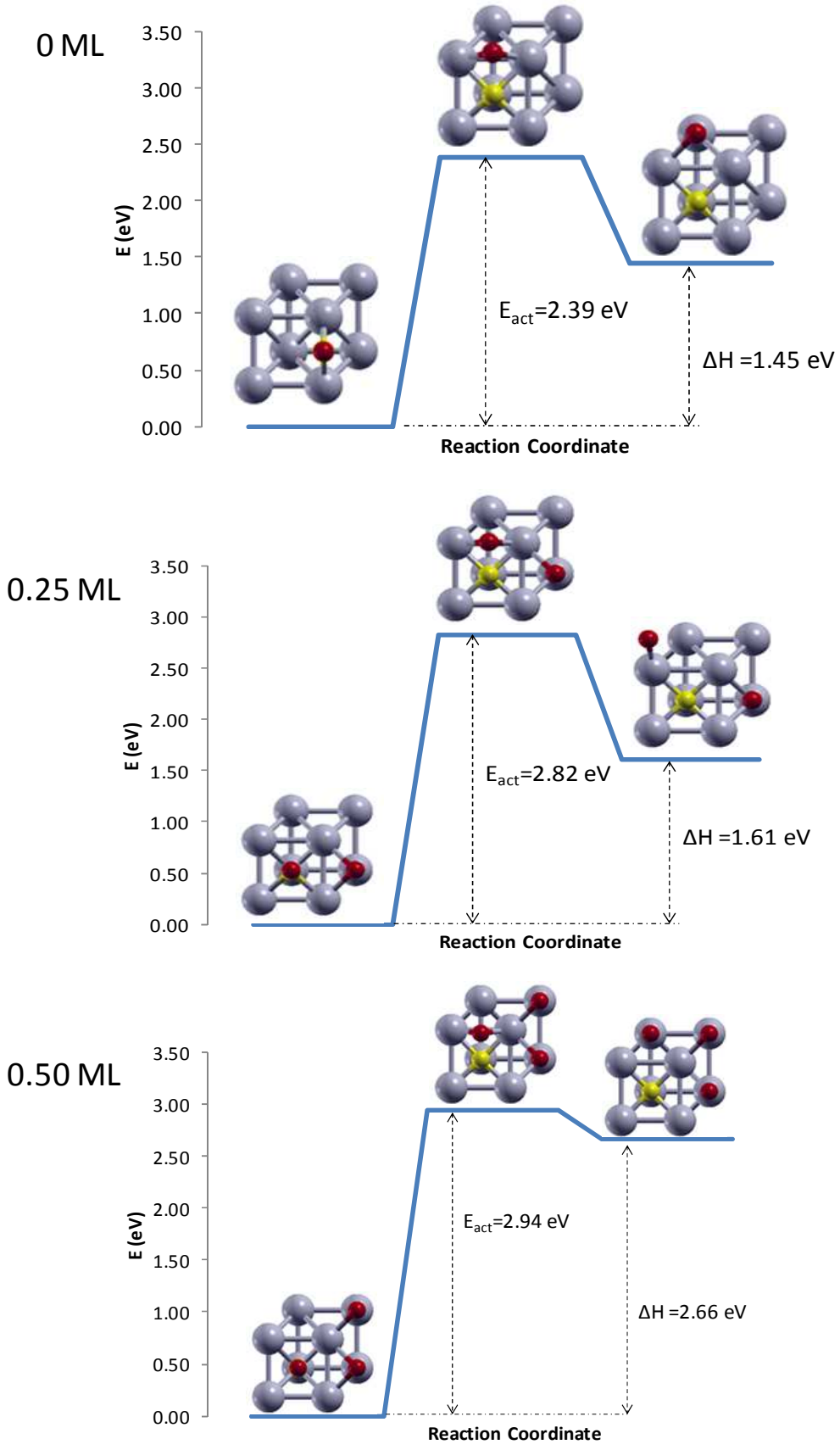

Figure 21: Activation Energy of CO dissociation on Rh (100) 0ML; 0.25ML;0.50ML

Geometry description of 0 ML oxygen coverage

The mapping of the MEP has been performed by NEB calculations which is implementing CI method for the exact location the Transition State (TS). The initial and final state at the metal surface are found according to the systematic procedure abovementioned. As depicted in Figure 21 it is possible to evince that the dissociation reaction is endothermic for 1.45 eV. At the initial state CO is positioned at the bridge adsorption site, the C-O distance is 1.18 Å and the CO molecule is perfectly perpendicular to the metal slab plane. The TS presents C and O atoms already cleaved, with a distance of 1.99 Å and forming a C-Rh-O angle of 58.55°. The C-Rh distance is 2.02 Å and the Rh-O distance is 2.05 Å. The final state has a geometry which is close to the Transition state, with a C-O distance of 2.87 Å, a C-Rh distance of 1.94 Å and a O-Rh bond length of 2.16 Å As clearly seen in Figure 7, the TS appears to have a late geometry. The activation energy of the process is 2.39 eV and the nature of TS is late

Geometry description of 0.25 ML oxygen coverage

The presence of an oxygen atom onto the Rh (100) surface, affects the endothermicity of the CO dissociation, as it increases the energy difference between reactant and product to 1.61 eV. The most stable initial position for CO is the hollow site, where CO molecule is perpendicular to the slab plane and the C-O distance is 1.20 Å. The TS is late, with the C-O complex which is already separated, whose relative distance is 2.00 Å and the C-Rh-O angle is 59.66°. The C-Rh distance is 1.97 Å while the Rh-O distance is 2.05 Å. The final geometry state is represented by C in hollow site and the O atom in the bridge position. The C-O relative distance is 3.49 Å, C-Rh distance is 1.95 Å and O-Rh distance is 1.94 Å. The angle relative to the three atoms, C-Rh-O angle, is 128°. The activation energy of the process is 2.82 eV with a late transition state.

Geometry description of 0.50ML oxygen coverage

The introduction of the second oxygen on the Rh (100) surface increases the energy difference between reactant and product with an endothermicity of 2.66eV. The initial state is found to have the 2 oxygen atoms which act as coverage of the surface in the hollow position, just like the CO molecule, which has a C-O distance of 1.18 Å. Just like all the previous case onto the Rh(100) surface, the molecule is perfectly perpendicular to the slab plane. The transition state has the typical features of a late TS, in which C and O atoms are already separated, with a C-O distance of 1.94 Å and a C-Rh-O angle of 58°. In this TS the C-Rh distance is 1.96 Å, while the O-Rh distance is 2.04 Å. This configuration is very close to the final state, which has both C and O in the remaining two hollow sites on the surface, with a C-

O distance of 3.01 Å, a C-Rh distance of 1.94 Å and a O-Rh distance of 2.22 Å. The angle between C-Rh-O is now 92.52°. The activation energy of this dissociation process is 2.94 eV. Enthalpy differences tend to increase together with activation energy of the process at increasing oxygen coverage.

Reaction pathways of CO dissociation on Rh (110) at different oxygen coverage

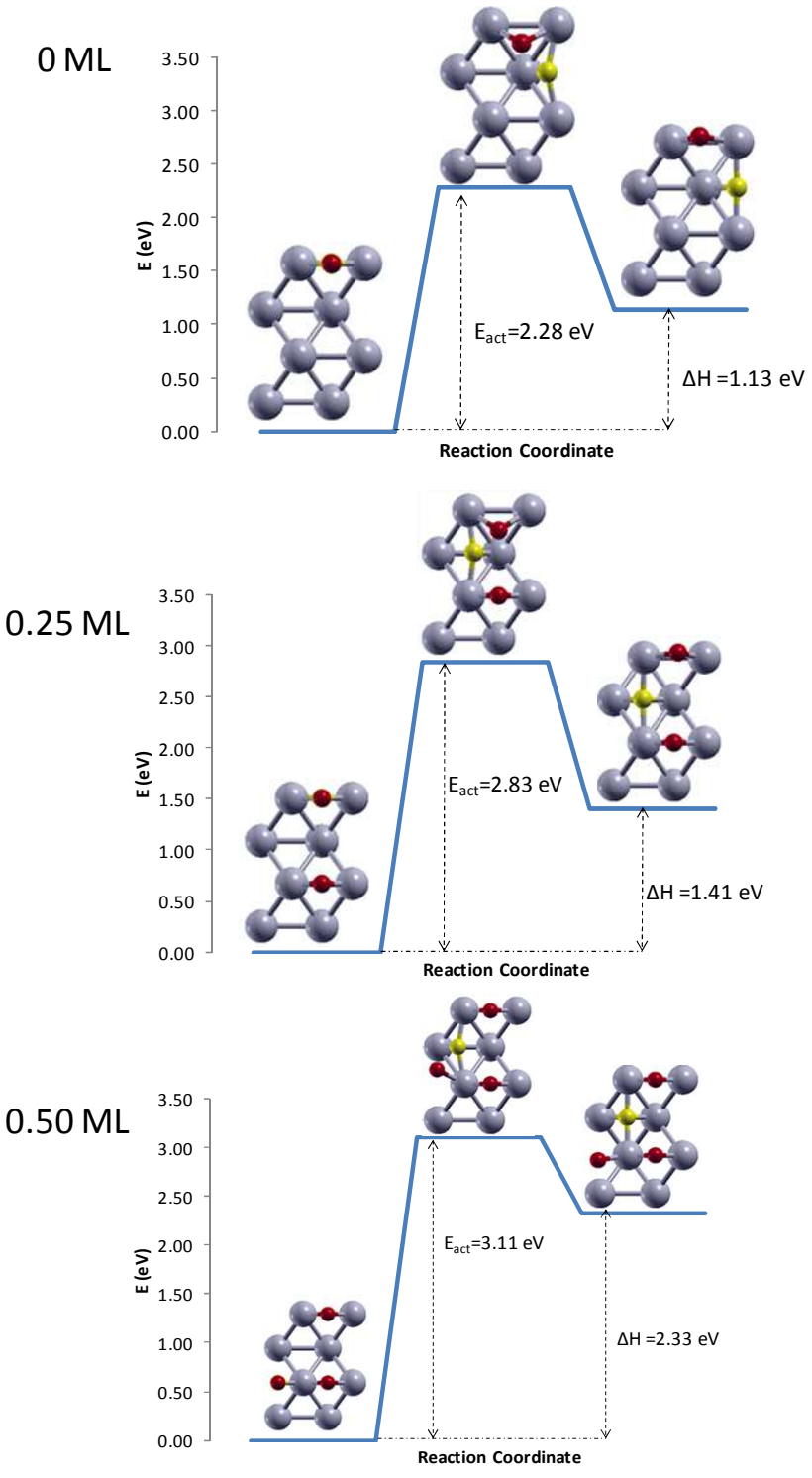

Figure 22: Activation Energy of CO dissociation on Rh (110) 0ML: 0.25ML;0.50ML

Geometry description of 0 ML oxygen coverage

CO dissociation on the Rh (110) with no oxygen coverage is an endothermic reaction for 1.13 eV. The most stable adsorption site for CO is shortbridge, which is perfectly perpendicular to the plane of the Rh slab. C-O distance is 1.18 Å. The TS is late, thus very similar to the geometrical configuration of product. In fact C and O atom are already separated with a mutual distance of 1.90 Å, forming a intermediate angle of C-Rh-O of 55.7°, with C-Rh distance of 1.99 Å and a O-Rh distance of 2.06 Å. The final position, with C in longbridge position and O in shortbridge position, has a C-O distance of 2.99 Å, and an intermediate angle of C-Rh-O 100°. The C-Rh distance is 1.93 Å and the O-Rh distance is 1.96 Å. The activation energy of the process is 2.28 eV with late TS.

Geometry description of 0.25ML oxygen coverage

The introduction in shortbridge position of an extra oxygen atom acting as spectator to the reaction increases the endothermicity of the dissociation process to 1.41 eV. The most stable adsorption site for CO molecule is shortbridge, with a geometry of the initial state very similar to the 0 ML dissociation reaction. The C-O distance of the perfectly perpendicular CO molecule to the slab surface is 1.18 Å. The TS presents a CO molecule already cleaved, thus assuming a late TS. The C-O distance is 1.84 Å and the C-Rh-O angle is 55.3°. The C-Rh bond length is 1.92 Å and O-Rh bond length is 2.04 Å. The final position has C molecule in longbridge position and O in shortbridge position, separated by 3.0 Å with a relative angle C-Rh-O of 101.8°. C-Rh bond is 1.91 Å long and O-Rh bond is 1.96 Å long. The activation energy of the process is 2.83 eV with late TS.

Geometry description of 0.50ML geometry coverage

The introduction of a second atom of oxygen as spectator in the reaction increases the energy difference between product and reactant to 2.33 eV. The most stable adsorption site for CO is shortbridge, with a C-O distance of 1.17 Å. The CO molecule is perfectly perpendicular to the slab plane. The TS is very similar to those at 0 ML and 0.25 ML coverage, with C and O already separated by 1.61 Å. The angle between C-Rh-O is 47.1°. The distance C-Rh and O-Rh are respectively 1.97 Å and 2.04 Å. The TS is late. The final state presents C in longbridge position and O in shortbridge position. Their mutual distance is 3.0 Å and the angle between C-Rh-O is 100.8°. The C-Rh distance is now 1.94 Å and O-Rh is 1.95 Å. The energy barrier for this dissociation reaction is 3.11 eV with late TS. The enthalpy differences increases as the oxygen coverage increases. The activation energy of the reactions increases for increasing oxygen coverage.

Reaction pathways of CO dissociation on Rh (111) at different oxygen coverage

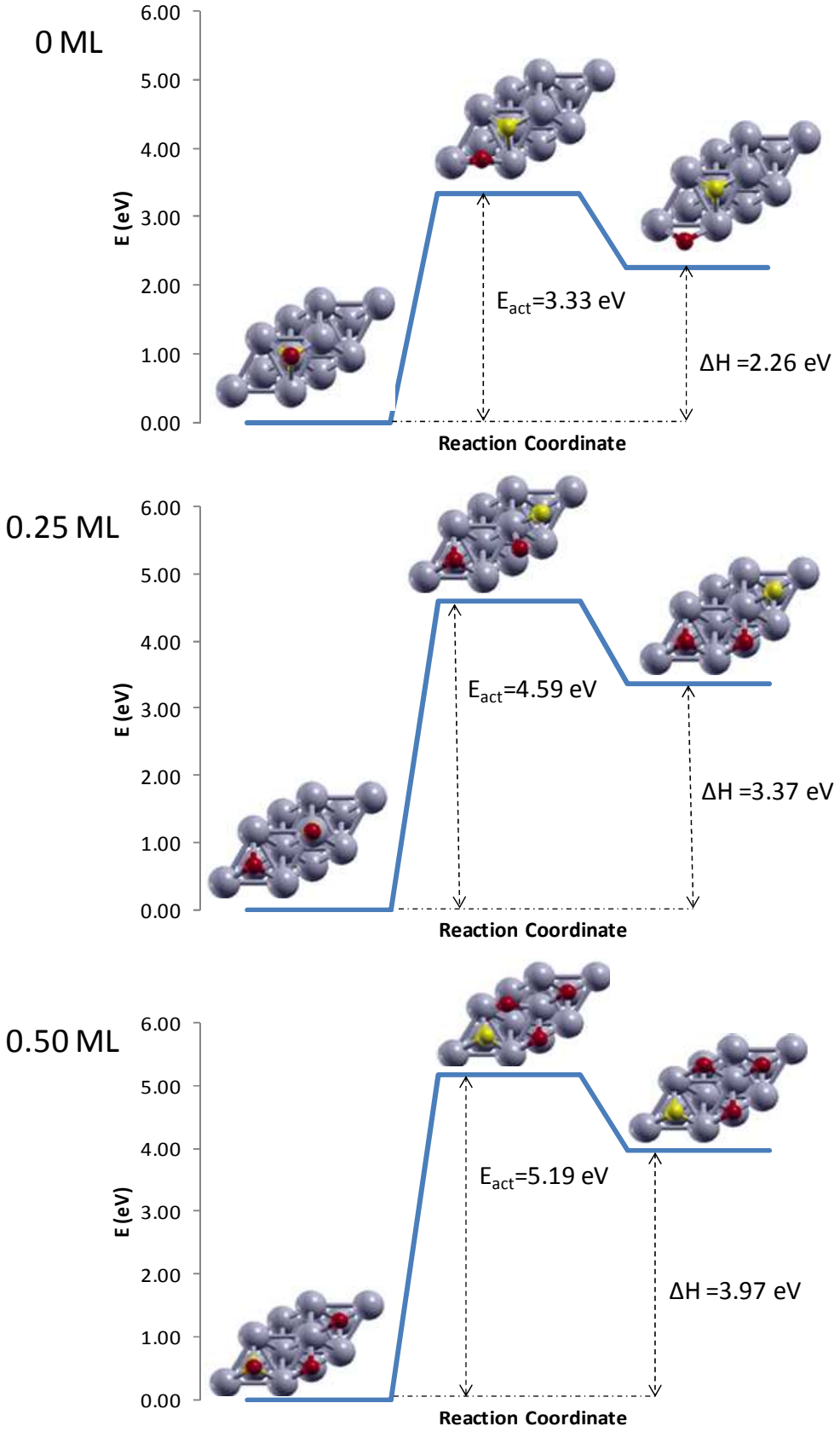

Figure 23: Activation Energy of CO dissociation on Rh (111) 0ML;0.25ML;0.50ML

Geometry description of 0ML oxygen coverage

CO dissociation on Rh (111) surface is an endothermic process for 2.26 eV. The most stable initial adsorption site for CO molecule is hcp. The molecule is perfectly perpendicular to the plane of the slab, and the C-O distance is 1.19 Å. The TS is late, with CO molecule cleaved into C and O, whose reciprocal distance is 2.15 Å and whose angle with Rh is 64°. The C-Rh distance is 1.97 Å and the O-Rh distance is 2.07 Å. The final state has both C and O adsorbed onto hcp sites, with a reciprocal distance of 2.74 Å. They form an angle C-Rh-O of 87°. The C-Rh bond is 1.94 Å and the O-Rh bond is 2.05 Å long. The activation energy of the process is 3.33 eV and the TS is late.

Geometry description of 0.25ML oxygen coverage

The introduction of an oxygen onto the surface, adsorbed in fcc position, increases the endothermicity of the dissociation process to 3.37 eV. The initial most stable adsorption site for the CO molecule is top. It is normal to the slab surface and the C-O distance is 1.16 Å. The TS of the reaction has C and O already separated by a mutual distance of 1.66 Å. The angle they form with the Rh atom is 49.5°, with the two side C-Rh and O-Rh respectively 1.95 Å and 2.00 Å long. In the final position C and O are adsorbed onto fcc sites and they are separated by 2.72 Å. They form a angle in between C-Rh-O of 87.4°. The C-Rh distance is 1.91 Å, while O-Rh distance is 2.02 Å. The activation energy for the process is 4.59 eV. TS is late.

Geometry description of 0.50MLoxygen coverage

The addition of a second oxygen in the fcc position as spectator to the reaction increases the endothermicity of the dissociation process to 3.97 eV. The most stable adsorption site for CO is fcc. The molecule is perfectly perpendicular to the plane and the C-O distance is 1.18 Å. TS is late, with C and O already separated by 1.93 Å. The bond length of C-Rh and O-Rh are 1.97 Å and 2.01 Å respectively. The angle formed by the three atoms C-Rh-O is 58.0°. The final state has both C and O relaxed in fcc position, thus having all fcc sites occupied. The C-O distance is 2.73 Å and the angle C-Rh-O is 87.4°. C-Rh bond is 1.94 Å long and O-Rh is 2.01 Å long. The activation energy of the dissociation process is 5.19 eV with late TS. Activation energies of the dissociation process together with enthalpy differences increase as oxygen coverage increases.

Reaction pathways of CO dissociation on Pt (100) at different oxygen coverage

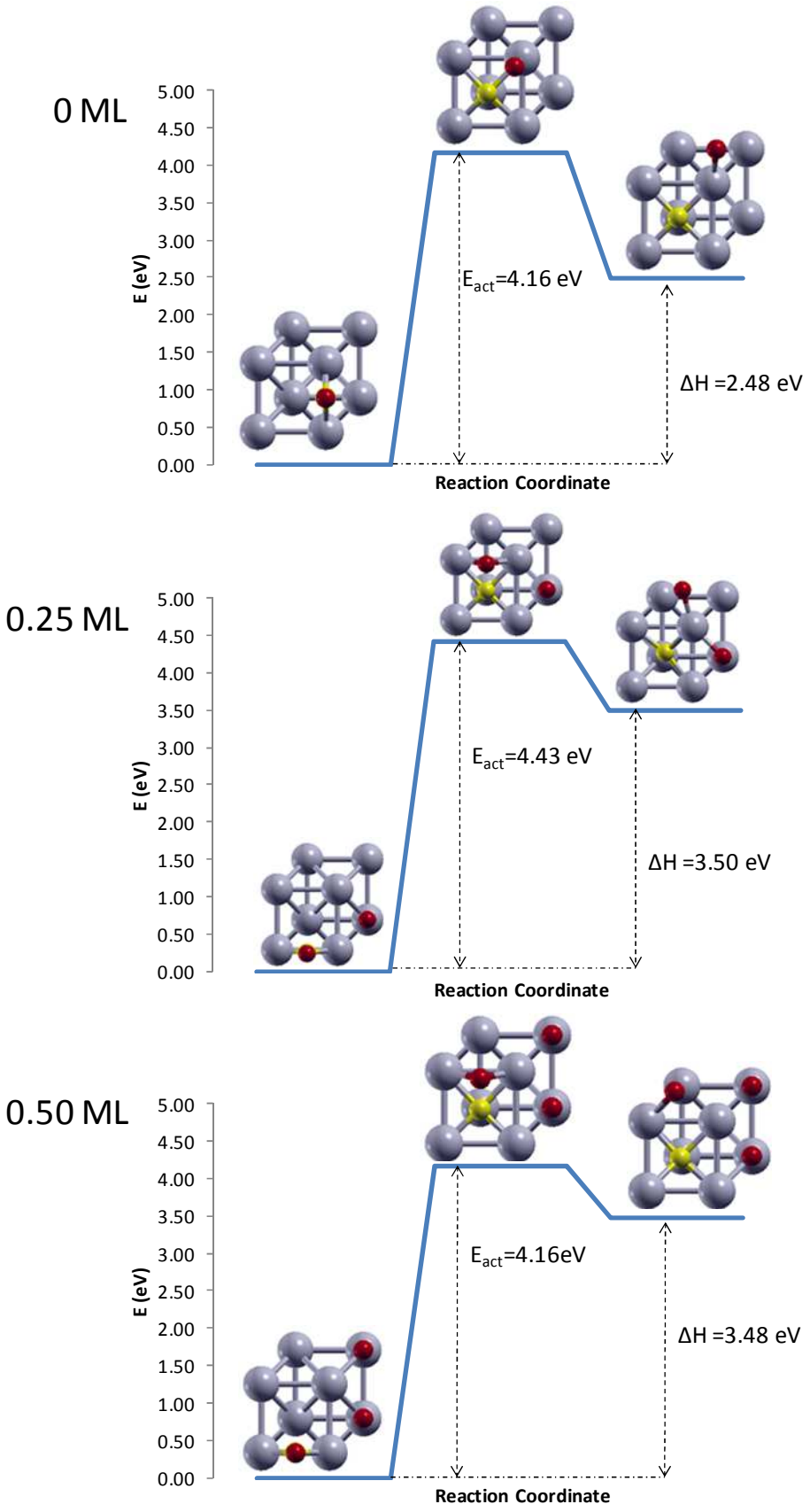

Figure 24: Energy of CO dissociation on Pt (100) 0ML;0.25ML; 0.50ML

Geometry description of 0ML oxygen coverage on Pt (100)

The CO dissociation on the Pt (100) surface with no oxygen coverage is an endothermic reaction for 2.48 eV. The most stable adsorption site for the CO molecule is the bridge position, where C-O distance is 1.18 Å and the bond line is perfectly perpendicular to the surface plane. The TS is late, with C-O atoms separated by a distance of 1.78 Å. The C-Pt is 2.06 Å, while O-Pt length is 1.98 Å. The angle formed by C-Pt-O is 52.0°. The final state presents the C atom adsorbed in the hollow site and O atom in the bridge position with a mutual distance of 3.55 Å. The C-Pt bond length is 2.01 Å and O-Pt bond length is 1.98 Å. They form an angle C-Pt-O of 125.8°. The activation energy of the process is 4.16 eV with late TS.

Geometry description of 0.25ML oxygen coverage on Pt (100)

The addition of an oxygen atom in the fcc position as spectator to the reaction changes the energy difference between reactant and products to 3.50 eV. CO is adsorbed in bridge position, with a C-O distance of 1.17 Å. The molecule is perfectly perpendicular to the surface. The TS is late, with C adsorbed in the position hollow and O in a sort of bridge position. C and O are separated by 1.97 Å. The distance respect to Rh of C and O is respectively 2.05 Å and 2.08 Å. The angle C-Rh-O is 57.1°. The final position presents C in a hollow position, and O in an hybrid position between bridge and hollow. The mutual C-O distance is 3.48 Å, with C-Rh distance 2.04 Å and O-Rh distance 1.91 Å. The activation energy of this process is 4.43 eV with late TS.

Geometry description of 0.50ML oxygen coverage on Pt (100)

The introduction of a second oxygen atom as spectator in the reaction environment decreases the endothermicity of the reaction respect to the 0.25ML configuration to 3.48 eV. The most stable adsorption site is again the bridge one, with a C-O distance of 1.18 Å and the molecule which is perfectly perpendicular to the platinum surface. The TS is clearly very similar to the 0.25 ML configuration, with C in a hollow position and O in a sort of bridge position. Their reciprocal distance is 1.92 Å , with a C-Pt distance of 2.06 Å and a O-Pt distance of 2.08 Å. The angle formed by C-Pt-O is 55.5°. The final state of the reaction presents both C and O in hollow positions, divided by 3.0 Å. The C-Pt distance is 2.02 Å and O-Pt is 2.14 Å. The activation energy of the process is 4.16 eV. The TS is late. Trends of activation energy do not follow the oxygen coverage. The activation energy is maximum for the 0.25ML oxygen coverage, and then decreases to 4.16eV for 0.50ML. Enthalpy differences have the maximum value on 0.25ML and then decreases for 0.50ML oxygen coverage.

Reaction pathways of CO dissociation on Pt (110) at different oxygen coverage

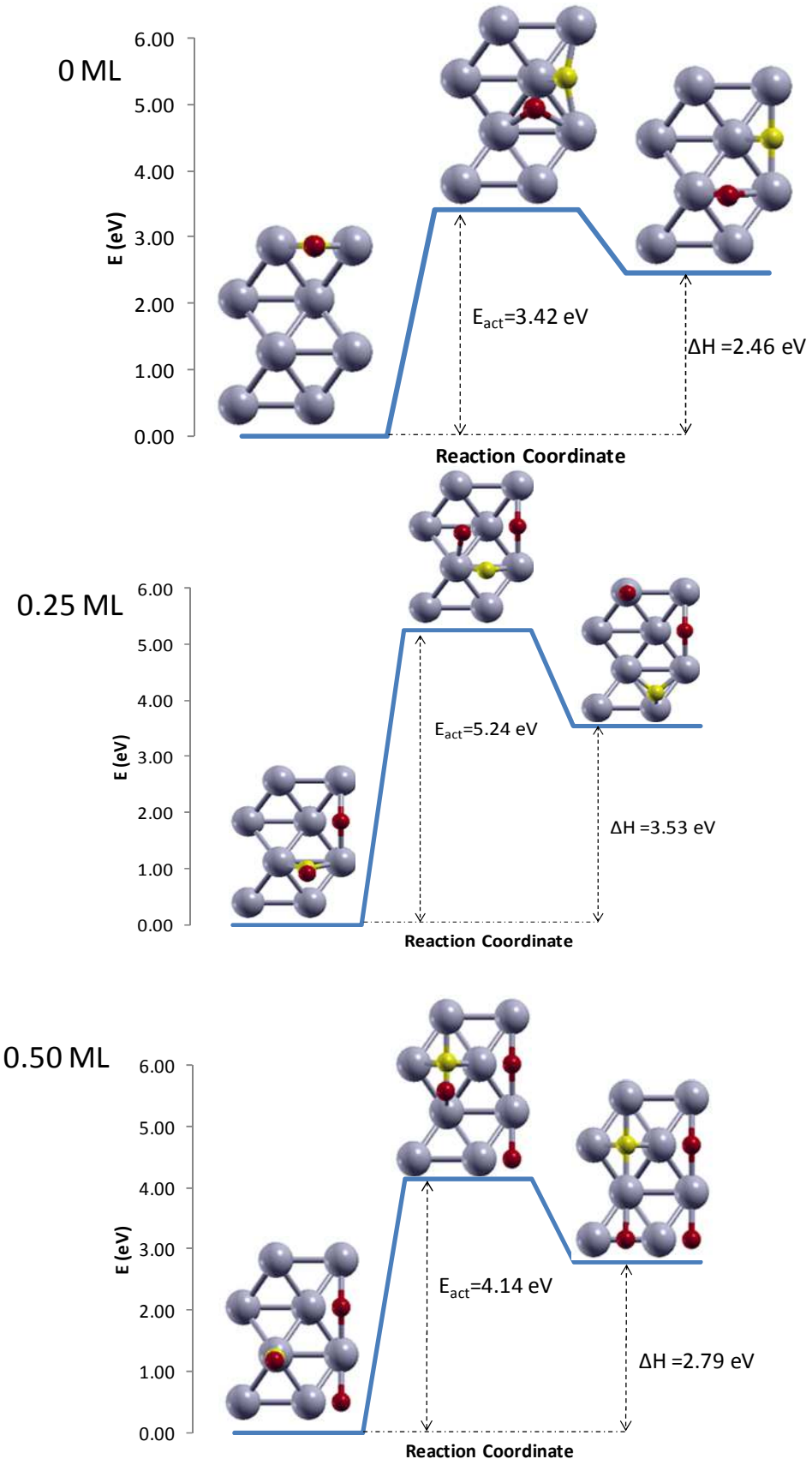

Figure 25: Energy of CO dissociation on Pt (110) 0ML;0.25ML; 0.50ML

Geometry description of 0ML oxygen coverage on Pt (110)

CO dissociation is an endothermic reaction for 2.46 eV on the Pt (110) surface. The most stable adsorption site for CO is the shortbridge, with the CO molecule perpendicular to the metal slab. The C-O distance is 1.18 Å. TS of the dissociation reaction is late, with C and O approximately in their final position, and well cleaved. C-O mutual distance is 1.95 Å, with C-Pt distance 2.06 Å and O-Pt distance 2.11 Å. The angle C-Pt-O is 55.8°. The final state presents C in longbridge position and O in shortbridge position. Their reciprocal distance is 3.07 Å with C-Pt distance of 2.02 Å and O-Pt distance of 2.00 Å. The angle C-Pt-O is wide 99.2°. The activation energy for this process is 3.42 eV with late TSs.

Geometry description of 0.25ML oxygen coverage on Pt (110)

The introduction of an adsorbed oxygen atom in the longbridge position increases the energy difference between reactant and product to 3.53 eV. The most stable adsorption site for the CO molecule is a shortbridge position, with a C-O distance of 1.17 Å. The TS presents a late behavior since C and O are separated by 2.16 Å. The C-Pt distance is 1.93 Å and the O-Pt distance is 2.06 Å. The angle they form with the Pt atom in between is 65.5°. The product is has C adsorbed in between shortbridge and hollow sites, and the O atom in a top position. Their distance is 5.54 Å. They distance from Pt is 1.90 Å for C and 4.30 Å for O. The angle C-Pt-O is 121.4°. The activation energy of the process is 5.24 eV with late geometry of TS.

Geometry description of 0.50ML oxygen coverage on Pt (110)

The CO dissociation on Pt (110) 0.50ML is less endothermic than the same dissociation at 0.25ML. The difference in energy between product and reactant is 2.79 eV, with both oxygen adsorbed on the longbridge position. The most stable adsorption site for CO is top, with a C-O distance of 1.18 eV. The TS of this dissociation is late, with C and O that are separated by 2.25 Å. The C-Pt distance is 2.08 Å and the O-Pt distance is 1.90 Å. The angle C-Pt-O is 68.6°. The final position has both C and O positioned at longbridge sites, with a reciprocal distance of 4.08 Å. C-Pt distance is 2.01 Å while O-Pt distance is 2.08 Å. The angle formed C-Pt-O is quite flat, that is 171°. The activation energy of this process is 4.14 eV with late TS. The maximum enthalpy difference is for the 0.25ML oxygen coverage surface followed by 0.50ML and 0ML. The trend of activation energy follows the same trend: 0.25>0.50>0ML.

Reaction pathways of CO dissociation on Pt (111) at different oxygen coverage

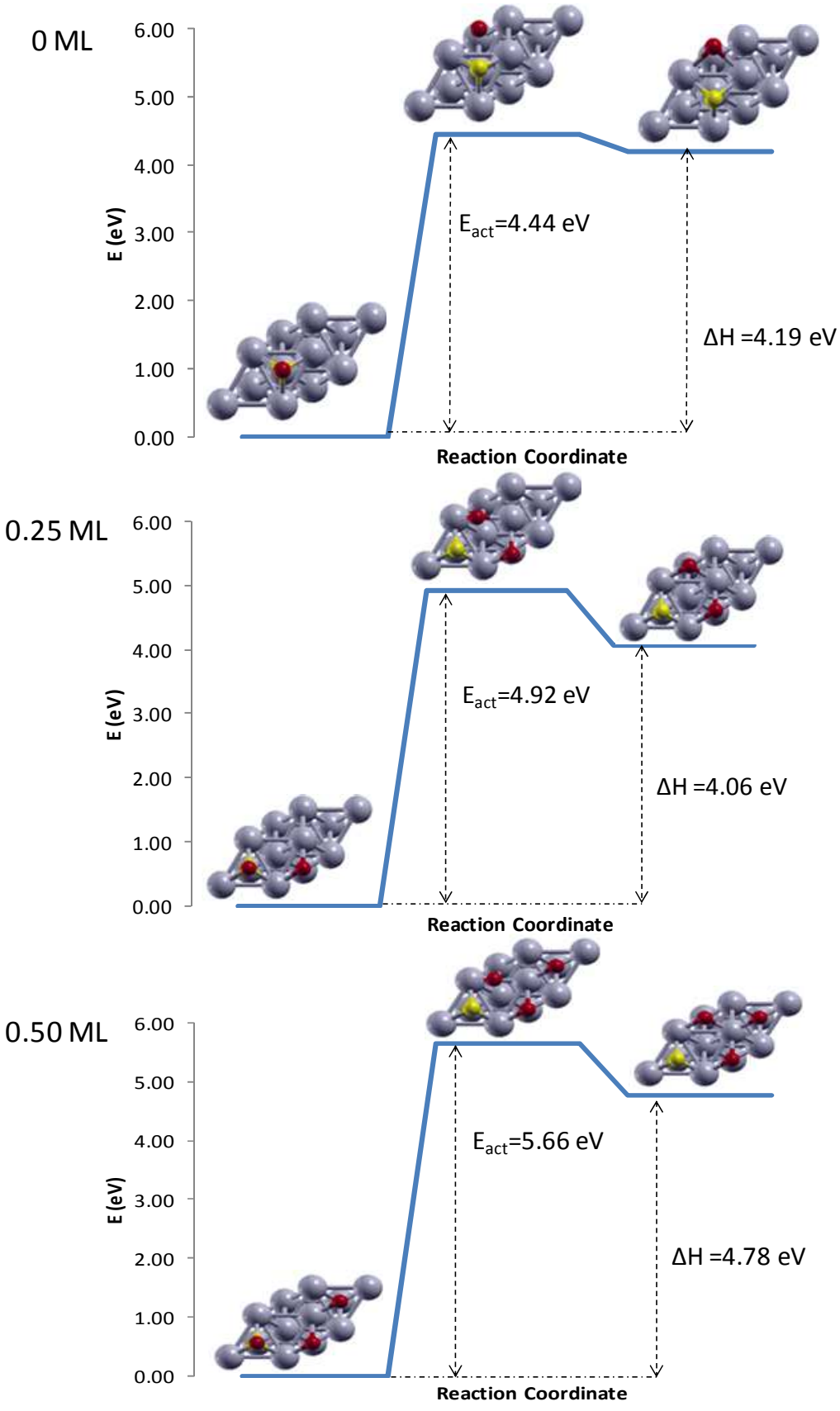

Figure 26: Energy of CO dissociation on Pt (111) 0 ML; 0.25 ML; 0.50ML

Geometry description of 0ML oxygen coverage

CO dissociation is an endothermic reaction on Pt (111) surface for 4.19 eV. The most stable position for the adsorption of CO is the hcp site. The CO molecule is perpendicular to the surface of the metal slab, with a C-O distance of 1.19 Å. The TS for the reaction is very late, with C and O configuration very similar to the product. The C-O distance of the atoms is 1.68Å, with a C-Pt distance of 1.94 Å and a O-Pt distance of 2.54 Å. The angle formed by C-Pt-O is 41.2°. The final state has C in hcp position and O in fcc position. Their mutual distance is 2.51 Å, with a C-Pt distance of 1.96 Å, and a O-Pt distance of 2.17 Å. The angle formed by C-Pt-O is 74.6°. The activation energy of this dissociation reaction is 4.44 eV with late TS.

Geometry description of 0.25ML oxygen coverage

A oxygen spectator atom is introduced in fcc position. The endothermicity of the dissociation process decreases to 4.06 eV. The initial most stable position for CO is fcc. CO molecule is perpendicular to the plane formed by the metal slab, with a C-O distance of 1.18 Å. The TS for this reaction is late, since C and O are well cleaved, with C in hollow position and O occupying a sort of bridge position, 2.11 Å reciprocally distant. The distance C-Pt and O-Pt are respectively 1.95 Å and 2.13 Å. The angle in between C-Pt-O is 62.1° wide. The final state has both C and O in fcc position, with a mutual distance of 2.85 Å. The distance C-Pt is 1.95 Å while O-Pt distance is 2.10 Å. The angle C-Pt-O is 89.3°. The activation energy for the process is 4.92 eV with late TS.

Geometry description of 0.50ML oxygen coverage

A second oxygen spectator is added and the process shows an energy difference between product and reactant of 4.78 eV. The initial most stable CO site is the fcc site, with a perpendicular molecule to the metal slab surface. The C-O distance is 1.18 Å. The TS has a geometry analogous to that of 0.25ML, with C in hollow position and O in a sort of bridge position. The C-O mutual distance is in this case 1.79 Å, with C-Pt distance of 2.00 Å and O-Pt distance of 2.05 Å. The angle formed by C-Pt-O is 52.4°. The final state shows both C and O adsorbed on fcc sites, with a C-O distance of 2.83 Å. The C-Pt distance is 2.00 Å and O-Pt distance is 2.06 Å. The angle C-Pt-O is 88.5°.The activation energy for this process is 5.66 eV with late TS. Enthalpy differences among different surfaces follow the trend of 0.50ML>0ML>0.25ML; activation energy follow 0.50ML>0.25ML>0ML trend.

Reaction pathways of CO dissociation on Cu (100) at different oxygen coverage

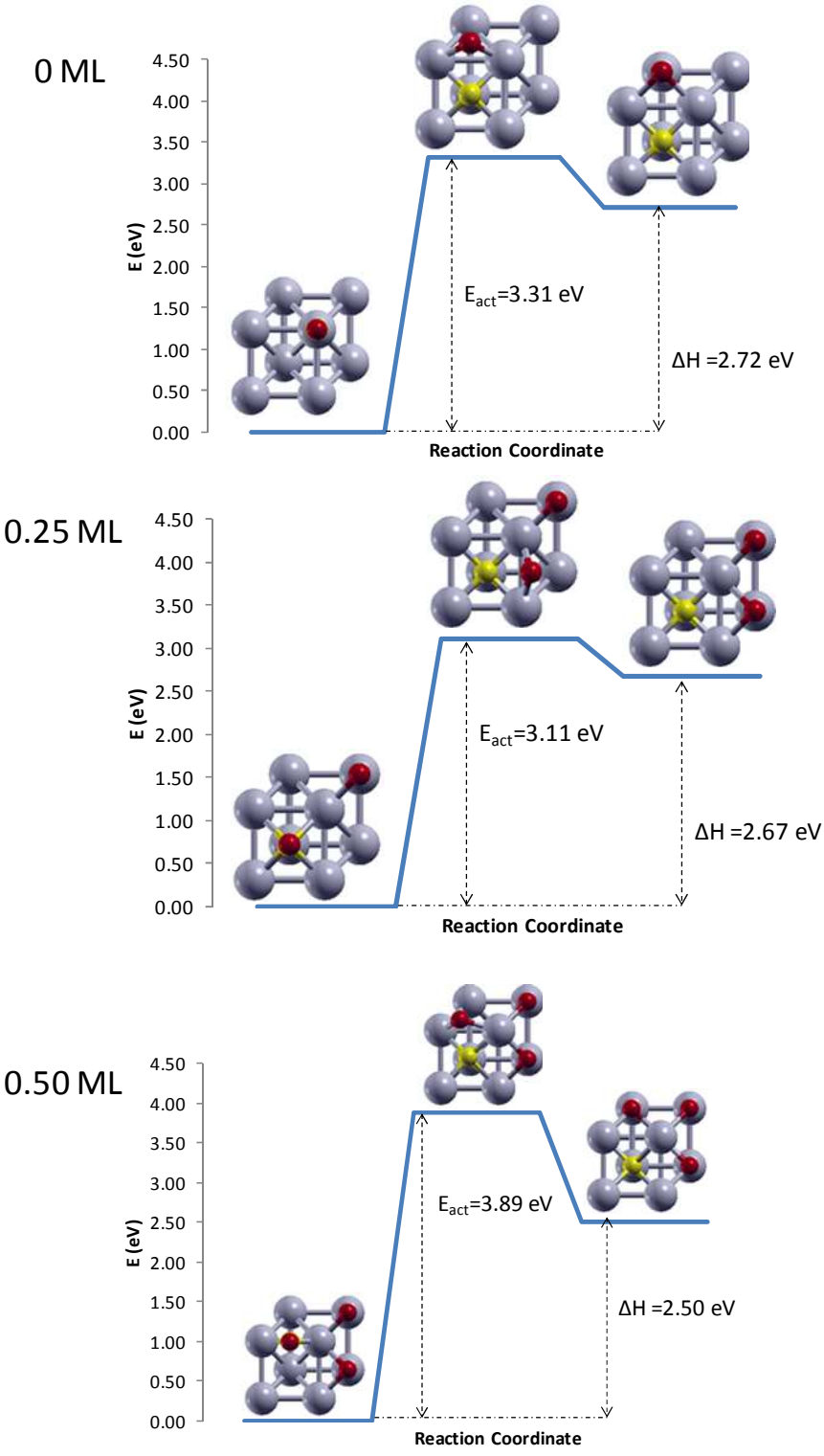

Figure 27: Energy of CO dissociation on Cu (100) 0 ML;0.25ML;0.50ML

Geometry description of 0ML oxygen coverage on Cu (100)

The CO dissociation on Copper surface (100) is an endothermic reaction for 2.72 eV. The most stable adsorption site for CO is the top position. The molecule is perpendicular to the

plane identified by the metal slab with a C-O distance of 1.15 Å. The TS is very late, with a geometrical disposition of the C and O atoms very close to their final position. The C-O mutual distance is 2.05 Å with C-Cu distance of 1.90 Å and a O-Cu distance of 1.93 Å. The angle formed by the two atoms with the copper atom is 64.7°. The final position shows both C and O atoms adsorbed onto hollow positions, with a mutual distance of 2.73 Å. The C-Cu distance is 1.82 Å and the O-Cu distance is 2.05 Å. The angle C-Cu-O is in the product state 89.7°. The activation energy of the dissociation process is 3.31 eV with late TS.

Geometry description of 0.25ML oxygen coverage on Cu (100)

The introduction of a oxygen atom in fcc adsorption site as spectator to the dissociation process lowers the energy difference between product and reactant to 2.67 eV. The most stable adsorption position for CO molecule is the hollow site, which the molecule occupies standing in a perfect vertical respect to the plane identified by the metal slab. The C-O distance is now 1.19 Å. The TS is similar to the 0 ML one , thus late. C occupies a hollow position while O is adsorbed in a sort of bridge position. Their reciprocal distance is 2.01 Å, with C-Cu bond length of 1.83 Å and O-Cu bond length of 1.91 Å. The angle identified by C-Cu-O is 64.9°. The final state has both C and O in hollow position, separated by 2.83 Å. C-Cu distance is 1.84 Å while O-Cu bond is 2.04 Å long. The angle identified by C-Cu-O is 93.7° wide. The activation energy of this dissociation process is 3.11 eV with late TS.

Geometry description of 0.50ML oxygen coverage on Cu (100)

The introduction of the second oxygen atom as spectator to the dissociation reaction in fcc site decreases the endothermicity of the process to 2.50 eV. The most stable adsorption site for CO is the bridge position, which is occupied by a perfectly perpendicular molecule, with a C-O distance of 1.15 Å. The TS does not differ from those on Cu (100) at 0ML and 0.25ML coverage. C is adsorbed onto the hollow site, while O occupies a sort of bridge position. They are completely separated with a geometry typical of a late TS. Their reciprocal distance C-O is 1.89 Å. C-Cu are 1.95 Å far away, while O-Cu are separated by 2.05 Å. The final state has both C and O adsorbed onto hollow sites, separated by 2.87 Å. The distance C-Cu is 1.83 Å while O-Cu 2.27 Å. The angle formed by C-Cu-O is 88.4°. The activation energy of this CO dissociation is 3.89 eV and late TS. The enthalpy differences among different surfaces follow the trend of 0ML>0.25ML>0.50ML; activation energy follow 0.50ML>0ML>0.25ML trend.

Reaction pathways of CO dissociation on Cu (110) at different oxygen coverage

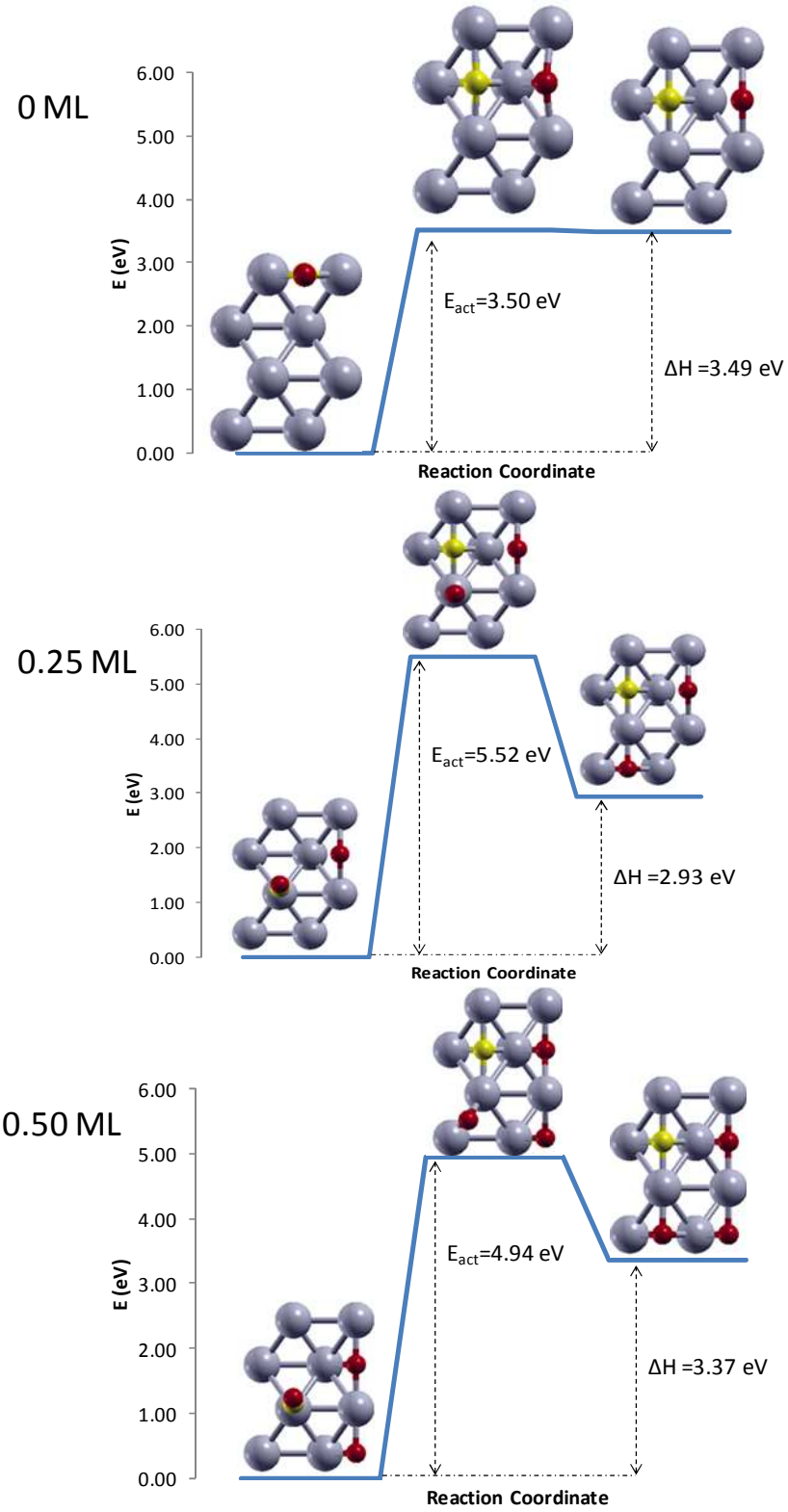

Figure 28: Energy of CO dissociation on Cu (110) 0ML;0.25ML;0.50ML

Geometry description of 0ML oxygen coverage on Cu (110)

The CO dissociation on Cu(100) is substantially a barrierless reaction, with the same order of magnitude of difference of energy between product and reactant and activation energy of the process. The energy difference is 3.49 eV. The most stable adsorption site for CO is the shortbridge position with a perfectly vertical C-O bond, 1.16 Å long. The TS is very late, and it shows both C and O separated in their final longbridge position. They are separated by 2.35 Å, forming a mutual angle respect to the Cu atom underlying in between C-Cu-O of 67.8°. The C-Cu distance is 2.04 Å and the O-Cu distance is 2.17 Å. The final state has the same adsorption position but with C and O a little bit further. They are separated by 2.59 Å and the angle C-Cu-O with the underlying metal atom is 73.9°. The C-Cu distance is 2.05 Å and the O-Cu distance is 2.24 Å. The activation energy of the process is 3.50 eV and TS is late.

Geometry description of 0.25ML oxygen coverage on Cu (110)

The energy difference between product and reactant is 2.93 eV for 0.25ML oxygen coverage. The reaction is endothermic. The most stable adsorption position for CO is top position, with a C-O distance of 1.15 Å. The TS is late, with C already cleaved from O and occupying the longbridge position. C-O distance is 1.95 Å. C-Cu distance is 1.86 Å and O-Cu distance is 1.78 Å. The angle in between C-Cu-O is 65.1°. The final position presents both C and O adsorbed onto longbridge position, cleaved by 3.65 Å. The C-Cu distance is 1.82 Å and the O-Cu distance is 1.84 Å. The angle identified by C-Cu-O is 173.1°. The activation energy of the dissociation reaction is 5.52 eV with late TS.

Geometry description of 0.50ML oxygen coverage on Cu (110)

The introduction of the second oxygen atom adsorbed onto the longbridge position increases the endothermicity of the dissociation at 0.50ML respect to the 0.25ML to 3.37 eV. CO assumes a position which is very similar to the 0.25ML initial site, with a tilted top position and a C-O distance of 1.15 Å. The TS of the reaction is similar to that of 0.25ML, with C and O well cleaved and C occupying the longbridge position. The C-O mutual distance is 3.11 Å. C-Cu distance is 1.82 Å while O-Cu is 1.77 Å. The angle formed by C-Cu-O is 119.7°. The final state has both C and O adsorbed onto longbridge position, with a mutual C-O distance of 3.65 Å. The C-Cu distance is 1.82 Å and the O-Cu distance is 1.83 Å. The angle formed by C-Cu-O is 178.6°. The activation energy of the process, characterized by a late TS, is 4.94 eV. Enthalpy differences follow the following trend: 0ML>0.50ML>0.25ML; activation energies follow a different trend: 0.25ML>0.50ML>0ML.

Reaction pathways of CO dissociation on Cu (111) at different oxygen coverage

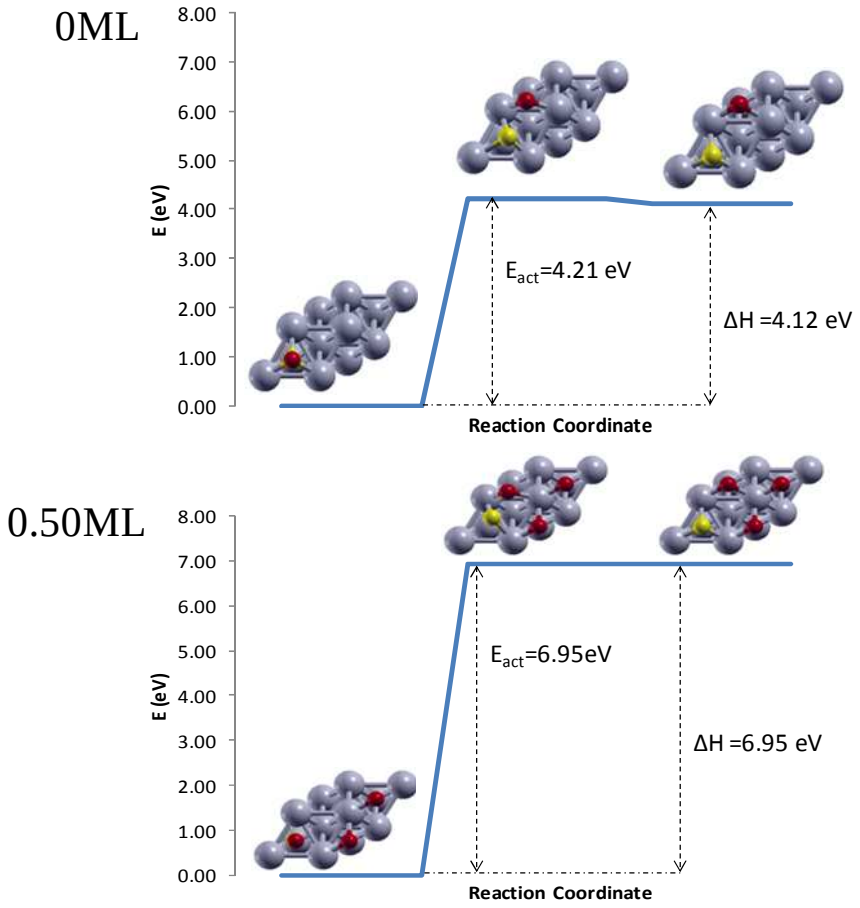

Figure 29: Energy of CO dissociation on Cu (111) 0ML;0.25ML; 0.50ML

Geometry description of 0ML oxygen coverage on Cu (111)

CO dissociation on the Cu (111) surface is endothermic for 4.12 eV. The initial position for CO is the fcc site, which the CO occupies staying perpendicular to the plane of the metal slab. The C-O distance is 1.18 Å. The TS is late, having a geometrical structure which is similar to the final state. C and O are separated by 1.88 Å and well cleaved. C-Cu distance is 1.89 Å, while O-Cu distance is 1.96 Å. The angle formed by C-Cu-O is 58.5°. The final state shows both C and O adsorbed onto fcc sites. Their mutual distance is 2.58 Å with a C-Cu distance of 1.88 Å and a O-Cu distance of 1.90 Å. The angle highlighted by C-Cu-O is 86.1°. The activation energy for this process is 4.21 eV with late TS.

Geometry description of 0.50ML oxygen coverage on Cu (111)

The introduction of two oxygen atoms as spectator to the CO dissociation reaction, both adsorbed onto fcc site, brings the energy difference between product and reactant to 6.95 eV. The most stable adsorption site for CO adsorption is the fcc. The C-O distance in the perpendicular bond respect to the plane identified by the metal slab is 1.15 Å. The TS is very

late, with a geometry which is substantially identical to the product. Both C and O are already settled in the final fcc position, and they are cleaved by a C-O distance of 1.85 Å. The C-Cu distance is 1.92 Å while the O-Cu distance is 1.92 Å. The angle C-Cu-O is 57.2°. The final state has two atoms in fcc position, separated by 2.58 Å. The C-Cu distance is 1.96 Å and the O-Cu distance is 1.94 Å. The C-Cu-O angle is 82.4°. The activation energy of the dissociation process is 6.95 eV with late TS.

Reaction pathways of CO dissociation on Ag (100) at different oxygen coverage

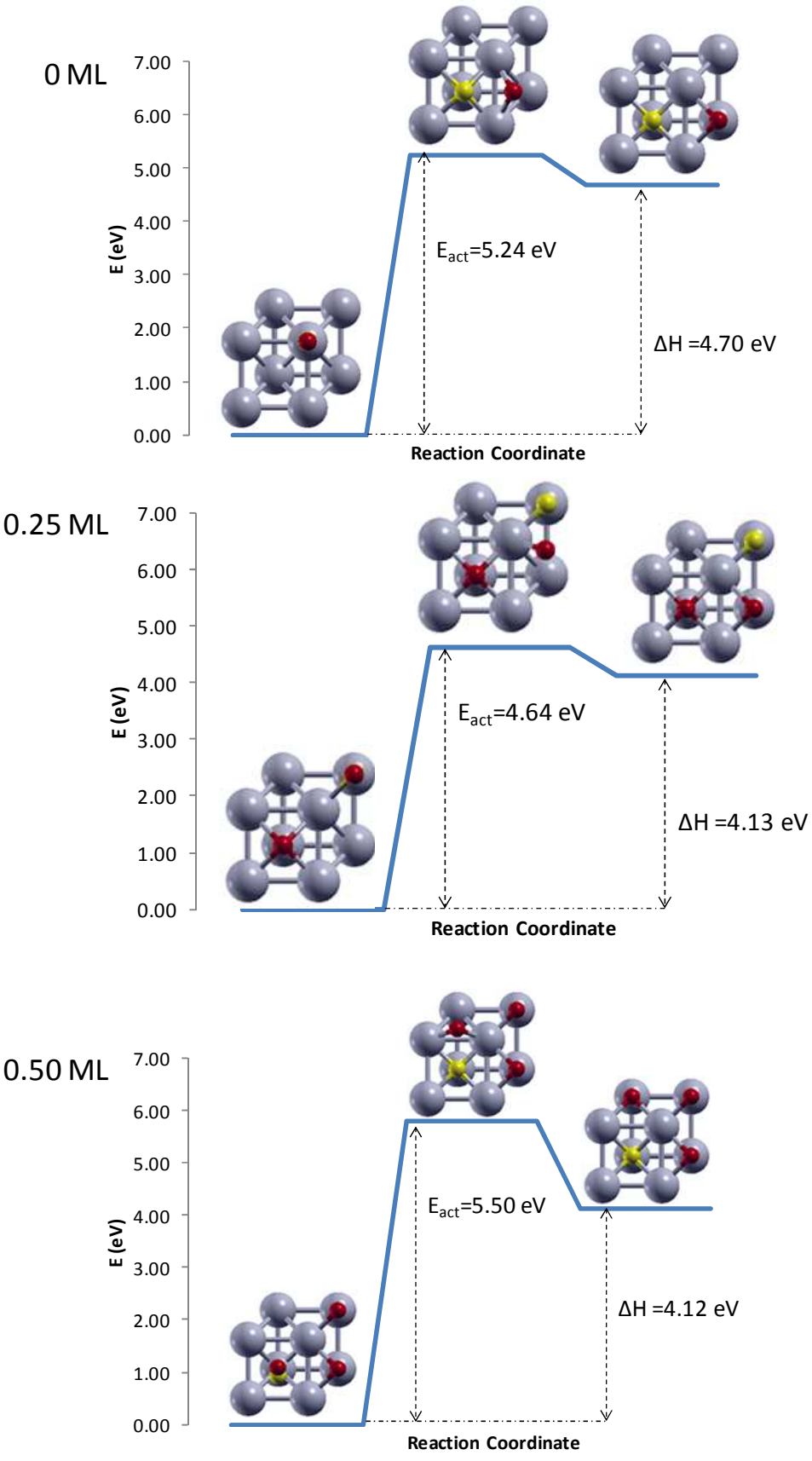

Figure 30: Energy of CO dissociation on Ag (100) 0ML;0.25ML;0.50ML

Geometry description of 0ML oxygen coverage on Ag (100)

The CO dissociation on Ag (100) metal surface is an endothermic reaction for 4.70 eV. The most stable adsorption site for CO is top, in which CO is perfectly perpendicular to the metal surface. The C-O distance is 1.15 Å. The TS is late, with C and O well separated by 2.27 Å. The C-Ag distance is 2.16 Å and the O-Ag distance is 2.16 Å too. The angle formed by C-Ag-O is 63.4°. The final state shows both C and O occupying the fcc sites, a geometrical configuration very simlar to the TS. C-O are separated by 3.08 Å, with C-Ag distance of 2.08 Å and O-Ag distance of 2.29 Å. The angle formed by C-Ag-O is for the finale state 89.6°. The activation energy for this dissociation process is 5.24eV and the TS is late.

Geometry description of 0.25ML oxygen coverage on Ag (100)

The introduction of a oxygen atom as spectator to the dissociation process in the fcc position lowers the endothermicity of the reaction respect to the 0 ML reaction. The energy difference between product and reactant is 4.13 eV. The most stable adsorption site for the CO molecule is top position. The C-O bond distance is 1.17 Å. The C-O bond is perpendicular respect to the plane identified by the silver slab. The TS shows C and O already cleaved, both in hybrid position between bridge and hollow, a late TS geometrically very similar to that of 0ML. The C-O distance is 2.40 Å, with C-Ag distance of 2.07 Å and O-Ag distance of 2.14 Å. The angle C-Ag-O is 69.7°. The final state shows both C and O adsorbed on fcc sites, cleaved by 3.13 Å. C-Ag distance is 2.08 Å and O-Ag distance is 2.34 Å. The angle C-Ag-O is 90.0°. The activation energy of the process is 4.64 eV with late TS.

Geometry description of 0.50ML oxygen coverage on Ag (100)

The introduction of two spectator oxygen atoms both in fcc position leaves the energy difference between product and reactant substantially unaltered, with a endothermicity of 4.12eV. The most stable adsorption site for CO molecule is the hollow site. The molecule is slightly tilted with a C-O distance of 1.14 Å. The TS is late, and very similar to both those of 0 ML and 0.25ML. C assumes a hollow position, while O has a mixed position between bridge and hollow. Their mutual distance is 2.35 Å. The C-Ag distance is 2.09 Å, and the O-Ag distance is 2.17 Å. The angle C-Ag-O is 67.2°. The final state shows both C and O adsorbed on hollow sites, divided by 2.94 Å. The C-Ag distance is 2.17 Å, while O-Ag distance is 2.17 Å too. The angle C-Ag-O is 85.2°. The activation energy of the process is 5.50 eV with late TS. Enthalpy differences among different oxygen coverage follow the following trend: 0ML>0.25ML>0.50ML, while the activation energy follows this scheme: 0.50ML>0ML>0.25ML.

Reaction pathways of CO dissociation on Ag (110) at different oxygen coverage

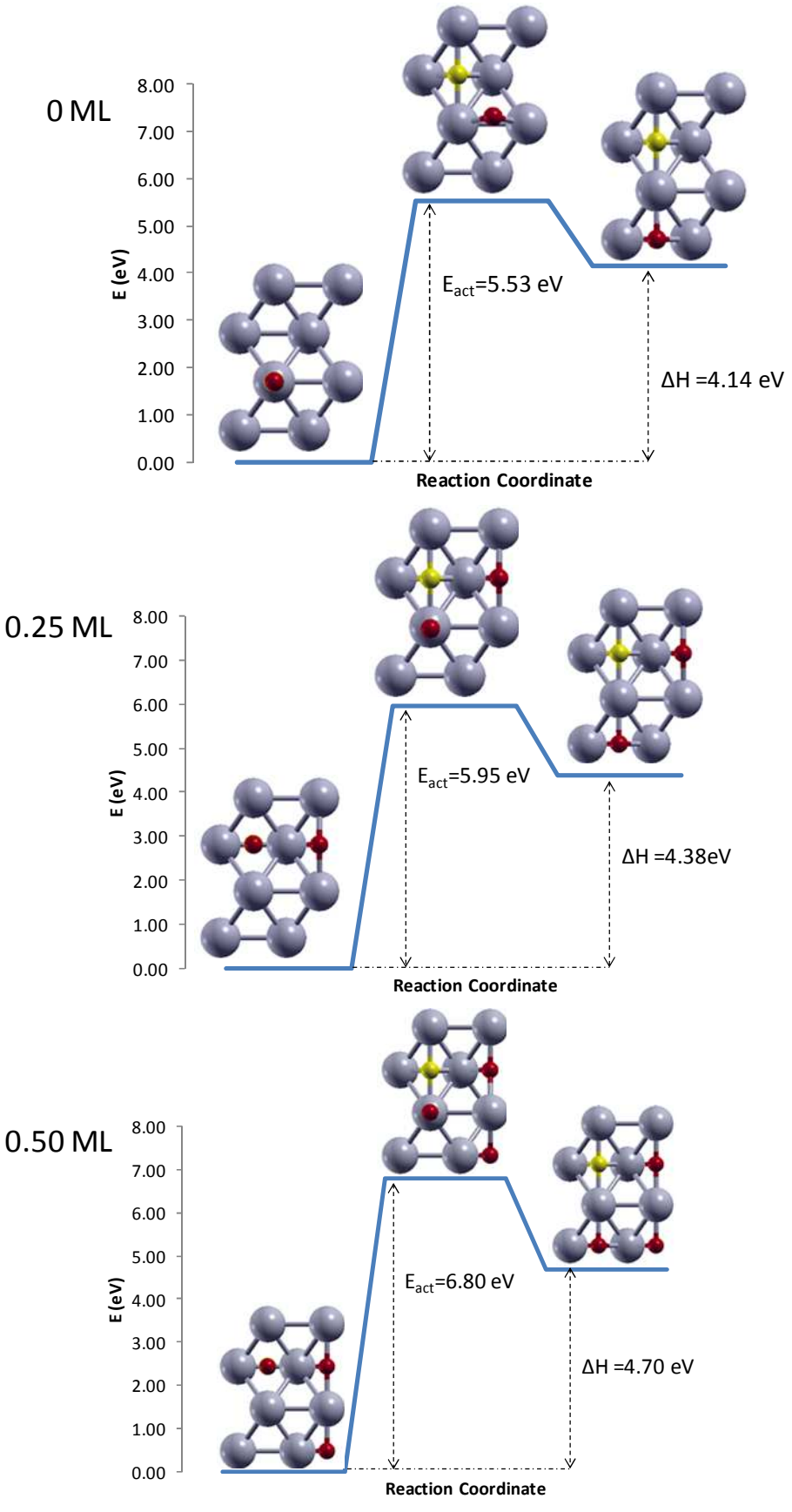

Figure 31: Energy of CO dissociation on Ag (110) 0ML;0.25ML;0.50ML

Geometry description of 0ML oxygen coverage on Ag (110)

The CO dissociation reaction is endothermic on the Ag (110) surface for 4.14 eV. The most stable adsorption site is top position for CO. The molecule is perfectly perpendicular to the plane identified by the metal slab, with a C-O distance of 1.15 Å. The TS is late, with C positioned at the longbridge position and O atom on the shortbridge site. Their mutual distance is 2.69 Å, and C-Ag bond length is 2.10 Å while O-Ag bond length is 2.08 Å. The angle in between is 80.0°. The final state shows to have both C and O in longbridge positions. The C-O reciprocal distance is 4.16 Å, equally divided into C-Ag distance of 2.08 Å and O-Ag 2.08 Å. The angle C-Ag-O is 176.6°. The activation energy of the dissociation process is 5.53 eV with late TS.

Geometry description of 0.25ML oxygen coverage on Ag (110)

The introduction of a oxygen atom as spectator to the dissociation process increases the endothermicity of the dissociation reaction to 4.38eV. The most stable adsorption site for CO is the longbridge position, where CO is perfectly perpendicular to the plane identified by the metal slab. The C-O bond length is 1.15 Å. The TS is late, with C and O already separated. C-O distance is 2.66 Å, with C-Ag distance of 2.08 Å and a O-Ag distance of 1.96 Å. The angle C-Ag-O is 82.2°. The final state shows both C and O on the longbridge positions, separated by 4.16 Å equally divided between 2.08 Å of C-Ag and O-Ag bond length. The angle in between C-Ag-O is 176.1°. The activation energy of the process is 6.95 eV. TS is late.

Geometry description of 0.50ML oxygen coverage on Ag (110)

The introduction of the second oxygen spectator atom increases the endothermicity of the reaction to 4.70eV. The most stable adsorption site is the same of 0.25ML oxygen coverage, with CO molecule adsorbed in the shortbridge position, with the C-O bond perpendicular to the plane identified by the metal slab and 1.15 Å long. The TS is analogous to that of 0.25ML: C is in the longbridge position, well separated from the O atom which is occupying a sort of top position. Their reciprocal distance is 2.74 Å. The C-Ag distance is 2.06 Å while the O-Ag distance is 1.97 Å. The angle C-Ag-O is 85.5°. The final state presents both C and O adsorbed on longbridge position, divided by 4.16 Å equally divided between the C-Ag bond length of 2.08 Å and O-Ag one, long 2.08 Å too. The activation energy of this dissociation process is 6.80eV with late TS. Trend of enthalpy difference follow the following pattern: 0ML<0.25ML<0.50ML; trend of activation energy follow the same trend 0ML<0.25ML<0.50ML.

Reaction pathways of CO dissociation on Ag (111) at different oxygen coverage

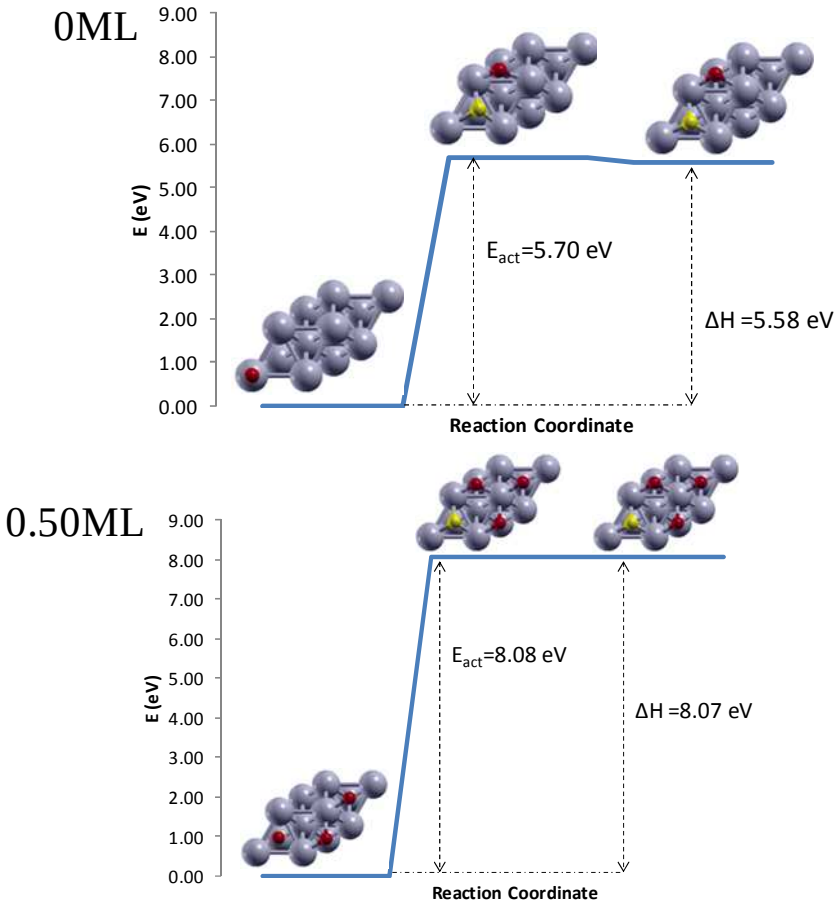

Figure 32: Energy of CO dissociation on Ag (111) 0ML;0.25ML;0.50ML

Geometry description of 0ML oxygen coverage

CO dissociation on Ag (111) metal slab is an endothermic reaction for 5.58eV. The most stable adsorption site for CO is the top, with CO molecule which is perpendicular to the plane of the metal slab. C-O bond length is 1.15 Å. The TS is very late, since the geometry of the TS is similar to the final state. In fact, even if a little bit tilted both C and O occupy the final fcc position, and are well cleaved. Their mutual C-O distance is 2.38 Å. C-Ag distance is 2.08 Å while O-Ag is 2.15 Å. The angle C-Ag-O is 68.5°. The final state shows C and O in the middle of fcc positions, divided by 2.94 Å. The C-Ag distance is 2.06 Å, while O-Ag distance is 2.13 Å. The angle C-Ag-O is 89.1°. The activation energy of this dissociation process is 5.70 eV with late TS.

Geometry description of 0.50ML oxygen coverage

The presence of two oxygen atoms spectator to the dissociation process brings the energy difference between product and reactant to 8.07eV. The most stable adsorption site for CO molecule is fcc, with a C-O bond long 1.14 Å and perpendicular to the plane identified by the

metal slab. The TS is very late. C and O atoms are well separated and on the verge of occupying the fcc sites of the final state. C and O are divided by 2.69 Å. C-Ag bond is 2.10 Å long while O-Ag is 2.15 Å. The angle C-Ag-O is 78.7°. The final state is similar to the TS, with distances and angles stretched. C-O distance is 2.91 Å. C-Ag bond length is 2.10 Å while O-Ag is 2.16 Å. The angle formed by C-Ag-O is 86.3°. The activation energy of the dissociation process is 8.08e and the TS is very late.

Elementary Step: CH → C+H

CH dissociation has been analyzed on four different metals (rhodium, platinum, copper and silver) and on three different surfaces ((100),(110),(111)). Each reaction step is analyzed on the same metal for the three different surfaces in terms of geometry of the initial, final and Transition State, together with an analysis of the activation energy.

Reaction pathway of CH dissociation on Rhodium surfaces

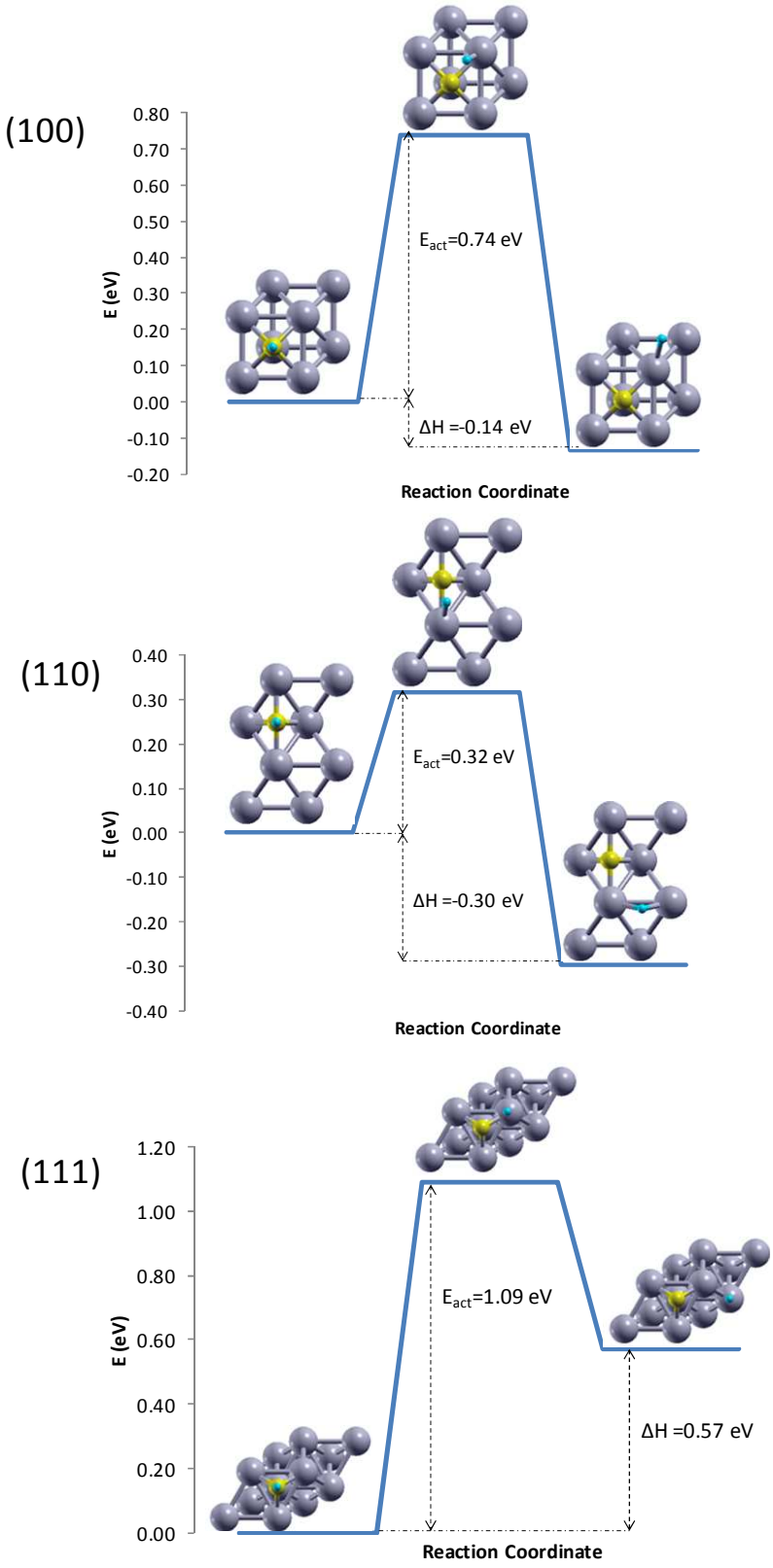

Figure 33: Energy of CH dissociation on Rh (100),Rh (110) and Rh (111) surface

Geometry description of CH dissociation on Rh (100)

CH dissociation reaction on Rh (100) is an exothermic reaction for -0.14eV. The most stable adsorption site for CH molecule is the hollow position. CH molecule is perpendicular to the plane identified by the rhodium slab. The C-H distance is 1.17 Å. The TS has a late geometrical configuration, with C and H perfectly cleaved. The C atom occupies the hollow site, while H atom is on a hybrid top-hollow position. Their mutual distance is 1.33 Å. The C-Rh distance is 2.01 Å, the H-Rh distance is 1.75 Å and the angle C-Rh-H in between is 40.8°. The final state of the dissociation has C in hollow position and H in bridge position divided by a reciprocal distance of 3.30 Å. The C-Rh distance is 1.99 Å and the H-Rh distance is 1.77 Å. The angle in between is 122.7°.The activation energy of the reaction is 0.74 eV with late TS.

Geometry description of CH dissociation on Rh (110)

The CH dissociation on Rh (110) surface is an exothermic reaction for -0.30eV. The most stable adsorption site for the CH molecule is longbridge, where CH molecule binds perfectly perpendicular to the plane identified by the metal surface. The C-H distance is 1.12 Å. The TS is late, with C and H molecule which are perfectly cleaved at the highest energy point of the MEP. C is adsorbed on the longbridge position, while H is in a hybrid top-longbridge position, analogous to the TS of the Rh (100). Their mutual C-H distance is 1.43 Å, with C-Rh distance of 1.94 Å and H-Rh distance of 1.69 Å. The angle formed in between C-Rh-H is 45.6°. The final state presents C in longbridge position and H in shortbridge position. Their reciprocal distance C-H is 2.83 Å, with C-Rh distance of 1.93 Å and H-Rh distance of 1.75 Å. The angle in between C-Rh-H is 100.3°. The activation energy of the dissociation reaction is 0.32 eV with late TS.

Geometry description of CH dissociation on Rh (111)

CH dissociation reaction on RH (111) is an endothermic reaction for 0.57 eV. Hcp is the most stable adsorption site for CH, which is perpendicular to the plane identified by the slab and has a C-H distance of 1.10 Å. The TS is late, with C and H atoms that are separated. C atom occupies the hcp position while H stands in a hybrid top-hcp position which geometrically reminds those TS of Rh (100) and Rh (110). The mutual C-H distance is 1.42 Å. The C-Rh distance is 1.97 Å and the H-Rh distance is 1.69 Å. The angle C-Rh-H is 44.7°. The final state has both C and H atoms in hcp position separated by 2.73 Å the C-Rh distance is 1.91 Å and the H-Rh distance is 1.82 Å. The angle C-Rh-H is 94.0°. The activation energy of the process is 1.09 eV with late TS.

Reaction pathway of CH dissociation on Platinum surfaces

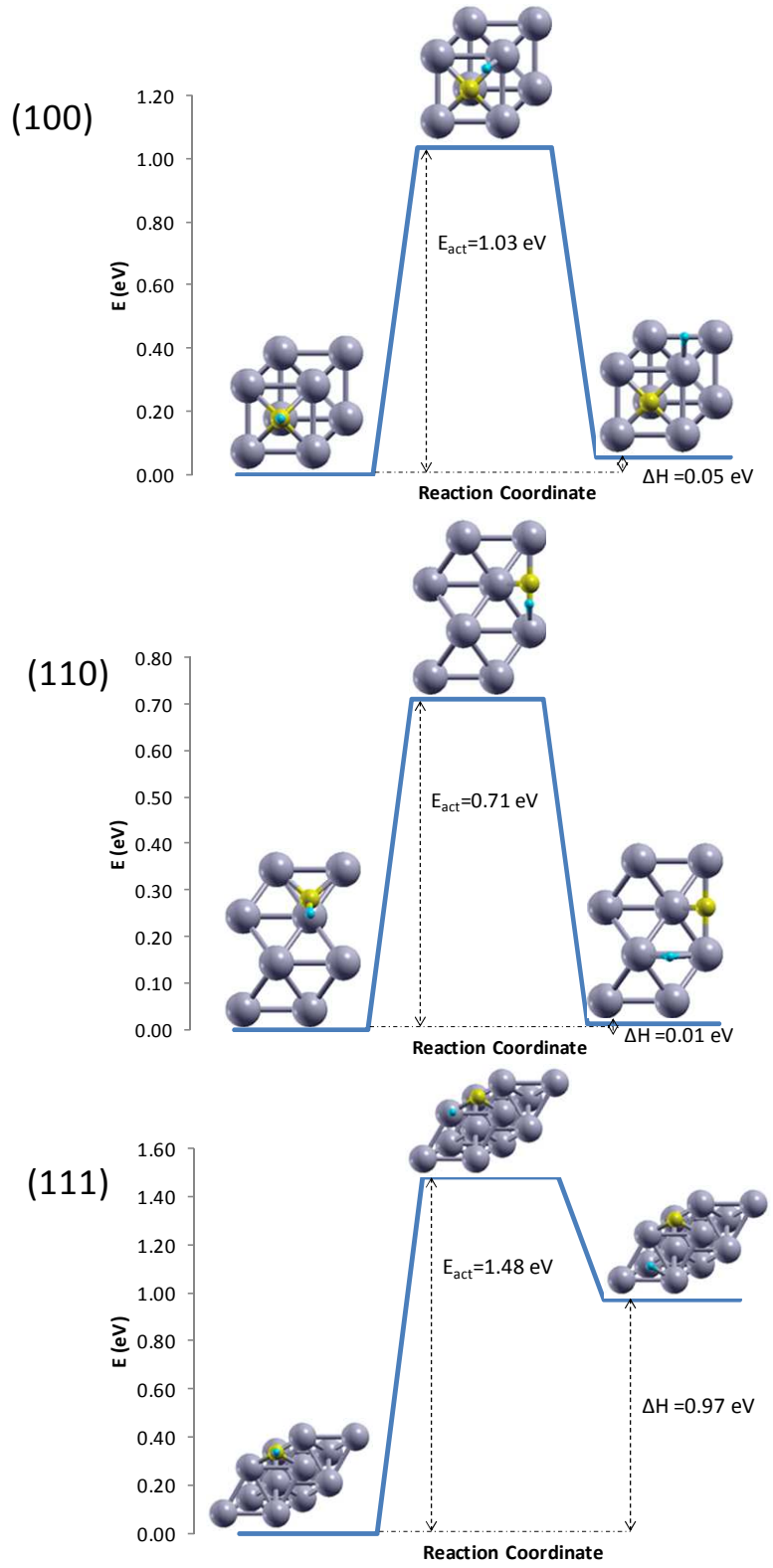

Figure 34: Energy of CH dissociation on Pt (100),Pt (110) and Pt (111) surface

Geometry description of CH dissociation on Pt (100)

The CH dissociation is a athermic reaction, with a difference in energy between product and reactant of 0.05eV. The search for the most stable adsorption site finds hollow one as the initial position of the MEP, with C-H bond which is perfectly perpendicular to the metal slab plane and has a C-H distance of 1.10 Å. The TS is late. C and H are already separated by 1.53 Å. The C-Rh distance is 2.08 Å and the H-Rh distance is 1.67 Å. The angle in between is C-Rh-H with 46.7°. This TS appears to be quite similar to Rh (100) TS. The final position hasC in hollow position and H in bridge position, separated by 3.33 Å. The C-Rh distance is 2.02 Å while the H-Rh distance is 1.76 Å. The angle C-Rh-H is 123.1°. The activation energy of the dissociation reaction is 1.03eV and the TS is late.

Geometry description of CH dissociation on Pt (110)

The CH dissociation on Pt (110) molecule is a athermic reaction, with a energy difference between reactant and product of 0.01 eV. The initial most stable adsorption site for CH is a hybrid shortbridge-hollow site, with C and H slightly tilted and a C-H distance of 1.10 Å. The TS is late, with C and H separated. It is also analogous to the TS of CH dissociation on Rh (110). C-H distance is 1.94 Å, C-Pt distance is 2.04 Å and H-Pt distance is 1.59 Å. The angle in between C-Pt-H is 63.0°. The final state is with C in longbridge position and H in shortbridge position. Their mutual distance is 2.83 Å, with C-Pt distance of 2.02 Å and H-PT distance of 1.77 Å. The angle in beween C-Pt-H is 96.1°. The activation energy of the process is 0.71 eV with late TS.

Geometry description of CH dissociation on Pt (111)

CH dissociation on Pt (111) is an endothermic reaction for 0.97 eV. The most stable adsorption site for CH molecule is the fcc site, which is occupied by the molecule in a perfect perpendicular direction respect to the metal plane identified by the Platinum plane. The C–H distance is 1.10 Å. The Transition State appears to be late, with C and H already separated, and with a geometry which is similar to the Rh (111) one. C-H distance is 1.69 Å. C-Pt distance is 2.04 Å and H-Pt distance is 1.62 Å. The angle in between is 53.4°. The final state presents both C and H atoms adsorbed onto fcc sites, divided by 2.84 Å. The C-Pt distance is 1.94 Å, H-Pt bond is 1.89 Å long and the angle in between C-Pt-H is 95.6°. The activation energy of the process is 1.48 eV with a late TS.

Reaction pathway of CH dissociation on Copper surfaces

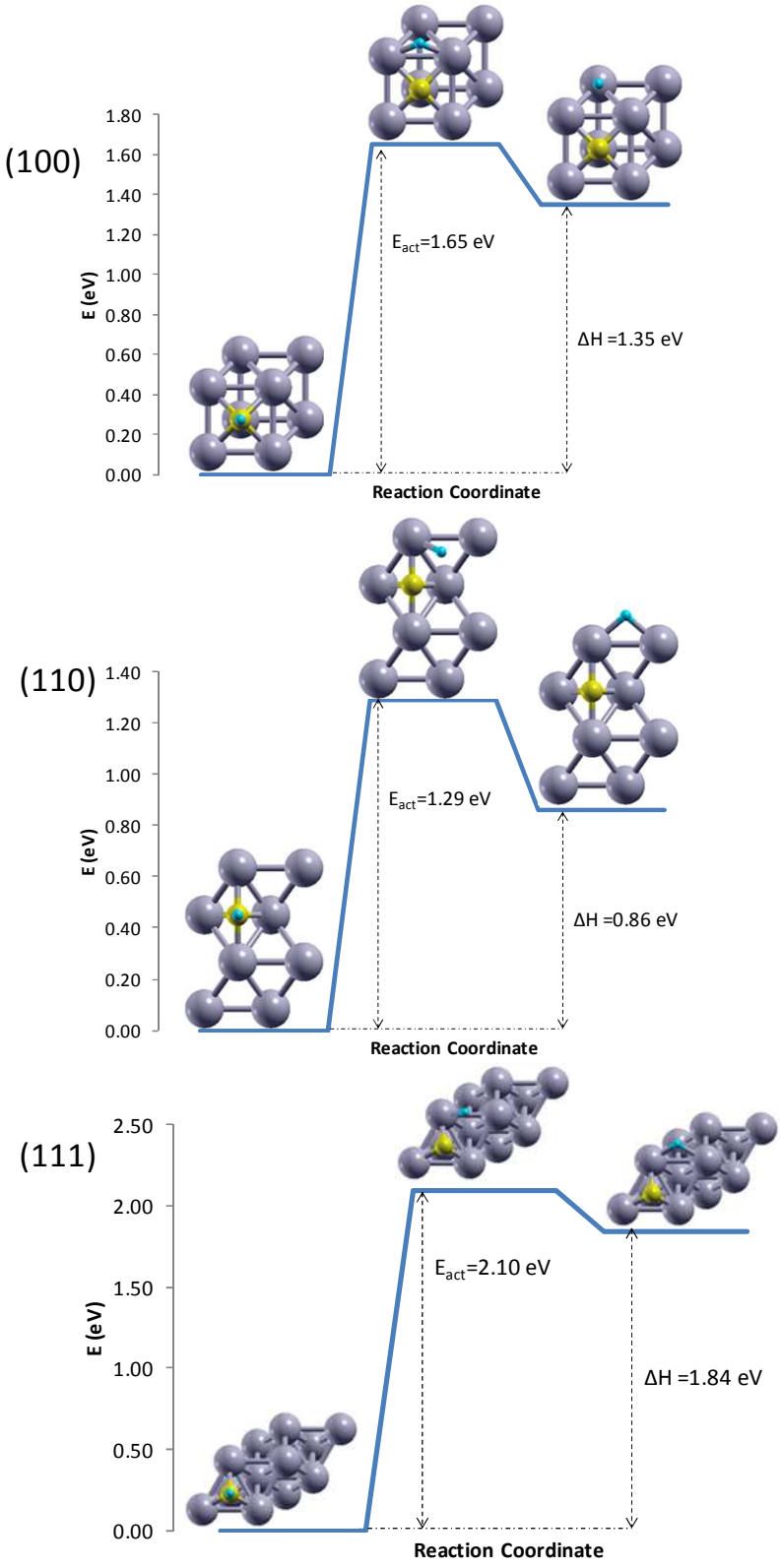

Figure 35: Energy of CH dissociation on Cu (100), Cu (110) and Cu (111) surfaces

Geometry description of CH dissociation on Cu (100)

CH dissociation on Cu (100) surface is an endothermic reaction for 1.35eV. The most stable adsorption site for CH is hollow. The CH molecule has a C-H bond length which is of 1.11 Å. The molecule is perpendicular to the metal surface. The TS is late, with C and H well cleaved; C is occupying the hollow site and H is occupying a sort of bridge position. Their mutual distance is 1.89 Å. The C-Cu distance is 1.90 Å and the H-Cu distance is 1.69 Å. The angle C-Cu-H is 63.3°. The final state has both C and H in hollow position. They have a C-H distance of 2.58 Å , C-Cu distance of 1.88 Å and H-Cu distance of 1.86 Å. The angle in between is 87.5°. The activation energy of the dissociation reaction is 1.65eV and the TS is late.

Geometry description of CH dissociation on Cu (110)

CH dissociation on Cu (110) is an endothermic reaction for 0.86 eV. The most stable adsorption site for CH molecule is longbridge. The length of the C-H bond is 1.10 Å and the bond is perfectly perpendicular to the plane identified by the metal surface. The TS is late, with C and H separated by 1.86 Å. C and H respectively occupy longbridge and a hybrid short-longbridge position. The C-Cu distance is 1.86 Å and the H-Cu distance is 1.62 Å. The angle C-Cu-H is 64.3°. The final state has C in longbridge position and H in hollow position. The C-H distance is 3.22 Å and the C-Cu distance is 1.85 Å. Finally the H-Cu distance is 1.74 Å. The angle C-Cu-H is 127.8°. The activation energy of the process is 1.29 eV with late TS.

Geometry description of CH dissociation on Cu (111)

The dissociation reaction on the Cu (111) surface is endothermic for 1.84 eV. The most stable adsorption site for the slab is the fcc. The length of the C-H bond, which is perpendicular to the plane identified by the metal slab, is 1.10 Å. The TS has the features of a lateness, with C atom in the fcc site and H onto a sort of bridge site. The C-H distance is 1.38 Å. C-Cu distance is 1.87 Å and H-Cu distance is 1.67 Å. The C-Cu-H angle is 45.5°. The final state has both C and H in fcc position, which mutual distance C-H is 2.59 Å. C-Cu distance is 1.88 Å and H-Cu distance is 1.69 Å. The angle in between C-Cu-H is 93.1°. The activation energy of the dissociation process is 2.10 eV with late TS.

Reaction pathway of CH dissociation on Silver surfaces

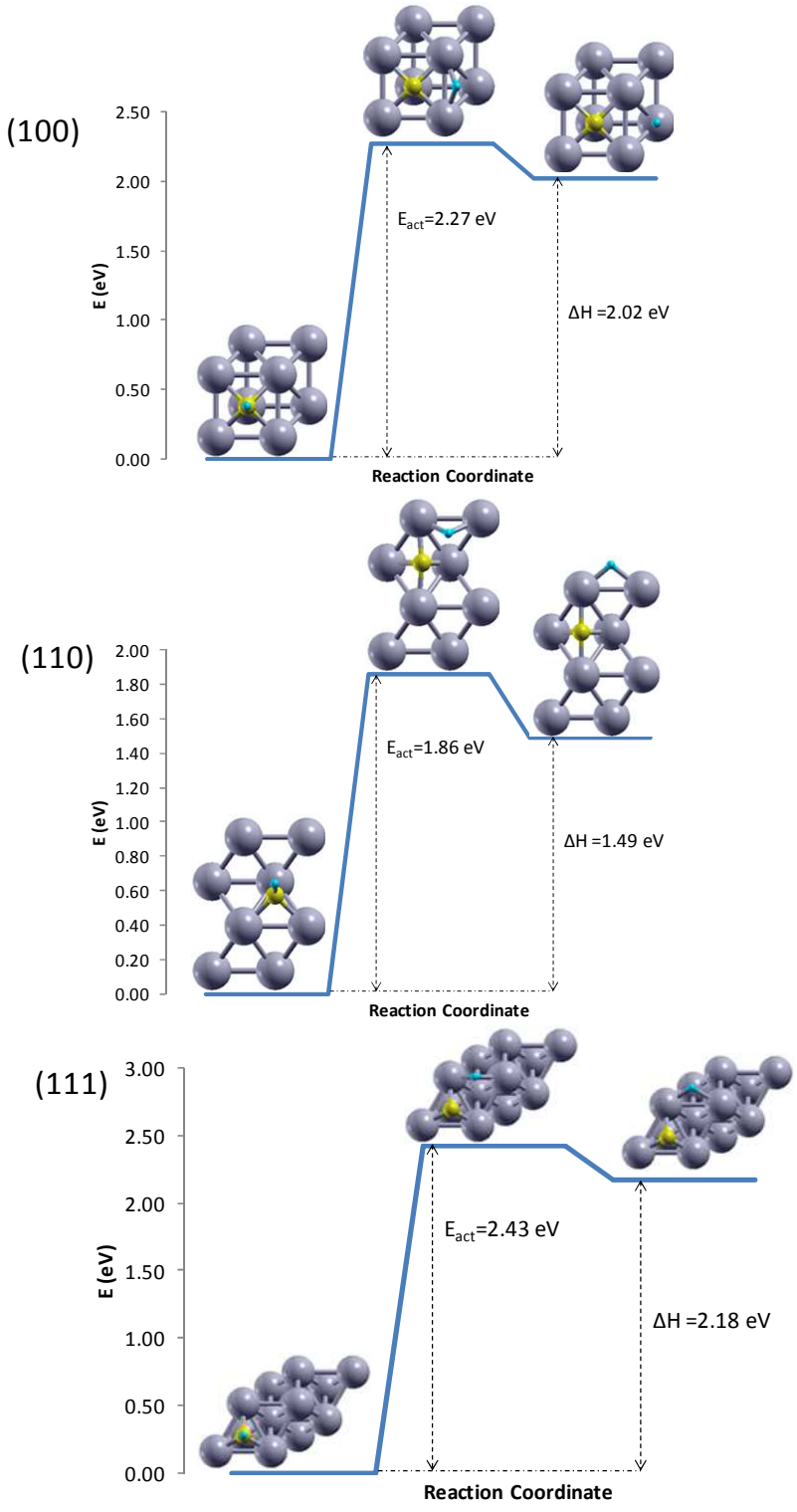

Figure 36: Energy of CH dissociation on Ag (100), Ag (110) and Ag (111) surfaces

Geometry description of CH dissociation on Ag (100)

CH dissociation on Ag (100) is an endothermic reaction for 2.02 eV. The most stable adsorption site for CH is hollow, which is occupied by a perfectly perpendicular CH molecule

respect to the plane identified by the metal slab. The C-H bond length is 1.11 Å. The TS is very similar to that of Cu (100) with the typical features of lateness. C occupies a hollow position, while H is in a sort of bridge position. Both atoms are well separated by 2.12 Å. The C-Ag distance is 2.16 Å and the H-Ag distance is 1.84 Å. The angle identified by C-Ag-H is 63.6°. The final state has both C and H adsorbed on hollow position, divided by 2.94 Å. The C-Ag distance is now 2.11 Å and the H-Ag distance is 2.10 Å. The angle C-Ag-H is now 88.8°. The activation energy of the process is 2.27 eV with late TS.

Geometry description of CH dissociation on Ag (110)

The CH dissociation reaction is an endothermic reaction for 1.49 eV on Ag (110) surface. The search for the most stable adsorption site finds CH in a hybrid shortbridge-hollow position, very similar to initial position of CH dissociation on Pt (110). CH molecule occupies a tilted position with a C-H bond length of 1.10 Å. The TS has the characteristics of lateness, with C and H well cleaved and respectively occupying long- and shortbridge position. The TS is similar to CH dissociation onto Cu (110). The C-H mutual distance is 1.96 Å, with C-Ag distance of 2.11 Å and H-Ag distance of 1.84 Å. The C-Ag-H angle is 59.2°. The final state has C in longbridge position, while H occupies a hollow site. The C-H distance is 3.58 Å; the singular C-Ag and H-Ag distances are respectively 2.09 Å and 1.88 Å. The angle C-Ag-H is 129.2°. The activation energy of the process is 1.86 eV and TS is late.

Geometry description of CH dissociation on Ag (111)

CH dissociation is an endothermic reaction for 2.18 eV on Ag (111). The most stable adsorption site is the fcc, occupied by a perfectly perpendicular to the plane of the metal surface C-H molecule, whose C-H bond length is 1.10 Å. The TS is late, with C occupying the fcc position and H, well cleaved, in a sort of bridge position, 1.88 Å far away from C. C-Ag distance is 2.11 Å and H-Ag distance is 1.77 Å. The C-Ag-H angle is 57.2°. The final state has both C and H in fcc position, separated by 2.96 Å. The single C-Ag distance is 2.08 Å and H-Ag distance is 1.85 Å. The C-Ag-H angle is 97.3°. The activation energy of this dissociation reaction is 2.43eV and the TS is late.

Elementary Step: $CH_2 \rightarrow CH+H$

CH_2 dissociation has been analyzed on four different metals (rhodium, platinum, copper and silver) and on three different surfaces ((100),(110),(111)). Each reaction step is analyzed on the same metal for the three different surfaces in terms of geometry of the initial, final and Transition State, together with an analysis of the activation energy.

Reaction pathway of CH_2 dissociation on Rhodium surfaces

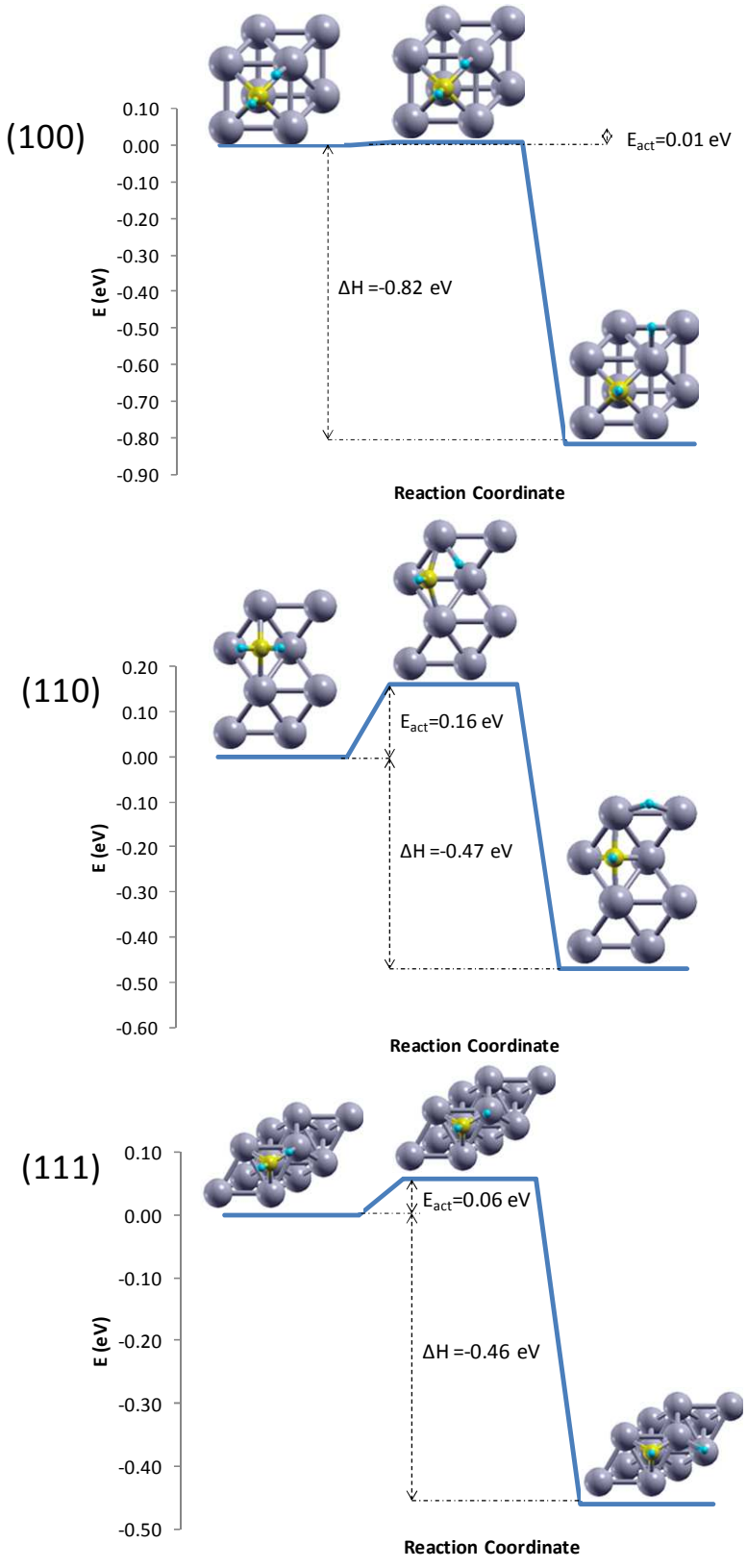

Figure 37: : Energy of CH_2 dissociation on Rh (100), Rh (110) and Rh (111)

Geometry description of CH_2 dissociation on Rh (100)

CH_2 dissociation on Rh (100) is an exothermic reaction for -0.82 eV. The most stable initial adsorption site for CH_2 molecule is the hollow one, which CH_2 occupies being tilted towards the top position. C-H bond length for the CH_2 molecule is 1.11 Å, with a H-C-H angle of 90.1°. A first screening of the NEB calculation found a saddle point which had a geometrical composition between the relaxed initial position and the Transition State and had an energy level lower than that of reactant. Thus, that intermediate image was relaxed and a new NEB calculation started from a configuration of CH and H already separated, meaning that the position had a late geometrical configuration respect to the CH_2 molecule. This image has both CH and H molecule already separated. The TS found in the second NEB is for this reason late, with CH and H that appear to have the same geometrical configuration of the second initial position. C-H distance in the CH molecule is now 1.11 Å but the C-H distance of the cleaved H atom is 1.61 Å. The C-Rh distance is 2.15 Å, while H-Rh distance is 1.60 Å. The C-Rh-H angle is 48.1°. The final state is represented by CH adsorbed on the hollow site in perfectly vertical position respect to the plane identified by the metal slab, with a C-H distance of 1.10 Å. The C-H distance of CH molecule respect to the separated H atom is 3.08 Å. The C-Rh distance is 2.12 Å. The H-Rh distance is 1.77 Å. The C-Rh-H angle is 104.5°. The activation energy of the dissociation process is practically null, 0.01 eV with late TS.

Geometry description of CH_2 dissociation on Rh (110)

CH_2 dissociation on Rh (110) is an exothermic reaction for -0.47 eV. The most stable adsorption site for the initial CH_2 molecule is longbridge, with both H perpendicular to the C-Rh bond. Both C-H distances are 1.11 Å, with a H-C-H angle of 111.8°. The TS is late, with CH molecule which is well cleaved from the H atom. The C-H distance in the C-H molecule is 1.11 Å, and the distance C-H cleaved is 1.60 Å. The angle C-Rh-H is 48.0°. The C-Rh distance is 2.10 Å, while the H-Rh distance is 1.71 Å. The final state presents CH adsorbed on the longbridge site, while H is located on the shortbridge position. The C-H distance in the CH molecule is 1.13 Å, while the C-H distance from the H separated is 2.88 Å. The C-Rh-H angle is 101.6°. C-Rh distance is 1.95 Å and H-Rh distance is 1.77 Å. The activation energy of the entire dissociation process is 0.16 eV and the TS is late.

Geometry description of CH_2 dissociation on Rh (111)

CH_2 dissociation on Rh (111) is an exothermic reaction for -0.46eV. The most stable initial adsorption site is the fcc one, occupied by a tilted CH_2 molecule, whose C-H distance is 1.11 Å and H-C-H angle is 98.5°. As already described for CH_2 dissociation on Rh (100) a first

screening of the NEB calculation found a saddle point between the relaxed initial configuration of the CH_2 molecule and the TS. This intermediate position had a geometrical configuration similar to the TS and an energy level lower than that of the adsorbed CH_2 molecule on the metal surface. For this reason the new position was relaxed and introduced as a initial position of a new NEB calculation, which started from a geometrical configuration already similar to the TS. This is the reason why this TS is intended to be late. The C-H bond length in the CH molecule is 1.10 Å. The C-H distance from the H cleaved atom is 1.49 Å. The C-Rh distance is 2.05 Å while the H-Rh distance is 1.63 Å. The C-Rh-H angle is 46.0°. The final state has CH molecule adsorbed in the fcc position, with a C-H bond long 1.10 Å and perfectly perpendicular to the plane identified by the metal surface. The C-H cleaved atom distance is 2.74 Å. The C-Rh distance is 1.99 Å, while the H-Rh distance is 1.81 Å. The C-Rh-H angle is 92.4°. The activation energy of the dissociation process is 0.06 eV with late TS.

Reaction pathway of CH_2 dissociation on Platinum surfaces

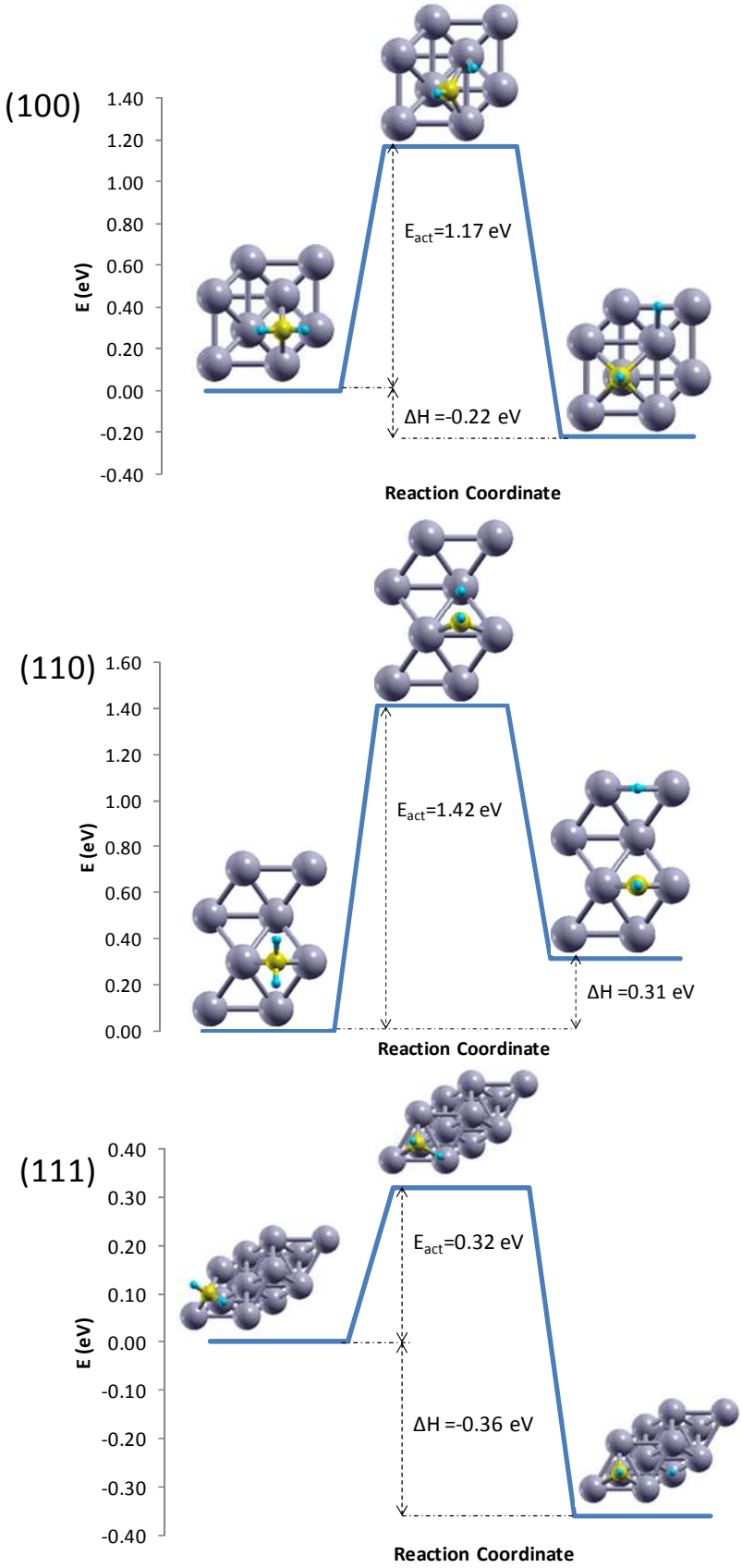

Figure 38: Energy of CH_2 dissociation on Pt (100), Pt (110) and Pt (111) surfaces

Geometry description of CH_2 dissociation on Pt (100)

CH_2 dissociation on Pt (100) is an exothermic reaction for -0.22 eV. The most stable initial state for CH_2 is bridge position, with both H atoms perpendicular to the direction identified by the C-Pt bond. The C-H distance in the CH_2 molecule is 1.10 Å, with a H-C-H angle of 114.2°. The TS appears to be half way between early and late, with CH and H well separated. The C-H distance in the CH molecule is 1.09 Å, while the C-H cleaved distance is 1.47 Å. The C-Pt distance is 2.01 Å, the H-Pt distance is 1.67 Å. The C-Pt-H angle is 46.0°. The final state shows CH in hollow position with C-H bond length of 1.10 Å and perpendicular to the plane identified by the metal slab.H is adsorbed on a bridge position. The C-H distance is 3.22 Å, with C-Pt distance of 2.19 Å and H-Pt distance of 1.76 Å. The C-Pt-H angle is 108.5°. The activation energy of the dissociation process is 1.17 eV and the TS is mixed early and late.

Geometry description of CH_2 dissociation on Pt (110)

CH_2 dissociation on Pt (110) is an endothermic reaction for 0.31 eV. The most stable initial adsorption site for CH_2 is shortbridge, with H atoms normal to the direction identified by the C-Pt bond. The C-H bond length is 1.10 Å, with a H-C-H angle of 115.2°. The TS is intermediate between early and late, with CH and H cleaved but still close. C-H distance in the CH molecule is 1.10 Å, while C-H separated distance is 1.55 Å. C-Pt distance is 1.93 Å and H-Pt distance is 2.34 Å. The C-Pt-H angle is 41.1°. The final state has C-H bond length of the CH molecule of 1.10 Å, with the molecule adsorbed in the fcc position. The H atom is adsorbed in the opposite shortbridge position, 4.01 Å far away from the molecule. The activation energy of the dissociation process is 1.42 eV and the nature of the TS is intermediate between early and late.

Geometry description of CH_2 dissociation on Pt (111)

CH_2 dissociation on Pt (111) is an exothermic reaction for -0.36 eV. The most stable adsorption site for CH_2 is the bridge position, with both H atoms normal to the direction identified by the C-Pt bond. C-H distance is 1.10 Å and the H-C-H angle is 112.7°. The TS of the reaction is late, with CH and H well cleaved. The C-H distance in the CH molecule is 1.10 Å, while the C to the H atom separated distance is 1.43 Å. The C-Pt distance is 2.13 Å while the H-Pt distance is 1.66 Å. The C-Pt-H angle is 41.9°. The final state of the dissociation reaction has CH in fcc position as well as H atom. The mutual C-H separated distance is 2.85 Å. The C-H distance in the H molecule still remains 1.10 Å. The C-Pt-H angle is 94.4°. C-Pt distance is 2.00 Å and H-Pt distance is 1.87 Å. The activation energy of the dissociation process is 0.32 eV and the TS is late.

Reaction pathway of CH_2 dissociation on Copper surfaces

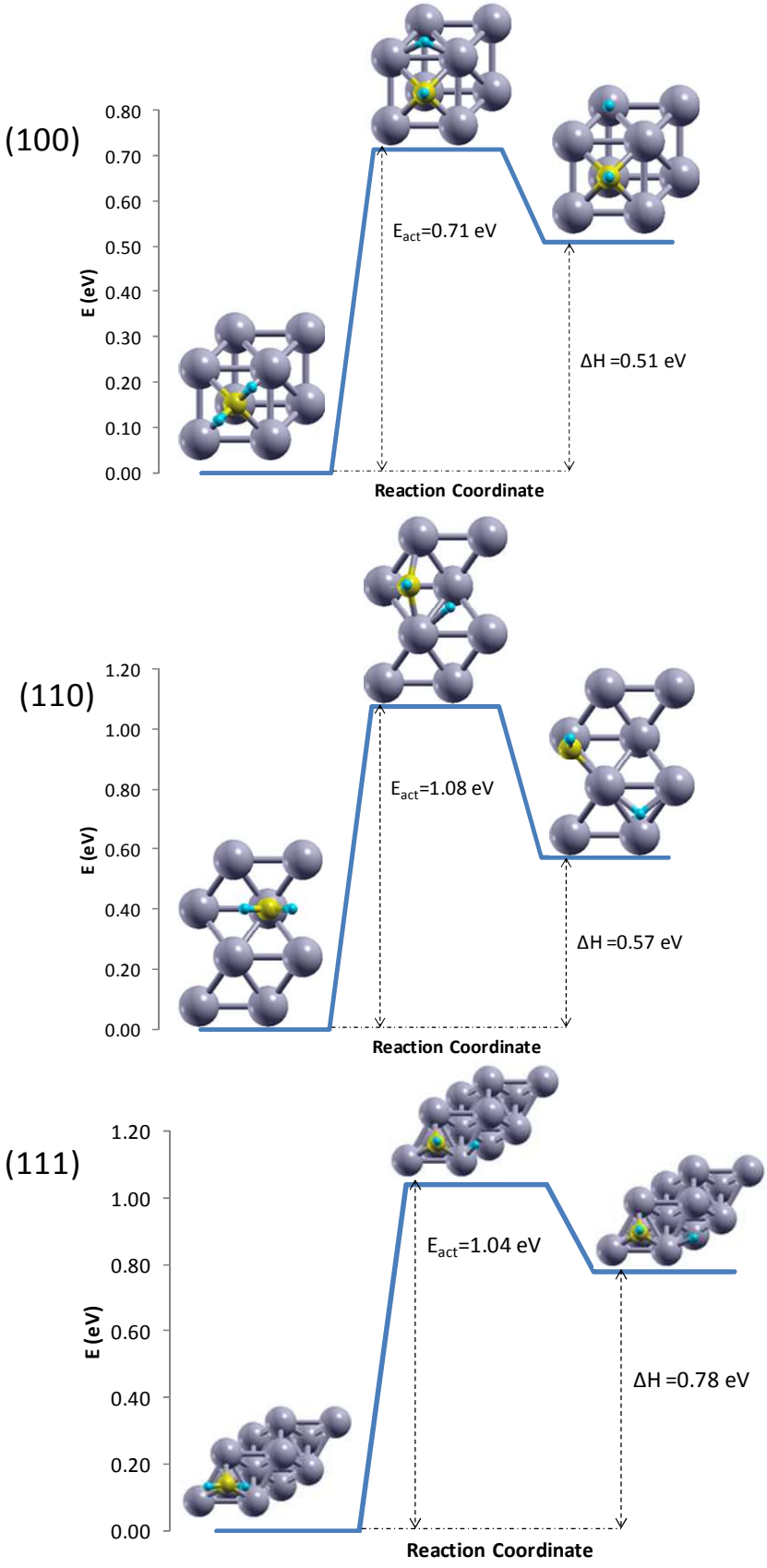

Figure 39: Energy of CH_2 dissociation on Cu (100), Cu (110) and Cu (111) surfaces

Geometry description of CH_2 dissociation on Cu (100)

CH_2 dissociation on Cu (100) is an endothermic reaction for 0.51 eV. The most stable adsorption site for CH_2 is hollow, with both H atoms at 1.12 Å from the atom with an angle H-C-H of 99.0°. The TS is late, with CH in hollow position and H in a sort of bridge position. The C-H bond length in the CH molecule is 1.10 Å, while the distance of C from the H cleaved atom is 1.76 Å. The C-Cu distance is 2.05 Å while the H-Cu distance is 1.68 Å. The C-Cu-H angle is 55.1°. The final state of the dissociation elementary act has both CH and H in hollow position. The C–H bond in CH molecule is still 1.10 Å while the C-H distance is 4.94 Å. The C-Cu distance is 2.00 Å while the H-Cu distance is 1.87 Å. The C-Cu-H angle is 85.0°. The activation energy of the process is 0.71 eV with late TS.

Geometry description of CH_2 dissociation on Cu (110)

CH_2 dissociation on Cu (110) is an endothermic reaction for 0.57 eV. The most stable adsorption site for CH_2 is the hollow one, with C-H distance of 1.11 Å and a H-C-H angle of 105.6°. The TS of the reaction is late, with a geometrical conformation of CH and H. CH and H appear to be cleaved with a C-H bond length in the CH molecule of 1.10 Å. The distance C-H separated is instead 1.73 Å. The C-Cu-H angle is 56.3°. The C-Cu distance is 1.96 Å and the H-Cu distance is 1.67 Å. The final state presents both CH and H in hybrid position shortbridge-hollow. The C-H bond length in the CH molecule is 1.10 Å while the C-H distance is 3.58 Å. The C-Cu distance is 1.98 Å and the H-Cu distance is 1.70 Å. The C-Cu-H angle is 152.8°. The activation energy of the process is 1.08 eV and the TS is late.

Geometry description of CH_2 dissociation on Cu (111)

CH_2 dissociation on Cu (111) is an endothermic reaction for 0.78 eV. The most stable adsorption site for CH_2 is fcc, with a C-H distance of 1.11 Å and H-C-H angle is 105.4°. The TS is late, with the geometrical configuration that has lost all the initial features of the reactant and resembles the product. The CH molecule appears well cleaved from the H atom, with a C-H bond length in the CH molecule of 1.09 Å. The C-H distance instead is 1.84 Å. The C-Cu distance is 1.91 Å and the H-Cu is 1.58 Å. The C-Cu-H angle is 62.8°. The final state has both CH and H adsorbed onto two adjacent fcc position. The C-H bond length is still 1.10 Å while the distance between the CH molecule and the H atom is increased to the 2.60 Å. The C-Cu distance is now 1.91 Å and the H-Cu distance is 1.67 Å. The C-Cu-H angle is 92.9°. The activation energy of the dissociation process is 1.04 eV and the TS is late.

Reaction pathway of CH_2 dissociation on Silver surfaces

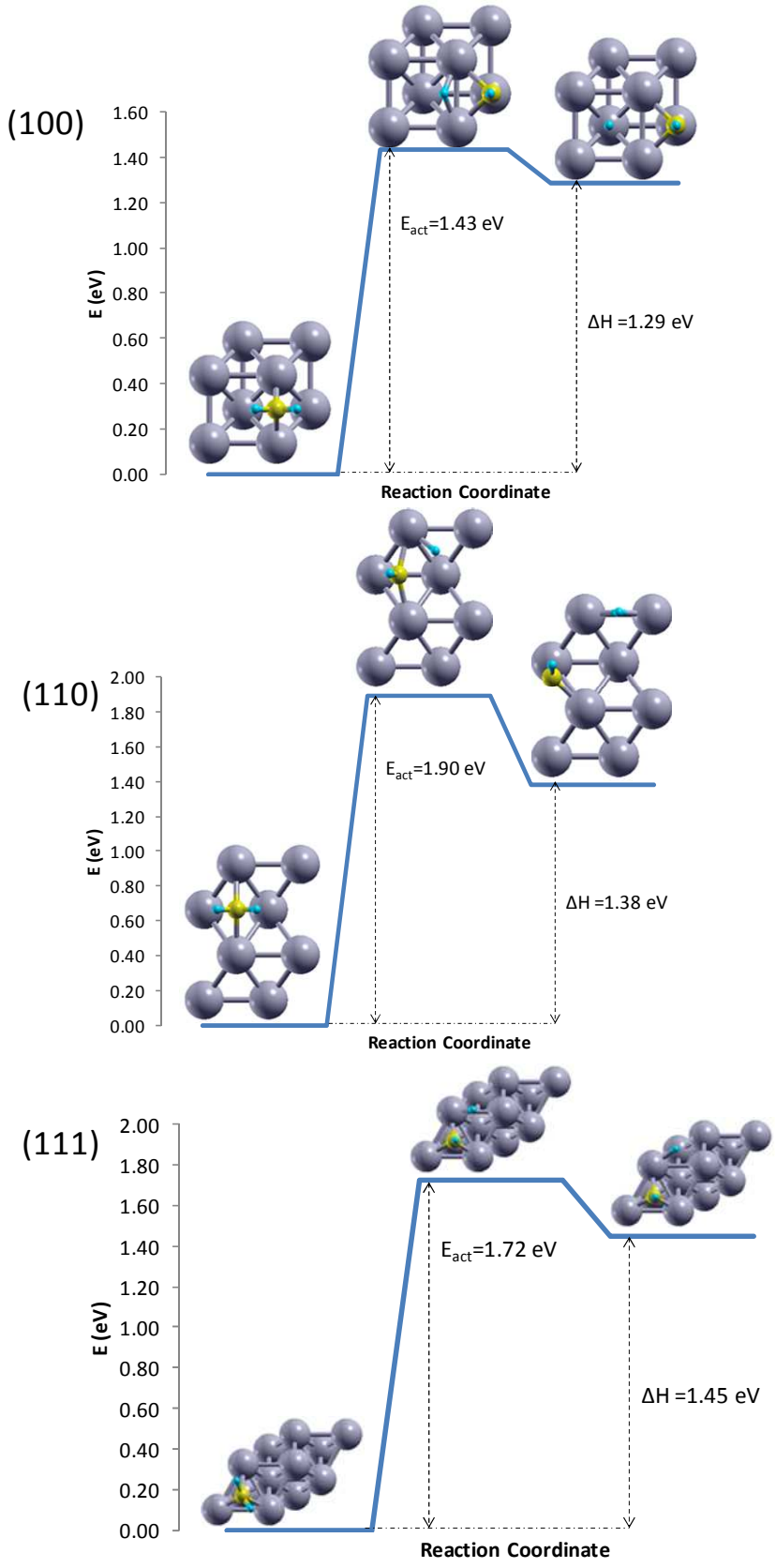

Figure 40: : Energy of CH_2 dissociation on Ag (100), Ag (110) and Ag (111) surfaces

Geometry description of CH_2 dissociation on Ag (100)

CH_2 dissociation on Ag (100) is an endothermic reaction for 1.29 eV. The most stable adsorption site for CH_2 molecule is bridge with the two H atoms perpendicular to the direction identified by the C-Ag bond. The C-H distance is 1.10 Å and the H-C-H angle is 111.6°. The TS is late, with CH and H well cleaved. The C-H bond length in the CH molecule is 1.09 Å while the distance of CH molecule and H atom is 2.07 Å. The C-Ag distance is 2.28 Å while H-Ag distance is 1.83 Å. The C-Ag-H angle is 59.2°. The final state presents both CH and H adsorbed on hollow site, with a mutual C-H distance of 2.98 Å the C-H bond length in the CH molecule still remains 1.11 Å, while the C-Ag distance is 2.22 Å and the H-Ag distance is 2.10 Å. The C-Ag-H angle is 87.2°. The activation energy of the dissociation process is 1.43 eV and TS is late.

Geometry description of CH_2 dissociation on Ag (110)

CH_2 dissociation on Ag (110) is an endothermic reaction for 1.38 eV. The most stable adsorption site for CH_2 molecule is longbridge with the two H atoms positioned in the direction perpendicular to that identified by the C-Ag bond. The C-H distance is 1.10 Å and the H-C-H angle is 110.5°. The TS is late, with CH well cleaved from the H atom. The C-H bond length in CH molecule is 1.11 Å while C-H distance, intended as the distance between CH molecule and H atom is 2.01 Å. The C-Ag-H angle is 59.2°. the C-Ag distance is 2.22 Å while the H-Ag distance is 1.79 Å. The final state product presents CH in a hybrid hollow-shortbridge position, while H is adsorbed on a shortbridge position. The mutual C-H distance in the CH molecule is 1.10 Å, while the C-H distance of the two molecules is 4.11 Å. The C-Ag distance is 2.13 Å and the H distance is 4.62 Å. The C-Ag-H angle is 62.8°. The activation energy of the process is 1.90 eV and the TS is late.

Geometry description of CH_2 dissociation on Ag (111)

CH_2 dissociation on Ag (111) is an endothermic reaction for 1.45 eV. The most stable initial position for CH_2 is the fcc position. The C-H distance is 1.10 Å and the H-C-H angle is 106.7°. The TS of the reaction appears to be late, with CH in fcc position and H atom in a sort of a bridge position. The C-H bond length is 1.10 Å while the C-H distance between the CH and H molecules is 1.80 Å. The C-Ag distance is 2.10 Å and the H-Ag distance is 1.74 Å. The C-Ag-H angle is 55.0°. The final state shows both CH and H adsorbed in fcc position separated by 2.97 Å. The C-H bond length in the CH molecule is 1.10 Å. The C-Ag distance is 2.10 Å and the H-Ag distance is 1.83 Å. The C-Ag-H angle is 97.5°. The activation energy of the dissociation process is 1.72 eV.

Summary of the CO dissociation

The following table is collecting all parameters of interest described in the previous pages about CO dissociation. This parameters will be exploited in Chapter 4 for the validation of semiempirical models that are BEP and UBI.

Metal surface	Coverage Effect (ML)	ΔH_r (eV)	E_{act}(eV)	Nature of the Transition State
Rh(100)	0	1.45	2.39	Late
	0.25	1.61	2.82	Late
	0.50	2.66	2.94	Late
Rh(110)	0	1.13	2.28	Late
	0.25	1.41	2.83	Late
	0.50	2.33	3.11	Late
Rh(111)	0	2.26	3.33	Late
	0.25	3.37	4.59	Late
	0.50	3.97	5.19	Late
Pt(100)	0	2.48	4.16	Late
	0.25	3.50	4.43	Late
	0.50	3.48	4.16	Late
Pt(110)	0	2.46	3.42	Late
	0.25	3.53	5.24	Late
	0.50	2.79	4.14	Late
Pt(111)	0	4.19	4.44	Late
	0.25	4.06	4.92	Late
	0.50	4.78	5.66	Late
Cu(100)	0	2.72	3.31	Late
	0.25	2.67	3.11	Late
	0.50	2.50	3.89	Late
Cu(110)	0	3.49	3.50	Late
	0.25	2.93	5.52	Late
	0.50	3.37	4.94	Late
Cu(111)	0	4.12	4.21	Late

Metal surface	Coverage Effect (ML)	ΔH_r (eV)	E_{act}(eV)	Nature of the Transition State
	0.25			
	0.50	6.95	6.95	Late
Ag(100)	0	4.70	5.24	Late
	0.25	4.13	4.64	Late
	0.50	4.12	5.50	Late
Ag(110)	0	4.14	5.53	Late
	0.25	4.38	5.95	Late
	0.50	4.70	6.80	Late
Ag(111)	0	5.58	5.70	Late
	0.25			
	0.50	8.07	8.08	Late

Table 2: Evaluation of ΔH_r, E_{act} and Nature of the Transition State for CO dissociation

Summary of the CH dissociation

The following table is collecting all parameters of interest described in the previous pages about CH dissociation. This parameters will be exploited in Chapter 4 for the validation of semiempirical models that are BEP and UBI.

Metal surface	ΔH_r (eV)	E_{act}(eV)	Nature of the Transition State
Rh (100)	-0.14	0.74	Late
Rh(110)	-0.30	0.32	Late
Rh(111)	0.57	1.09	Late
Pt (100)	0.05	1.03	Late
Pt(110)	0.01	0.71	Late
Pt(111)	0.97	1.48	Late
Cu (100)	1.35	1.65	Late
Cu(110)	0.86	1.29	Late
Cu(111)	1.84	2.10	Late
Ag (100)	2.02	2.27	Late
Ag(110)	1.49	1.86	Late

Metal surface	ΔH_r (eV)	E_{act}(eV)	Nature of the Transition State
Ag(111)	2.18	2.43	Late

Table 3: Evaluation of ΔH_r, E_{act} and Nature of the Transition State for CH dissociation

Trends of enthalpy difference and activation energy of the process have a stable order, which is always respected among different surfaces of the same metal. in terms of enthalpy difference and activation energy of the dissociation , the minimum value is (110), followed by (100) and (111). The characteristics of the TSs remains late over all surfaces.

Summary of the CH_2 dissociation

The following table is collecting all parameters of interest described in the previous pages about CH dissociation. This parameters will be exploited in Chapter 4 for the validation of semiempirical models that are BEP and UBI.

Metal surface	**ΔH_r (eV)**	**E_{act}(eV)**	**Nature of the Transition State**
Rh (100)	-0.82	0.01	Late
Rh(110)	-0.47	0.16	Late
Rh(111)	-0.46	0.06	Late
Pt (100)	-0.22	1.17	Intermediate
Pt(110)	0.31	1.42	Intermediate
Pt(111)	-0.36	0.32	Late
Cu (100)	0.51	0.71	Late
Cu(110)	0.57	1.08	Late
Cu(111)	0.78	1.04	Late
Ag (100)	1.29	1.43	Late
Ag(110)	1.38	1.90	Late
Ag(111)	1.45	1.72	Late

Table 4: Evaluation of ΔH_r, E_{act} and Nature of the Transition State for CH_2 dissociation

Trends exist for enthalpy difference and activation energy on different surfaces of the same metal. Excluding the dissociation of CH_2 on Pt, which is characterized by a different kind of TS, the difference of enthalpy is decreasing in this sense: (100)<(110)<(111); the activation energy is always decreasing in this sense for the same metal: (100)<(111)<(110).

CHAPTER 4. BEP and UBI assessment.

This chapter, on the basis of the data calculated in chapter 3, performs a detailed assessment of BEP relationship and UBI-QEP method, in order to highlight the validity and understand the limitations of each approach.

4. Assessment of BEP and UBI method

Chapter 4 deals with the analysis of DFT and MEP data collected and described in Chapter 3 for the validation and assessment of semi-empirical methods and correlations. Among all the methods present in literature, this work is focused on the validation of BEP and UBI methods, which are widely used in chemical catalysis. The assessment step needs the location and deep understanding of universalities that hold among different metals, different surfaces of the same metal, different classes of reaction that exploits different surfaces of different metals. This understanding step is crucial not only for the validation of a model which is able to predict the activation energy of a chemical step given thermo-chemical properties of the reactant-product environment, but also for the comprehension of the chemical-physics of the reacting systems. The Chapter 4 is organized into two parts: in the first part the BEP method is validated for CO, CH and CH_2 dissociation, while in the second UBI method is analyzed and validated for the same reactions. Each section will provide a zoom in from the most general grouping among all dissociation reactions to the analysis of the effect of metal or surface on the single reaction path and consequently on its activation energy.

Assessment of Brønsted–Evans–Polanyi relation (BEP)

BEP model, as described in Chapter 2, reveals that for reactions exists a linear relationship between the activation energy of the process and the difference in enthalpy between reactants and products for the dissociative adsorption. The assessment and validation gives an answer to the question of which classes of reaction conform this semiempirical relationship.

BEP validation on dissociation reactions

The whole amount of DFT data and calculation referring to the dissociation reactions of CO, CH and CH_2 molecules are collected in a plot of activation energy (E_{act}) against enthalpy change (ΔH).

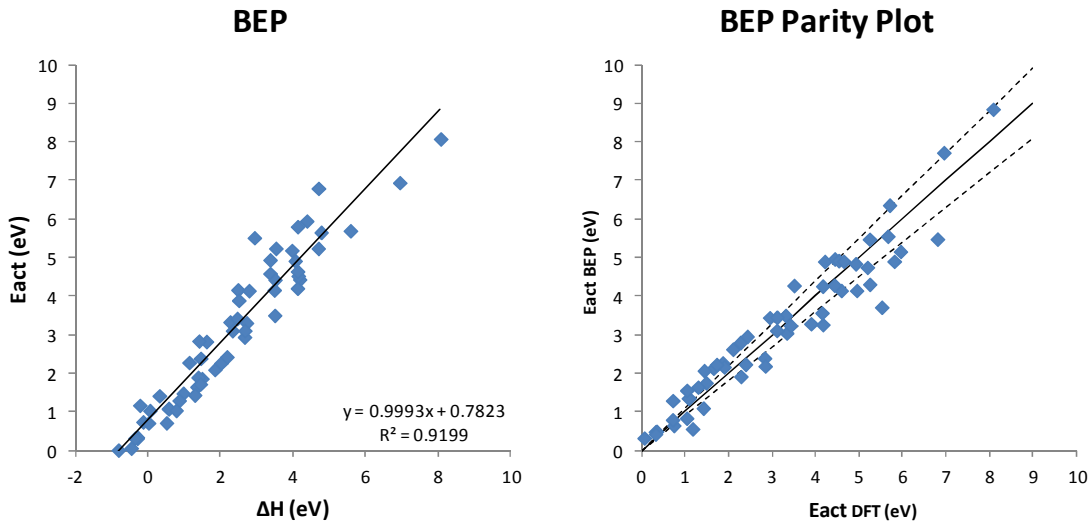

Figure 41: Plots of activation energy (Eact) against the enthalpy change(ΔH) (on the left) and parity plot of activation energy calculated by BEP and DFT (on the right) for CO, CH, CH_2 dissociation on various metals, surfaces and oxygen coverage

We can notice that for a first order interpolation such as that of BEP method, all dissociative reactions investigated fall into the same line for the range of enthalpy change investigated, which is approximately 10 eV. This is due to the fact that all dissociative reactions of CO, CH and CH_2 are characterized by the same nature of the Transition State (TS), which is late. The fact that the TSs have a geometrical configuration that is late is also confirmed by the slope of the BEP interpolation line, which is 1.00, a value that is very close to one. As reported in the work of Michaelides et al. [9] a slope close to the unity reveals for surface dissociation reactions to have late TSs. The low dispersion of data along the interpolation line is confirmed by the parity plot on the right of the figure above, which is confirming the fact that all dissociation reactions are characterized by the same TS.

In order to highlight universalities of dissociations among structures and metals we will now analyze different trends for different effects.

BEP validation on dissociation reactions on Rh surfaces.

The first effect this analysis is interested in is the effect of metal. DFT data have been collected for CO, CH and CH_2 dissociation on the rhodium surfaces for the interpretation of the BEP line.

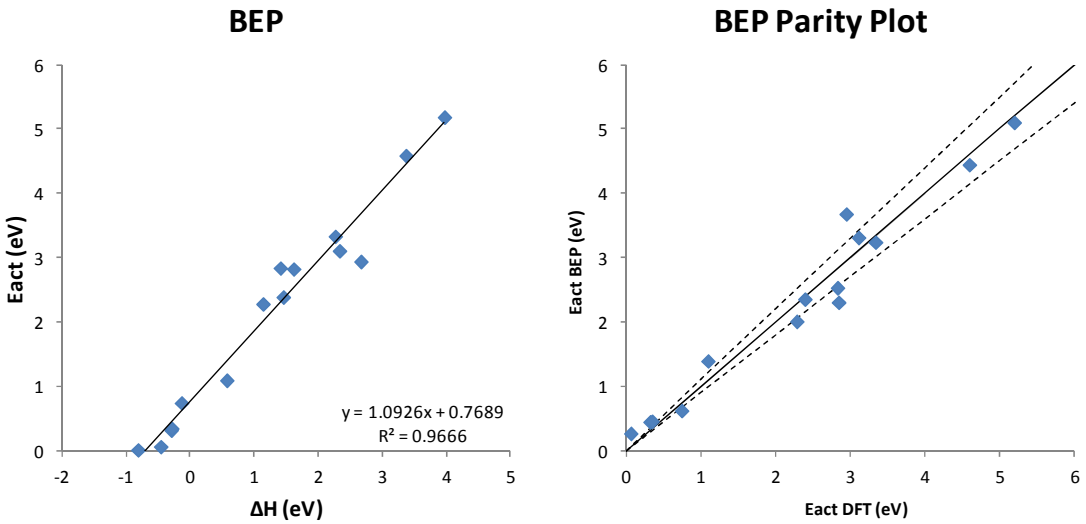

Figure 42: Plots of activation energy (Eact) against the enthalpy change(ΔH) (on the left) and parity plot of activation energy calculated by BEP and DFT (on the right) for CO, CH, CH_2 dissociation on different surfaces of Rh metal

Rhodium surfaces are characterized by the presence of late TS, and this is evident in the value of the slope of the BEP interpolation line which is more than one (1.09), clearly indicating a late TS. Both slope and intercept (0.77) of the line do not differ from the general trend, meaning that Rh surfaces perfectly suit the general trend. The dispersion of BEP calculated data is good, as represented in the parity plot of the right of Figure 42 and presented by the R^2=0.97 of the distribution along the BEP line.

BEP validation on dissociation reactions on Pt surfaces.

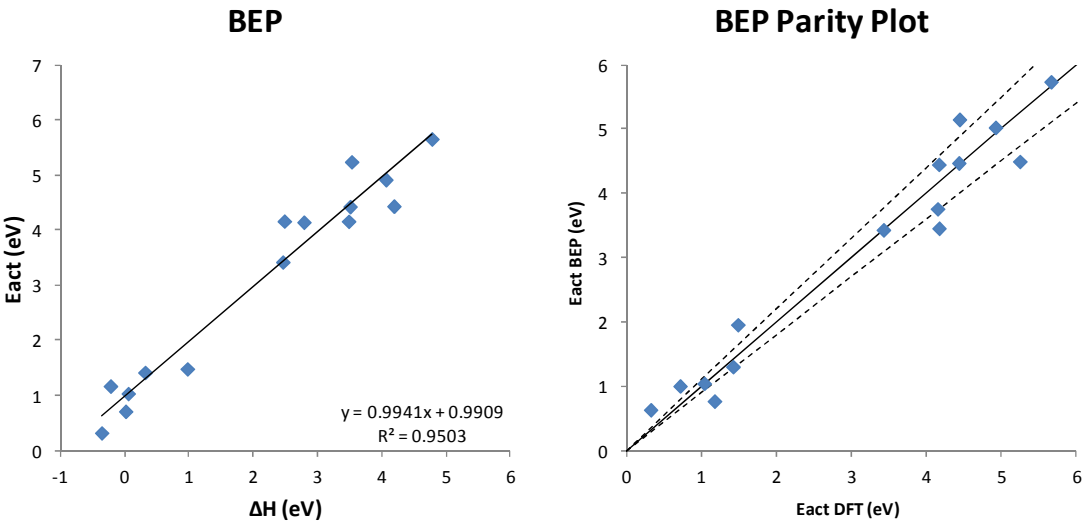

Figure 43: Plots of activation energy (Eact) against the enthalpy change(ΔH) (on the left) and parity plot of activation energy calculated by BEP and DFT (on the right) for CO, CH, CH_2 dissociation on different surfaces of Pt metal

BEP evaluation among CO, CH and CH_2 dissociation reaction on platinum surfaces has been presented in the figure above. The slope of the interpolation line is close to one, with a value of 0.99, meaning that the general trend for the nature of the TSs on platinum is late. The intercept is now slightly changed from the general trend even if the dispersion of data along the interpolation line still remains good. This is due to the fact that the BEP theory has the advantage of having two parameters (slope and intercept of the line) that can be changed for a good predictivity of the model. The parity plot on the right of the figure proves a good ability of BEP to predict the activation energy of dissociative step on Platinum surfaces, within the ±10% corridor.

BEP validation on dissociation reactions on Cu surfaces.

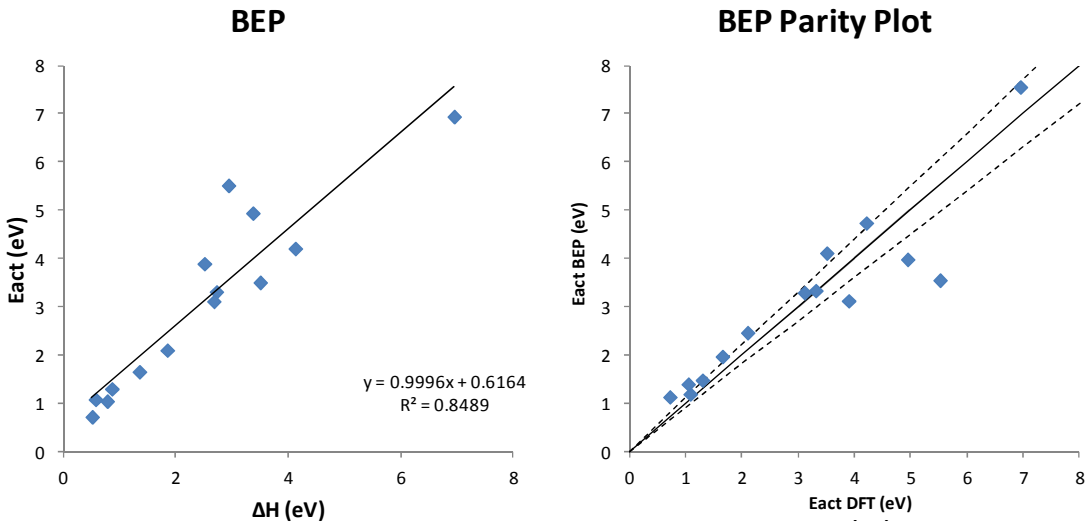

Figure 44: Plots of activation energy (Eact) against the enthalpy change(ΔH) (on the left) and parity plot of activation energy calculated by BEP and DFT (on the right) for CO, CH, CH_2 dissociation on different surfaces of Cu metal

Dissociation reaction universality have been investigated on copper surfaces for CO, CH and CH_2 dissociation reactions. The BEP interpolation model is now more scattered respect to the previous metals, especially for the two points that lie outside the copper BEP general line, which are Cu (110) 0.25ML and Cu (110) 0.50ML. In this case the general trend is not followed because sterical effects due to the small lattice constant of the copper surface attend. The character of the TS remains late, with a slope of 0.99, perfectly aligned with the general trend, even if the dispersion of data is worsened by the presence of two outliers. Parity plot on the right of Figure 44 confirms this misalignment between DFT value for activation energy and BEP foreseen one.

BEP validation on dissociation reactions on Ag surfaces.

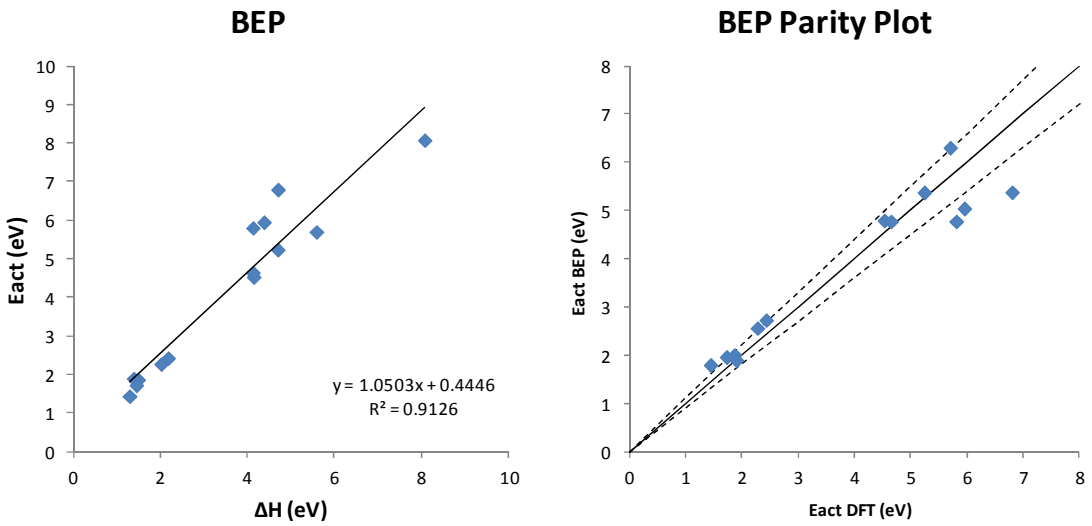

Figure 45: Plots of activation energy (Eact) against the enthalpy change(ΔH) (on the left) and parity plot of activation energy calculated by BEP and DFT (on the right) for CO, CH, CH_2 dissociation on different surfaces of Ag metal

Dissociation reaction universalities have been investigated on silver surfaces, with the results reported in Figure 45. The character of the TSs remains late, as described in Table 2-3 as it is announced by the slope of the BEP interpolation line which is higher than the unity. The dispersion of data remains good, as verified by the R^2=0.91 on the plot on the left of the Figure 45 and the parity plot on the right of it. The intercept of the line is changed respect to the global BEP line (0.44) even if the general trend is respected.

BEP validation on dissociation reactions on (100) surfaces.

The second subsection of this BEP assessment analysis deals with the interpretation and exploiting of universalities that can exist among dissociation reactions that occur on the same low index surfaces, but catalyzed by different type of metals. The focus is aimed at highlighting the similarities and differences that occur among different metal catalyst, identifying general BEP trends, whenever possible.

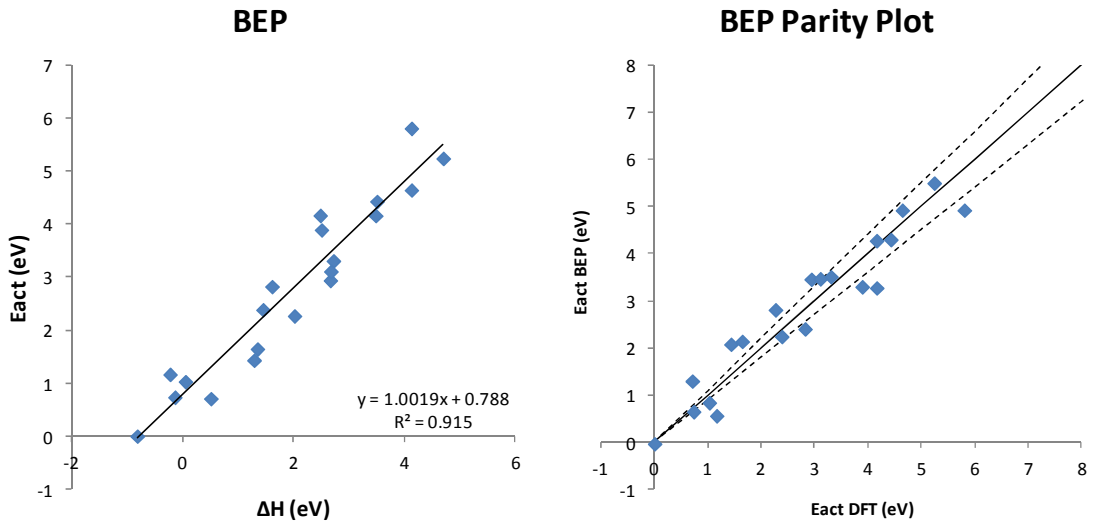

Figure 46: Plots of activation energy (Eact) against the enthalpy change(ΔH) (on the left) and parity plot of activation energy calculated by BEP and DFT (on the right) for CO, CH, CH_2 dissociation on (100) metal surfaces

CO, CH and CH_2 dissociation DFT data have been collected among different metal supports (Rh, Pt, Cu, Ag) on the same structure (100). The slope of the BEP interpolation line is 1.00, implying the presence of a late TS for dissociations investigated. The intercept of the line is 0.79, which gives an idea of the order of magnitude of the activation energy of the process. The dispersion of data is good, with an R^2=0.92, which means that universalities are valid for dissociation reactions on different metal clusters with the same (100) structure.

BEP validation on dissociation reactions on (110) surfaces.

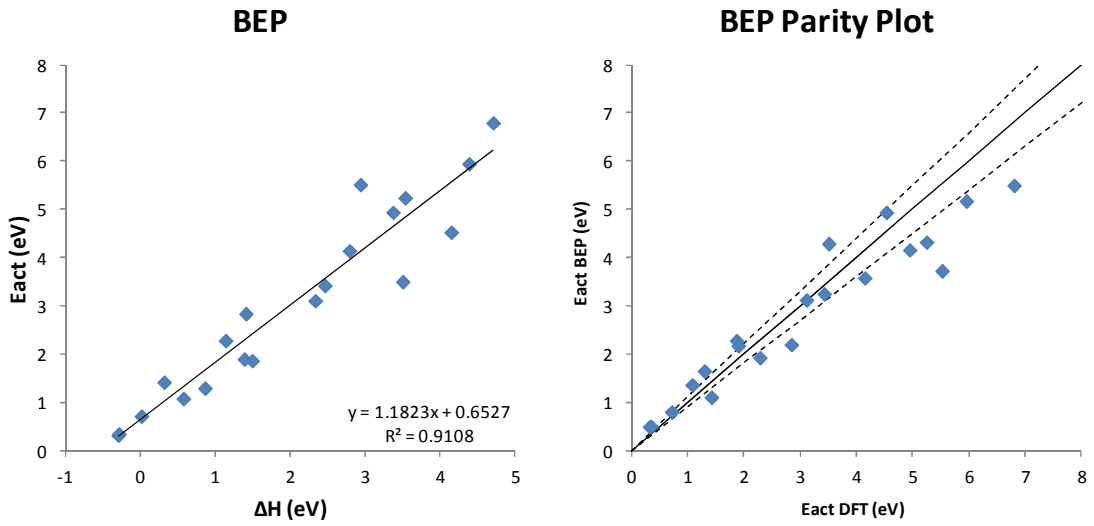

Figure 47: Plots of activation energy (Eact) against the enthalpy change(ΔH) (on the left) and parity plot of activation energy calculated by BEP and DFT (on the right) for CO, CH, CH_2 dissociation on (110) metal surfaces

BEP relationship has been investigated for dissociations on different metals for the (110) surfaces. The slope of the BEP interpolation line is higher than 1 (1.18), meaning that the TSs of dissociation reactions on (110) is very late. The fact of taking samples for the BEP assessment that are smaller and smaller tends to give to the BEP interpolation a character which is more sensible to small changes and to local electronic or sterical effects. The intercept of the line remains in line with the general trend (0.65) and the dispersion of data, presented by both R^2=0.91 and the parity plot on the right of the figure above, is good. Among different metals for dissociation reaction the character of the TS is kept constant and late on (110) surfaces. The point far away from the confidential bound is the Cu(110) surface at 0.25ML of oxygen coverage, which has strong steric effects on the geometrical configuration of the TS.

BEP validation on dissociation reactions on (111) surfaces.

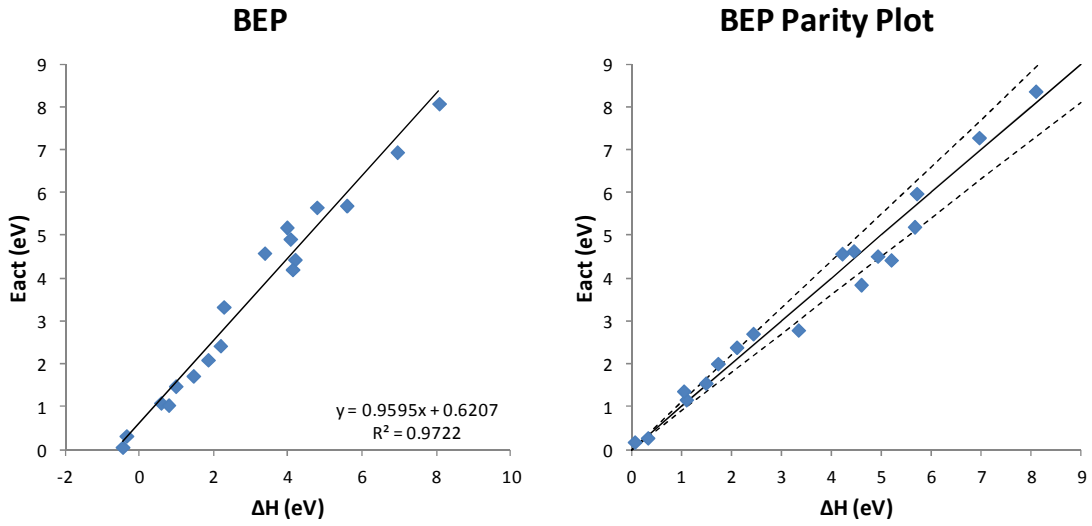

Figure 48: Plots of activation energy (Eact) against the enthalpy change(ΔH) (on the left) and parity plot of activation energy calculated by BEP and DFT (on the right) for CO, CH, CH_2 dissociation on (111) metal surfaces

BEP trends have been investigated for dissociation reactions on the (111) metal surfaces of (Rh, Pt, Cu, Ag). The slope of the interpolation line confirms the presence of late TSs on (111) surfaces with a numerical value of 0.96, very close to 1. The geometrical nature of the TS is kept constant among different metals of the three dissociation reactions, and this is confirmed by the very small dispersion of data along the BEP interpolation line and along the parity plot reported on the right of the figure above. All points tend to stay within the ±10% corridor.

BEP validation on dissociation reactions of biatomic molecules

BEP assessment has been performed for dissociation of biatomic molecules. The focus of this section is the search of stronger universalities or differences respect to a general dissociation framework, analyzing in details BEP scaling trends for CO and CH molecules dissociation, excluding the presence of CH_2 DFT data.

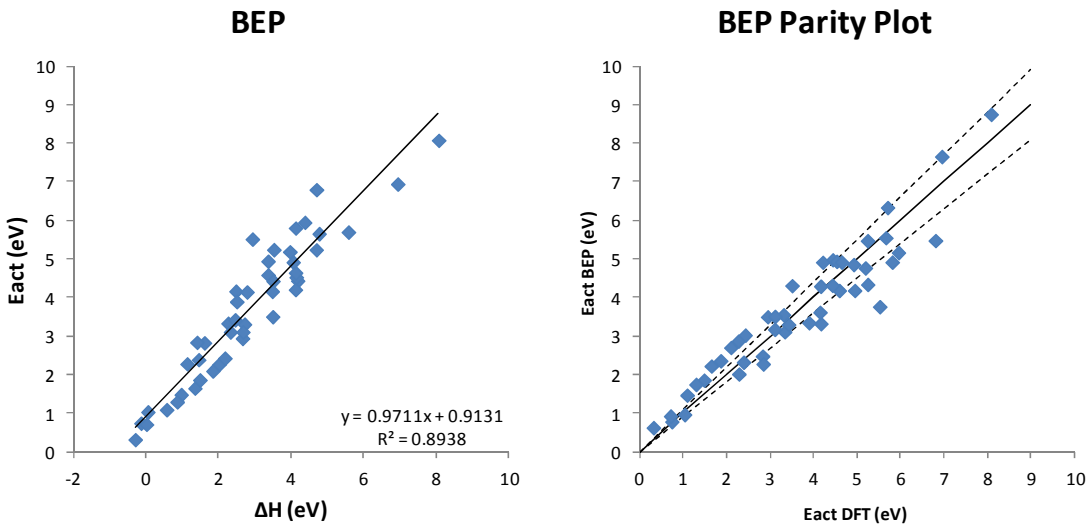

Figure 49: Plots of activation energy (Eact) against the enthalpy change(ΔH) (on the left) and parity plot of activation energy calculated by BEP and DFT (on the right) for CO, CH dissociation on various metals, surfaces and oxygen coverage

CH and CO dissociation data are collected for the identification of universalities that are typical only of biatomic molecules dissociation. The general plot, collecting all DFT data presents a late character of the TSs. This is analogous of the general dissociation BEP trend. The slope of the BEP interpolation line is 0.97 and the intercept is 0.91, a value which is higher respect to the general dissociation line. This suggests that the dissociation of biatomic molecules intrinsically requires a higher activation energy respect to the dissociation of a CH_2 molecule.

BEP validation on dissociation reactions of biatomic molecules on Rh surfaces

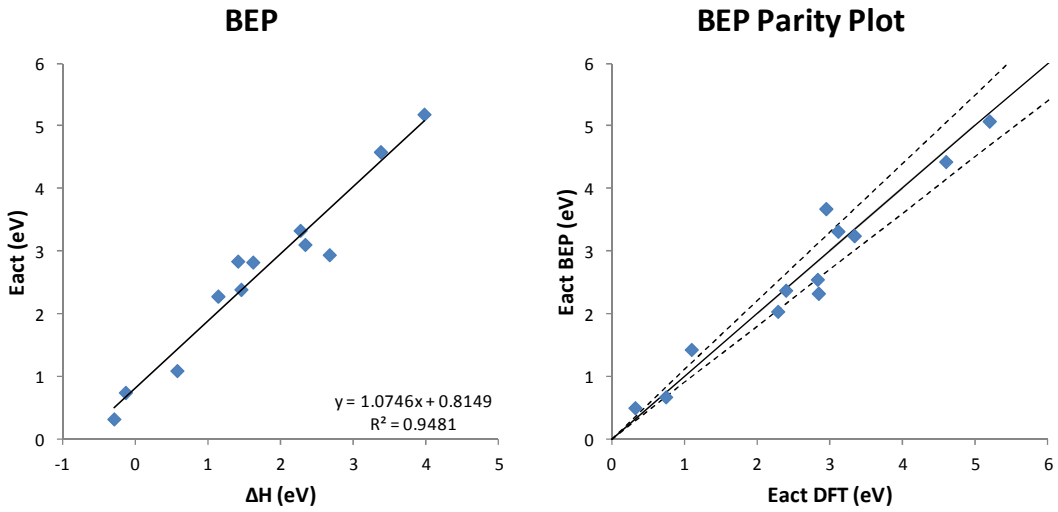

Figure 50: BEP analysis (on the left) and parity plot of activation energy calculated by BEP and DFT (on the right) for CO, CH dissociation on Rh metal

The effect of metal is investigated for dissociation of the class of biatomic molecules on rhodium surfaces and for different oxygen coverage. The slope of the BEP interpolation line respect to the CH_2 comprehensive one is remained practically unaltered (1.07 versus 1.09) still indicating the late nature of the TSs on rhodium. The intercept of the line has increased from 0.77 to 0.81, indicating that the energy for the dissociation of a biatomic molecule is intrinsically higher than for the dissociation of a CH_2 molecule. Analogies are present for dissociations of bi- and triatomic molecules for dissociations on rhodium surfaces.

BEP validation on dissociation reactions of biatomic molecules on Pt surfaces

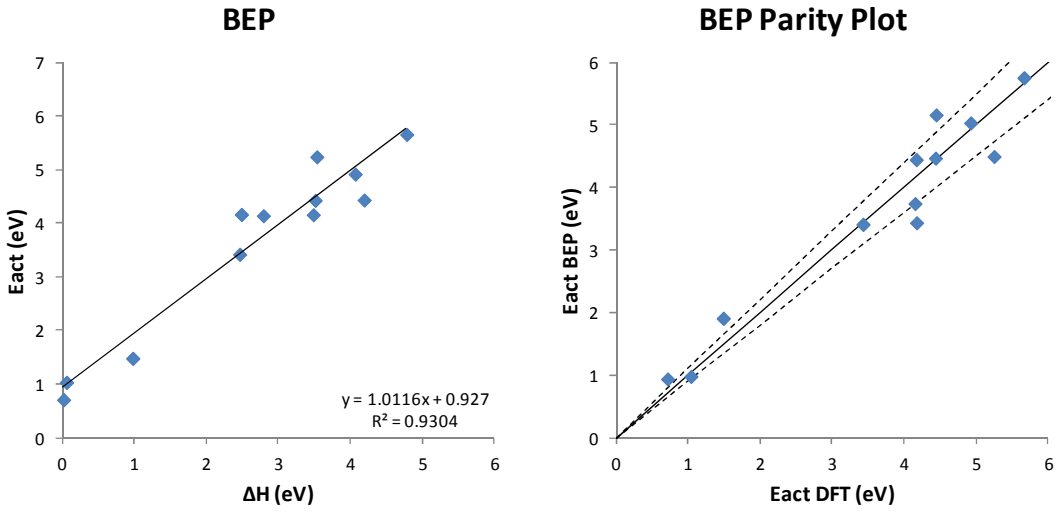

Figure 51: Plots of activation energy (Eact) against the enthalpy change(ΔH) (on the left) and parity plot of activation energy calculated by BEP and DFT (on the right) for CO, CH dissociation on Pt metal

Universalities for dissociation of biatomic molecules have been investigated analyzing the effect of the change of structure for the same platinum metal. The slope of the BEP interpolation line has a value of 1.01, respect to a 0.99 value of the global dissociation BEP trend. This means that the nature of the TS has remained the same among platinum. TSs still have late configuration. The parity plot on the right confirms that the BEP relationship is able to predict the activation energy of a dissociative step for biatomic molecules within the confidential bound of ±10% because of analogies between bi- and triatomic dissociation TS geometries.

BEP validation on dissociation reactions of biatomic molecules on Cu surfaces

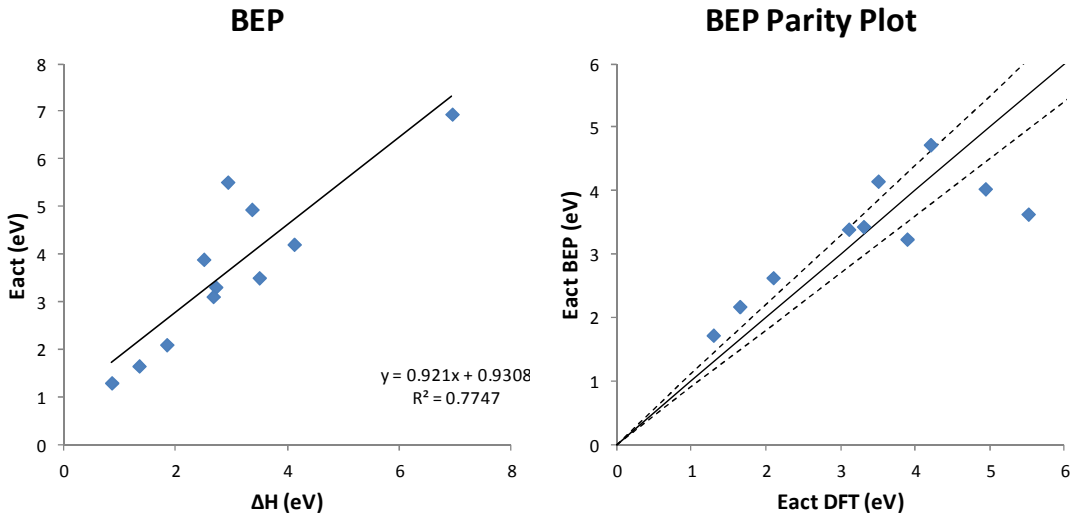

Figure 52: Plots of activation energy (Eact) against the enthalpy change(ΔH) (on the left) and parity plot of activation energy calculated by BEP and DFT (on the right) for CO, CH dissociation on Cu metal

The effect of structure change for the activation energy of biatomic dissociation reactions has been studied for the copper surface. The slope of the BEP interpolation line has the value of 0.92 which is representative for the lateness of TSs characterizing this class of reactions. Respect to the global BEP plot, the intercept of the line has increased to a value of 0.93, respect to 0.62. This is a warning for the fact that dissociation of biatomic molecules intrinsically needs higher quantity of energy. The two points affected by sterical effects still lie outside the confidential bound and affect the R^2 index, which is worsened respect to the global case because of a smaller sample.

BEP validation on dissociation reactions of biatomic molecules on Ag surfaces

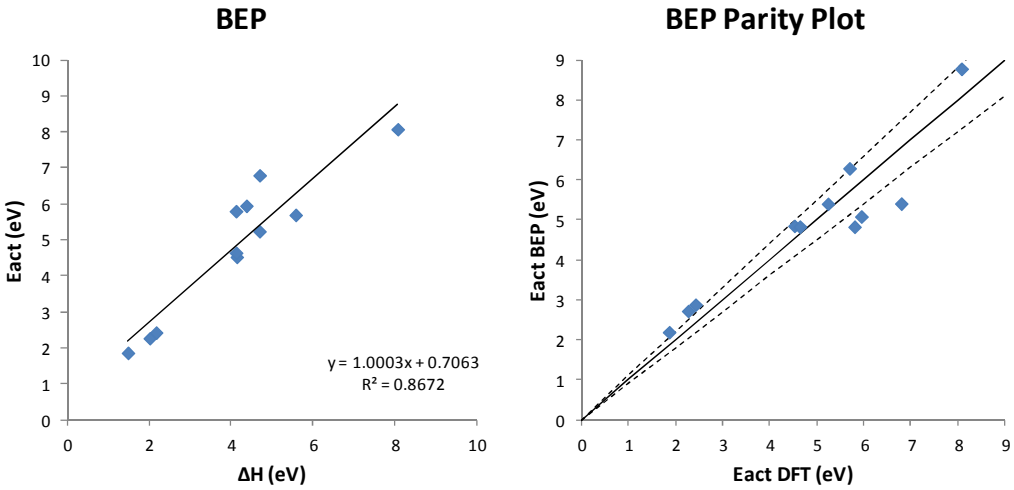

Figure 53: Plots of activation energy (Eact) against the enthalpy change(ΔH) (on the left) and parity plot of activation energy calculated by BEP and DFT (on the right) for CO, CH dissociation on Ag metal

The effect of change of structure of the catalyst for the activation energy of the biatomic dissociative steps on silver catalysts has been investigated in Figure 53. The slope of the BEP interpolation line is 1, indicating the perfect late nature of the TSs on silver surfaces. The intercept of the line has increased from 0.44 to 0.71, indicating that the intrinsic energy needed for the dissociation of biatomic molecules is higher respect to that needed for the dissociation of CH_2 molecules. The dispersion of data along the interpolation line is 0.87, with the BEP model which is able to predict the activation energy of dissociative steps of biatomic molecules on silver surfaces.

BEP validation on dissociation reactions of biatomic molecules on (100) surfaces

In the three following paragraphs the effect of the change of metal type within the same slab structure on the activation energy of dissociation steps of biatomic molecules is analyzed. The aim of this assessment is the clear identification of universalities among the same class of reaction, which is the dissociation of biatomic molecules and on the same structure of the catalyst. The assessment of BEP relationships is the consequence of the identification of these general rules of similarities.

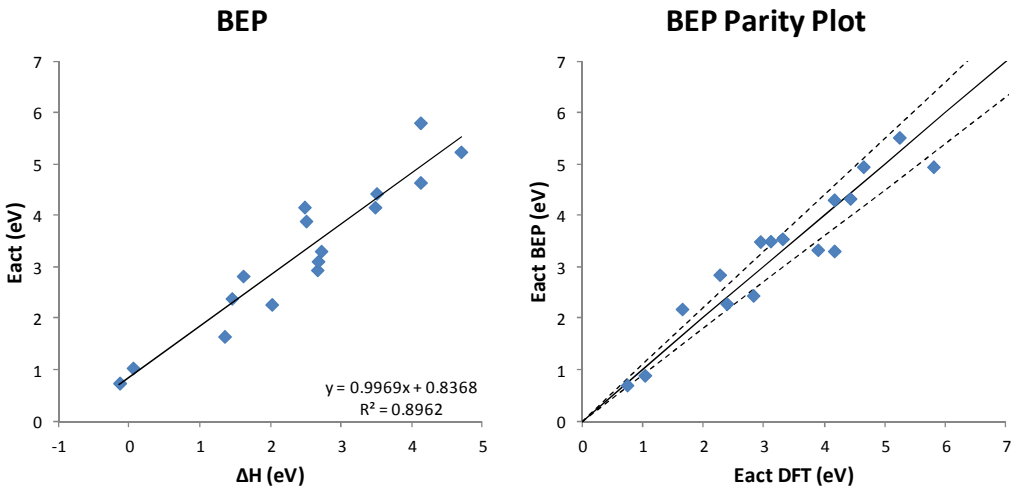

Figure 54: Plots of activation energy (Eact) against the enthalpy change(ΔH) (on the left) and parity plot of activation energy calculated by BEP and DFT (on the right) for CO, CH dissociation on (100) metal surfaces

DFT data have been collected in a plot of activation energy against enthalpy change for CO and CH dissociation reactions on (100) surfaces. The character of the TSs is still late, having the BEP line a slope of 1.00. The scattering of data is still acceptable, with a R^2=0.90, as confirmed by the parity plot on the right of Figure 54. The intercept between the analogous plot for CO, CH and CH_2 dissociation reactions is higher (0.84 against 0.79).

BEP validation on dissociation reactions of biatomic molecules on (110) surfaces

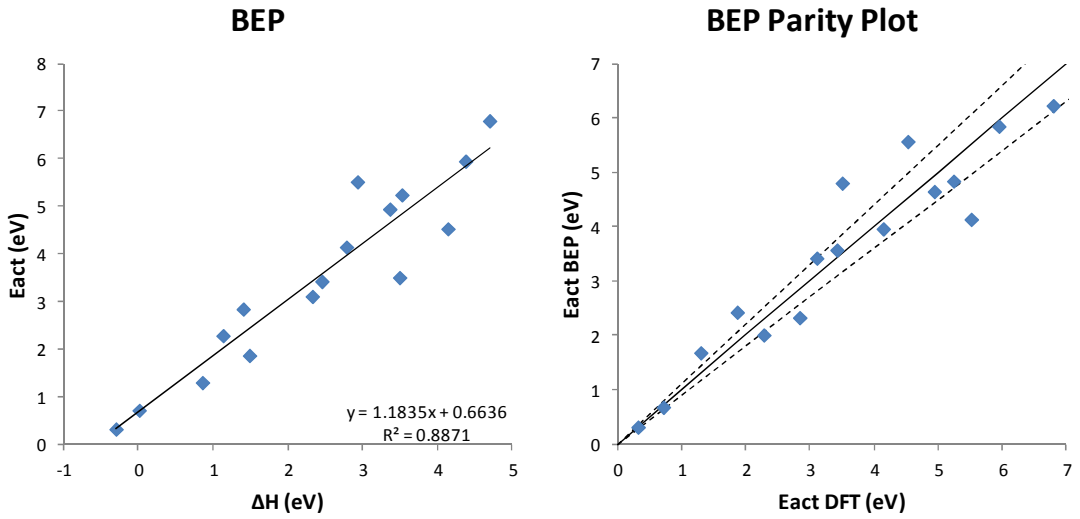

Figure 55: Plots of activation energy (Eact) against the enthalpy change(ΔH) (on the left) and parity plot of activation energy calculated by BEP and DFT (on the right) for CO, CH dissociation on (110) metal surfaces

The effect of change of metal type on the activation energy of dissociation reactions of biatomic molecules has been investigated collecting DFT data for (110) surfaces. The slope of the line has the value that indicates the presence of a late TS (1.18), confirming the

conclusions regarding geometrical configuration of Table 2-3. The intercept of the BEP interpolation line is 0.66 and the dispersion of data is represented by a R^2=0.89. Parity plot on the right of the figure above shows the ability of BEP relationship to evaluate the activation energy of a dissociation process for biatomic molecules on (110) metal surfaces, highlighting the presence of analogies for TSs among this class of reaction.

BEP validation on dissociation reactions of biatomic molecules on (111) surfaces

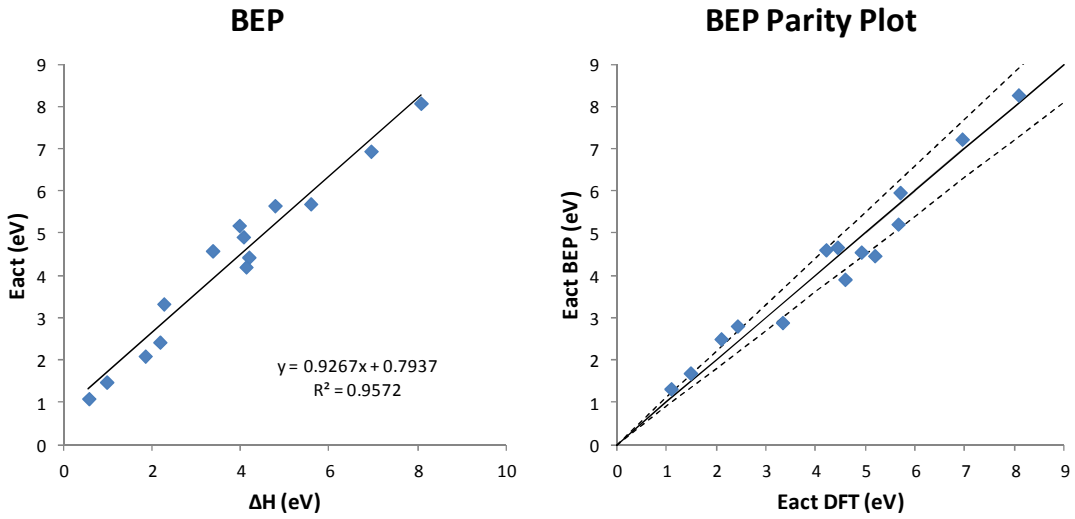

Figure 56: Plots of activation energy (Eact) against the enthalpy change(ΔH) (on the left) and parity plot of activation energy calculated by BEP and DFT (on the right) for CO, CH dissociation on (110) metal surfaces

The effect of the change of metal on the activation energy of the dissociation reaction for biatomic molecules on (111) surfaces is analyzed in this paragraph. The slope of the line (0.93) is indicating the presence of late TSs for CO and CH dissociation on (111) surfaces. The nature of the TSs influences also the dispersion of data along the BEP interpolation line. R^2=0.96 is representative for a TS character that remains constant for this surface, for the class of reaction of biatomic molecules. The parity plot on the right of the figure above proves that the comparison between DFT and BEP data belong to the ±10% corridor.

BEP validation on dehydrogenation reactions

BEP assessment has been performed for the class of dehydrogenation reactions, that are represented by the CH and CH_2 dissociation. A global BEP plot is reported for this class of reaction.

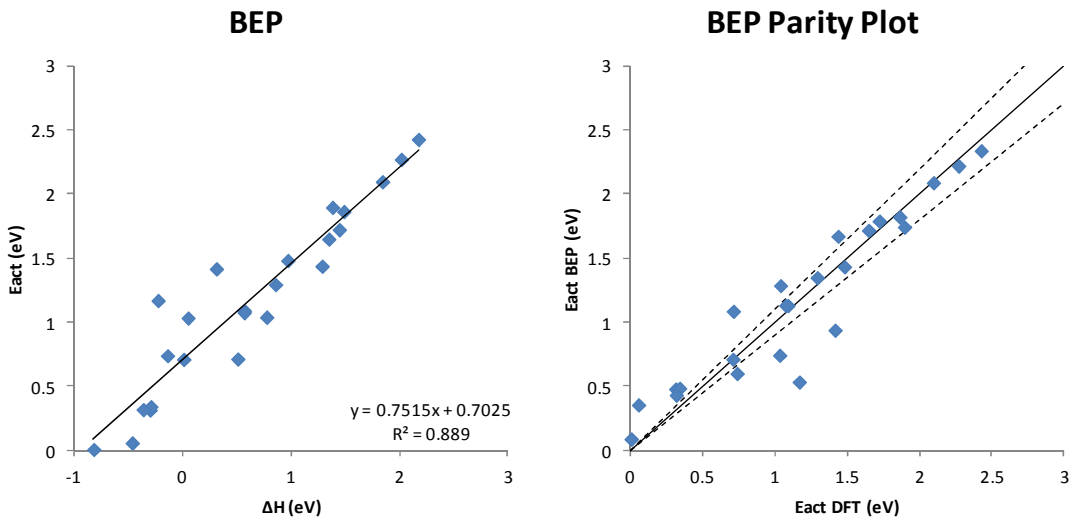

Figure 57: BEP plot (on the left) and parity plot of activation energy calculated by BEP and DFT (on the right) for CH_2, CH dissociation reaction

The BEP plot shows that the model is able to predict the activation energy of a dehydrogenation dissociative step. The slope of the BEP interpolation line is 0.75, which accounts for the late nature of the TSs for this class of reaction, while the intercept is 0.7025. No further investigation on the metal or structure effects have been conducted for this class of reaction.

BEP validation on dissociation reactions of triatomic molecules, CH_2 dissociation

The second class of reaction whose universalities have been investigated is the dissociation of triatomic molecules. The collected DFT data for this class have been the dissociation of CH_2 molecule on rhodium, platinum, copper and silver on (100), (110) and (111) metal surface. For this reason, this section corresponds to the identification of BEP trends and universalities of triatomic and CH_2 dissociation because CH_2 dissociation reaction has been investigated as representative for all triatomic molecules dissociation.

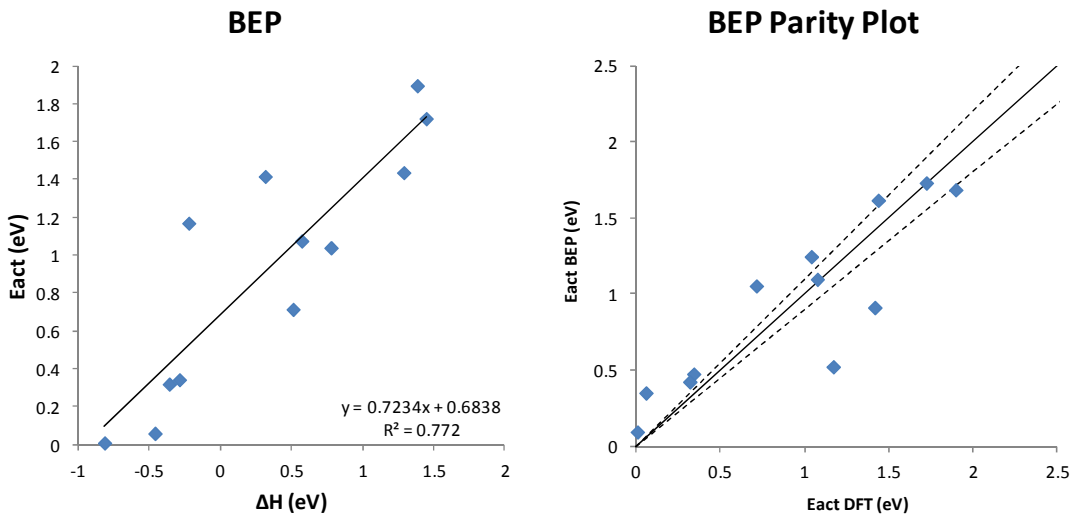

Figure 58: Plots of activation energy (Eact) against the enthalpy change(ΔH) (on the left) and parity plot of activation energy calculated by BEP and DFT (on the right) for CH_2 dissociation on all metal surfaces

The slope of the BEP line shows a slope of 0.7234, which implies the presence of a late TSs among all dissociation. Two points are unrelated to the BEP line, and this is due to the fact that these two outliers are referred to the Pt (100) and Pt (110) surface dissociation, which are characterized by an intermediate TS between early and late (Table 4). If one could exclude the two outliers point from the BEP interpolation, one would notice a slope of the BEP line of would increase to 0.7953 and the dispersion of data would be better, for the points characterized by the late TS.

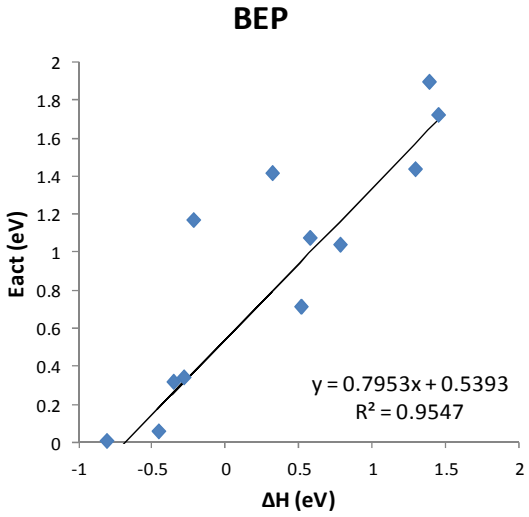

Figure 59: Plot of activation energy (Eact) against enthalpy change (ΔH) and BEP interpolation of points characterized by a late TS for CH_2 dissociation

This case can be taken as negative example for the identification of what universalities are. The power of BEP theory lies in the conservation of the characteristics of the TSs among the class of reaction analyzed. BEP works appropriately provided that universalities are conserved; a critical analysis of semiempirical methods is always needed. However, the BEP trend presents the typical features of late TS with a good predictivity of the model, apart from the two outliers.

BEP validation on dissociation reactions of CH_2 on Rh surfaces

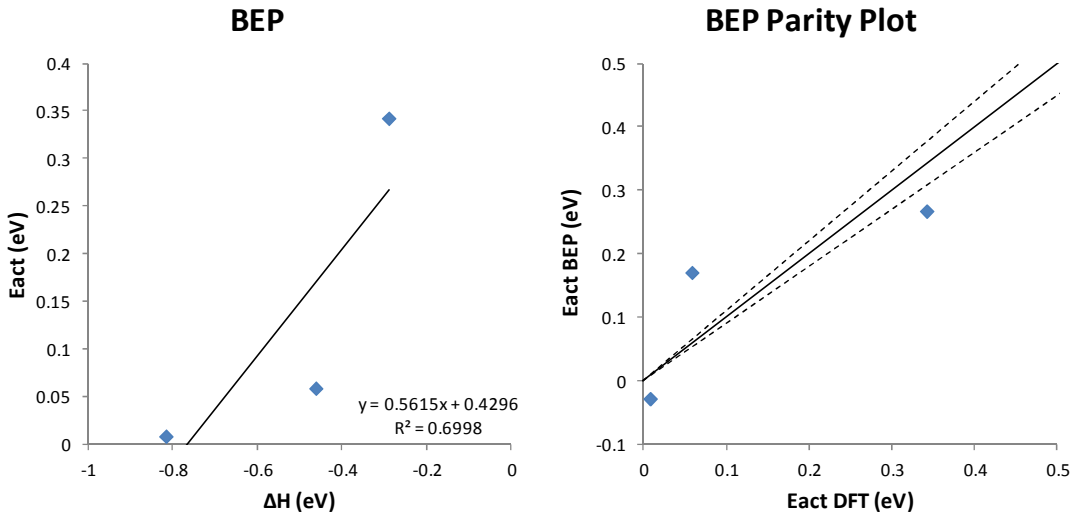

Figure 60: Plots of activation energy (Eact) against the enthalpy change(ΔH) (on the left) and parity plot of activation energy calculated by BEP and DFT (on the right) for CH_2 dissociation on rhodium surfaces

Universalities of CH_2 dissociation have been investigated for dissociation on rhodium surfaces (100), (110), (111). The slope of the BEP interpolation suggests the presence of a mixed early and late TS, but the slope of this interpolation is affected by the small sample size, which is the minimum for a linear interpolation. The distribution of the data along the BEP interpolation line is affected too by the small sample taken into account, with no point belonging to the ±10% corridor in the parity plot on the right.

BEP validation on dissociation reactions of CH_2 on Pt surfaces

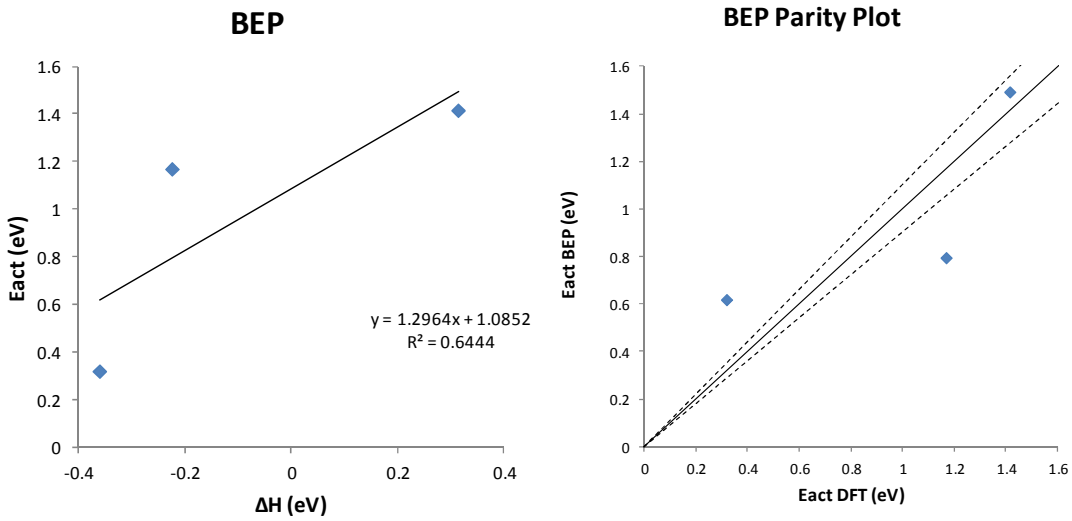

Figure 61: Plots of activation energy (Eact) against the enthalpy change(ΔH) (on the left) and parity plot of activation energy calculated by BEP and DFT (on the right) for CH_2 dissociation on platinum surfaces

BEP trends have been investigated on Pt (100), (110) and (111) surfaces. The BEP interpolation is affected by the presence of two points that do not belong to the general trend of late TSs. However the BEP analysis can be conducted, but with a slope of 1.2964, which is due to the two outliers, and the dispersion that is too elevated, with just one point belonging to the 10% confidential bound of the parity plot on the right. This is both due to the presence of different natures of the TSs both to the small sample considered.

BEP validation on dissociation reactions of CH_2 on Cu surfaces

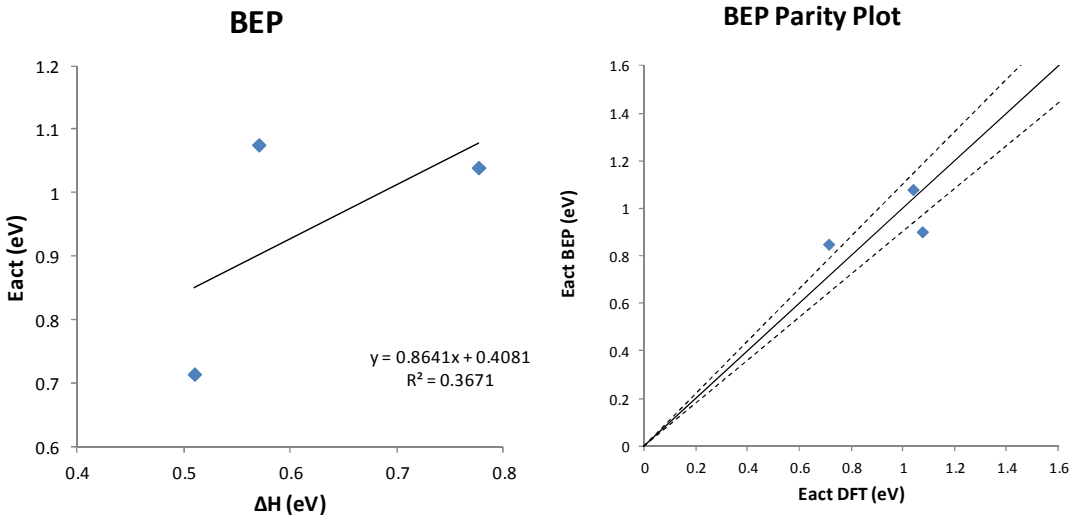

Figure 62: Plots of activation energy (Eact) against the enthalpy change(ΔH) (on the left) and parity plot of activation energy calculated by BEP and DFT (on the right) for CH_2 dissociation on copper surfaces

CH_2 dissociation data are used for the BEP assessment and investigation of universalities among different surfaces for copper catalysts. The slope of the BEP interpolation line is 0.8641, thus agreeing with the general trend which states that CH_2 dissociation on copper have late TSs. The dispersion of data appears to be high if only evaluated by R^2=0.3671 but this is because the narrow range of enthalpy difference, which introduces a larger dispersion if seen in a small scale. The parity plot on the right of the figure above shows that even with a higher dispersion, the DFT and BEP activation energy are not far from the 10% limits, because of the same nature of the TSs.

BEP validation on dissociation reactions of CH_2 on Ag surfaces

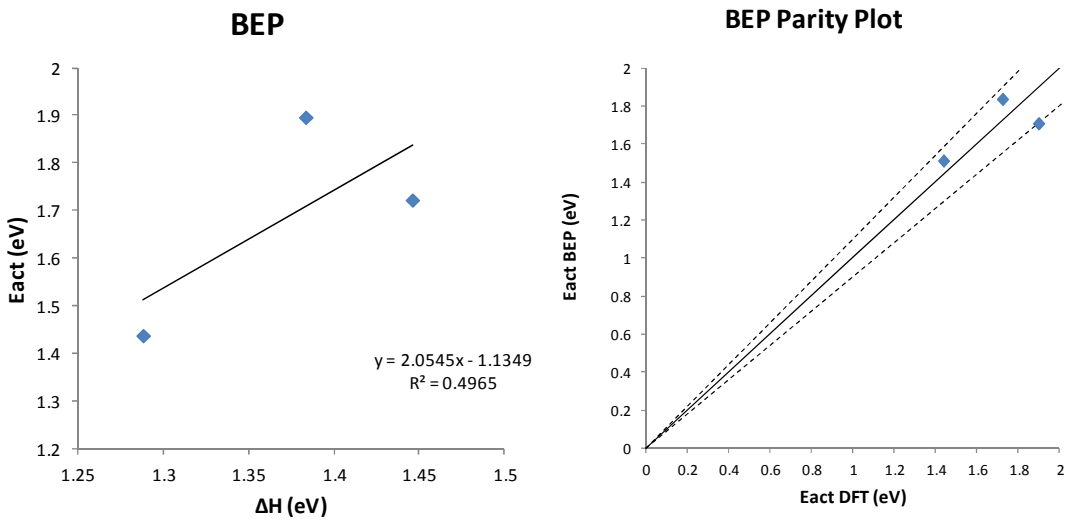

Figure 63: Plots of activation energy (Eact) against the enthalpy change(ΔH) (on the left) and parity plot of activation energy calculated by BEP and DFT (on the right) for CH_2 dissociation on silver surfaces

CH_2 dissociation has been investigated exploiting the same metal, which is silver, on the three different low index surfaces that are (100), (110) and (111). The slope of the BEP interpolation line is 2.0545 which is much higher than the expected value for late transition states as the ones on silver surfaces are. The motivation for this lies in the small sample which amplifies the minimum errors, making the interpolation to lose its physical interpretation. More tests are needed for the validation of the BEP line. The small sample also affects the dispersion of data at R^2=0.4965, even if the parity plot on the right shows that three points belong to the 10% limits. This is because the R^2 is an index of the how well data fit the statistical model, and do not give information about the quantity of scattering of the single points.

BEP validation on dissociation reactions of CH_2 on (100) surfaces

This section of the work deals with the identification of general trends of dissociation reactions for triatomic molecules respect to the same low index surfaces, whose benchmark is represented by DFT data coming from CH_2 dissociation.

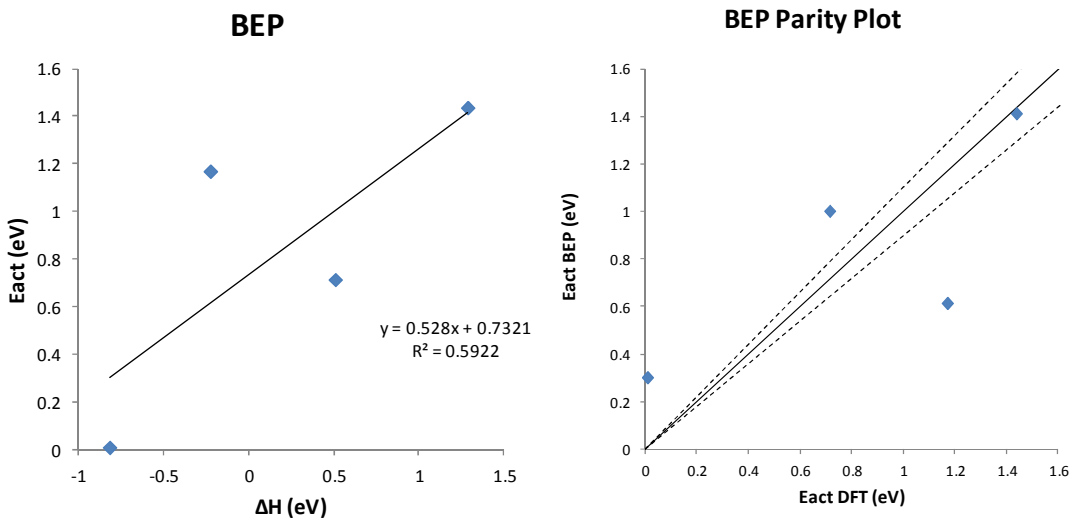

Figure 64: Plots of activation energy (Eact) against the enthalpy change(ΔH) (on the left) and parity plot of activation energy calculated by BEP and DFT (on the right) for CH_2 dissociation on (100) surfaces

BEP trends are herein investigated on (100) surfaces for CH_2 dissociation. All slab spear to belong to a single BEP trend but one, that is the point referring to the reaction on Pt (100), which is characterized by a intermediate early and late TS. All other metals show a late nature of the TSs. This discrepancy causes the point referring to Pt (100) to be far away from the others and thus not belonging to the same interpolation line. If one could exclude the Pt (100) from this analysis, the interpolation BEP line would be with a higher slope and with a smaller data dispersion. Parity plot on the right shows two points whose activation energy has been overestimated by BEP relationship, one underestimated. This discrepancy is explained by the change of the nature of TSs.

BEP validation on dissociation reactions of CH_2 on (110) surfaces

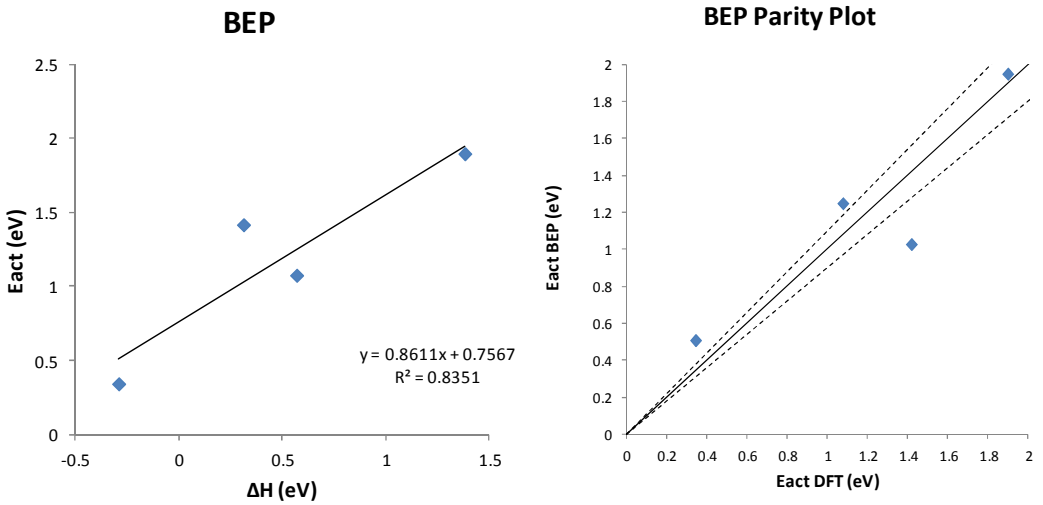

Figure 65: Plots of activation energy (Eact) against the enthalpy change(ΔH) (on the left) and parity plot of activation energy calculated by BEP and DFT (on the right) for CH_2 dissociation on (110) surfaces

The search of general trend for triatomic molecules dissociation has analyzed the effect of change of metal for the same low index (110) surface. Three points belong to one BEP trend, while the fourth one lies apart from the general trend. That the point refers to Pt (110), which has the mixed early and late TS. If one could exclude from the BEP interpolation this point, the resulting line would have a higher slope, typical of late TSs, and a lower data dispersion. In the parity plot above, there are two point where the BEP activation energy is overestimated while it is underestimated for Pt (110).

BEP validation on dissociation reactions of CH_2 on (111) surfaces

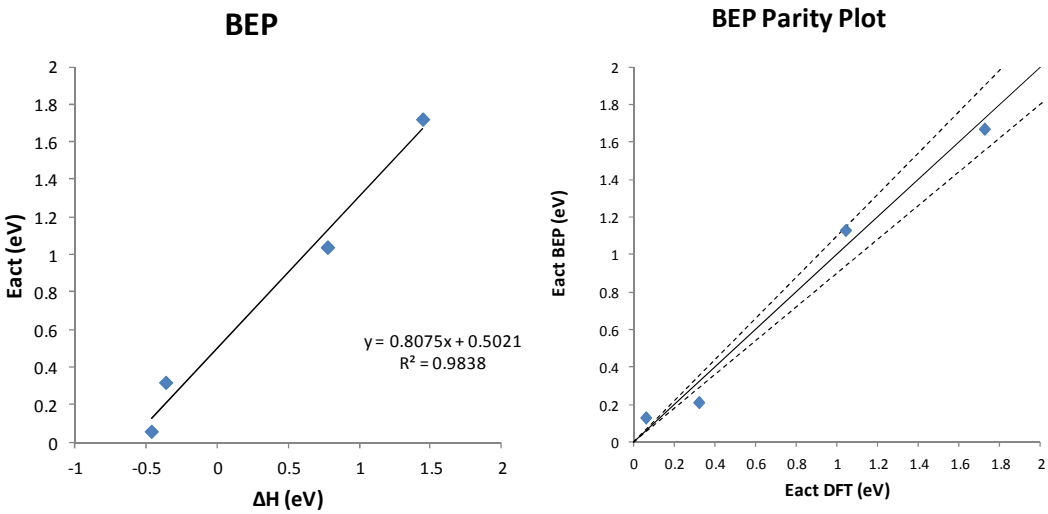

Figure 66: Plots of activation energy (Eact) against the enthalpy change(ΔH) (on the left) and parity plot of activation energy calculated by BEP and DFT (on the right) for CH_2 dissociation on (111) surfaces

CH_2 dissociation has been investigated on all (111) surfaces on Rh, Pt, Cu, Ag metals. The search of general trends show a good agreement between BEP and DFT calculations, implying that the nature of TSs is late on all the four metals analyzed. This behavior is reflected on the slope of the interpolation line which is 0.8075. The dispersion of data is very good, with a R^2=0.9838. As the parity plot on the right of Figure 66 is showing, the BEP interpolated energies belong to the ±10% corridor.

BEP validation on dissociation reactions of CH molecule

The analysis of universalities for the validation of BEP relationship needs the definition of a class of reactions. This section of the work deals with the analysis of DFT data coming from the class of reaction which is a reaction itself, the CH dissociation.

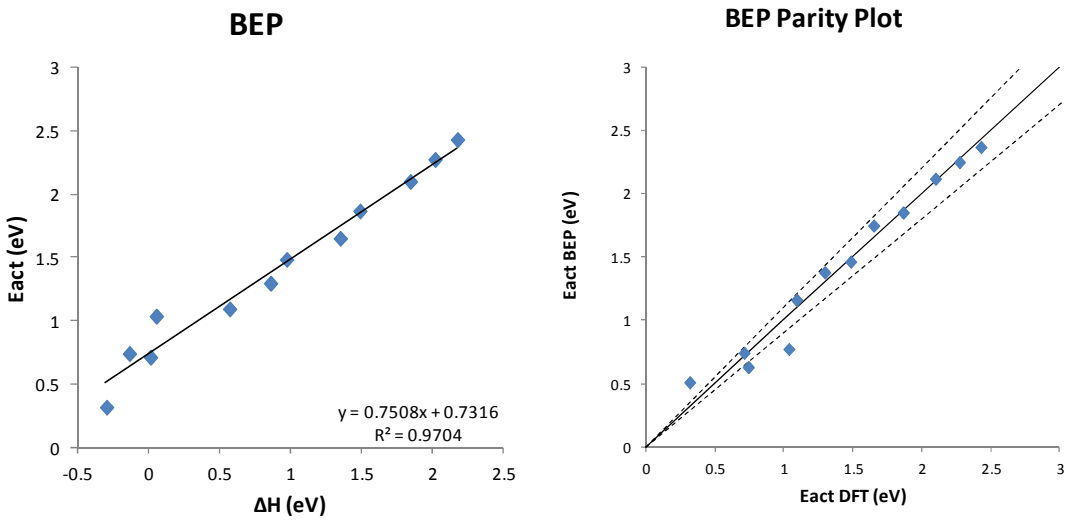

Figure 67: Plots of activation energy (Eact) against the enthalpy change(ΔH) (on the left) and parity plot of activation energy calculated by BEP and DFT (on the right) for CH dissociation on all metals and surfaces

All DFT data of CH dissociation performed on rhodium, platinum, copper and silver on the (100), (110) and (111) metal surface are reported in the plot above for the investigation of unique trend of BEP relationship. The nature of the TSs is late for this class of reaction as described in Chapter 3 and indicated by the slope of the BEP interpolation line, which is 0.7508. The low data dispersion is index of the fact that the nature of the TSs remains the same among all metals and surfaces, but also because the unbalancing of reactants and products on the various metals and surfaces is comparable and follows the same trends. For example, adsorption energy of CH on Rh (100) is higher than on Rh (111) which is higher than on Rh (110). The behavior of the C+H system chases the following order for rhodium surfaces: (100)>(110)>(111). The (100)>(111)>(110) is kept on all metals for CH adsorption

stability, while (100)>(110)>(111) order is constant for C+H adsorption stability. This clear trend gives regularity to the trends, identifying a net BEP interpolation line which holds a low dispersion of the calculated data. Parity plot on the right of the figure above shows that the BEP interpolated data lie on the bisect of the first quadrant. Universalities are in this case evident for CH molecule dissociation.

BEP validation on dissociation reactions of CH on Rh surfaces

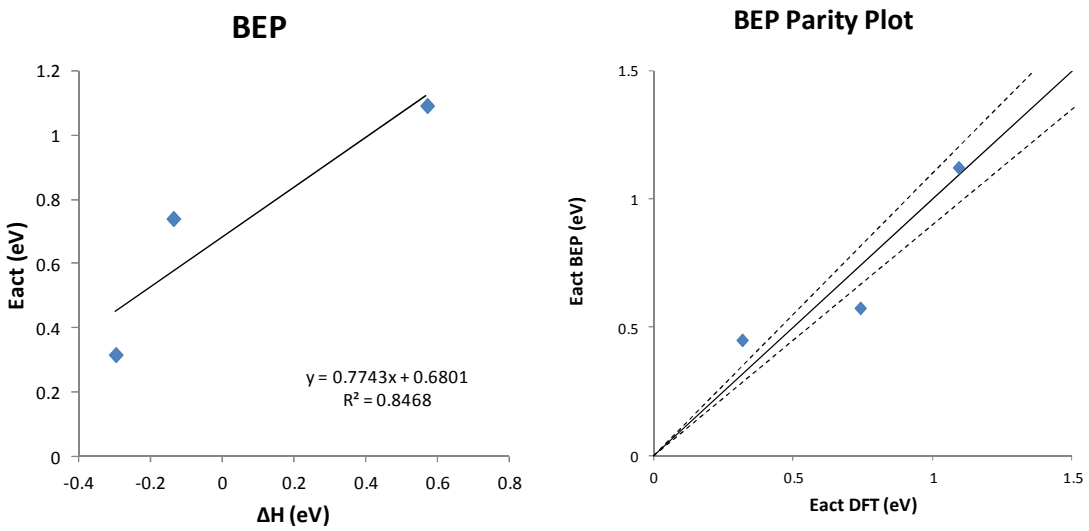

Figure 68: Plots of activation energy (Eact) against the enthalpy change(ΔH) (on the left) and parity plot of activation energy calculated by BEP and DFT (on the right) for CH dissociation on rhodium surfaces

BEP assessment has been performed on rhodium surfaces at three low index metal surfaces (100),(110),(111). The BEP interpolation line through this point has a slope which indicates the nature of a late TSs. Its value is in fact 0.77, that has to be compared to a reference value of 1. The dispersion of the point along the BEP line is R^2=0.85, with the parity plot on the right of figure above which do not belong to the ±10% confidential bounds. This discrepancy is simply due to a numerical problem, linked to the fact that the activation energy of the dissociation process on those two rhodium surfaces is numerically small. Even a little discrepancy between the BEP calculated value and the DFT one is larger than the 10% of the measure.

BEP validation on dissociation reactions of CH on Pt surfaces

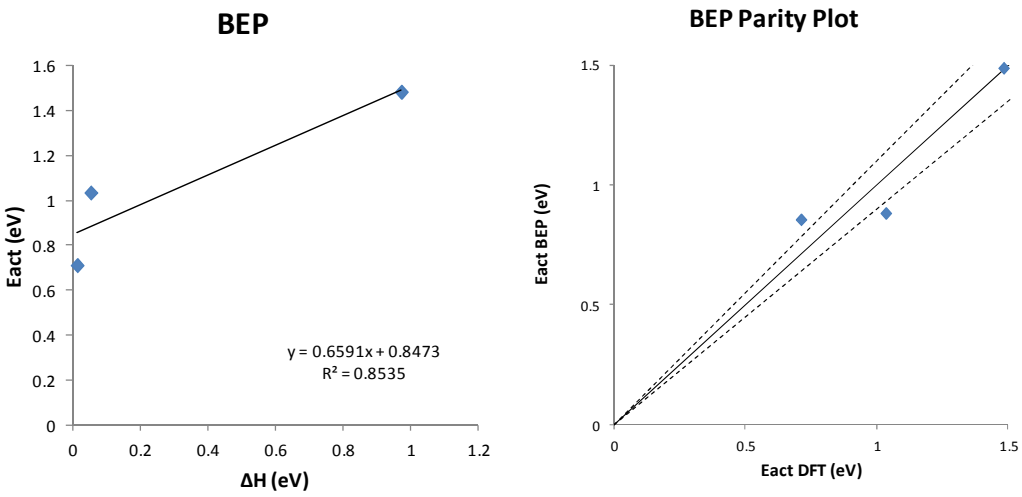

Figure 69: Plots of activation energy (Eact) against the enthalpy change(ΔH) (on the left) and parity plot of activation energy calculated by BEP and DFT (on the right) for CH dissociation on platinum surfaces

The validation and investigation of BEP relationships have been performed for platinum (100),(110),(111) surfaces. The slope of the line is 0.66 and confirms the fact that CH dissociation has a late TS. This value is close to one, even if the small sample of three data introduces an error which is also affecting the parity plot on the right of the figure above. The small R^2=0.85 appears to represent a good agreement between BEP foreseen activation energy and the DFT collected ones but two points are outside the ±10% corridor. This is due to the fact that the sample is represented only by three data, and any small error can affect the interpolation.

BEP validation on dissociation reactions of CH on Cu surfaces

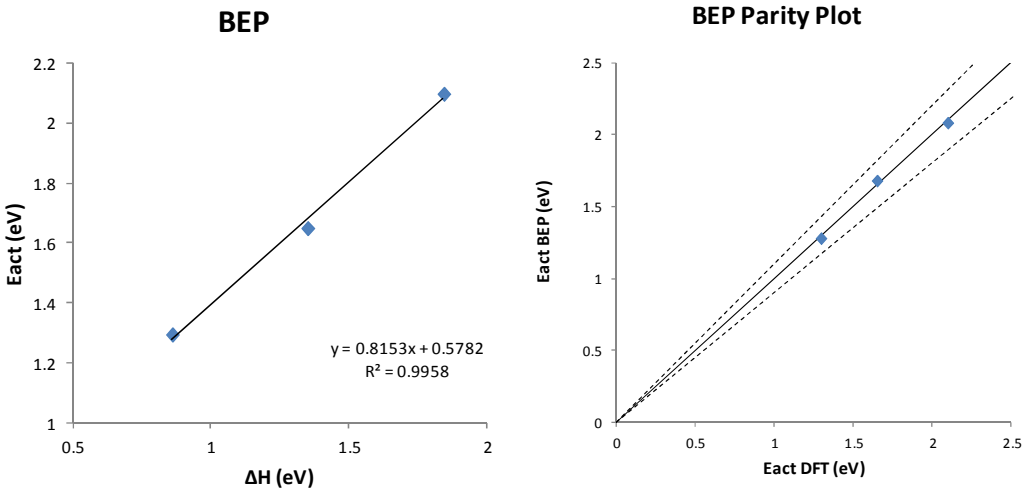

Figure 70: Plots of activation energy (Eact) against the enthalpy change(ΔH) (on the left) and parity plot of activation energy calculated by BEP and DFT (on the right) for CH dissociation on copper surfaces

Copper metal provides a clear example of the existence of universalities and analogies for CH dissociation TSs which are the basis for the existence of BEP relationship. In this case the slope of the BEP interpolation line is 0.82, which perfectly confirms the late nature of the TSs on Cu. In this case the absence of any scattering of the interpolated values on the BEP line is the perfect confirm that the TS of the CH dissociation maintains the same nature and, mutatis mutanda, the geometrical configurations among all surfaces. The parity plot on the right of Figure 70confirms the very little scattering from the interpolation BEP line.

BEP validation on dissociation reactions of CH on Ag surfaces

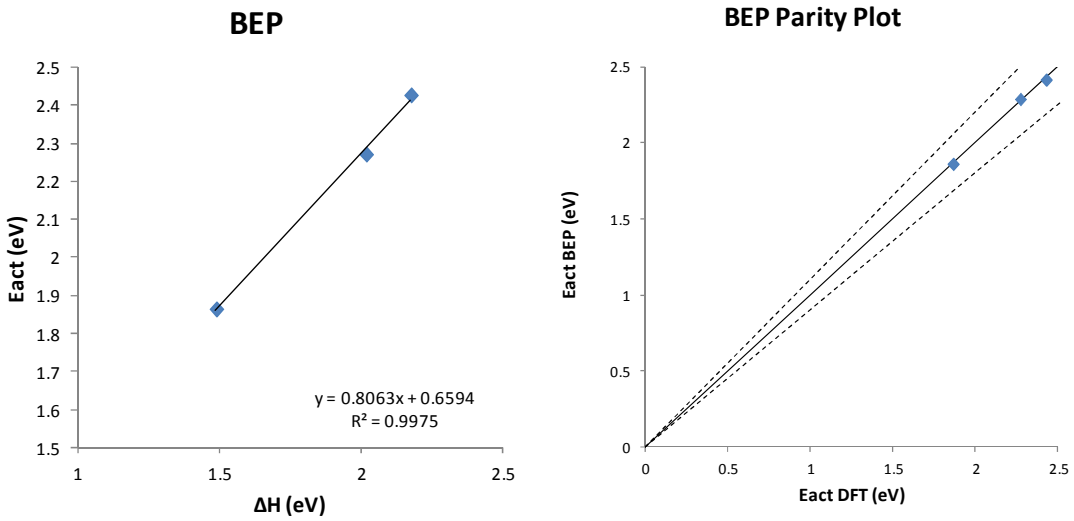

Figure 71: Plots of activation energy (Eact) against the enthalpy change(ΔH) (on the left) and parity plot of activation energy calculated by BEP and DFT (on the right) for CH dissociation on silver surfaces

Ag (100), (110) and (111) surfaces provide a clear example of universalities that hold among different surfaces for CH dissociation. In fact the slope of the interpolation BEP line is 0.8063, very close to the value of CH dissociation on Cu and also in this case the value is confirming the late nature of the TS. The very low scattering of data along the BEP line is also further proof of the nature of lateness of the TSs, with the same geometrical configuration among all different surfaces and the same order of destabilization for reactants and products for silver surfaces. This good agreement between BEP theory and DFT collected data is evident in the R=0.9975 of the distribution of points along the interpolation line and in the parity plot on the right, with the three points staying upon the bisect of the first quadrant.

BEP validation on dissociation reactions of CH on (100) surfaces

In this section of the chapter the investigation on universalities and the search for analogies between the TSs of CH dissociation among the same surfaces, collecting data coming from

different metals. The quest is to find if and why BEP relationships hold among different metals for the same surface.

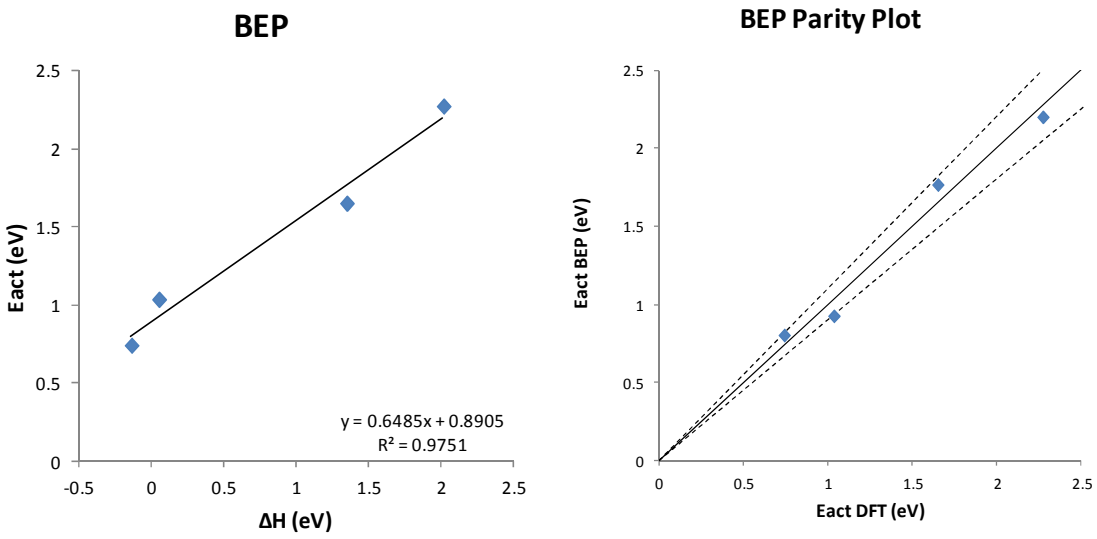

Figure 72: Plots of activation energy (Eact) against the enthalpy change(ΔH) (on the left) and parity plot of activation energy calculated by BEP and DFT (on the right) for CH dissociation on (100) surfaces

CH dissociation data have been collected for the same (100) slab structure for the four Rh, Pt, Cu, Ag metals. The result shows a slope of the BEP interpolation line which is 0.65 and shows the clear nature of the Transition State of CH dissociation on the (100) surface, which is late. The intercept is 0.89, which gives the idea of the order of magnitude of the dissociation energies. Moreover, the very little dispersion of the data along the interpolation line shows that the geometry and the electronic state of the Transition State is kept on each metal surface, no matter the metal analyzed. Parity plot on the right of the figure shows that all BEP against DFT points belong to the ±10% corridor.

BEP validation on dissociation reactions of CH on (110) surfaces

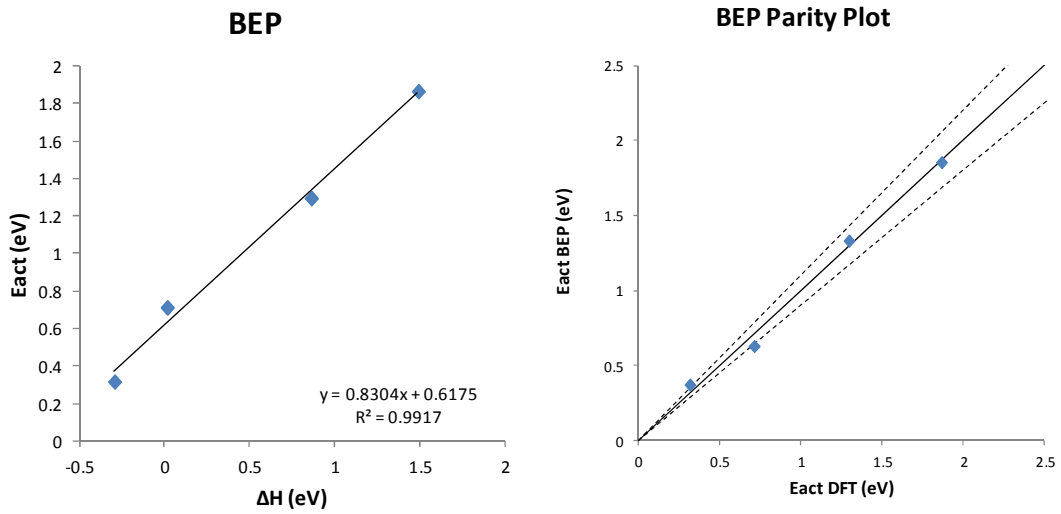

Figure 73: Plots of activation energy (Eact) against the enthalpy change(ΔH) (on the left) and parity plot of activation energy calculated by BEP and DFT (on the right) for CH dissociation on (110) surfaces

A BEP analysis has been performed on CH dissociation for the (110) metal surface. The universalities, that are the analogies present among different TSs of this class of reaction still holds. BEP line is valid and validated. The slope of the BEP interpolation line is slightly increasing respect to that of (100) surface, going to 0.83, but showing however the late nature of the TS on this surface. The R^2=0.99 indicates that the geometrical and electronic structure of the Transition State on (110) surfaces is kept constant for all metals. Parity plot on the right show that all points stay within the confidential bounds.

BEP validation on dissociation reactions of CH on (111) surfaces

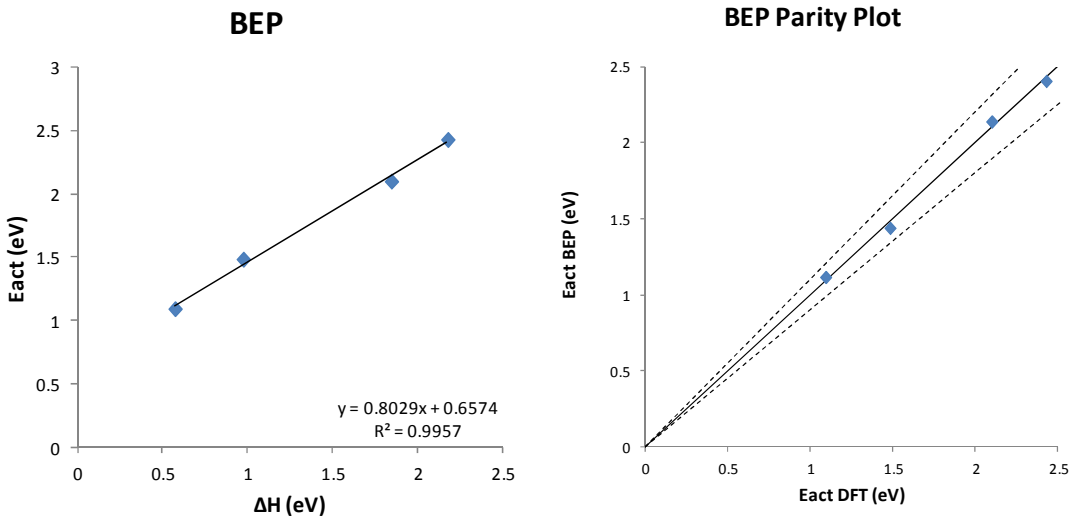

Figure 74: Plots of activation energy (Eact) against the enthalpy change(ΔH) (on the left) and parity plot of activation energy calculated by BEP and DFT (on the right) for CH dissociation on (111) surfaces

BEP analysis is focused on the CH dissociation for the selected metals on the (111) surface. The collected data proves to have a slope of 0.80 which shows the clear late nature of the Transition State on (111) surfaces of CH dissociation, in line with the value of the global plot. The intercept of the plot is 0.73, which is aligned to the values of the same class of reaction. The low scattering of data along the BEP line is a typical feature of CH dissociation, due to the fact that the Transition State keeps the same geometrical and electronic structure among all Transition States on (111) surface. Each BEP versus DFT point stay on the bisector of the first quadrant, proving a good theory to theory agreement.

BEP validation on dissociation reactions of CO molecule

The analysis of universalities for the validation of BEP relationship is focused in this section of the work on the class of CO dissociation reactions. The framework is structured with the first analysis of a global BEP trend, then to the analysis of the structure effect on the same metal and finally to the metal effect on the same structure. The aim is the individuation and validation of BEP trends for the selected class of reaction.

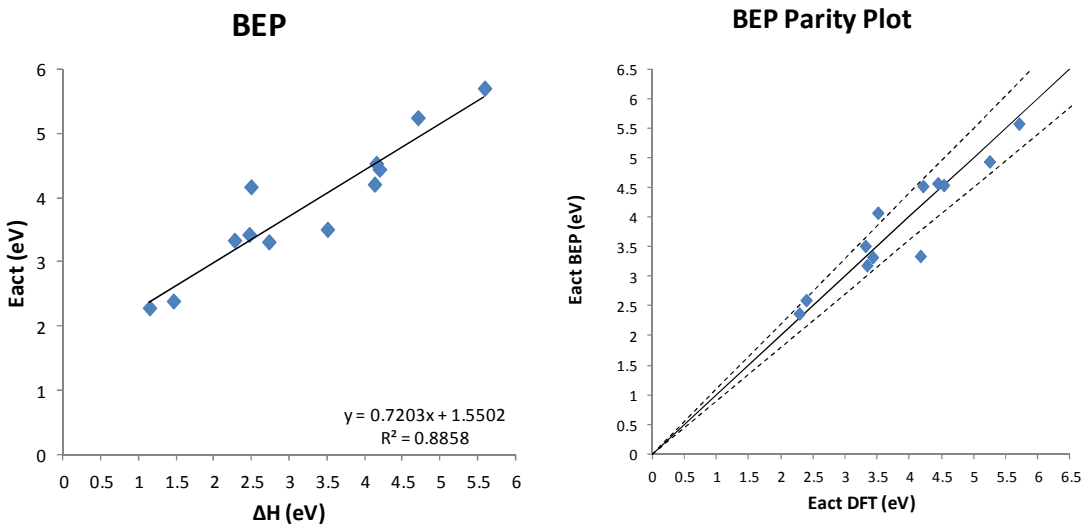

Figure 75: Plots of activation energy (Eact) against the enthalpy change(ΔH) (on the left) and parity plot of activation energy calculated by BEP and DFT (on the right) for CO dissociation on all metals and surfaces

Universalities among CO dissociation on rhodium, platinum, copper and silver (100), (110), (111) surfaces are herein investigated. No oxygen coverage is considered in this section of the work. The BEP interpolation line shows a slope of 0.72, indicating the late nature of TSs of CO dissociations, as reported in Table 2. The intercept of the BEP line is 1.55, showing that CO dissociation needs a higher intrinsic energy for the cleavage of the C-O bond respect for example of C-H bond. The R^2=0.898 is a good indicator of the data dispersion, which are

more scattered than those referring to CH dissociation. This is due to the fact that C and O molecules do not show clear trends in the destabilization of the reactant system (CO adsorbed) and the product system (C and O cleaved adsorbed) as indicated in the B.E. description paragraph. There is no clear order of destabilization for reactants and products thus the TSs have the same geometrical nature, but are affected by an additional electronic effect which is further scattering data along the BEP line.

BEP validation on dissociation reactions of CO on Rh surfaces

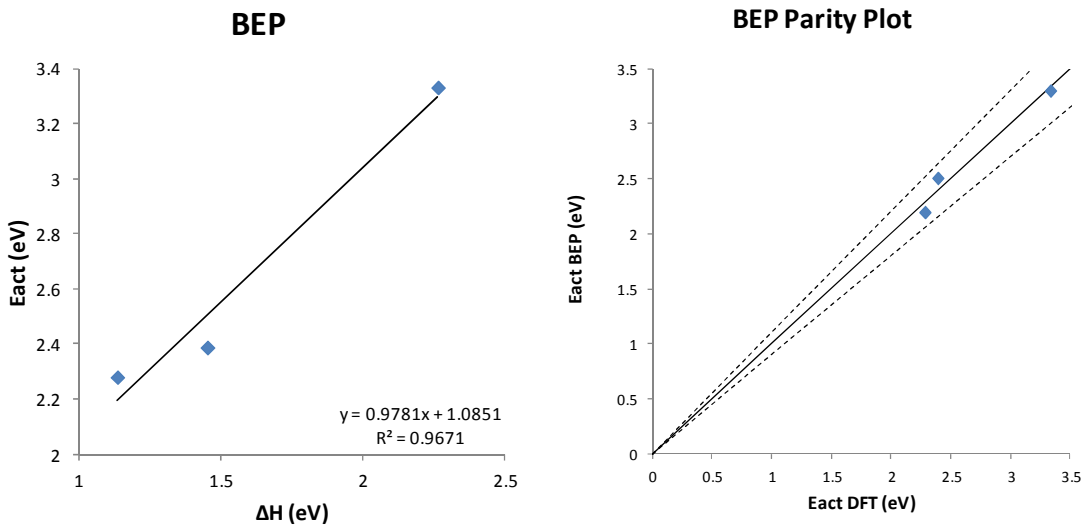

Figure 76: Plots of activation energy (Eact) against the enthalpy change(ΔH) (on the left) and parity plot of activation energy calculated by BEP and DFT (on the right) for CO dissociation on rhodium surfaces

CO dissociation DFT data have been collected for all Rh at the three different metal surfaces. The results shows a good agreement between the BEP interpolation line and the DFT data. The theory to theory comparison confirms the presence of late TSs on the various rhodium surfaces with a slope of 0.98 for the BEP line. The data dispersion is very good, with a R^2=0.97. This is confirmed also by the parity plot on the right-hand side of the figure above, which has all the points obtained from the interpolation with a lower error than 10% respect to the DFT ones. The existence of universalities is confirmed for the CO dissociation on rhodium surfaces.

BEP validation on dissociation reactions of CO on Pt surfaces

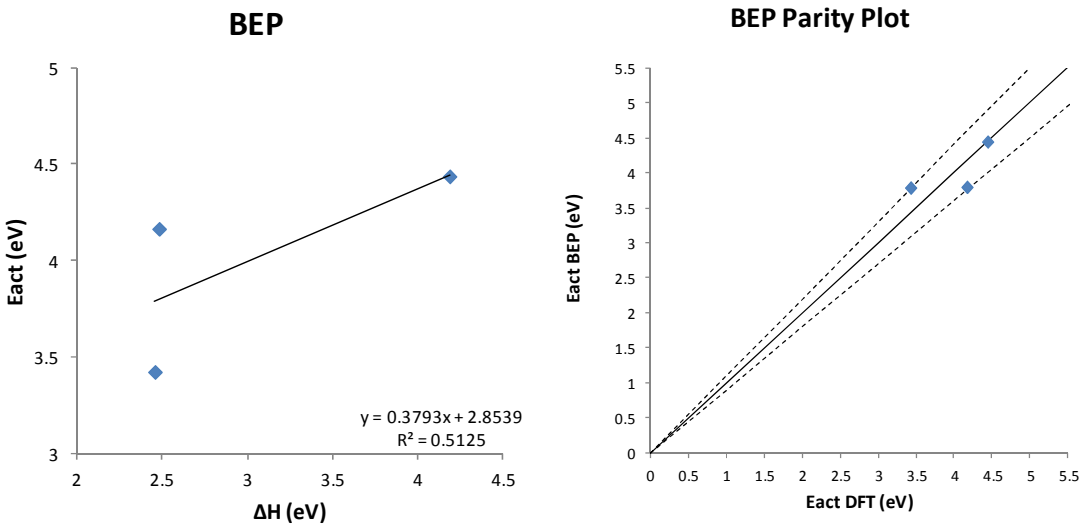

Figure 77: Plots of activation energy (Eact) against the enthalpy change(ΔH) (on the left) and parity plot of activation energy calculated by BEP and DFT (on the right) for CO dissociation on platinum surfaces

CO dissociation universalities have been analyzed for platinum surfaces. The result is affected by the small smaple used for the BEP interpolation, which presents a slope of 0.38, index of a early TSs, and a intercept of 2.85, value of activation energy which does not fit the global trend. More points are needed for the validation of this BEP line.

BEP validation on dissociation reactions of CO on Cu surfaces

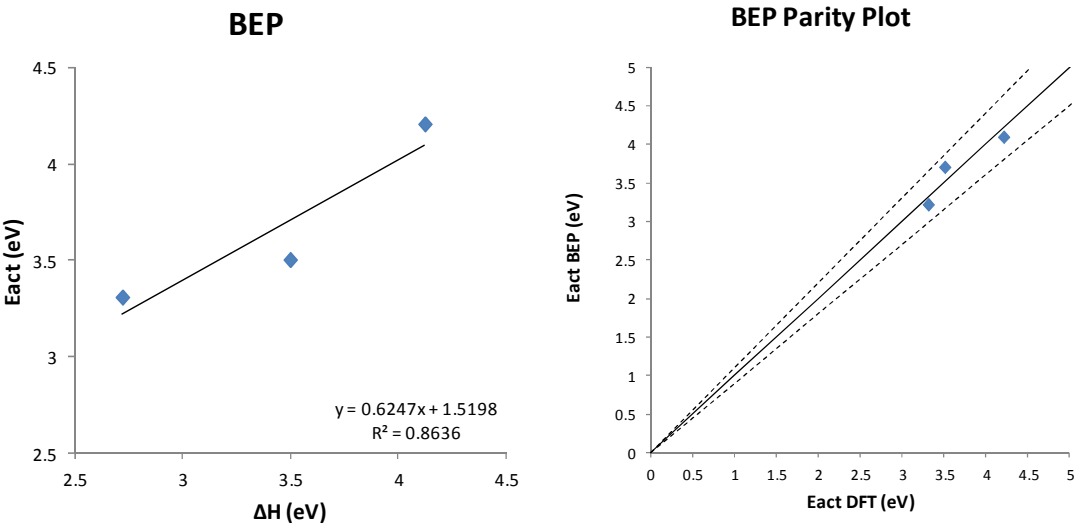

Figure 78: Plots of activation energy (Eact) against the enthalpy change(ΔH) (on the left) and parity plot of activation energy calculated by BEP and DFT (on the right) for CO dissociation on copper surfaces

CO dissociation DFT data have been collected for the individuation of a BEP trend among different surfaces of the same copper metal slab. The result shows a slope of 0.62, confirming

the late character of the TSs on copper metal, and the intercept is 1.52, in line with the general trend for activation energy. The dispersion of data is good, with the parity plot on the right of Figure 78 that shows the alignment of DFT and BEP data within the ±10% corridor. The existence of analogies are confirmed on copper surfaces.

BEP validation on dissociation reactions of CO on Ag surfaces

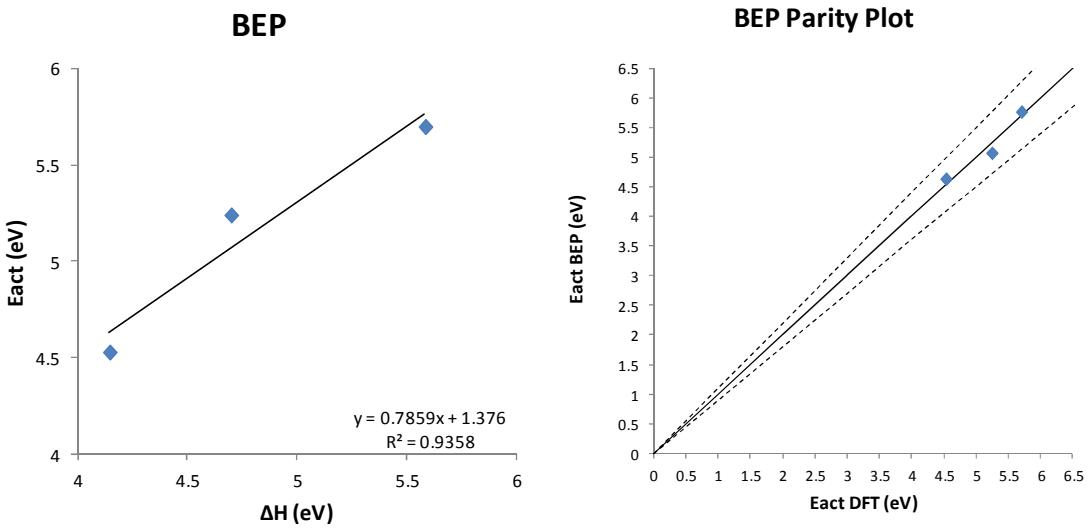

Figure 79: Plots of activation energy (Eact) against the enthalpy change(ΔH) (on the left) and parity plot of activation energy calculated by BEP and DFT (on the right) for CO dissociation on silver surfaces

The BEP interpolation line for CO dissociation on (100) (110) and (111) surfaces on silver metal shows a slope which is indicating the presence of a late TS among the different surfaces. The intercept is 1.38 which is aligned with the previous reported interpolation. The dispersion of data is good, with a R^2=0.94 and a parity plot on the right of the figure presented above which shows all points belonging to the ±10% limits. The existence of a general BEP trend among different surfaces on silver metal is confirmed.

BEP validation on dissociation reactions of CO on (100) surfaces

In this section of the chapter the quest of universalities is analyzed for CO dissociation on the same metal structure at different metals. The first analysis is referring to (100) surfaces for rhodium, platinum, copper and silver.

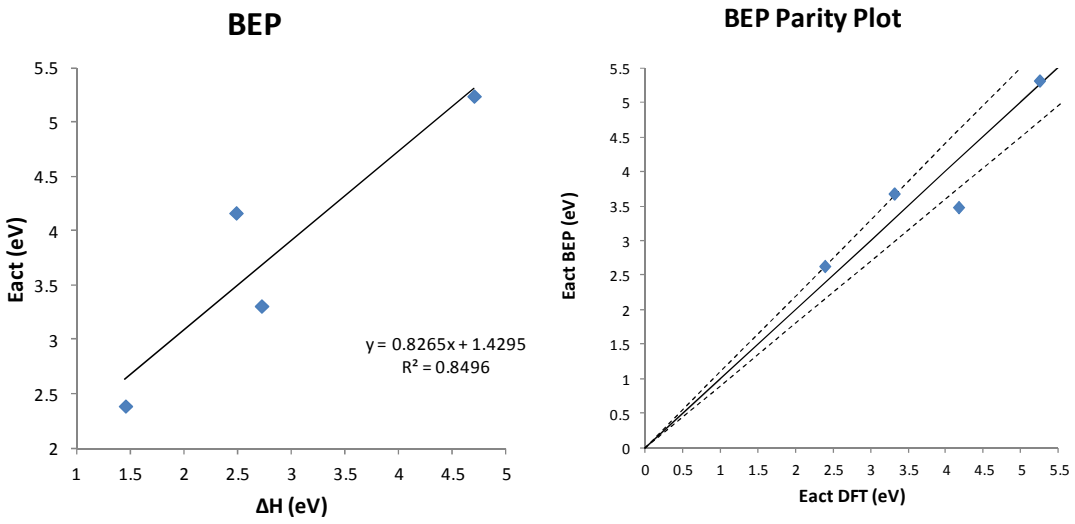

Figure 80: Plots of activation energy (Eact) against the enthalpy change(ΔH) (on the left) and parity plot of activation energy calculated by BEP and DFT (on the right) for CO dissociation on (100) surfaces

The analysis of CO dissociation for the four selected metals of (100) surface brings to the identification of a BEP interpolation line whose slope is 0.83 implying the presence of a late TS. The data dispersion is good with a R^2=0.85, as confirmed by the parity plot on the right-hand side of the figure above. The existence of analogies among the same metal structure for different metals is confirmed for the (100) surfaces for the dissociation of carbon monoxide.

BEP validation on dissociation reactions of CO on (110) surfaces

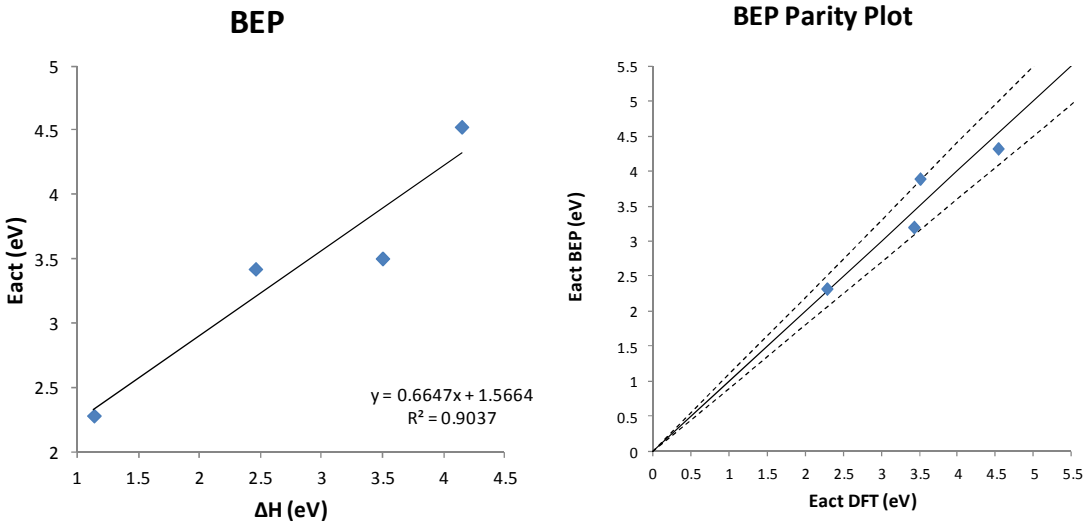

Figure 81: Plots of activation energy (Eact) against the enthalpy change(ΔH) (on the left) and parity plot of activation energy calculated by BEP and DFT (on the right) for CO dissociation on (110) surfaces

BEP assessment has been performed for CO dissociation on (110) surface, with the investigation of general trends for TSs. The slope of 0.66 indicates an intermediate early and

late TS, with a late character that is prevalent. This confirms the late character of TSs for CO dissociation. The intercept is 1.57, aligned with the activation energy of the global CO dissociation. The data dispersion is good as indicated in the parity plot on the right of Figure 81, with all points belonging to the 10% confidential limits for the theory to theory comparison between DFT and BEP.

BEP validation on dissociation reactions of CO molecule on (111) surfaces

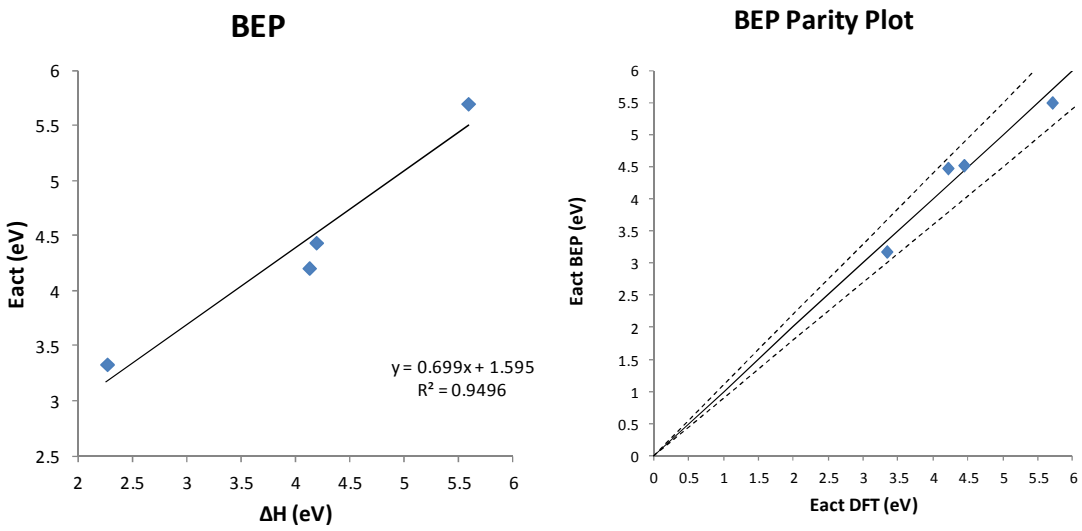

Figure 82: Plots of activation energy (Eact) against the enthalpy change(ΔH) (on the left) and parity plot of activation energy calculated by BEP and DFT (on the right) for CO dissociation on (111) surfaces

CO dissociation universalities have been investigated for the CO dissociation on (111) metal surfaces. The slope of the BEP interpolation line is 0.70, aligned with the global BEP trend for CO dissociation and with the geometry of the TSs. The intercept is aligned with the general BEP too, with a value of 1.60. Data dispersion represented in the parity plot of the right is good, with all data belonging to the 10% corridor.

BEP validation on dissociation reactions of CO molecule: oxygen coverage effect

In the last part of BEP validation the focus is moved to the insertion of oxygen coverage effects in the CO dissociation seen in the previous paragraphs. The cleavage of the structure and metal effects on universalities from the oxygen coverage effects is due to the fact that the interpretation of both effects together could lead to a not clear identification of general trends.

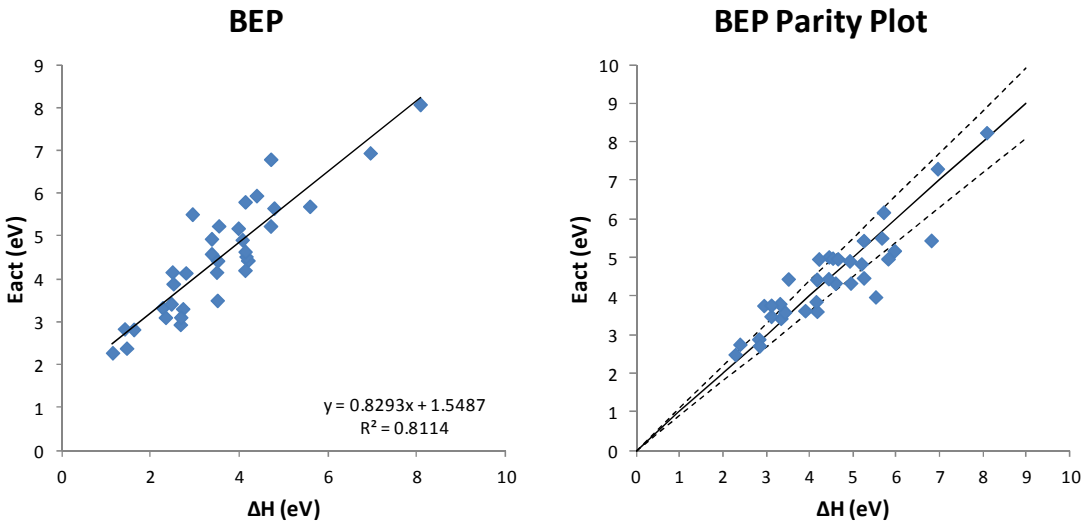

Figure 83: Plots of activation energy (Eact) against the enthalpy change(ΔH) (on the left) and parity plot of activation energy calculated by BEP and DFT (on the right) for CO dissociation on all metals and surfaces at 0, 0.25, 0.50 ML oxygen coverage.

CO dissociation data have been collected on the same plot for all metals (Rh, Pt, Cu, Ag) for all low index surfaces ((100),(110),(111)) and for each different oxygen coverage situation (0,0.25,0.50ML). The BEP interpolation line shows a slope of 0.83, which according to the literature is representative of late TSs. The insertion of oxygen does not change the nature of TSs for CO dissociation. The slope respect to the absence of coverage for CO dissociation has increased. The intersect of BEP line is remained the same (1.55 against 1.55) because the order of magnitude of the activation energy for CO dissociation has remained the same, even with added oxygen atoms. The range of enthalpy difference has increased to 10eV. Data are more scattered respect to the no coverage CO dissociation because oxygen coverage introduces further electronic contribution and steric effects to the determination of TSs. The good agreement between BEP and DFT is presented in the parity plot on the right of Figure 83.

BEP validation on dissociation reactions of CO on Rh surfaces: oxygen coverage

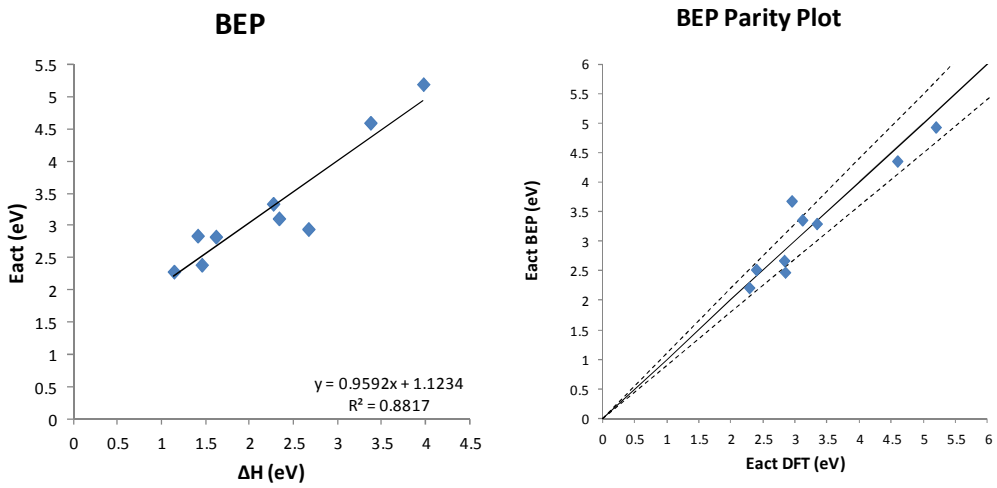

Figure 84: Plots of activation energy (Eact) against the enthalpy change(ΔH) (on the left) and parity plot of activation energy calculated by BEP and DFT (on the right) for CO dissociation on rhodium at 0, 0.25, 0.50 ML oxygen coverage

CO dissociation on rhodium surfaces show late TSs as confirmed by the slope of the line. The slope and the intercept is close between the coverage and no-coverage dissociation (0.96 against 0.98; 1.12 against 1.09). The dispersion of data is with a low scattering with R^2=0.88. All points tend to stay in the ±10% corridor except for the Rh (100) 0.5ML activation energy, because CO introduces a higher steric effect respect to all others in the TS, while its geometry does not appear to change among surfaces. Universalities are confirmed to exist for rhodium surfaces with oxygen coverage.

BEP validation on dissociation reactions of CO on Pt surfaces: oxygen coverage

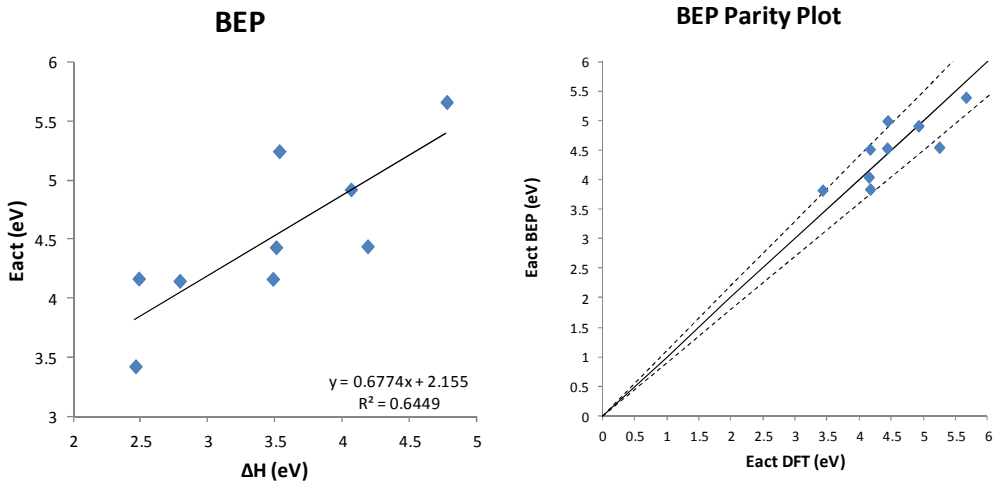

Figure 85: Plots of activation energy (Eact) against the enthalpy change(ΔH) (on the left) and parity plot of activation energy calculated by BEP and DFT (on the right) for CO dissociation on rhodium at 0, 0.25, 0.50 ML oxygen coverage

CO dissociation DFT data for 0.25 and 0.50 ML oxygen coverage have been analyzed together with 0ML for platinum surfaces. The slope of the BEP interpolation line confirms the fact that TS is quite late, with a value of 0.68. This value is higher than the no-coverage slope (0.68 against 0.38) which needed more points for the validation of global trend. The result with more points is closer to the general BEP slope. Data dispersion is R^2=0.64, and all data fit the parity plot, staying within the ±10% corridor.

BEP validation on dissociation reactions of CO on Cu surfaces: oxygen coverage

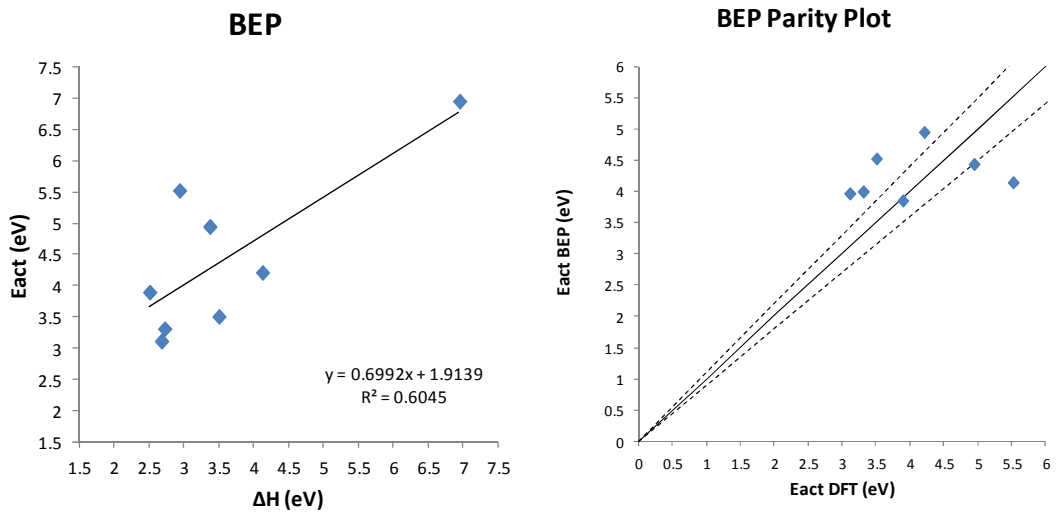

Figure 86: Plots of activation energy (Eact) against the enthalpy change(ΔH) (on the left) and parity plot of activation energy calculated by BEP and DFT (on the right) for CO dissociation on copper at 0, 0.25, 0.50 ML oxygen coverage

Copper shows for the BEP interpolation of oxygen coverage dependency for CO dissociation a slope of BEP interpolation line of 0.70. The value of 0.62 for the no coverage dissociation trend is comparable. The intercept has increased from 1.52 to 1.91, with a worsening of the data dispersion (R^2=0.60). This dispersion has to be addressed to steric effects affecting the geometry of TSs, since copper has the smallest lattice constant among all metals considered. The trends in enthalpy difference do not follow the same trends of the activation energy as indicated in chapter 3. This two effects turn out to introduce spurious contribution in the identification of a unique and clear BEP trend.

BEP validation on dissociation reactions of CO on Ag surfaces: oxygen coverage

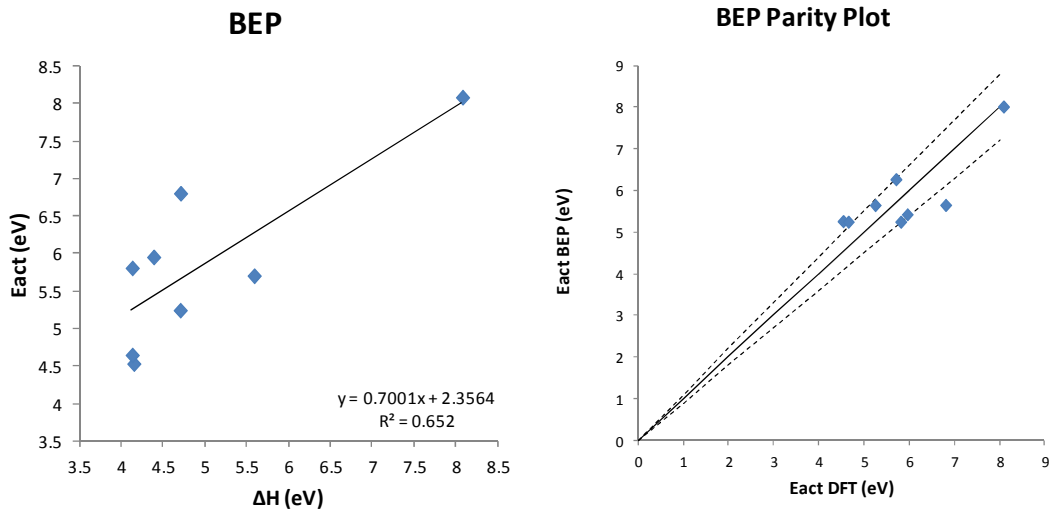

Figure 87: Plots of activation energy (Eact) against the enthalpy change(ΔH) (on the left) and parity plot of activation energy calculated by BEP and DFT (on the right) for CO dissociation on silver at 0, 0.25, 0.50 ML oxygen coverage

CO dissociation on silver surfaces show late TSs as confirmed by the slope of the line which is 0.70. Respect to the absence of oxygen coverage, the slope of the line has decreased, while both the intercept and the dispersion of data have increased. However the parity plot on the right-hand of the figure above shows a good agreement between DFT and BEP interpolation line.

BEP validation on dissociation reactions of CO on (100) surfaces: oxygen coverage

In this section of the chapter the quest of universalities is analyzed for CO dissociation on the same metal structure at different metals, including points referring to 0, 0.25, 0.50 ML. The first analysis is referring to (100) surfaces for rhodium, platinum, copper and silver.

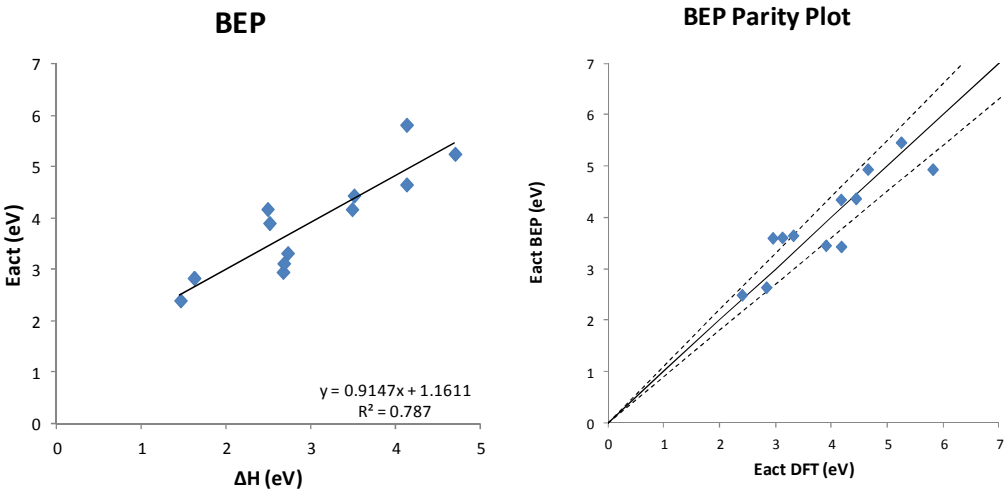

Figure 88: Plots of activation energy (Eact) against the enthalpy change(ΔH) (on the left) and parity plot of activation energy calculated by BEP and DFT (on the right) for CO dissociation on (100) surface at 0, 0.25, 0.50 ML oxygen coverage

The dissociation of carbon monoxide has been investigated on the (100) surfaces at the three oxygen coverage (0, 0,25, 0,50 ML). The slope of the BEP interpolation line is 0.91, representing the late nature of TSs on (100) surfaces. The slope of the BEP line has increased respect to the no-coverage interpolation (0.83) and the intersect has moved to 1.16. the data dispersion has increased, with a R^2=0.79 respect to 0.85, because sterical effects are moving the linearity of the BEP line. The parity plot on the right describes a good agreement between BEP and DFT data.

BEP validation on dissociation reactions of CO on (110) surfaces: oxygen coverage

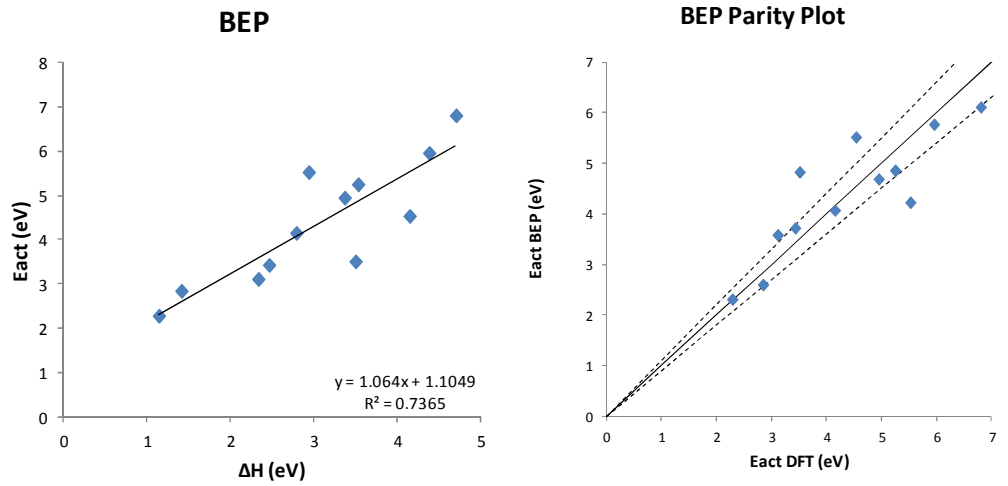

Figure 89: Plots of activation energy (Eact) against the enthalpy change(ΔH) (on the left) and parity plot of activation energy calculated by BEP and DFT (on the right) for CO dissociation on (110) surface at 0, 0.25, 0.50 ML oxygen coverage

CO dissociation reaction has been investigated on all (110) surfaces, with each oxygen coverage (0,0.25,0.50 ML). Universalities have been found to exist among different oxygen coverage, and the slope of the BEP line (1.064) identifies the presence of late TSs. The value is higher of the reference one because of data dispersion, with a R^2=0.7365. Two exceptions from the general trend, outside the ±10% corridor in the parity plot, are Cu 0 and 0.25ML which are affected by steric effects due to the small lattice constant of the metal itself.

BEP validation on dissociation reactions of CO on (111) surfaces: oxygen coverage

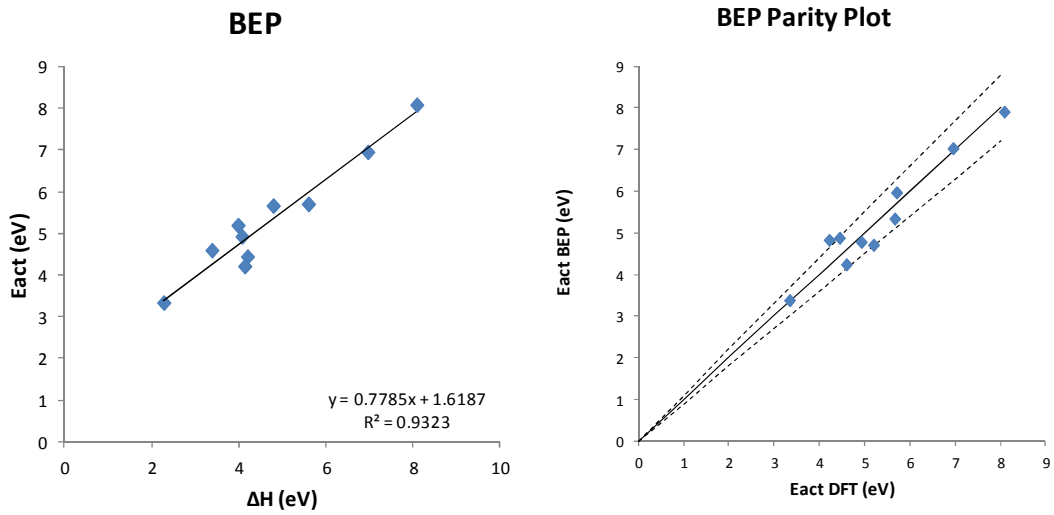

Figure 90: Plots of activation energy (Eact) against the enthalpy change(ΔH) (on the left) and parity plot of activation energy calculated by BEP and DFT (on the right) for CO dissociation on (111) surface at 0, 0.25, 0.50 ML oxygen coverage

The DFT data coming from CO dissociation on (111) surfaces at the three different oxygen coverage have been plotted for the identification of overall trends for the validation of BEP line. The slope of the line is 0.78, close to the value of 0.70 respect to the no-coverage CO dissociation on (111) surfaces. The nature of the TSs remains late, as the intercept which passes from 1.60 to 1.62 with the oxygen coverage. The dispersion of data is good, with all points belonging to the 10% corridor. This characteristic of good dispersion is commonly found for (111) surface, which is the most crowded among (100) and (110).

Comparison table for BEP assessment

The data for BEP interpolation obtained in the previous paragraphs are reported in the following comparison table.

Reaction	Metal	Surface	E_a^0	γ_P	R^2
All	All	All	0.7823	0.9993	0.9199
All	Rh	All	0.7689	1.0926	0.966
All	Pt	All	0.9909	0.9941	0.9503
All	Cu	All	0.6164	0.9996	0.8489
All	Ag	All	0.4446	1.0503	0.9126
All	All	(100)	0.788	1.0019	0.915
All	All	(110)	0.6527	1.1823	0.9108
All	All	(111)	0.6207	0.9595	0.9722
CH,CO	All	All	0.9131	0.9711	0.8938
CH,CO	Rh	All	0.8149	1.0746	0.9481
CH,CO	Pt	All	0.927	1.0116	0.927
CH,CO	Cu	All	0.9308	0.921	0.7747
CH,CO	Ag	All	0.7063	1.0003	0.8672
CH,CO	All	(100)	0.8368	0.9969	0.8962
CH,CO	All	(110)	0.6636	1.1835	0.8871
CH,CO	All	(111)	0.7937	0.9267	0.9572
CH,CH_2	All	All	0.7025	0.7515	0.889
CH_2	All	All	0.6838	0.7234	0.772
CH_2	Rh	All	0.4296	0.5615	0.6998
CH_2	Pt	All	1.0852	1.2964	0.6444
CH_2	Cu	All	0.4081	0.8641	0.3671
CH_2	Ag	All	-1.1349	2.0545	0.4965
CH_2	All	(100)	0.7321	0.528	0.5922
CH_2	All	(110)	0.7567	0.8611	0.8351
CH_2	All	(111)	0.5021	0.8075	0.9838
CH	All	All	0.7316	0.7508	0.9704
CH	Rh	All	0.6801	0.7743	0.8468
CH	Pt	All	0.8473	0.6591	0.8535
CH	Cu	All	0.5782	0.8153	0.9958
CH	Ag	All	0.6594	0.8063	0.9975
CH	All	(100)	0.8905	0.6485	0.9751
CH	All	(110)	0.6175	0.8304	0.9917
CH	All	(111)	0.6574	0.8029	0.9957
CO	All	All	1.5502	0.7203	0.8858
CO	Rh	All	1.0851	0.9781	0.9671

Reaction	Metal	Surface	E_a^0	γ_P	R^2
CO	Pt	All	2.8539	0.3793	0.5125
CO	Cu	All	1.5198	0.6247	0.8636
CO	Ag	All	1.376	0.7859	0.9358
CO	All	(100)	1.4295	0.8265	0.8496
CO	All	(110)	1.5664	0.6647	0.9037
CO	All	(111)	1.595	0.699	0.9496
CO, oxygen coverage	All	All	1.5487	0.8293	0.8114
CO oxygen coverage	Rh	All	1.1234	0.9592	0.8817
CO oxygen coverage	Pt	All	2.155	0.6774	0.6449
CO oxygen coverage	Cu	All	1.9139	0.6992	0.6045
CO oxygen coverage	Ag	All	2.3564	0.7001	0.652
CO oxygen coverage	All	(100)	1.1511	0.9147	0.787
CO oxygen coverage	All	(110)	1.1049	1.064	0.7365
CO oxygen coverage	All	(111)	1.6187	0.7785	0.9323

Table 5: Comparison table for BEP fitting parameters.

The table above reports the interpolation data for the BEP relationship. As these data show, the nature of the TSs among the different classes of reaction is kept, as it is indicated by the values of the slope of the line. The slopes belong to the range between 0.6 and 1, thus indicating a late TS. Different values are outliers due to the fact that the interpolation sample was to small.

Assessment of UBI-QEP method

The second part of the chapter deals with the validation and assessment of the UBI-QEP method. The method, illustrated in chapter 2, has the advantage of needing only one fitting parameter respect to BEP. The fitting parameter Φ is representative for the nature of the TSs of the class of reaction analyzed. This is a preliminary analysis with the specific aim of the identification of a validity range of the method. In each class of reaction the effect of metal and surface is examined following the same scheme exploited the assessment of BEP relationship. The UBI-QEP method assessed is the revision proposed by Maestri and Reuter [20].

UBI validation on dissociation reactions

UBI validation has been performed for the class of dissociative steps, including all DFT data coming from the dissociation of CO, CH, CH_2 molecules obtained on all metals of all surfaces.

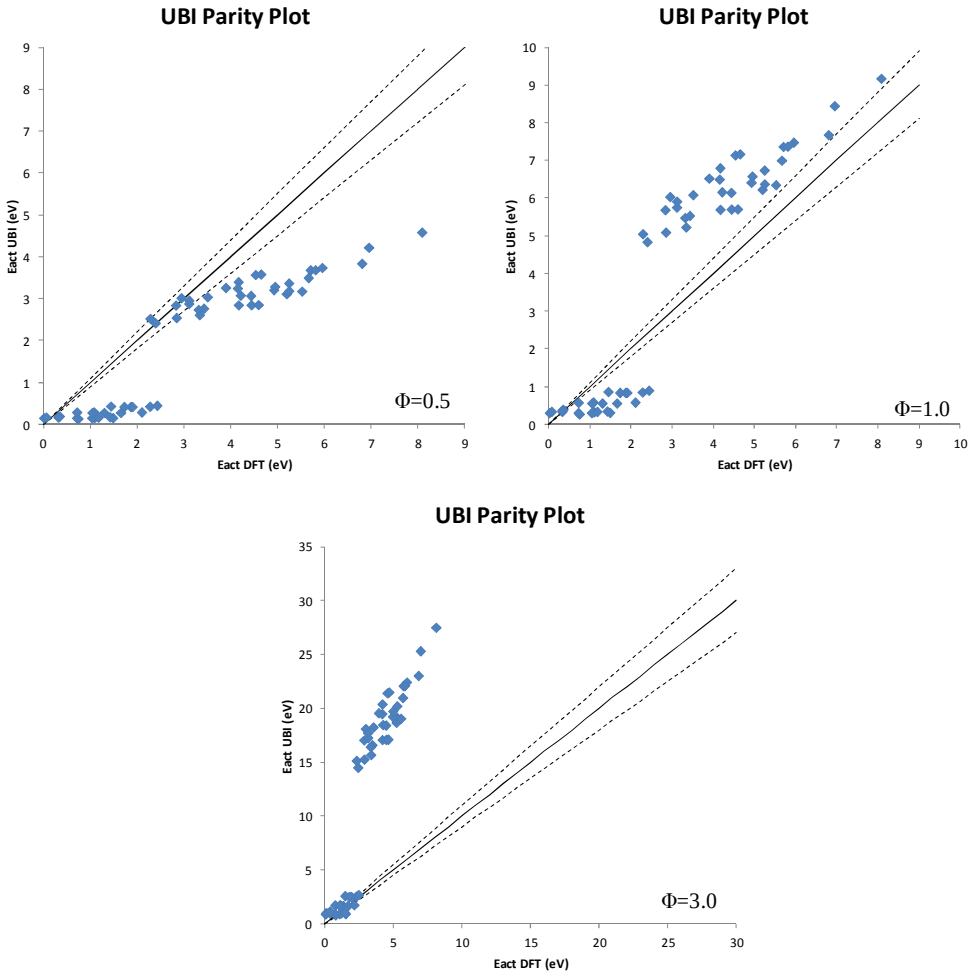

Figure 91: Parity plot of activation energy calculated by UBI and DFT for CO, CH, CH_2 dissociation on various metals, surfaces and oxygen coverage at different interpolation parameters

UBI method relies on the fitting of one parameter Φ which is representative for the nature of the TSs of the class of reaction. The Φ parameter can be related to the slope of the BEP interpolation line. A second interpolation parameter is missing respect to the BEP method, because the intersect of the BEP line is intrinsically inside the UBI method due to Morse potentials employed in its formulation. Φ is responsible for a vertical shift of UBI data on a parity plot, as shown in Figure 91, while the curving of data cannot be "manually" turned with a further external parameter. Given this first statement, the discussion will go through different classes of reaction for the individualization of general trends for UBI method.

UBI validation on dissociation reactions on Rh surfaces

The UBI assessment passes through the analysis of DFT data coming from CO, CH, CH_2 dissociation on the same metal, and on different low index surfaces.

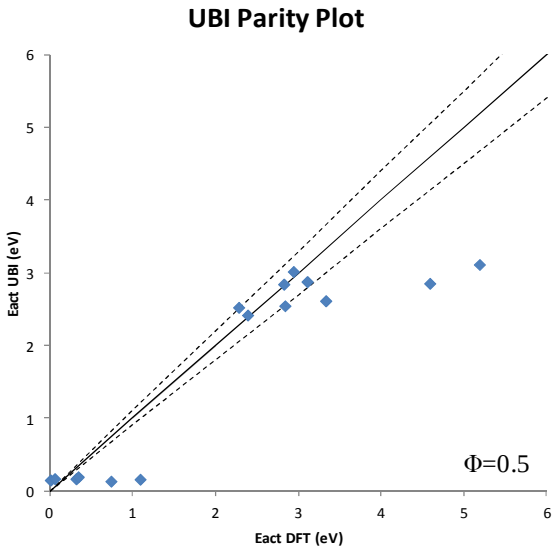

Figure 92: Parity plot of activation energy calculated by UBI and DFT for CO, CH, CH_2 dissociation on rhodium surfaces

The figure above shows the UBI foreseen activation energies for dissociation reactions on rhodium surfaces. The UBI method does not account for general universalities among different molecule dissociations on rhodium surfaces.

UBI validation on dissociation reactions on Pt surfaces

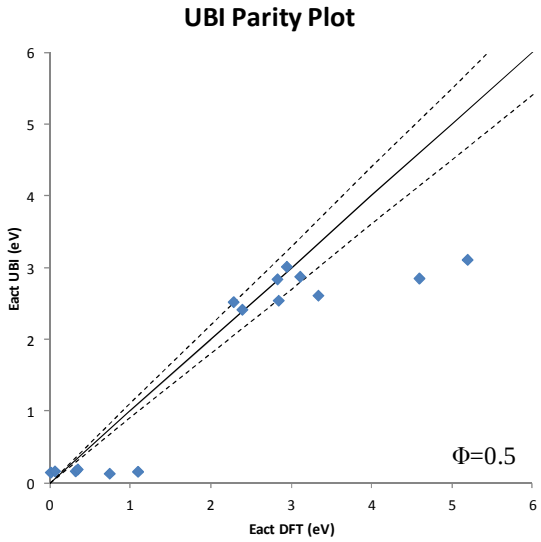

Figure 93: Parity plot of activation energy calculated by UBI and DFT for CO, CH, CH_2 dissociation on platinum surfaces

The plot above shows that for the dissociation of molecules of platinum surfaces UBI method cannot provide predictivity, even with a change in the fitting parameter Φ.

UBI validation on dissociation reactions on Cu surfaces

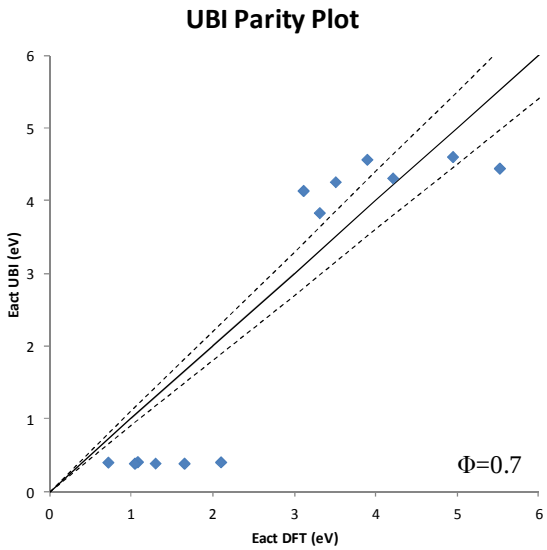

Figure 94: Parity plot of activation energy calculated by UBI and DFT for CO, CH, CH_2 dissociation on copper surfaces

As shown by the figure above, the UBI method cannot guarantee predictivity for the class of CO, CH, CH_2 dissociation on copper surfaces.

UBI validation on dissociation reactions on Ag surfaces

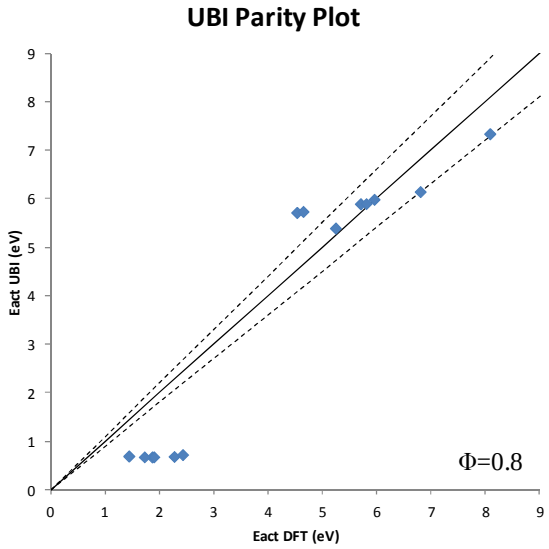

Figure 95: Parity plot of activation energy calculated by UBI and DFT for CO, CH, CH_2 dissociation on silver surfaces

The UBI method cannot adequately predict activation energy for CO, CH, CH_2 dissociation reactions on silver surfaces.

BEP validation on dissociation reactions on (100) surfaces.

The UBI assessment deals in this section with the analysis of the change of metal support for dissociation reactions studied on the same low index surfaces.

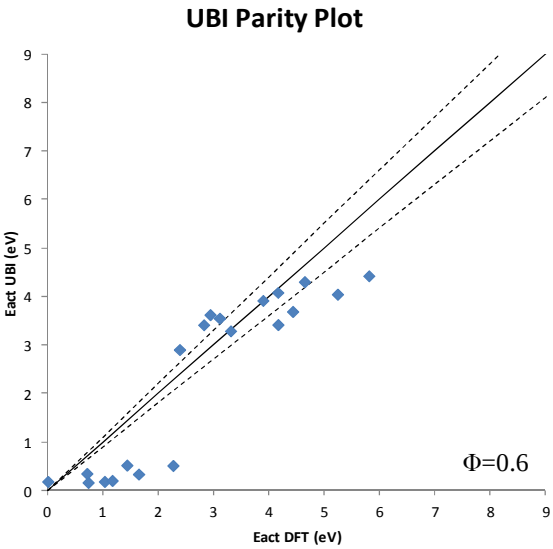

Figure 96: Parity plot of activation energy calculated by UBI and DFT for CO, CH, CH_2 dissociation on (100) surfaces

UBI method cannot find a unique trend for dissociation reactions occurring on the same (100) structure surface among different metals.

BEP validation on dissociation reactions on (110) surfaces.

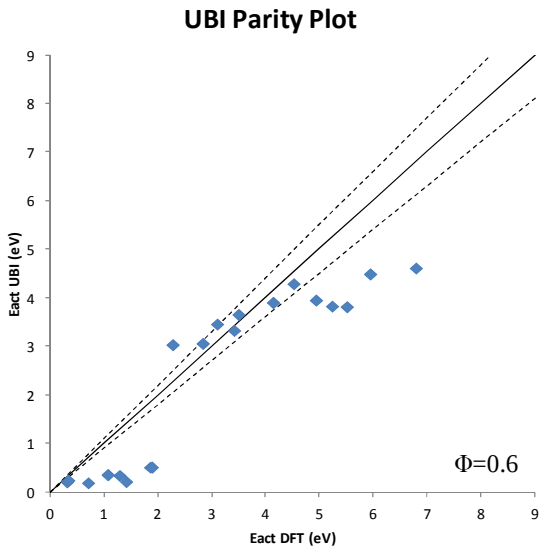

Figure 97: Parity plot of activation energy calculated by UBI and DFT for CO, CH, CH_2 dissociation on (110) surfaces

UBI method cannot find a unique trend for dissociation reactions occurring on the same (110) structure surface among different metals.

BEP validation on dissociation reactions on (111) surfaces.

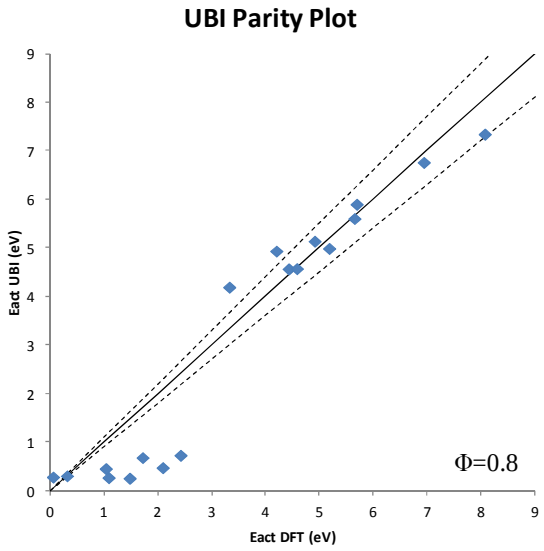

Figure 98: Parity plot of activation energy calculated by UBI and DFT for CO, CH, CH_2 dissociation on (111) surfaces

UBI method cannot find a unique trend for CO, CH, CH_2 dissociation occurring on the same (111) structure surface among different metals.

UBI validation on dissociation reactions of biatomic molecules

The second class of reaction analyzed for UBI assessment is the dissociation of biatomic molecules, which are in this work represented by CO and CH. The analysis of global trends and then the effect of structure and metal is reported in this section of the work.

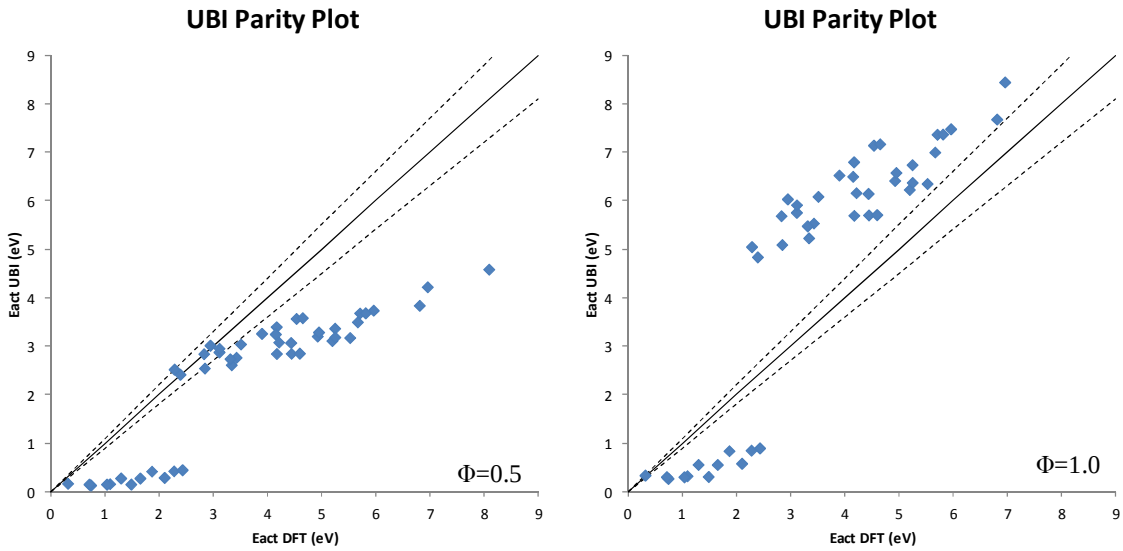

Figure 99: Parity plot of activation energy calculated by UBI and DFT for CO, CH dissociation on various metals,surfaces and oxygen coverage.

UBI method does not have a predictive power even if validated in the class of the dissociation of biatomic molecules. As previously explained, the fitting parameter is only responsible for a vertical shift of data in the parity plots. A change in the fitting parameter Φ does not predict data coming from the class of biatomic molecules dissociation.

UBI validation on dissociation reactions of biatomic molecules on Rh surfaces

The effect of metal is for UBI assessment is analyzed for the search of predictivity on rhodium surfaces for CO and CH dissociation reactions.

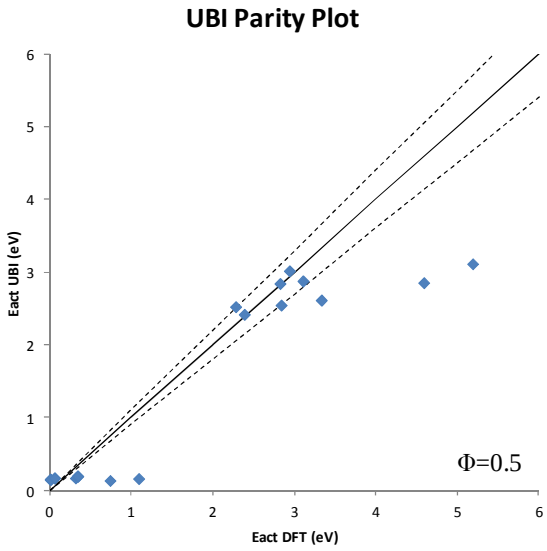

Figure 100: Parity plot of activation energy calculated by UBI and DFT for CO, CH dissociation on rhodium surfaces

No clear trend for the activation energy predictivity of the UBI method can be accounted for different biatomic molecules dissociation.

UBI validation on dissociation reactions of biatomic molecules on Pt surfaces

The effect of structure change in the dissociation of biatomic molecules is investigated on platinum catalysts.

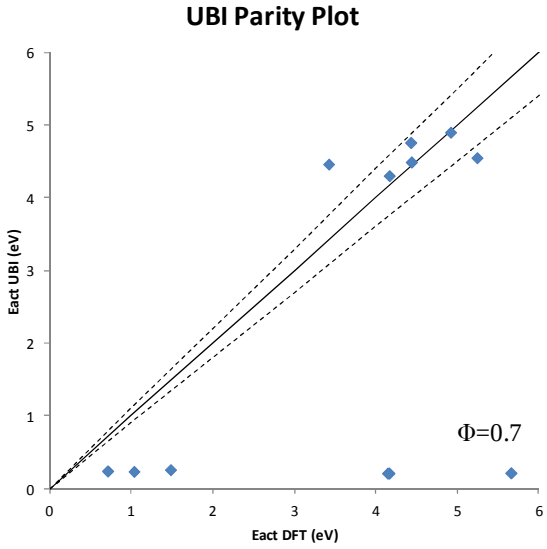

Figure 101: Parity plot of activation energy calculated by UBI and DFT for CO, CH dissociation on platinum surfaces

The UBI method does not have predictive power on platinum surfaces for the calculation of activation energy of dissociation reactions of biatomic molecules. The fitting parameter Φ, even if changed, is not able to fit the collected DFT data.

UBI validation on dissociation reactions of biatomic molecules on Cu surfaces

DFT against UBI calculated data have been analyzed for biatomic molecules dissociation on copper surfaces.

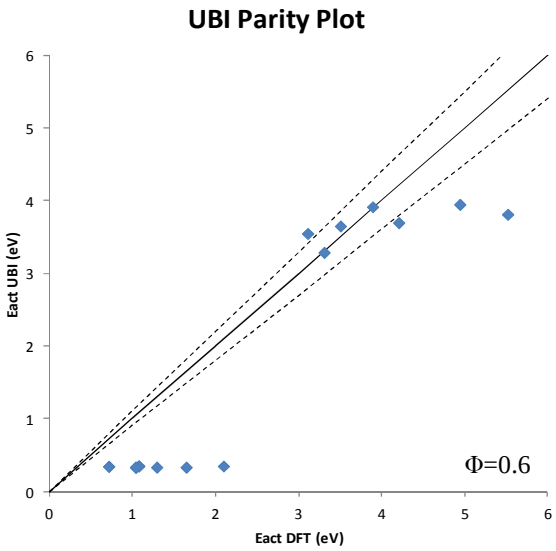

Figure 102: Parity plot of activation energy calculated by UBI and DFT for CO, CH dissociation on copper surfaces

UBI method ,as shown by the figure above, cannot fit DFT data for a general class of dissociation of biatomic molecules. The fitting parameter Φ does not have any physical sense for this distribution.

UBI validation on dissociation reactions of biatomic molecules on Ag surfaces

The effect of structure change on the same silver catalysts has been analyzed in the following paragraph.

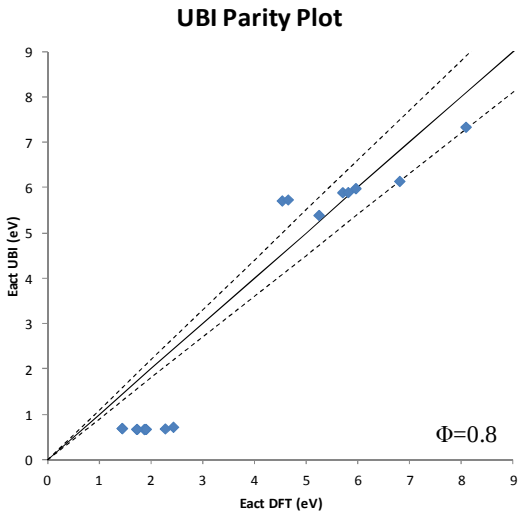

Figure 103: Parity plot of activation energy calculated by UBI and DFT for CO, CH dissociation on silver surfaces

UBI method does not have predictive power for the class of reaction of the dissociation of biatomic molecules, because the fitting parameter Φ cannot interpolate activation energy data coming from different reactant molecules.

UBI validation on dissociation reactions of biatomic molecules on (100) surfaces

In the following paragraphs the effect of the change of metal type within the same slab structure on the activation energy of the dissociation steps of biatomic molecules is assessed. The purpose of this type of analysis is the identification, if present, of clear universalities among the class of dissociation of biatomic molecules on the same structure of the catalyst. The first low index structure investigated is (100) for CO and CH dissociations.

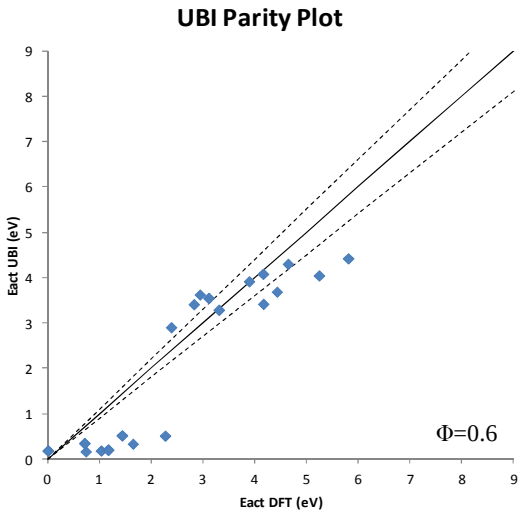

Figure 104: Parity plot of activation energy calculated by UBI and DFT for CO, CH dissociation on (100) surfaces

No clear trend is recognized for the UBI method of the dissociation of biatomic molecules on (100) surface. The fitting parameter Φ is not predictive for the calculation of activation energies of dissociation reactions of biatomic molecules on (100) surfaces.

UBI validation on dissociation reactions of biatomic molecules on (110) surfaces

DFT against UBI activation energy data have been collected for dissociation reactions of biatomic molecules on (110) surfaces.

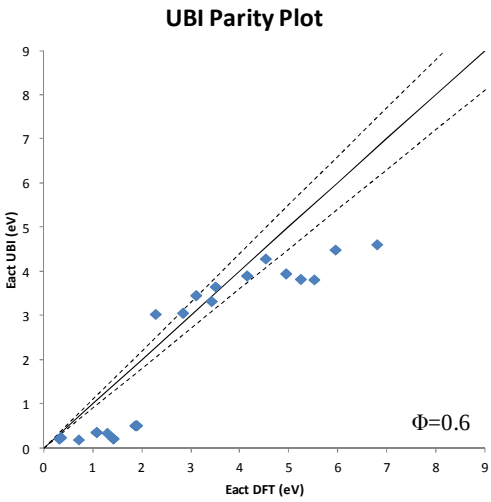

Figure 105: Parity plot of activation energy calculated by UBI and DFT for CO, CH dissociation on (110) surfaces

The UBI method shows to have bad predictivity respect to the dissociation of biatomic molecules.

UBI validation on dissociation reactions of biatomic molecules on (111) surfaces

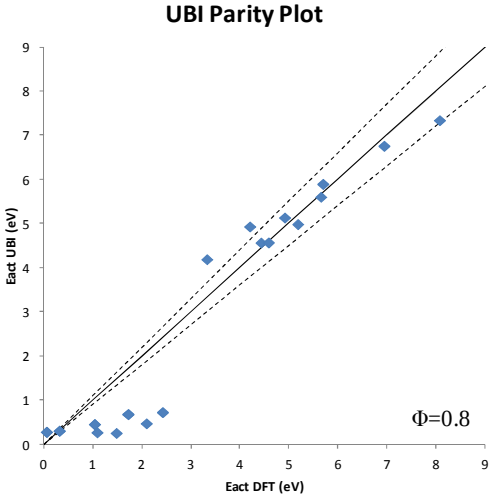

Figure 106 Parity plot of activation energy calculated by UBI and DFT for CO, CH dissociation on (111) surfaces

The UBI method is not predictive for the class of dissociation of biatomic molecules on (111) metal surfaces. The fitting parameter Φ does not interpolate DFT data neither has a physical meaning.

UBI validation on dissociation reactions of triatomic molecules, CH_2 dissociation

The second class of reaction upon which UBI method has been investigated if the dissociation of triatomic molecules. The collected DFT data collected for this class of reaction have been the dissociation of CH_2 molecule on (100),(110),(111) surfaces on rhodium, platinum, copper and silver surfaces. For this reason, the UBI assessment on triatomic molecule corresponds also with UBI validation for CH_2 dissociation. The analysis deals with all DFT data collected.

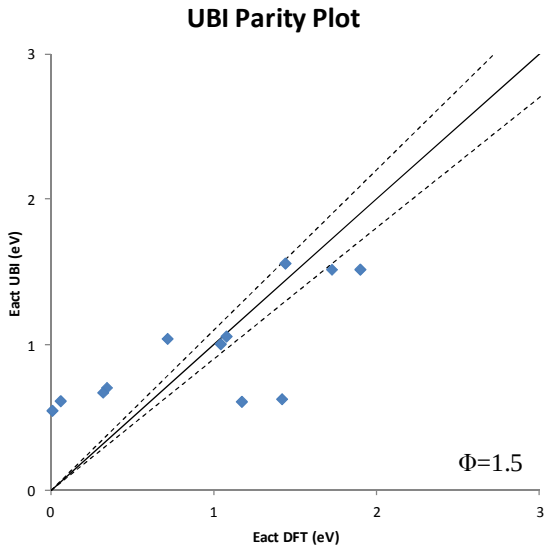

Figure 107: Parity plot of activation energy calculated by UBI and DFT for CH_2 dissociation on various metals and surfaces

UBI method cannot account for the trends of activation energy of the CH_2 dissociation on rhodium, platinum, copper, silver metal on (100),(110) and (111) surfaces.

UBI validation on dissociation reactions of CH_2 on Rh surfaces

UBI validation on rhodium metal for the three different low index metal surfaces (100) (110) and (111) has been performed in this section of the work.

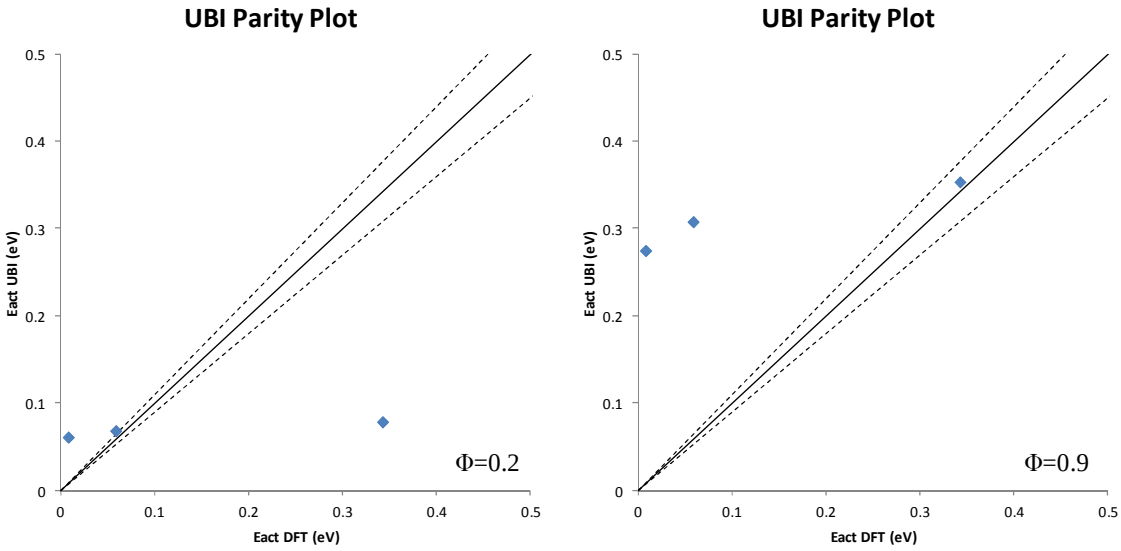

Figure 108: Parity plot of activation energy calculated by UBI and DFT for CH_2 dissociation on rhodium metal surfaces with two different fitting parameters (Φ=0.2; Φ=0.9)

The UBI method does not account for the effect of change of surface on the same metal catalyst for the class of CH_2 dissociation. In Figure 108 trends for UBI against DFT data are collected for two different fitting parameters. The UBI method cannot predict DFT activation energy for this class of reaction.

UBI validation on dissociation reactions of CH_2 on Pt surfaces

UBI assessment has been performed for CH_2 dissociation on Pt surfaces (100),(110), (111).

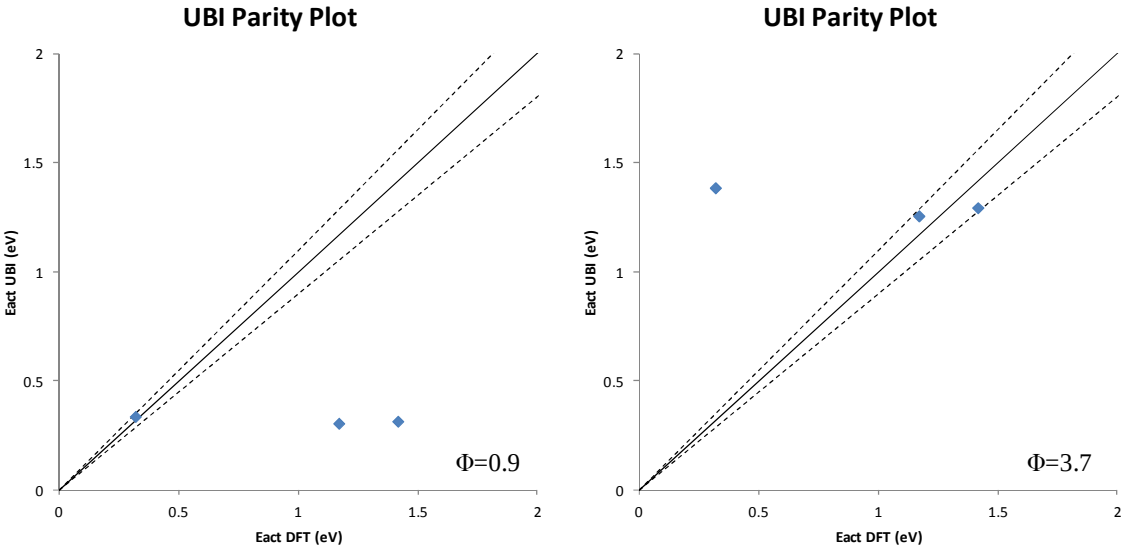

Figure 109: Parity plot of activation energy calculated by UBI and DFT for CH_2 dissociation on platinum metal surfaces with two different fitting parameters (Φ=0.9; Φ=3.7)

As shown in Figure 109, UBI method cannot account for structure effect on platinum surfaces. The use of two different Φ only partially covers the behavior of this class of reaction.

UBI validation on dissociation reactions of CH_2 on Cu surfaces

The effect of structure change has been analyzed for the dissociation of CH_2 molecule on copper surfaces.

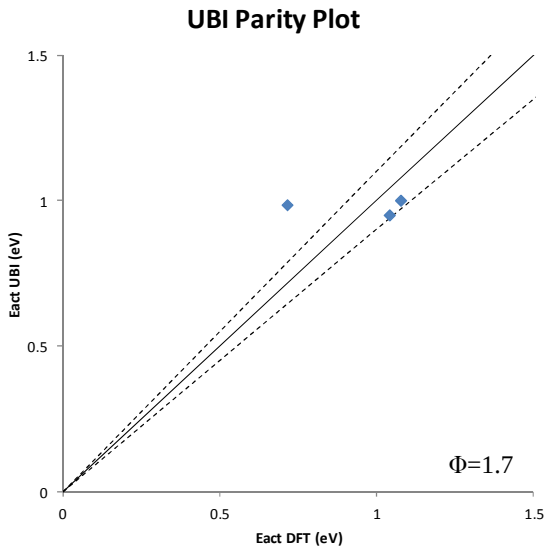

Figure 110: Parity plot of activation energy calculated by UBI and DFT for CH_2 dissociation on copper metal surfaces

UBI method cannot predict the change of activation energy of CH_2 molecule with the change of metal structure. Two out of three parameters stay within the 10% corridor on the parity plot, but this is a random circumstance.

UBI validation on dissociation reactions of CH_2 on Ag surfaces

The effect of change of catalyst structure within the same metal for the class of triatomic molecules dissociation has been studied for CH_2 dissociations on silver.

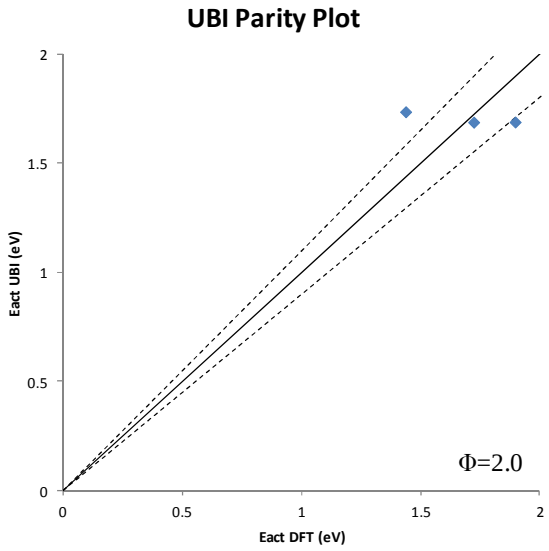

Figure 111: Parity plot of activation energy calculated by UBI and DFT for CH_2 dissociation on silver metal surfaces

The UBI method cannot predict the effect of change of metal structure relying on the only Φ as fitting parameter. Only one point out of three belongs to the 10% limits.

UBI validation on dissociation reactions of CH_2 on (100) surfaces

This section of the work deals with the identification of UBI trends for dissociation of triatomic molecules analyzing in particular the effect of change of metal within the same structure of catalyst. The first collection of data reported refers to (100) surfaces.

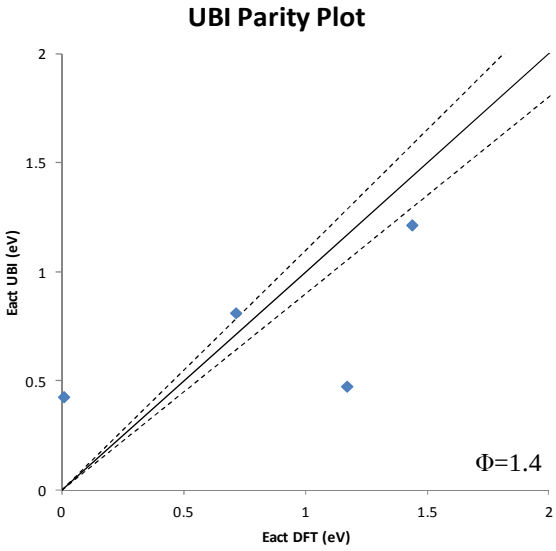

Figure 112: Parity plot of activation energy calculated by UBI and DFT for CH_2 dissociation on (100) metal surfaces

A general trend for UBI method has been investigated for the (100) surface. The method, even with a custom fitting parameter Φ, cannot predict in a reliable manner the effect of change of metal within the same structure.

UBI validation on dissociation reactions of CH_2 on (110) surfaces

A general trend for the UBI assessment has been investigated for CH_2 dissociation within the same (110) for the change of metal support.

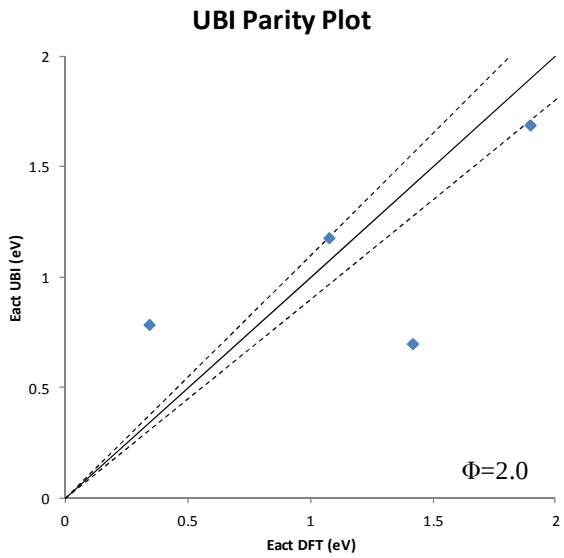

Figure 113: Parity plot of activation energy calculated by UBI and DFT for CH_2 dissociation on (110) metal surfaces

UBI method cannot account for the change of metal support on the same structure of the catalyst.

UBI validation on dissociation reactions of CH_2 on (111) surfaces

Finally, CH_2 dissociation trends for the change of metal within the same catalyst structure have been analyzed on (111) surface. A UBI validation has been performed for this class of reaction.

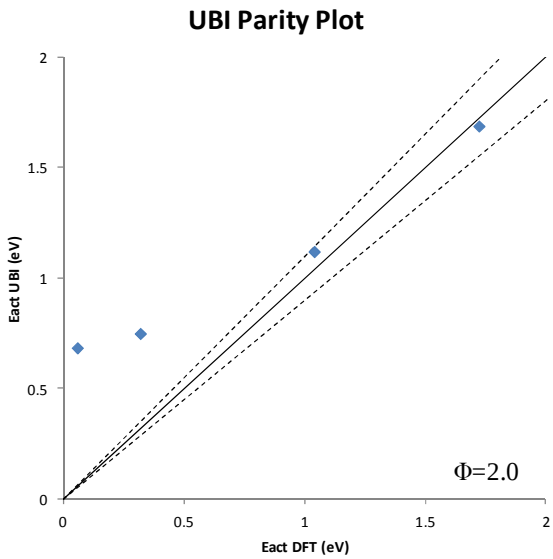

Figure 114: Parity plot of activation energy calculated by UBI and DFT for CH_2 dissociation on (111) metal surfaces

UBI method cannot account for the different metal supports on (111) surfaces for CH_2 dissociation.

UBI validation on dissociation reactions of CH molecule

The analysis of UBI method has been performed for the class of reaction CH dissociation. In the following paragraphs UBI is validated with data coming from the DFT calculations of CH dissociation on rhodium, platinum, copper and silver for (100),(110),(111) surfaces. All these data are collected for the validation of UBI in the following plot, then the analysis will focus on the metal effect first and then to the surface effect on UBI method.

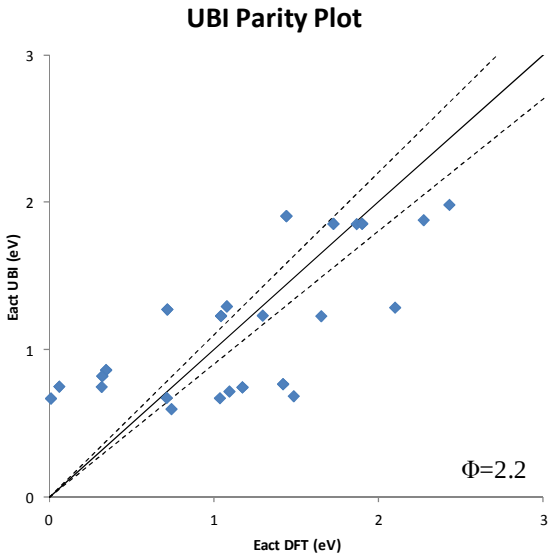

Figure 115: Parity plot of activation energy calculated by UBI and DFT for CH dissociation on various metals and surfaces

The UBI method cannot predict the activation energy of a reactive step of CH dissociation among different structures and different metals relying on a single fitting parameter. As shown in Figure 115, DFT data for the CH dissociation on each metal and each surface are not predicted by the UBI method, even if universalities exists among different TSs for CH dissociation, as proved by the BEP theory.

UBI validation on dissociation reactions of CH molecule on Rh surfaces

The effect of change of surface within the same metal has been investigated for rhodium (100),(110),(111) surfaces.

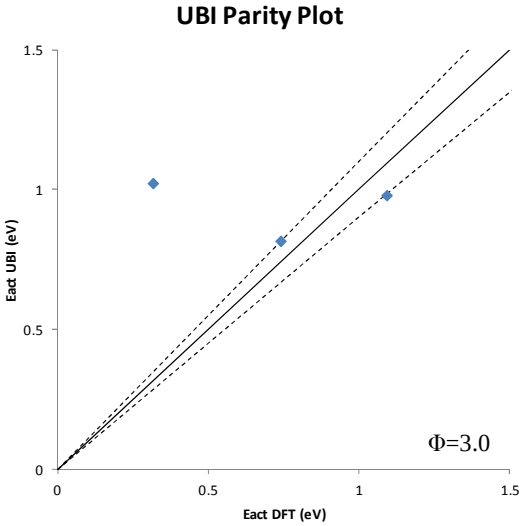

Figure 116: Parity plot of activation energy calculated by UBI and DFT for CH dissociation on rhodium surfaces

UBI method does not account for the structure change of rhodium for CH dissociation. As shown in Figure 116, a unique fitting parameter cannot predict the trends of different surfaces.

UBI validation on dissociation reactions of CH molecule on Pt surfaces

The survey of UBI method has been performed for platinum (100),(110),(111) surfaces for CH dissociation.

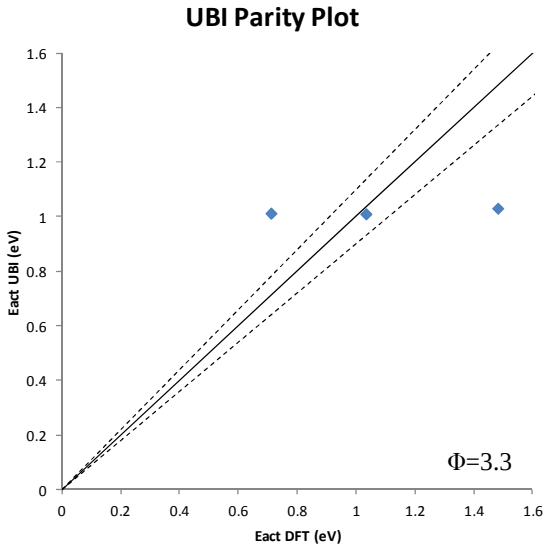

Figure 117: Parity plot of activation energy calculated by UBI and DFT for CH dissociation on platinum surfaces

The analysis of the effect of the change of metal structure for the same metal in the same class of reaction confirms the fact that UBI method cannot appropriately predict activation energies of dissociation step using a unique fitting parameter Φ among different structures. In particular for CH dissociation of platinum surfaces, the UBI foreseen activation energy have the same value, while the DFT ones are well separated, as depicted by the parity plot of Figure 117.

UBI validation on dissociation reactions of CH molecule on Cu surfaces

Copper metal is used for the investigation of UBI method among different catalyst structures. DFT data are collected among Cu(100),Cu(110),Cu(111) surfaces.

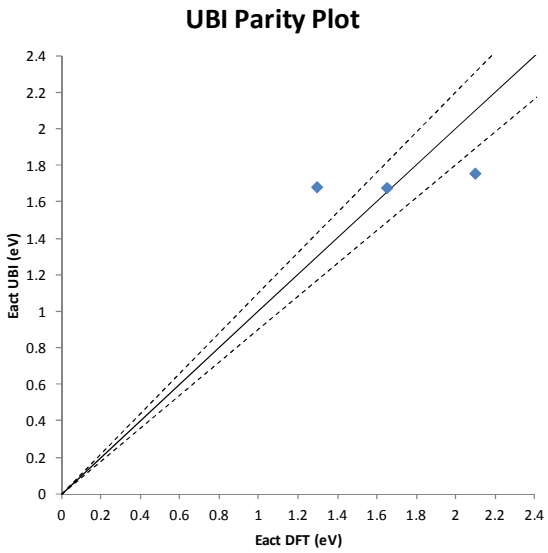

Figure 118: Parity plot of activation energy calculated by UBI and DFT for CH dissociation on copper surfaces

Copper surfaces are a further proof that UBI method cannot predict activation energy of CH dissociation among different surface structure.

UBI validation on dissociation reactions of CH molecule on Ag surfaces

CH dissociation data obtained by DFT calculations on silver surfaces are used for the evaluation of the structure effect on UBI method.

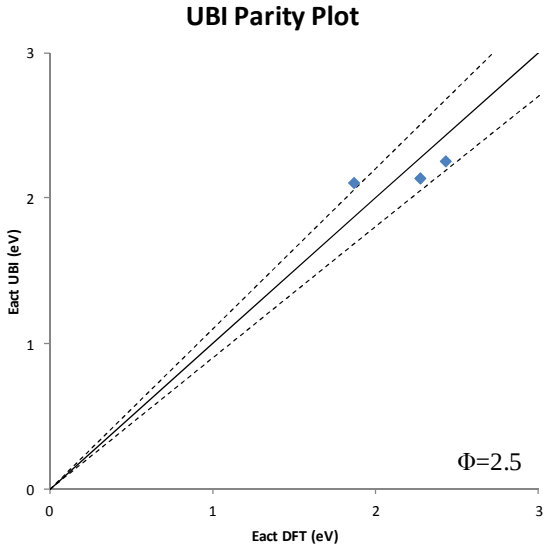

Figure 119: Parity plot of activation energy calculated by UBI and DFT for CH dissociation on silver surfaces

The parity plot of Figure 119 shows the existence of a relationship that links DFT calculations and UBI method with a fitting parameter of Φ=2.5. This value does not have any physical

sense and the right UBI-DFT interpolation for CH dissociation of silver surfaces is a random result.

UBI validation on dissociation reactions of CH molecule on (100) surfaces

In this section of the chapter the structure effect is analyzed for UBI assessment on CH dissociation reaction. Data collected for the same low index surface for different metals are collected together. This first paragraph refers to DFT data of (100) surface.

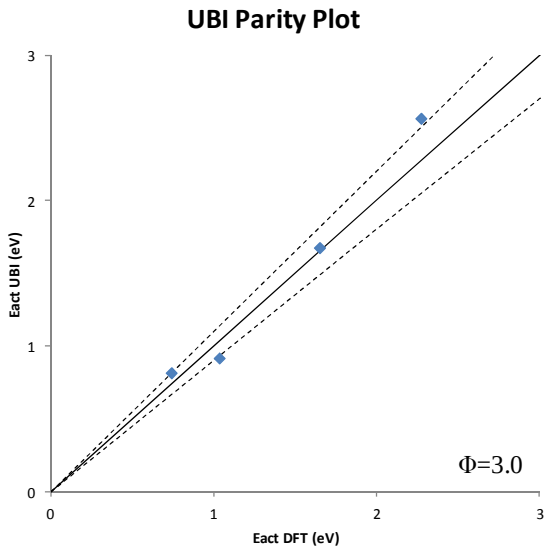

Figure 120: Parity plot of activation energy calculated by UBI and DFT for CH dissociation on (100) surfaces

The (100) surface offers a validation among different metals of the existence of predictivity of the UBI method of DFT data on different metals for the same low index surface. The fitting parameter of UBI is Φ=3.0. Although this surface does not have any particular difference with the other two examined, this result is unexpected and needs the enlargement of the sample for a better understanding of the trend.

UBI validation on dissociation reactions of CH molecule on (110) surfaces

DFT data collected for CH dissociation on (110) surfaces are employed for the validation of UBI trend among different metals for the same surface.

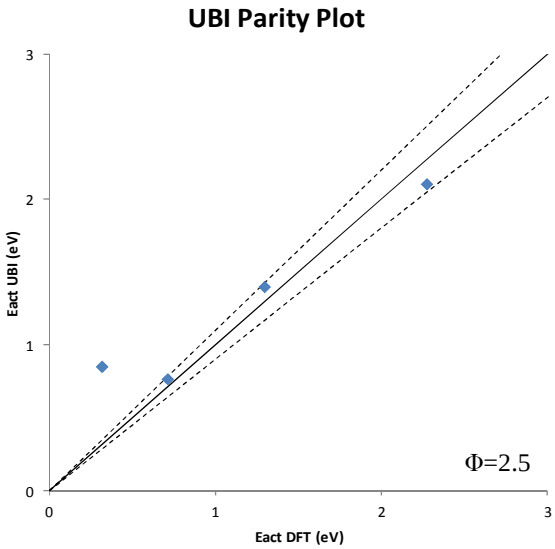

Figure 121: Parity plot of activation energy calculated by UBI and DFT for CH dissociation on (110) surfaces

The existence of metal sensitive general UBI trend is not confirmed nor contradicted by the plot for CH dissociation on (110) surfaces. The fitting parameter Φ=2.5 predicts three out of four dissociation energy calculated by DFT. The fourth point is referring to rhodium surface, which does not have any different features respect to others. An increasing number of DFT data for CH dissociation on (110) surfaces are needed for a better estimation of this trend.

UBI validation on dissociation reactions of CH molecule on (111) surfaces

In this section of the work DFT data collected for CH dissociation on (111) surfaces are employed for the validation of UBI trend among different metals for the same surface.

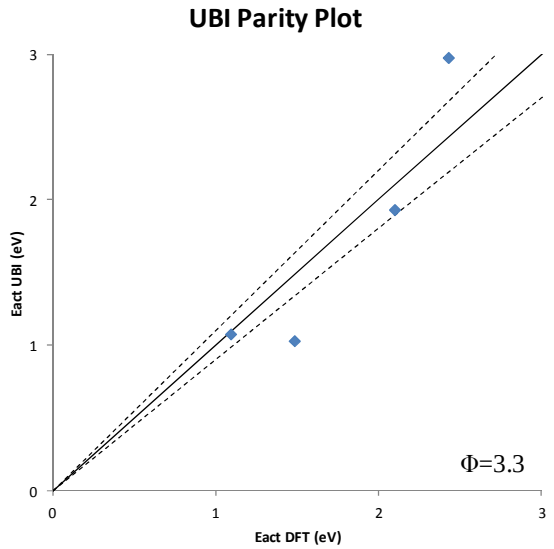

Figure 122: Parity plot of activation energy calculated by UBI and DFT for CH dissociation on (111) surfaces

UBI method cannot predict activation energy for CH dissociation on (111) surfaces, having a high dispersion of data along the parity plot. Moreover the fitting parameter Φ=3.3 does not have physical sense.

UBI validation on dissociation reactions of CO molecule

UBI method have been investigated for the class of reaction of the CO dissociation, excluding the presence of oxygen coverage. UBI method has been investigated for the rhodium, platinum, copper and silver (100),(110),(111) surfaces at 0ML oxygen coverage, so to distinguish between different contribution to the UBI method. The oxygen coverage effect will be analyzed in the following sections of the Chapter. The first plot reports DFT data of CO dissociation among all metals and all surfaces.

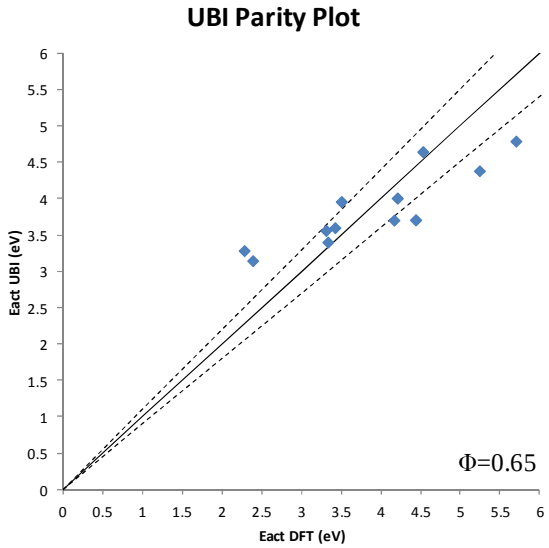

Figure 123: Parity plot of activation energy calculated by UBI and DFT for CO dissociation on all metals and surfaces

CO dissociation at 0ML oxygen coverage is better estimated by the UBI method respect to the previous classes of reaction. The fitting parameter Φ=0.65 is representative of a late TS, as reported in Table 2.

UBI validation on dissociation reactions of CO molecule on Rh surfaces

The effect of structure change is analyzed in this section, collecting together DFT data coming from CO dissociation on rhodium surfaces.

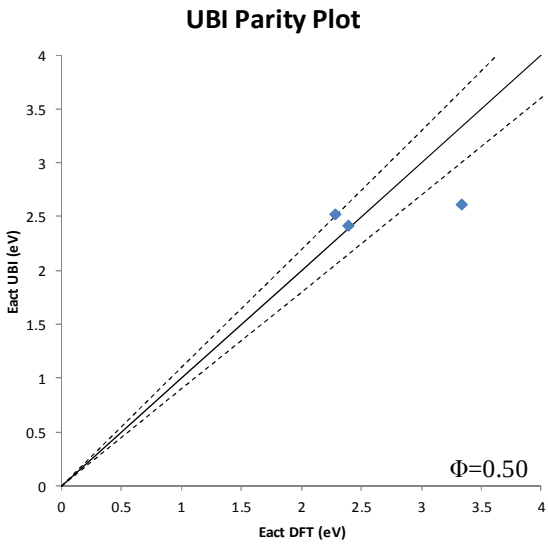

Figure 124: Parity plot of activation energy calculated by UBI and DFT for CO dissociation on rhodium surfaces

UBI method shows to have the ability of predictivity for the change of catalyst structure on rhodium surfaces. The fitting parameter Φ=0.50 shows and mixed early and late TS, which does not fit the exact nature of the dissociations on rhodium. There still is an outlier point on the UBI assessment.

UBI validation on dissociation reactions of CO molecule on Pt surfaces

DFT data have been collected for CO dissociation at 0ML oxygen coverage on platinum surfaces.

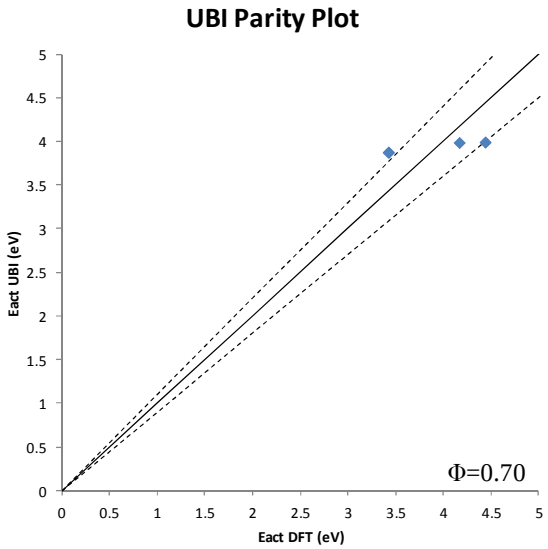

Figure 125: Parity plot of activation energy calculated by UBI and DFT for CO dissociation on platinum surfaces

UBI method shows predictivity and a good correlation for DFT activation value on platinum surfaces. The value of the fitting parameter Φ=0.70 is representative for the late nature of TSs for CO dissociation on platinum surfaces. Each point on the parity plot belongs to the 10% confidential limit.

UBI validation on dissociation reactions of CO molecule on Cu surfaces

DFT data for the validation of UBI method accounting for the structure effect on copper catalyst have been collected in the following plot, which compares DFT and UBI activation energies for the process.

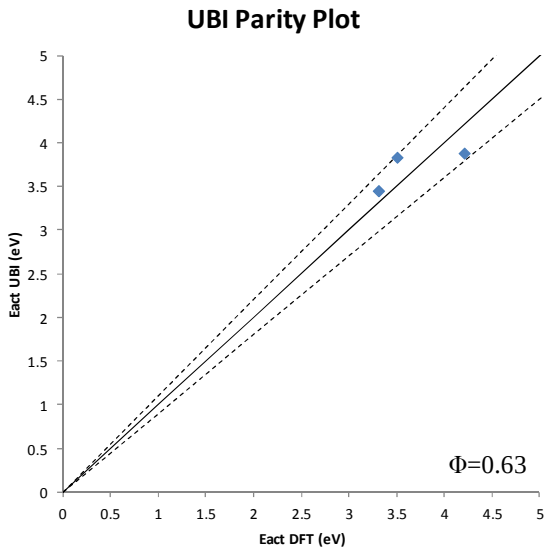

Figure 126: Parity plot of activation energy calculated by UBI and DFT for CO dissociation on copper surfaces

UBI method shows predictivity for the calculation of activation energies of CO dissociation on copper surfaces. The fitting parameter Φ=0.63 is close to the one on platinum surface (0.70) and is representative for the late TS on that metal surface. All three points belong to the ±10% confidential bound on the parity plot.

UBI validation on dissociation reactions of CO molecule on Ag surfaces

The effect of structure change on silver surfaces for CO dissociation is analyzed in the following plot.

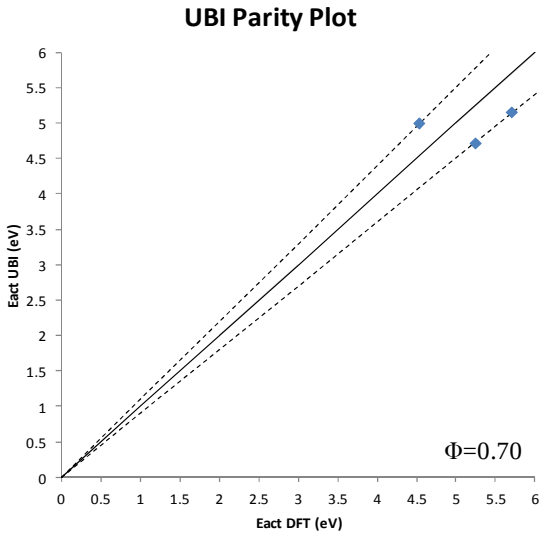

Figure 127: Parity plot of activation energy calculated by UBI and DFT for CO dissociation on silver surfaces

UBI method shows predictivity when accounting for structure effects for CO dissociation at 0ML oxygen coverage on silver surfaces. The fitting parameter Φ=0.70 shows the late nature of TSs on this class of reaction. The ±10% limits on the parity plot show to include all the three data.

UBI validation on dissociation reactions of CO molecule on (100) surfaces

The metal effect on UBI method has been accounted in this section. DFT data collected for CO dissociation on rhodium, platinum, copper and silver at 0ML oxygen coverage have been divided for each low index surfaces (100),(110),(111) to assess and understand the features of the UBI method. The first analysis deals with the (100) surface.

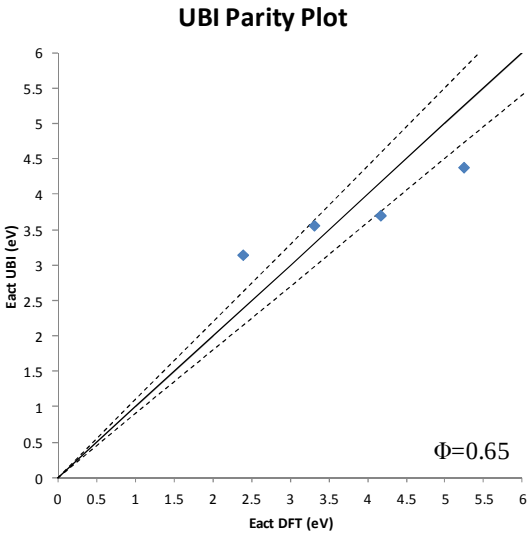

Figure 128: Parity plot of activation energy calculated by UBI and DFT for CO dissociation on (100) surfaces

UBI can predict the activation energy of a CO dissociation process. The best fitting parameter among all is represented by Φ=0.65, which leaves two out of four points out of the ±10% limits on the parity plot. This value accounts for the late nature of TSs of CO dissociation on (100) surfaces.

UBI validation on dissociation reactions of CO molecule on (110) surfaces

DFT data have been collected for CO dissociation process at 0ML oxygen coverage on (110) surfaces.

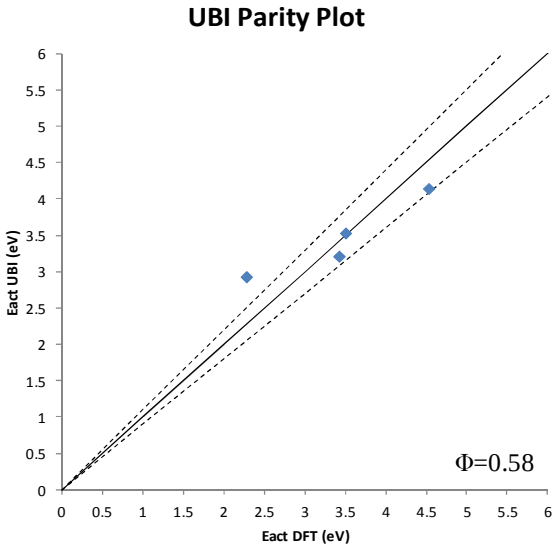

Figure 129: Parity plot of activation energy calculated by UBI and DFT for CO dissociation on (110) surfaces

UBI method has the predictivity for the calculation of activation energy of CO dissociation process on (110) surfaces. The best fitting parameter for the (110) structure is Φ=0.58, accounting for the late nature of TSs on (110) surfaces.

UBI validation on dissociation reactions of CO molecule on (111) surfaces

The effect of metal change for the same slab structure has been accounted here for (111) metal surfaces referring to CO dissociation at 0ML coverage.

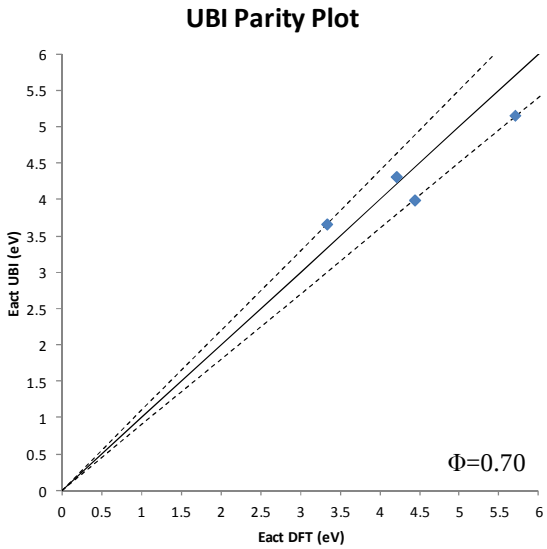

Figure 130: Parity plot of activation energy calculated by UBI and DFT for CO dissociation on (111) surfaces

(111) surface shows to be the best fit for UBI method referred to CO dissociation with no coverage. The fitting parameter of Φ=0.70 accounts for the late nature of TSs on this metal surface and all points belong to the ±10% corridor.

UBI validation on dissociation reactions of CO molecule: oxygen coverage

The last part of the validation of UBI method accounts for the presence of three possible oxygen metal coverage (0ML,0.25ML,0.50ML). Oxygen coverage effect is taken into account in this section in order to make a comparison between this work and work find in literature by Maestri and Reuter [20]. Data of the following plot are collected for CO dissociation on rhodium, platinum, copper, silver metals on (100),(110),(111) surfaces at the three oxygen coverage abovementioned.

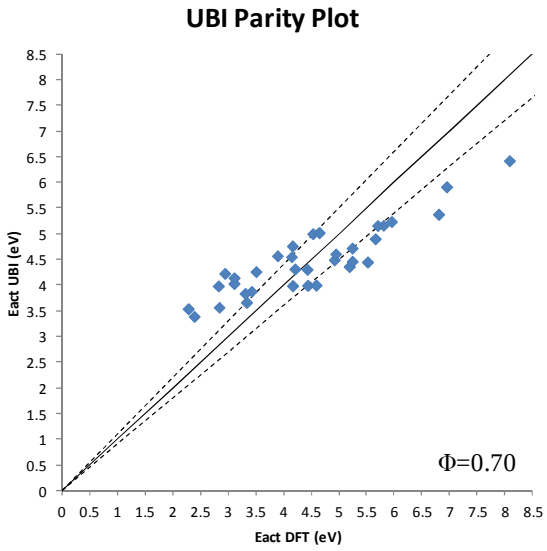

Figure 131: Parity plot of activation energy calculated by UBI and DFT for CO dissociation on all metals and surfaces at 0,0.25,0.50ML oxygen coverage

CO dissociation with coverage shows a unique trend among different metals, surfaces and oxygen coverage. The fitting parameter Φ=0.70 which is close to the no-coverage UBI interpolation accounts for the late nature of TSs of CO dissociation on each metal, each surface and each oxygen coverage, as indicated in Table 2. A unique fitting parameter does not have the power, however, to predict in appropriate way all DFT data. Universalities of UBI method for CO dissociation at various oxygen coverage are not respected.

UBI validation on dissociation reactions of CO on Rh surfaces: oxygen coverage

DFT data have been collected for CO dissociation on rhodium (100),(110),(111) surfaces at three oxygen coverage, in order to analyze the metal effect on this class of reaction.

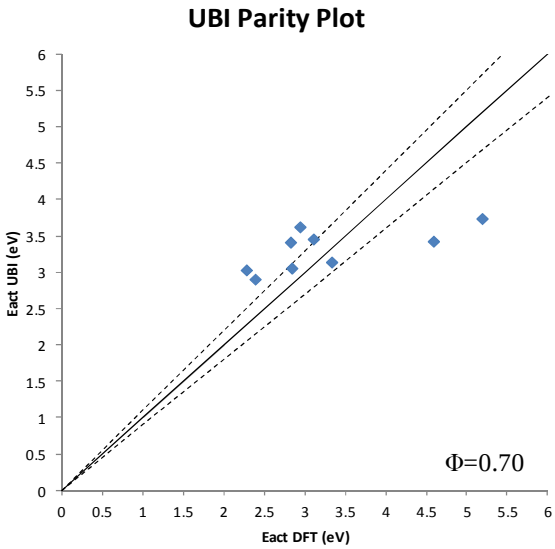

Figure 132: Parity plot of activation energy calculated by UBI and DFT for CO dissociation on rhodium surfaces at 0,0.25,0.50ML oxygen coverage

The coverage effect has the same character of the TSs, and is well predicted by the UBI method. The fitting parameter Φ=0.70 accounts for the late nature of the TS.

UBI validation on dissociation reactions of CO on Pt surfaces: oxygen coverage

DFT data coming from the CO dissociation on platinum surfaces at different oxygen coverage has been collected together analyzing the UBI trends.

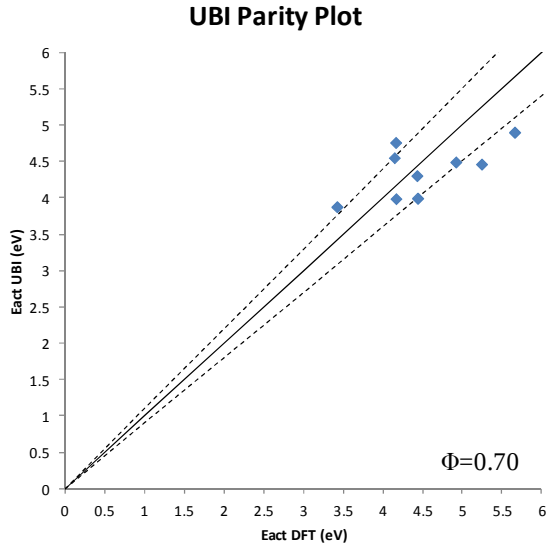

Figure 133: Parity plot of activation energy calculated by UBI and DFT for CO dissociation on platinum surfaces at 0,0.25,0.50ML oxygen coverage

The UBI method is able to account for different surfaces and oxygen coverage for the CO dissociation on platinum surfaces. The fitting parameter Φ=0.70 aligns with the rhodium value, and can be seen as an indication of the character of the TSs, which is late.

UBI validation on dissociation reactions of CO on Cu surfaces: oxygen coverage

DFT data for CO dissociation coming from the three low index surfaces (100),(110),(111) at the three different oxygen coverage are collected together for the investigation of UBI trends on the same metal, for different surfaces.

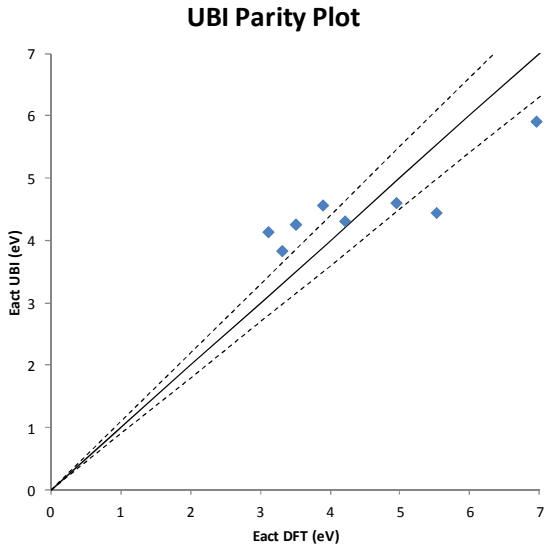

Figure 134: Parity plot of activation energy calculated by UBI and DFT for CO dissociation on copper surfaces at 0,0.25,0.50ML oxygen coverage

UBI method is able to predict DFT activation energy data for CO dissociation on copper surfaces with a good approximation, as depicted in the correspondent parity plot. The fitting parameter Φ=0.70 is the same of CO dissociation on rhodium and platinum surfaces, and this is index of universalities that can be found among different structures and oxygen coverage for the same class of reaction.

UBI validation on dissociation reactions of CO on Ag surfaces: oxygen coverage

DFT data for CO dissociation on silver surfaces obtained on the three (100),(110),(111) surfaces for the three different oxygen coverage. The assessment of UBI method has dealt with the search for universalities among different surfaces.

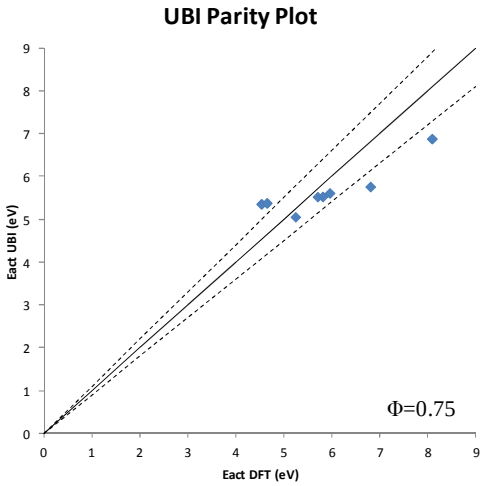

Figure 135: Parity plot of activation energy calculated by UBI and DFT for CO dissociation on silver surfaces at 0,0.25,0.50ML oxygen coverage

UBI method is able to account for different oxygen coverage on different surfaces for the CO dissociation on silver metal slabs. The fitting parameter Φ=0.70 is comparable to those used for rhodium, platinum and copper and the universalities are highlighted for this class of reaction. All in all, UBI shows good predictivity among different surfaces for CO dissocation at various oxygen coverage.

UBI validation on dissociation reactions of CO on (100) surfaces: oxygen coverage

UBI method has been investigated and assessed for the effect of change of metal within the same structure and different oxygen coverage. The search for universalities of the UBI method of this section starts with the analysis of data for (100) surface.

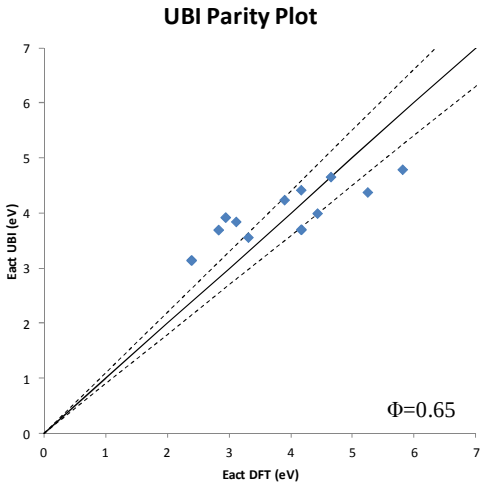

Figure 136: Parity plot of activation energy calculated by UBI and DFT for CO dissociation on (100) surfaces at 0,0.25,0.50ML oxygen coverage

The metal change effect for the (100) catalysts has been accounted in terms of UBI method and as result, UBI method is able to predict general trends for the same structure. The fitting parameter is Φ=0.65 which accounts for the late nature of the TSs on this type of slabs. Universalities have been found to exist among different metal for the (100) surfaces.

UBI validation on dissociation reactions of CO on (110) surfaces: oxygen coverage

The effect of metal change for different metal catalysts and different oxygen coverage has been investigated for UBI assessment on (110) surfaces.

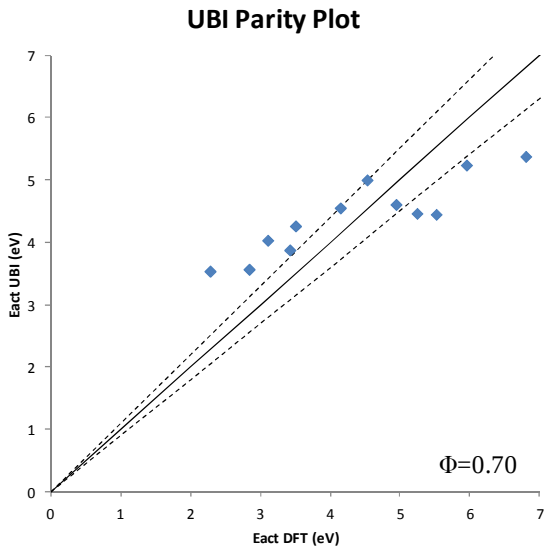

Figure 137: Parity plot of activation energy calculated by UBI and DFT for CO dissociation on (110) surfaces at 0,0.25,0.50ML oxygen coverage

UBI method shows a good predictivity for the activation energies of CO dissociation on (110) surfaces. The fitting parameter Φ=0.70 is representative for the late nature of TSs of the surface for CO dissociation.

UBI validation on dissociation reactions of CO on (111) surfaces: oxygen coverage

UBI method has been investigated for the effect of metal change on (111) surfaces of CO dissociation reaction at different oxygen coverage. This grouping is the same adopted by the work of Maestri and Reuter [20], in order to make a comparison between literature and the present work.

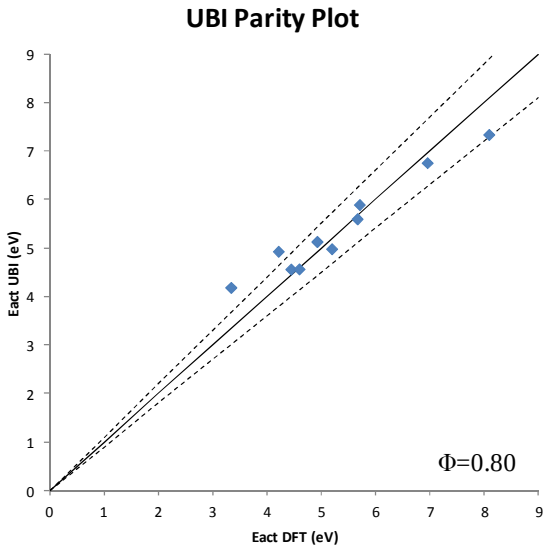

Figure 138: Parity plot of activation energy calculated by UBI and DFT for CO dissociation on (111) surfaces at 0,0.25,0.50ML oxygen coverage

UBI assessment on this DFT collected data has a good predictivity ability. Assuming a fitting parameter of Φ=0.80, which is representative for the late TSs of this class of reaction on (111) surfaces, the distribution shows a good theory-to-theory correspondence. The work by Maestri and Reuter [20] shows the same power ability of the UBI method, which has a narrower predictive range if compared to the BEP model, relying on one fitting parameter. Once the Φ parameter has been determined by reference DFT calculations, the activation energies can be computed as functions of the only binding energies. Considering the negligible cost of the computation of the B.E., the uncertainty that characterizes the UBI-QEP method is perfectly acceptable, with the intention of determining insights into reaction networks. A quantitative approach is out of the possibilities of the UBI-QEP model as it is, but it can provide a first screening in the identification of the prevalent reaction pathways of microkinetic modeling complex reaction schemes, where exhaustive first-principles treatment is prohibitive.

Conclusion and oulook

This chapter reports an assessment of BEP relationship and a preliminary analysis of UBI-QEP method. These two methods have been investigated for different classes of reaction.

Among these classes the BEP shows good predictivity and exploits universalities that hold among TSs. The change in the character of the TS misleads the BEP relationship.

The preliminary analysis of the UBI method has shown difficulties in predicting activation energies for different classes of reactions, which will be investigated by successive works.

Conclusions.

This Master Thesis work has dealt with the assessment of semiempirical methods for the prediction of structure sensitivity scaling relations for dissociation reactions. The aim of this work has been the validation of Brønsted-Evans-Polanyi (BEP) relations and UBI-QEP method which are widely used in heterogeneous chemical catalysis.

BEP can predict activation energies among different classes of reaction, thus allowing for the identification of "universalities" that hold among different surfaces, different metal type and different surface coverage. BEP method was found to be predictive from the most general class of dissociation reaction to the account of different coverage of the same metal surface. This good ability in the correlation of the activation energies relies upon the fact that the BEP model employs two parameters which are the slope and intercept. The nature of the Transition States (TSs) that characterizes the class of reaction influences the slope of the BEP interpolation line, which is close to the unity for late TSs and is independent of the class. The intercept of the BEP interpolation line is instead representative for the intrinsic activation energy of the process and varies from one class of reaction to another. BEP model has found to relate relatively well among different reactions with same TSs and different metals, in agreement with the existing previous works present in literature, and above all BEP is able to relate not only different classes of reaction, but also account for structure sensitivity.

UBI-QEP method is a one parameter method which has been assessed following the same scheme of BEP. UBI method has shown to be non-predictive for the general class of dissociation reactions and even for CH and CH_2 dissociation reactions. UBI method shows a predictivity within ±10% limits when analyzing CH and CH_2 dissociation on the same surface for different metal slabs. Instead UBI has been found to be predictive for CO dissociation, among different metals, different surfaces and different oxygen coverage. We found that UBI can relate different reactions on the same surface, while no clear trends have been found for the effect of structure, as reported for the first time in this work.

An investigation of catalytic reactions other than dissociations, such as disproportionation, can be evaluated for the quest of generality of these models. An analysis of applicability and limits of their uncertainty has to be performed with respect to explicit first-principles calculations. Possible modifications of the methods in order to make their prediction within a narrow variation with respect to the reference first principle calculation can be object of

successive works. Possible modifications can concern the development of relations between the nature of the TS (early or late) and the thermochemistry of the reactants and products.

On the whole, this Master Thesis has provided a first base for the development of structure dependent microkinetic models for the application of hierarchical multiscale methodology in heterogeneous catalysis.

Table of contents

Bibliography

[1] Maxwell IE- *Driving forces for studies in catalysis*. Stud Surf Sci Catal 101:1-9 (1996)

[2] G.Ertl, *Reactions at surfaces: from atoms to complexity*, Noble Lecture, December 8,2007

[3] G.A. Somorjai et al. *The surface reconstruction of the (100) crystal faces of iridium, platinum and gold; I. Experimental observations and possible structural models*, Surf.Sci. 103(1):189-217 (1981)

[4] G. Somorjai, *Introduction to Surface Chemistry and Catalysis* (Wiley, New York, 1994)

[5] W. A. Brown, R. Kose, and D. A. King, *Femtomole Adsorption Calorimetry on Single-Crystal Surfaces* Chem. Rev. 98, 797 (1998)

[6] H. Gross, C. Campbell, and D. A. King, *Metal-carbon bond energies for adsorbed hydrocarbons for calorimetric data*, Surf. Sci. 572, 179 (2004)

[7] J. K. Nørskov, M. Scheffler, and H. Toulhoat, *Density functional theory in surface science and heterogeneous catalysis*, MRS Bull. 31, 669 (2006)

[8] B. Hammer and J. K. Nørskov, *Theoretical surface science and catalysis- calculations and concepts*, Adv. Catal. 45, 71 (2000)

[9] Michaelides, A., Liu, Z. P., Zhang, C. J., Alavi, A., King, D. a., & Hu, P. (2003). *Identification of general linear relationships between activation energies and enthalpy changes for dissociation reactions at surfaces.* Journal of the American Chemical Society, 125(13), 3704–3705

[10] Michealides Hu, *Insight into microscopic reaction pathways in heterogeneous catalysis*, J.Am.Chem.Soc. 2000, 122, 9866-986

[11] Alavi, A., et al., *CO Oxidation on Pt(111): An Ab Initio Density Functional Theory Study*. Physical Review Letters, 1998. **80**(16): p. 3650-3653

[12] Eichler, A., *CO oxidation on transition metal surfaces: reaction rates from first principles.* Surface Science, 2002. **498**(3): p. 314-320

[13] J. K. Nørskov, T. Bligaard, A. Logadottir, S. Bahn, L. B. Hansen, M. Bollinger, H. Bengaard, B. Hammer, Z. Sljivancanin, M. Mavrikakis, Y. Xu, S. Dahl and C. J. H. Jacobsen, *Universality in heterogeneous catalysis*, J. Catal., 2002, 209, 275–278

[14] Mavrikakis M. Bäumer M. Freund H.-J. Nørskov J.K. *Structure sensitivity of CO dissociation on Rh surfaces*, Catalysis Letters Vol.81, 3-4 2002

[15] Wang, G.-C., et al., *Cluster and periodic DFT calculations of adsorption and activation of CO2 on the Cu(hkl) surfaces.* Surface Science, 2004. **570**(3): p. 205-217

[16] M. Gajdoš, A. Eichler and J. Hafner, *CO adsorption on close-packed transition and noble metal surfaces: trends from ab initio calculation*, J. Phys.: Condens. Matter 16 1141(2004)

[17] Maestri, M., *New Strategies in Chemical Synthesis and Catalysis*, B.Pignataro, Editor. 2012, Wiley-VCH. p. 219-246

[18] T. Bligaard, J.K. Nørskov, , , S. Dahl, J. Matthiesen, C.H. Christensen,, J. Sehested *The Brønsted–Evans–Polanyi relation and the volcano curve in heterogeneous catalysis , J.Cat.* Volume 224, Issue 1, 15 May 2004, Pages 206–217

[19] Wang, S., Temel, B., Shen, J., Jones, G., Grabow, L. C., Studt, F., Nørskov, J. K.. *Universal Brønsted-Evans-Polanyi relations for C-C, C-O, C-N, N-O, N-N, and O-O dissociation reactions*. Catalysis Letters, 141(3), 370–373(2011).

[20] Maestri, M. and K. Reuter, *Semiempirical Rate Constants for Complex Chemical Kinetics: First-Principles Assessment and Rational Refinement.* Angewandte Chemie International Edition, 2011. **50**(5): p. 1194-1197

[21] Salciccioli, M., M. Stamatakis, S. Caratzoulas, and D.G. Vlachos, *A review of multiscale modeling of metal-catalyzed reactions: Mechanism development for complexity and emergent behavior,* Chemical Engineering Science, 66 (2011) 4319-4355

[22] Sabbe, M.K., M.F. Reyniers, and K. Reuter, *First-principles kinetic modeling in heterogeneous catalysis: an industrial perspective on best-practice, gaps and needs*, Catalysis Science &Technology, 2 (2012) 2010-2024.).

[23] Musselwhite, N. and G.A. Somorjai, *Topics in Catalysis*, 56 (2013) 1277-1283(2013)

[24] Schlogl, R.,*Theory in Heterogeneous Catalysis; an Experimentalist's View,* Cattech, 5 (2001) 146-170*).*

[25] Somorjai GA, Frei H, Park JY, *Advancing the Frontiers in Nanocatalysis, Biointerfaces, and Renewable Energy Conversion by Innovations of Surface Techniques,* J Am Chem Soc 131:16589 (2009)

[26] Musselwhite, N. and G.A. Somorjai, *Topics in Catalysis, 56 (2013) 1277-1283*

[27] Rioux RD, Song H, Hoefelmeyer JD, Yang PD, Somorjai GA, *High-Surface-Area Catalyst Design: Synthesis, Characterization, and Reaction Studies of Platinum Nanoparticles in Mesoporous SBA-15 Silica* J Phys Chem B 109:2192(2005)

[28] Hohenberg, P.K., W. , *Inhomogeneous Electron Gas.* Physical Review, 1964. **136**(3B).

[29] Kohn, W. and L.J. Sham, *Self-Consistent Equations Including Exchange and Correlation Effects.* Physical Review, 1965. **140**(4A): p. A1133-A1138

[30] Henkelman, G., B.P. Uberuaga, and H. Jonsson, *A climbing image nudged elastic band method for finding saddle points and minimum energy paths.* The Journal of Chemical Physics, 2000. **113**(22): p. 9901-9904

[31] Masel, R., *Chemical Kinetics and Catalysis.* 2001, New York: John Wiley and Sons

APPENDIX

List of acronyms

DFT: Density Functional Theory

BEP: Brønsted-Evans-Polanyi

UBI-QEP: Unity Bond Index- Quadratic Exponential Potential

MEP: Minimum Energy Path

TS: Transition State

TSs: Transition States

Quantum espresso

Input File Structure

```
        calculation='relax'
        restart_mode='from_scratch'
        prefix='lattice',
        pseudo_dir = '/fermi/home/userexternal/fmotta00/Qe_pseudo',
        outdir='./tmp'
        nstep = 1000
 &system
    ibrav =4, celldm(1) =10.30961687, celldm(3)=4,
    nat=18, ntyp= 3,
    ecutwfc = 25, ecutrho= 250,
    occupations='smearing', smearing = 'mv', degauss = 0.001,
 &electrons
    mixing_mode='local-TF'
    diago_david_ndim = 8
    mixing_beta = 0.2
    conv_thr =  1.0d-6
    startingwfc = 'random',
    electron_maxstep = 500
/ATOMIC_SPECIES
Rh 1.00 Rh.pbe-nd-rrkjus.UPF
C  1.00 C.pbe-rrkjus.UPF
H  1.00 H.pbe-rrkjus.UPF
ATOMIC_POSITIONS alat
Rh    0.000000  0.000000000 0.000000000        0 0 0
Rh    0.250000  0.144337567 0.408248291        0 0 0
Rh    0.500000  0.288675133 0.816496582        0 0 0
Rh    0.500000  0.000000000 0.000000000        0 0 0
Rh    0.750000  0.144337567 0.408248291        0 0 0
```

Rh 1.000000 0.288675133 0.816496582 0 0 0

Rh 0.250000 0.433012701 0.000000000 0 0 0

Rh 0.500000 0.577350268 0.408248291 0 0 0

Rh 0.750000 0.721687834 0.816496582 0 0 0

Rh 0.750000 0.433012701 0.000000000 0 0 0

Rh 1.000000 0.577350268 0.408248291 0 0 0

Rh 1.250000 0.721687834 0.816496582 0 0 0

Rh 0.000000 0.000000000 1.224744873 0 0 1

Rh 0.500000 0.000000001 1.224744873 0 0 1

Rh 0.250000 0.433012701 1.224744873 0 0 1

Rh 0.750000 0.433012701 1.224744873 0 0 1

C 0.000000 0.000000000 1.500000000

H 0.000000 0.000000000 1.700000000

K_POINTS {automatic}

6 6 1 1 1 1